Hung Nguyen-Schäfer

# Rotordynamics of Automotive Turbochargers

Linear and Nonlinear Rotordynamics
– Bearing Design – Rotor Balancing

Springer

Rotordynamics of Automotive Turbochargers

Hung Nguyen-Schäfer

# Rotordynamics of Automotive Turbochargers

Linear and Nonlinear Rotordynamics
- Bearing Design - Rotor Balancing

 Springer

*Author*
Dr. Hung Nguyen-Schäfer
Bosch Mahle Turbo Systems
    GmbH & Co. KG
Stuttgart
Germany
Email: hung.nguyen-schaefer@bmturbosystems.com

# Preface

This book has arisen from my many years of experience in the automotive industry, as a development engineer and a senior expert of rotordynamics of automotive turbochargers. It is intended for senior undergraduates and graduates in mechanical engineering, research scientists, and practicing engineers who work on the rotordynamics of automotive turbochargers. It could be also used as a rotordynamic textbook in colleges and universities, and practical handbook of rotordynamics in the automotive turbochargers.

The topic of rotordynamics of automotive turbochargers is a widely interdisciplinary working field, firstly involving *rotordynamics* to study dynamics of rotating machines at very high rotor speeds and as well as to balance the rotor. Secondly, it involves *thermodynamics* and *turbo matching* to compute working conditions of the turbochargers. Thirdly, it involves *fluid and bearing dynamics* to compute the acting loads in the bearings at various operating conditions, and to design the hydrodynamic oil-film bearings. Lastly, it involves *applied tribology* to reduce bearing friction and wears of the journal and bearings. In order to understand the rotordynamic phenomena, readers are assumed to have some mathematical requisite backgrounds for modeling and simulating nonlinear rotordynamics of turbochargers. The author tries to keep the mathematics requirement as simple as possible in this book; however, without any mathematical background, it is quite difficult to comprehend and thoroughly understand the rotordynamic behaviors of the turbochargers.

Exhaust gas turbochargers used in the automobiles of personal, commercial vehicles, and off-road engines have some important discrepancies to the heavy turbomachines applied to the power plants, chemical, and aeroplane industries. The automotive turbochargers are much smaller compared to the industrial turbomachines. Therefore, they generally work at very high rotor speeds in various dynamically operating conditions, such as highly transient rotor speeds, variable pressures, high temperatures of exhaust gas, and as well as unsteady-state mass flow rates of the intake air and exhaust gas. The industrial turbomachines are larger and heavier, and often operate at a nearly stationary condition. Due to the large compressor and turbine wheels, they operate at relatively low rotational speeds from 3,000 rpm (Europe) or 3,600 rpm (US) in the power plants for the electrical frequency of 50 Hz or 60 Hz up to about 15,000 rpm in the chemical industries and aeroplanes. On the contrary, the exhaust gas turbochargers mostly work at the high rotor speeds from 150,000 rpm to 350,000 rpm in the automotive applications. Therefore, the unbalance force is much larger than the rotor weight, leading

to nonlinear characteristics of the oil-film bearings used in the automotive turbo-chargers. As a reason, nonlinear rotordynamics is usually applied to the turbo-chargers to study and compute the nonlinear rotor responses of the harmonic, sub-, and supersynchronous vibrations.

Moreover, turbocharger engineers in the industry have to confront many problems at once, namely good quality, feasibility, form tolerances at the mass-production, time to market (TTM), highly innovative products, and product price. The last one is a very important issue for the company. No matter how good the products are, but nobody could afford them because they are very expensive. Then, the question is, how long the company could survive without selling any product or always selling products at a loss. Parallel to the product price, turbo-chargers must be qualitative and innovative in terms of high efficiency, best low-end-torque, working at high temperatures of the exhaust gas, less or no wear of the bearings, and as well as low airborne noises. They should come to the market as soon as possible since the first bird gets the worm; i.e., despite highly innovative products, the time to market (TTM) is always shorter because the competitors never sleep. Additionally, the turbochargers should work in all operating conditions while they are produced at a possibly wide range of the form tolerances in the mass-production; e.g., radial and thrust bearings with the large form tolerances since producing them with the narrow ones increases the production cost, leading to rise in the product price.

All these boundary conditions make the turbocharger development in the industry much more difficult, especially in the nonlinear rotordynamics of turbocharger-ers. Therefore, development engineers of turbochargers need to have deeply understanding backgrounds of rotordynamics and bearing systems containing radial and thrust bearings applied to the automotive turbochargers. Furthermore, such issues of the rotor balancing and tribology in the bearings have to be coped with, so that the produced turbochargers work in any case at the given industrial development conditions. Customer requirements of the automotive turbochargers are very high, in terms of good rotordynamic stability, low airborne noises, less or no wear of the bearings at high oil temperatures, and as well as an acceptable product price.

Despite all careful efforts, there would be some unpredictable errors in this book. I would be very grateful to get your feedbacks and hints of errors. As a reason, readers of this book need to have a thorough analysis before applying it to their individual applications, and take their own responsibilities for possible damages.

Hung Nguyen-Schäfer
Stuttgart, Germany

# About the Author

Dr. Hung Nguyen-Schäfer is a senior expert in rotordynamics and bearing designs of turbochargers at Bosch Mahle Turbo Systems (BMTS) in Germany. He received B.Sc. and M.Sc. in mechanical engineering with nonlinear vibrations in fluid mechanics from the University of Karlsruhe, Germany in 1985; his Ph.D. degree in nonlinear thermo- and fluid dynamics from the same university. In 1988, he joined Bosch Company and worked as technical manager on many development projects of anti-lock braking and traction systems, high-pressure fuel injection systems, combustion engine systems, fluid cavitation, and electric drive turbochargers for automotive fuel cell systems (PEMFC). Since 2007, Dr. Nguyen-Schaefer has been in charge of rotordynamics and bearing designs of automotive turbochargers at Bosch Mahle Turbo Systems (BMTS) located in Stuttgart, the joint venture of Bosch and Mahle.

He has extensive experience in the fuel injection systems of gasoline, diesel, compressed natural gas (CNG), anti-lock braking systems, and automotive turbochargers, especially in rotordynamics and bearing designs. Moreover, he has authored many technical papers and reports, and supervised two Ph.D. and numerous Master's candidates. He holds several international patents in automotive applications and turbochargers. He lives with his wife and one son near Stuttgart in Germany.

# Contents

# Chapter 1
# Turbocharging Concepts

## 1.1  Introduction

The enacted average $CO_2$ emission for new passenger vehicles in Europe is limited to 120 g/km from 2012 (65% produced vehicles) to 2015 (100%). This emission limit is reduced to the ambitious long-term target of 95 g/km from 2020. Additionally, the average $CO_2$ emission limit for new light-duty commercial vehicles is 175 g/km from 2014 (70% manufactured vehicles) to 2017 (100%); and it is reduced to 147 g/km (ambitious long-term target) from 2020. To reduce carbon dioxide ($CO_2$) and nitrogen oxides ($NO_x$) exhausted by passenger and commercial vehicles and to improve the fuel consumption of the engines, we have already carried out many measures, e.g. high-pressure direct injection (HPDI), exhaust gas recirculation (EGR), variable valve train (VVT), variable compression (VC), and hybrid techniques [3]. Two other important aspects are downsizing of engines by reducing the number of cylinders or volumetric size of cylinders, and turbocharging. Engines with less number of cylinders or small cylinder volumes induce less friction power between the pistons and cylinders. Additionally, the total weight of the vehicle is also reduced due to small engines, leading to less driving friction. Evidently, small engines needs less fuel consumption; in turn, they produce less engine power. Small engines consume less fuel and therefore produce less carbon dioxide ($CO_2$) and as well as nitrogen oxides ($NO_x$). In the point of view of energy and air pollution, they have done a good job to sustain our energy resources and to keep the environment less polluted and clean.

However, it should make more fun at driving, especially with a large acceleration; it needs more power in the small engines. Hence, the specific power defined as the engine power per cylinder volume (kW/liter of cylinder) must be improved. Therefore, we have to capture an unused and cost-free energy source in the vehicles to boost the small engines.

After the combustion of fuel in the engine, a large energy of the exhaust gas still remains in the form of enthalpy at the engine outlet because the temperature of the exhaust gas is quite high (e.g. diesel 820°C to 850°C and gasoline 950°C to 1050°C). Generally, this enthalpy energy escapes from the engine to the environment. Why do we not capture it to boost the engine for improving its specific power? To do that, an exhaust-gas turbocharger is necessary to collect the exhaust

gas in the turbine, and compress the intake air in the compressor to a high pressure for the engine combustion. This procedure is called turbocharging.

The exhaust-gas turbocharger consists of the core unit (called CHRA: center housing and rotating assembly), turbine, compressor, and actuator. Both compressor and turbine wheels are mounted and fixed in the rotor shaft that is supported on the bearing system including two radial bearings and a thrust bearing. The exhaust gas expands in the turbine wheel and generates the rotational kinetic energy. The created turbine energy drives the rotor shaft and compresses the intake air to a high pressure by means of the compressor.

The concept of using exhaust-gas turbochargers takes advantages of improving specific engine power and reducing $CO_2$ and $NO_x$. They are either having the same power of the original engine but less fuel consumption, reducing carbon dioxide and as well as nitrogen oxides in the downsized engine or getting more power at the same fuel consumption in the turbocharged engine without downsizing for those who need more fun at driving. However, the first one is an important key to help us comply with the new emission law for the automotive vehicles.

Generally, turbocharged downsized engines with the same original power could save nearly 10% fuel consumption by reducing the cylinder volume by 25%. To abide by the current emission law of the automotive vehicles or to boost engines of passenger vehicles, two-stage turbochargers are applied to engines working at the large charge-air compression ratios higher than 4. The two-stage turbochargers consist of two single-stage turbochargers with different sizes that are sequentially set up in the engine. Some applications of different turbocharger types to the engines shall be discussed in the next section.

## 1.2   Applications of Turbochargers to Downsized Engines

In the automotive applications, single-stage turbochargers are normally used at the air compression ratio to nearly 2.5. There are two layouts of turbochargers with Exhaust Gas Recirculation (EGR) at low pressure (LP-EGR) and high pressure (HP-EGR). Due to reburning the exhaust gas by means of its recirculation to the engine, nitrogen oxides ($NO_x$) are reduced.

**a)   Single-Stage Turbochargers with EGR**
Figure 1.1 shows a single-stage turbocharger with high-pressure EGR (HP-EGR) in which the exhaust gas partly returns to the engine with a maximum of 50% EGR rate before entering the turbine. The EGR rate is defined as the ratio of the recirculation to outflow mass flow rates of the exhaust gas. The EGR valve regulates the EGR mass flow rate so that $NO_x$ emission fulfills the current emission law.
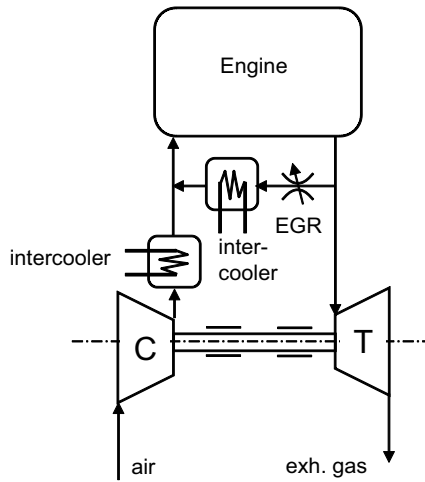
**Fig. 1.1** Schematic layout of a single-stage turbocharger with HP-EGR

Due to expansion energy of the exhaust gas, the turbine T propels the compressor C that compresses the intake air to the maximum pressure ratio of nearly 2.5. The compression process in the compressor brings the inlet air from the ambient condition to the high pressure and temperature as well. To maintain the compressed charge air with a large mass flow rate for the engine combustion, the intercooler cools it after the compressor; otherwise, the air mass flow rate is reduced due to low density of the charge air at high temperature. In case of turbochargers with high-pressure EGR, the pressure of the recirculated exhaust gas after the cooler must be higher than the charge air pressure at the engine inlet. Hence, the pressure ratio of the turbine is required high enough to overcome the charge air pressure. Generally, the turbine with HP-EGR is designed to be smaller than the one without HP-EGR, so that the exhaust gas pressure remains higher than the compressed charge air pressure. Therefore, the engine must works against the high exhaust gas pressure at the engine outlet. As a reason, the fuel consumption increases compared to the system without HP-EGR, especially at high turbocharging pressures. That is the reason why the HP-EGR valve should be closed as soon as the exhaust gas meets the requirements of the current emission law.

To overcome this disadvantage, the high-pressure EGR valve is replaced in the low-pressure site at the turbine outlet. The turbocharger layout shown in Fig.1.2 is called turbocharger with low-pressure EGR (LP-EGR). Its advantage is the engine working condition against the high pressure of the exhaust gas drops; therefore, the fuel performance becomes much more efficient.
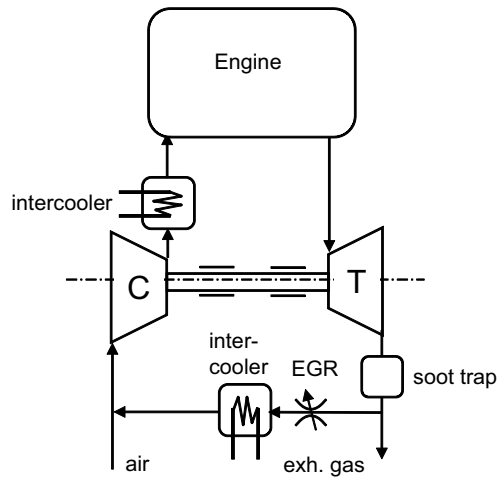
**Fig. 1.2** Schematic layout of a single-stage turbocharger with LP-EGR

However, the LP-EGR turbocharger has two disadvantages: firstly, the low exhaust gas pressure of the turbine outlet and pressure drop in the soot trap limit the LP-EGR mass flow rate, hence the EGR rate; secondly, the exhaust gas and ambient air mix together at the compressor inlet; they are compressed in the compressor to the higher pressure. Due to pressure increase in the compressor wheel, the exhaust gas condenses in the compressor wheel, leading to chemical erosion on the surface of the wheel. Additionally, the unburned hard particles in the exhaust gas impact and damage the aluminum compressor wheel at high rotor speeds, especially the blades at the inlet of the compressor wheel. To prevent the compressor wheel from such damages, it is usually coated by NiCr coating layer. that causes a reduction of the mass flow rate of the charge air and therefore the compressor power as well. Due to low-cycle fatigue (LCF) of the driving cycle, the lifetime of the compressor wheel is shortened.

**b) Biturbochargers**
Bi- or twin-turbo consists of two small turbochargers with the same volumetric size; they are parallel setup and operate at the same time in the entire rotor speed range (called parallel bi-/twin-turbo). The mass flow rate of the exhaust gas is divided into both turbines of the bi-turbo. In case of an engine with four cylinders, in which two cylinders provide exhaust gas for each turbocharger, as shown in Fig. 1.3. After compression and cooling, both compressors provide the engine with the total compressed charge air.
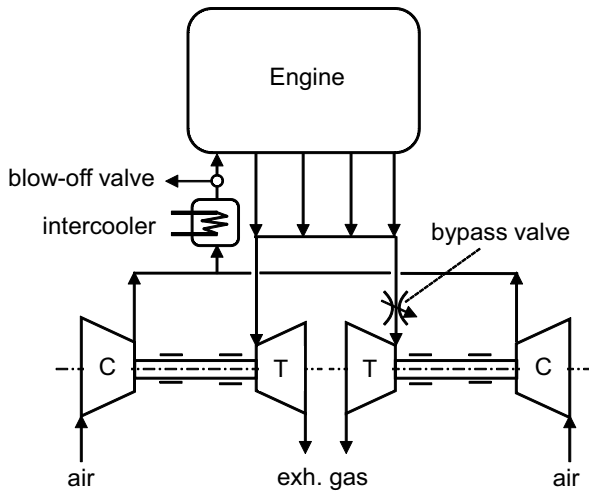
**Fig. 1.3** Schematic layout of a biturbocharger

At the small geometry of turbochargers, the rotor generally has small mass inertia moment that speeds up quickly to achieve the maximum torque; therefore, the transient behavior of the parallel bi-turbo is strongly improved in the low-end torque (LET). However, a small turbocharger delivers small air mass flow rate that alone does not fulfill the required nominal engine power. Hence, both small turbochargers operate parallel to deliver enough compressed charge air for the required nominal engine power.

In case of the sequential bi-turbo that is parallel setup and sequentially operates, only one of the bi-turbo, e.g. the left one operates alone at the low engine speed by closing the bypass valve. The small turbocharger builds up the charge air pressure much earlier, and improves the transient behavior of the turbocharger at the low engine speed. At high engine speeds, the other turbocharger (the right one) is additionally turned on by opening the bypass valve where both turbochargers work parallel like the parallel bi-turbo. Hence, the mass flow rate of the charge air increases to empower the engine at the high speeds. To strongly powered W-engines with 16 cylinders (e.g. Bugatti Veyron 16.4 Super Sport with a power of nearly 1200 hp), four single turbochargers (sequential quad turbo) are applied; every turbocharger is used for four cylinders (4 x 4).

**c) Two-Stage Turbochargers**
Two-stage turbochargers are used for high-pressure ratios in which two different volumetric sizes of turbochargers are sequentially setup and work at the given procedure regulated by the bypass valves (s. Fig. 1.4). Leaving the engine, the exhaust gas containing a large enthalpy is at high pressure and temperature; therefore, the turbocharger at the primary stage (C1, T1) is smaller than the secondary stage (C2, T2). In case of unregulated pressures in sequentially working condition for both stages in applications of commercial vehicles, the primary turbocharger is

normally about 15% smaller than the single-stage turbocharger; the secondary turbocharger is 15% larger than the single-stage one.

At the low engine speeds, only the small turbocharger works alone because of its small mass inertia moment; therefore, the transient behavior is significantly improved compared to the large one. During this time, the bypass valves are closed, and the waste gate in the secondary turbine T2 is fully opened, so that the secondary turbocharger is nearly decoupled from the two-stage turbocharger. At the middle engine speeds from about 1,500 rpm, both turbochargers work sequentially by means of the regulated bypass valves. As soon as the required charge air pressure is reached at the high engine speeds, only the secondary turbocharger works alone because the larger turbine T2 has a large efficiency at the high rotor speeds. In this case, the primary turbocharger will be decoupled from the two-stage turbocharger in which both bypass valves are fully opened.
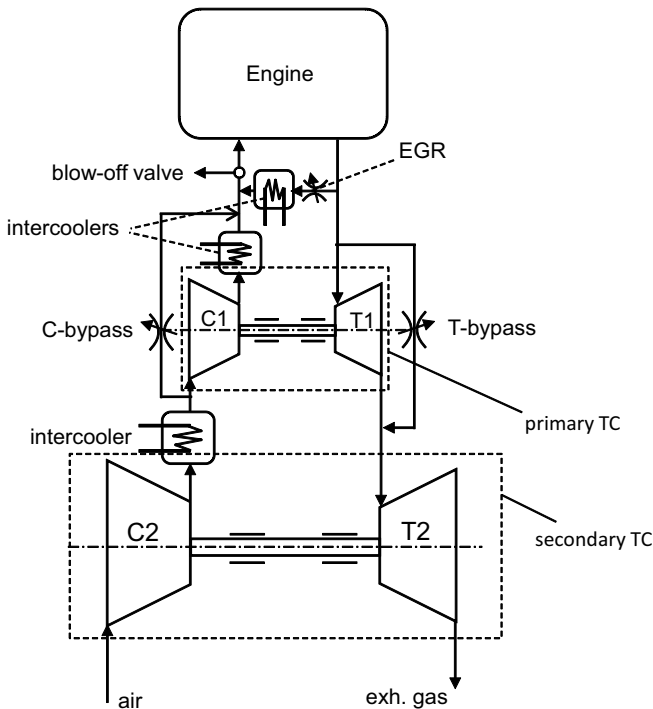


**Fig. 1.4** Schematic layout of a regulated 2-stage turbocharger with HP-EGR

Similar to the earlier turbochargers, the compressed charge air must be cooled by the intercoolers before entering the engine in order to maintain a high air mass flow rate for the required nominal engine power.

The pressure ratio of the two-stage turbocharger is displayed in Fig. 1.5. The compressor pressure ratio in the full load curve results from the product of the pressure ratios of the two compressors of the two-stage turbocharger. Due to

the small volumetric size of the primary turbocharger, its pressure load curve speeds up faster at the low engine speeds in order to receive a good transient response in the low-end torque.

The engine torques of the single- and two-stage turbochargers are compared to each other over the rotor speed of turbocharger, as illustrated in Fig. 1.6. The single-stage turbocharger is larger than the primary but smaller than the secondary stage of the two-stage turbocharger. Therefore, the transient response of the two-stage is better than the single-stage. The advantages of the two-stage turbocharger are better response behavior, high-pressure ratio of the compressed charge air, and higher engine torque in the entire operating speed range.
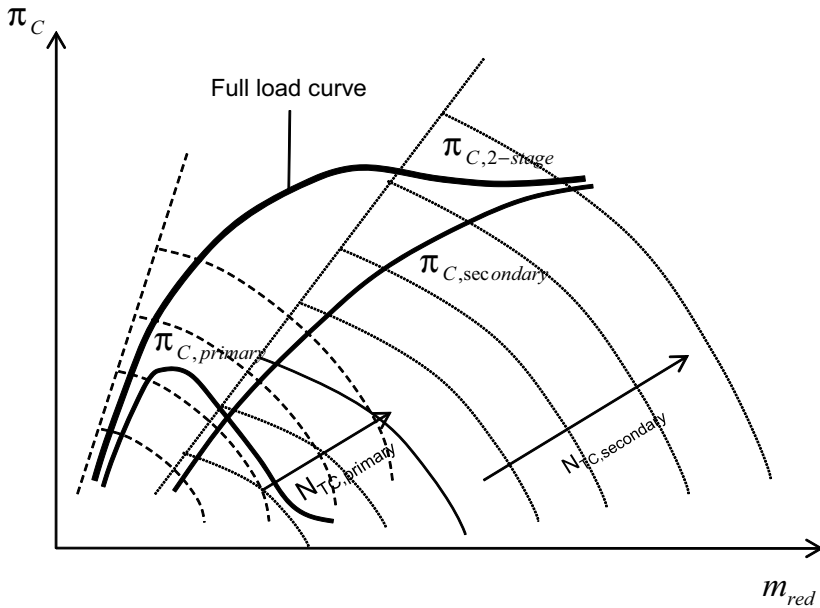


**Fig. 1.5** Pressure ratio of a regulated two-stage turbocharger
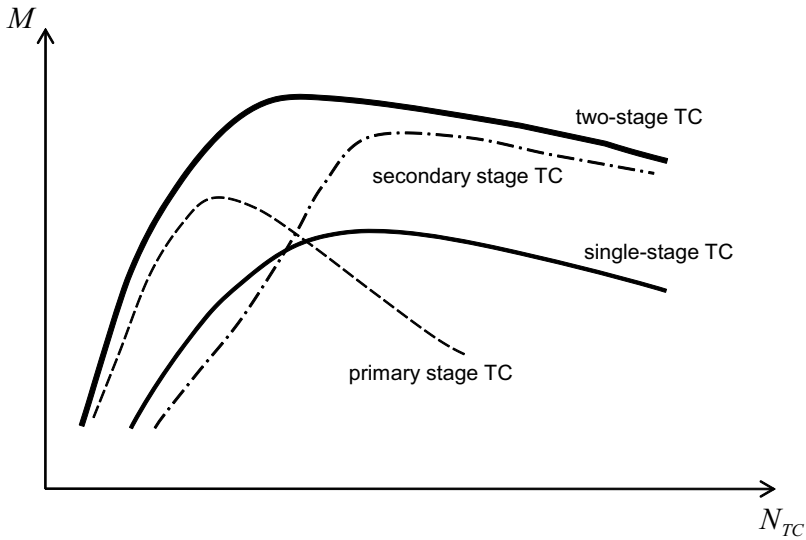
**Fig. 1.6** Engine torques of the single- and two-stage turbochargers

### d)   Electrically Driving Turbochargers (EDTC) in Fuel Cells

Automotive fuel cells are usually PEMFC type (Proton Exchange Membrane Fuel Cells). Gaseous hydrogen $H_2$ is supplied to the anode of the membrane electrode assembly (MEA) of the fuel cell. At the anode side, hydrogen molecules $H_2$ are catalytically split into hydrogen protons $H^+$ and electrons $e^-$. The protons cross over the humid membrane to the cathode; the electrons flow over the external load circuit to the cathode side of MEA. Oxygen in the supply air reacts with the crossed-over hydrogen protons and the electrons in the cathode, resulting in the exhaust gases, such as $N_2$, residual $O_2$, and water steam $H_2O$.

The transport of electrons between the anode and cathode of the MEA produces electric power at 250 Volts to 450 Volts DC. The generated electric power depends on the reaction pressure of the supply air and hydrogen in the fuel cell and as well as others parameters. Therefore, the charge air pressure should be 1.5 to 2 bars absolute, so that the fuel cell works in the optimum condition. In this case, the single-stage exhaust gas turbocharger compresses the supply air. However, at the low power working condition, the exhaust gas temperature is relatively low (between 80°C and 100°C) and its mass flow rate is quite small. Hence, an electric motor is required besides the turbine wheel to drive the compressor additionally. At increasing the fuel cell power, the mass flow rate of the exhaust gas increases; so, the turbine wheel generates energy enough to drive the compressor alone without the electric motor. In this case, the electric motor is turned off at once in order to spare the generated fuel cell power.

To avoid electric sparks and wear in the coal burst, the electric motor must work with a high alternative current supply voltage (VAC) that is inverted from the direct current voltage (VDC) of the fuel cell by a DC/AC inverter, as shown

in Fig. 1.7. The electric drive turbocharger normally operates at the maximum rotor speed of approximately 120,000 rpm because of its large compressor and turbine wheels. The used power of the electric motor is too high when the rotor speed exceeding 120,000 rpm to fulfill the required transient response $\tau_{90}$ (about 0.8 s) of the fuel cell. In this case, the fuel cell overall efficiency decreases. As a reason, the rotor speed of the EDTC is limited by nearly 120,000 rpm.
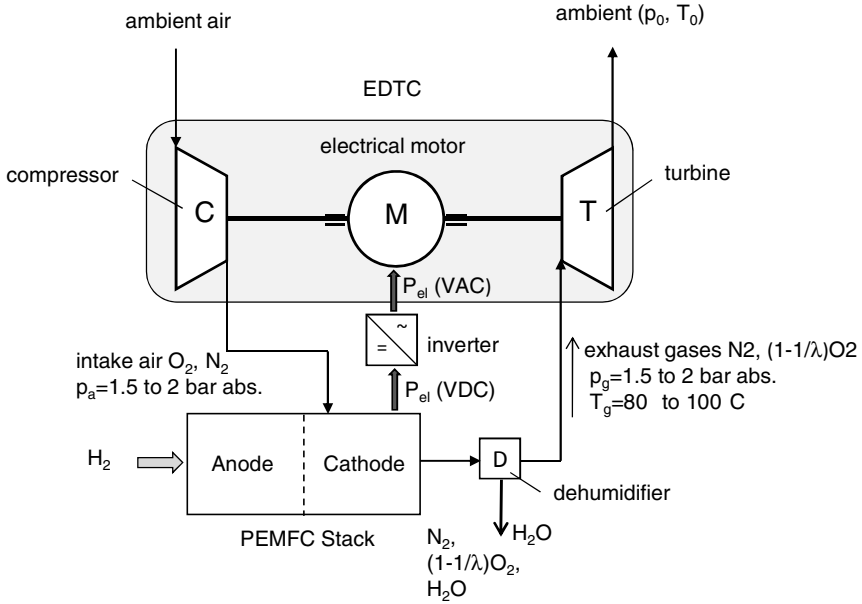


**Fig. 1.7** Schematic layout of EDTC in PEM-Fuel Cells

**e) Turbo-Compound**
Turbo-compound consists of a turbocharger and a second power turbine that uses the exhaust gas at a still high temperature of the turbocharger to generate an additional power for the engine. The turbine shaft is directly geared to the engine drive shaft to increase the engine torque, engine power, and as well as the engine efficiency.

## 1.3   Regulation of the Charge Air Pressure

There are three kinds of regulation of the charge air (i.e. compressed intake air) pressure in the automotive and industrial turbochargers: unregulated, wastegated (WG), and variable turbine geometry (VTG) turbochargers. The pressure ratio of the charge air varies from 2.0 to 2.5 in passenger vehicles, and 3.5 to 4.0 in commercial vehicles.

There is neither waste gate (WG) nor variable turbine geometry (VTG) in the unregulated turbochargers that are mostly applied to the commercial vehicles. Figure 1.8 shows the unregulated pressures of the exhaust gas and charge air in the engine. At increasing the engine speeds, more charge air is required; therefore, the charge air pressure is increased from the ambient pressure to the maximum pressure for the engine combustion. The charge air pressure is always higher than the exhaust gas pressure in the unregulated turbochargers.
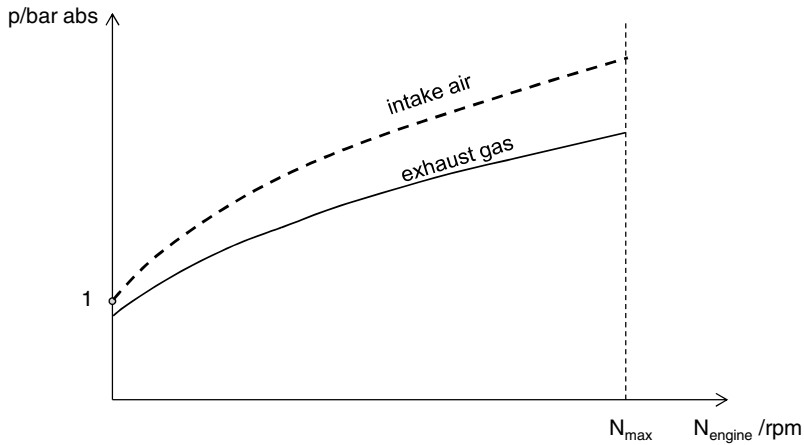


**Fig. 1.8** Unregulated pressures vs. engine speed

In case of the regulation of the charge air pressure, two measures are used in turbochargers: waste gate (WG) and variable turbine geometry (VTG). The pressure behavior of the wastegated turbocharger is shown in Fig. 1.9. As soon as the turbocharger reaches the maximum torque, the waste gate in the turbine is continuously open to regulate the charge air pressure remaining nearly constant. At high engine speeds, the exhaust gas pressure increases even higher than the charge air pressure because the flow resistance of the exhaust gas in the catalytic converter (CAT), diesel particle filter (DPF), and muffler increases with the mass flow rate.
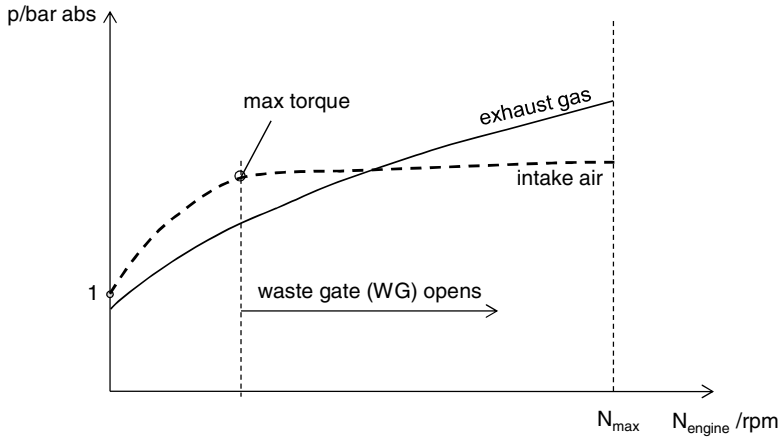
**Fig. 1.9** Regulated pressures of a wastegated turbocharger

Figure 1.10 shows the pressure behavior of a VTG turbocharger versus the engine speed. At low engine speeds, the VTG is in the minimum open position (i.e. min-flow position). Therefore, the exhaust gas pressure increases higher than the charge air pressure. After reaching the maximum torque, the VTG continuously further opens at increasing the engine speed in order to regulate the charge air pressure remaining constant. Shortly after opening the VTG, drops the exhaust gas pressure a little bit lower than the charge air pressure; then, it increases over the charge air pressure at high engine speeds. The pressure drop of the exhaust gas is resulted from suddenly opening the VTG. After that, the VTG continuously opens at increasing the mass flow rate of the exhaust gas to the maximum engine speed in order to keep the charge air pressure constant. At increasing the engine speed, more exhaust gas is produced, leading to the increase of the exhaust gas pressure due to the high flow resistance of the exhaust gas in the exhaust system containing the catalytic converter, diesel particle filter, and muffler.
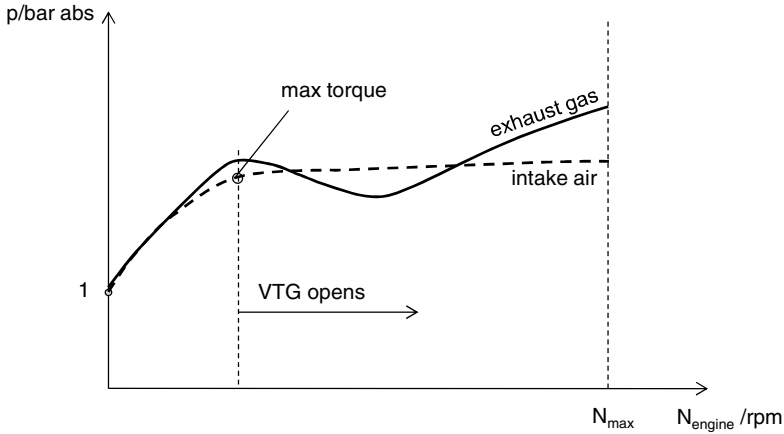
**Fig. 1.10** Regulated pressures of a VTG turbocharger

## 1.4 Required Charge Air Pressure of Downsized Engines

Depending on the engine power, cylinder volumetric size, and number of cylinders, the charge air pressure is determined at every engine speed. The engine power is calculated in

$$P_e = \dot{m}_f \eta_f Q_f = \dot{m}_a \eta_f Q_f \frac{\dot{m}_f}{\dot{m}_a} \tag{1.1}$$

where

$\dot{m}_f, \dot{m}_a$ are the mass flow rates of fuel and charge air;

$\eta_f$ is the fuel combustion efficiency;

$Q_f$ is the fuel heating value.

The air-fuel ratio is defined as

$$AFR \equiv \frac{\dot{m}_a}{\dot{m}_f} \tag{1.2}$$

The air-fuel ratio varies from 12 to 18 in applications to SI engines (spark-ignition gasoline engines) and from 18 to 70 to CI engines (compression-ignition diesel engines).

The required air mass flow rate for the engine combustion is resulted from the air density $\rho_a$, the cylinder total volume $V_{cyl}$, and the engine speed $N$ as follows:

$$\dot{m}_a = \eta_{vol} \rho_a V_{cyl} \frac{N}{n_R} \tag{1.3}$$

within

$V_{cyl} = zV_c$ where z is the number of cylinders,
$V_c$ is the single cylinder volume;
$\eta_{vol}$ is the volumetric efficiency;
N is the engine speed;
$n_R = 1$ for two-stroke; $= 2$ for four-stroke engine.

The $\lambda$ number (called relative air-fuel ratio) defines the ratio of the required air mass flow rate to the stoichiometric one for the combustion.

$$\lambda = \frac{\dot{m}_a}{\dot{m}_{a,stoich}} \tag{1.4}$$

The relative air-fuel ratio can be rewritten in the air-fuel ratio of the required AFR and the stoichiometric one as follows:

$$\lambda = \frac{AFR}{AFR_{stoich}} \tag{1.5}$$

where
$\lambda = 1$ at stoichiometric combustion;
$\lambda < 1$ at rich mixture (more unburned hydrocarbons in the exhaust gas);
$\lambda > 1$ at lean mixture (more residual oxygen in the exhaust gas).

In a stoichiometric combustion of gasoline with octane fuel ($C_8H_{18}$), $AFR_{stoich}$ equals 14.7. In applications of the SI gasoline engines, $\lambda$ would be chosen between 0.9 to 1.1 for an optimal fuel consumption and engine power.

Having combined equations (1.1), (1.2), and (1.3), the engine power becomes

$$P_e = \left( \eta_{vol} \rho_a V_{cyl} \frac{N}{n_R} \right) \eta_f Q_f \frac{1}{AFR} \tag{1.6}$$

In case of downsizing engines by means of smaller cylinder volume $V_{cyl}$ (i.e., less number of cylinders or smaller volume of each cylinder), the air density must be increased, so that the required nominal engine power is arrived according to eq. (1.6).

The smaller engine has less friction between the cylinders and pistons. Hence, the fuel mileage MPG (miles per gallon) is improved. In the turbocharged original engine, the cylinder volume remains unchanged; however, the engine power increases due to high density of the charge air. The density of charge air is increased by means of turbocharging. Assumed that the charge air is an ideal gas, the charge air pressure results in

$$p_a = \rho_a R_a T_a \tag{1.7}$$

where
$\rho_a$ is the charge air density;
$R_a$ is the charge air gas constant;
$T_a$ is the charge air temperature.

Inserting eq. (1.7) in eq. (1.6), the engine power becomes at the engine speed N

$$P_e = \left( \frac{\eta_{vol}\, p_a V_{cyl}}{R_a T_a} \cdot \frac{N}{n_R} \right) \eta_f Q_f \frac{1}{AFR} \tag{1.8}$$

The charge air temperature is calculated by

$$T_a = T_1 \left( 1 + \frac{1}{\eta_C} \left[ \left( \frac{p_a}{p_1} \right)^{\frac{\kappa_a - 1}{\kappa_a}} - 1 \right] \right) \tag{1.9}$$

where
$T_1$ is the inlet temperature of the intake air;
$p_1$ is the inlet pressure of the intake air;
$p_a$ is the charge air pressure;
$\eta_C$ is the isentropic compressor efficiency;
$\kappa_a$ is the isentropic exponent of the charge air ($\approx 1.4$).

Thus, the density ratio of the charge air to the ambient air is resulted from the state equation of an ideal gas.

$$\frac{\rho_a}{\rho_1} = \left( \frac{p_a}{p_1} \right) \left( \frac{T_a}{T_1} \right)^{-1} = \frac{\pi_C}{1 + \frac{1}{\eta_C} \left[ \pi_C^{\left( \frac{\kappa_a - 1}{\kappa_a} \right)} - 1 \right]} \tag{1.10}$$

where $\pi_C$ is the compression ratio of the charge air.

Figure 1.11 shows the density ratio and temperature of the charge air versus the compression ratio. The charge air density increases without using a charge-air in-tercooler to about two times the ambient air density at the compression ratio of 3, and an average compressor efficiency of 75%. In this case, the charge air tempera-ture $T_a$ rises from the ambient air temperature $T_1$ of 20°C to nearly 165°C. Note that the lower the compressor efficiency, the higher the charger air temperature, and the lower the charge air density, leading to the smaller mass flow rate of the charge air, in turn to reducing the engine power according to eq. (1.6). On the contrary, by the ideal isothermal intercooling after the compression, the charge air density is triple the ambient air density at the compression ratio of 3; i.e., 50% more than the charge air density in case of without using a charger-air intercooler. In practice, the density ratio of the charge air at the compression ratio of 3 is between 2 and 3 by using a charge-air intercooler in the turbocharger (s. Section 2.5).
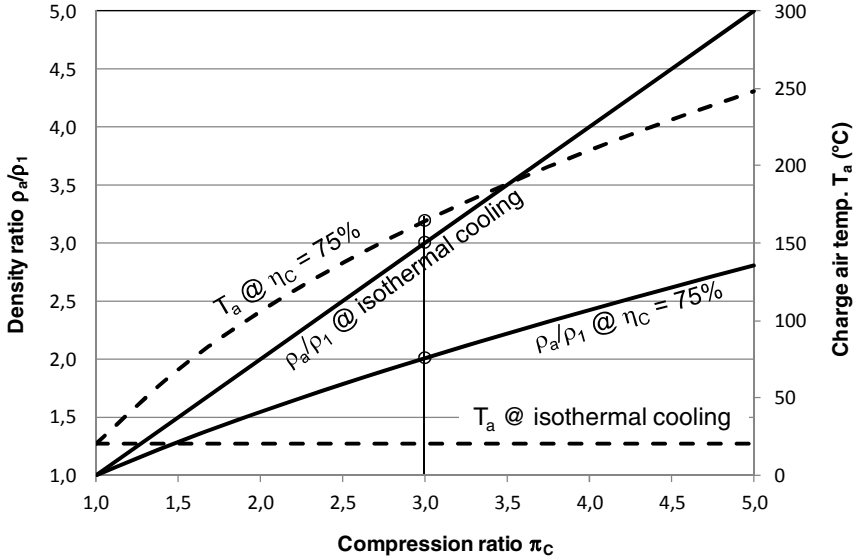
**Fig. 1.11** Density ratio and temperature of the charge air at $T_1 = 20°C$

The engine torque $M_e$ is resulted from the engine power $P_e$ and its rotational speed $\omega_e$.

$$P_e = M_e \omega_e = 2\pi N M_e \tag{1.11}$$

Thus,

$$M_e = \left( \frac{\eta_{vol} p_a V_{cyl}}{2\pi R_a T_a n_R} \right) \eta_f Q_f \frac{1}{AFR} \tag{1.12}$$

Equations (1.8) and (1.12) indicate that the engine power $P_e$ and engine torque $M_e$ do not increase so much even at high charge air pressure $p_a$ when the charge air temperature $T_a$ also increases. That is the reason why the charge air must be cooled after the compressor, as shown in Section 1.2. Note that the charge air density is the key issue in the engine turbocharging according to eq. (1.6), not the charge air pressure. To satisfy the requirement of the engine power and engine torque of the downsized engines, the charge air density must be increased by increasing the pressure and reducing the temperature of the charge air according to eqs (1.8), (1.9), and (1.10). Therefore, the turbocharger with intercoolers is applied to increasing the charge air mass flow rate of the turbocharger.

The mean effective pressure $p_{me}$ of the engine is used to characterize the engine performance; it is defined as the engine work produced in a cycle per the total cylinder volume displaced in the same cycle.

$$p_{me} = \frac{W_e}{V_{cyl}} = \frac{P_e n_R}{V_{cyl} N} \tag{1.13}$$

In order to maintain the same engine power of the downsized engine by reducing the total cylinder volume, the mean effective pressure $p_{me}$ must be increased by turbocharging.

$$P_e = \frac{p_{me} V_{cyl} N}{n_R} \tag{1.14}$$

To estimate the fuel consumption of the engine, the brake specific fuel consumption (bsfc) is defined as the required fuel mass flow rate per unit power of the engine.

$$bsfc = \frac{\dot{m}_f}{P_e} \tag{1.15}$$

The brake specific fuel consumption bsfc has the unit g/(kW.s) or g/kJ depending on the working conditions.

## References

1. Baines, N.C.: Fundamentals of Turbocharging. Concepts ETI, Inc. (2005)
2. Basshuysen, R., et al.: Gasoline Engine with Direct Injection. Vieweg and Teubner (2009)
3. Golloch, R.: Downsizing bei Verbrennungsmotoren. Springer, Heidelberg (2005)
4. Heywood, J.B.: Internal Combustion Engine Fundamentals. McGraw-Hill (1988)
5. Japikse, D., Baines, N.C.: Introduction to Turbomachinery. Concepts ETI, Inc. (1994)

# Chapter 2
# Thermodynamics of Turbochargers

## 2.1 Thermodynamic Characteristics

Some essential thermodynamic characteristics of gases are needed to know in the turbocharging. They have been usually applied to the turbocharging of engines, where the charge air and exhaust gas are assumed as compressible ideal gases.

- Total temperature $T_t$ in Kelvin (K) is resulted from the sum of the static $T_s$ (K) and dynamic temperatures $T_{dyn}$ (K). The static temperature is measured at the wall, where the gas velocity equals zero due to the viscous boundary layer.

$$T_t = T_s + T_{dyn} = T_s + \frac{c^2}{2c_p} \tag{2.1}$$

where c is the gas velocity, $c_p$ is the heat capacity at constant pressure.

- Total pressure $p_t$ is calculated from the isentropic gas equation as follows:

$$p_t = p_s \left( \frac{T_t}{T_s} \right)^{\frac{\kappa}{\kappa-1}} = p_s \left( 1 + \frac{\kappa-1}{2} M^2 \right)^{\frac{\kappa}{\kappa-1}} \tag{2.2}$$

where $p_s$ is the static pressure; $\kappa = c_p/c_v$, the isentropic exponent of gas; M is the Mach number of gas (M = c/a), in which a is the sonic speed.

- Specific total enthalpy $h_t$ is resulted from the sum of the gas specific enthalpy and specific kinetic energy of gas.

$$h_t = h + \frac{c^2}{2} \tag{2.3}$$

where the gas specific enthalpy h (enthalpy per mass unit, J/kg) is defined.

$$h = c_p (T - T_0) = u + \frac{p}{\rho} \tag{2.4}$$

within $\rho$ is the gas density; $T_0$ is the reference temperature; u is the specific internal energy of gas that equals the product of the heat capacity at constant volume $c_v$ and temperature difference of gas $\Delta T$; therefore, u = $c_v.\Delta T$.

## 2.2 Efficiencies of Compressor and Turbine

The compression process in the compressor is a polytropic process with increasing entropy due to friction and losses in the compressor. Figure 2.1 shows the compression process of the intake air 1→ 2, from the ambient pressure $p_1$ to the required charge air pressure $p_2$. The compressor efficiency $\eta_C$ is defined as the ratio of the isentropic total enthalpy change from 1t to 2st to the polytropic total enthalpy change from 1t to 2t. In other words, the compressor needs more energy in the polytropic compression process to compress the intake air from the state 1 to state 2 than the possibly minimal required energy of the compressor stage in the isentropic compression process.



$$\eta_C = \frac{\Delta h_{s,tt}}{\Delta h_{12,tt}} = \frac{T_{2st} - T_{1t}}{T_{2t} - T_{1t}}$$
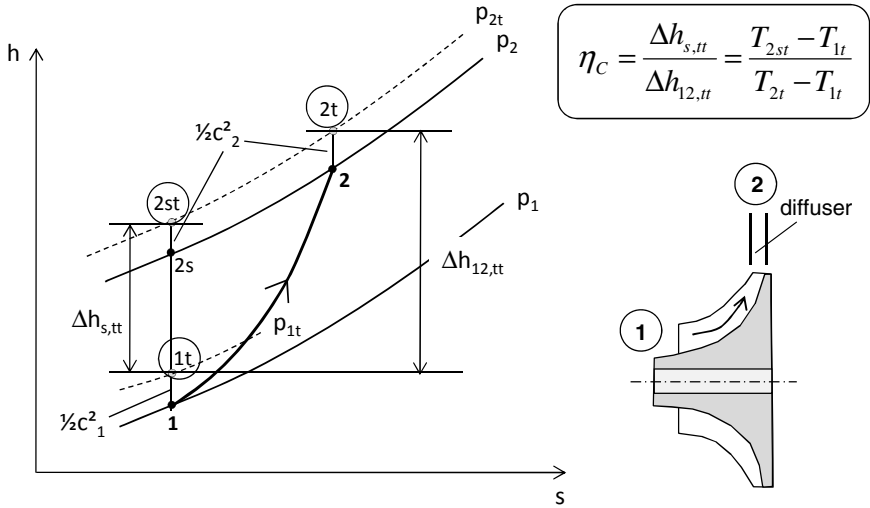
**Fig. 2.1** Compression process in the compressor stage

The total–total isentropic efficiency of the compressor stage (further called compressor) consisting of the compressor wheel and diffuser is expressed in

$$\eta_C = \frac{\Delta h_{s,tt}}{\Delta h_{12,tt}} = \frac{T_{2st} - T_{1t}}{T_{2t} - T_{1t}} \tag{2.5}$$

The total–total isentropic efficiency is generally used in the compressor since the kinetic energy of gas in the state 2 is transformed into the pressure energy in the diffuser to further increase the pressure of charge air.

Having used thermodynamic equations for the isentropic process, the compressor efficiency can be written in the total pressures and temperatures at the inlet and outlet of the compressor, and the isentropic exponent of the charge air $\kappa_a (\approx 1.4)$.

$$\eta_C = \frac{\left(\dfrac{p_{2t}}{p_{1t}}\right)^{\left(\frac{\kappa-1}{\kappa}\right)_a} - 1}{\left(\dfrac{T_{2t}}{T_{1t}}\right) - 1} \tag{2.6}$$

The compressor efficiency is determined by measuring the total pressures and temperatures at the inlet and outlet of the compressor according to Eq. (2.6). The maximum total–total isentropic efficiency of the compressor $\eta_C$ is normally between 70% and 80% at the design point of the compressor wheel.

Analogous to the compressor, the efficiency of turbine is resulted from the polytropic expansion process of the exhaust gas $3 \rightarrow 4$, from the exhaust gas pressure $p_3$ to the turbine outlet pressure $p_4$ (s. Fig. 2.2). The turbine efficiency $\eta_T$ is defined as the ratio of the polytropic total enthalpy change from 3t to 4t to the isentropic total enthalpy change from 3t to 4s. Physically speaking, the turbine delivers less output energy due to friction and losses in the polytropic expansion process than the possibly maximum energy given in the isentropic process.



$$\eta_T = \frac{a_T}{\Delta h_{s,ts}} = \frac{\Delta h_{34,tt}}{\Delta h_{s,ts}} = \frac{T_{4t} - T_{3t}}{T_{4s} - T_{3t}}$$
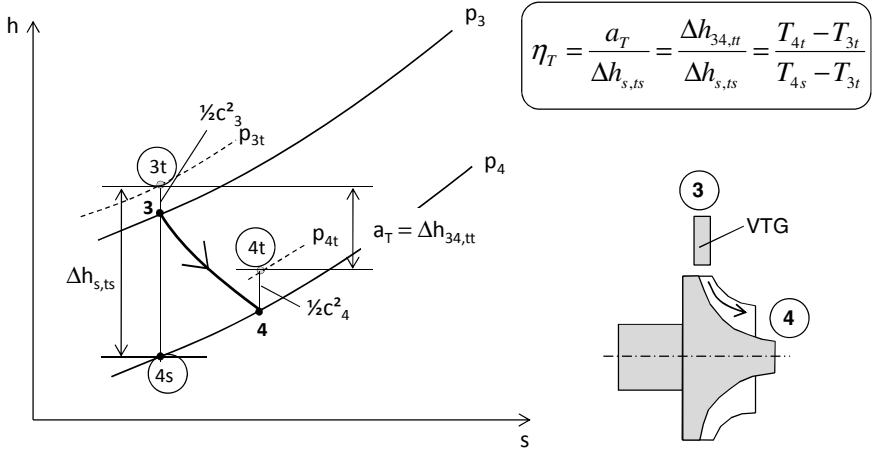
**Fig. 2.2** Expansion process in the turbine stage

The total-static isentropic efficiency of the turbine stage (further called turbine) consisting of the turbine wheel and variable turbine geometry (VTG) or waste gate (WG) is written as

$$\eta_T = \frac{\Delta h_{34,tt}}{\Delta h_{s,ts}} = \frac{T_{4t} - T_{3t}}{T_{4s} - T_{3t}} \tag{2.7}$$

The total-static isentropic efficiency is normally used in the turbine since the kinetic energy of gas in the state 4 does not generate the turbine power any longer.

Having applied thermodynamic equations to the isentropic process, the turbine efficiency can be expressed in the total pressure and temperature at the inlet and outlet of the turbine, and the isentropic exponent of the exhaust gas $\kappa_g$ ($\approx 1.32$).

$$\eta_T = \frac{1 - \left(\dfrac{T_{4t}}{T_{3t}}\right)}{1 - \left(\dfrac{p_{4s}}{p_{3t}}\right)^{\left(\frac{\kappa - 1}{\kappa}\right)_g}} \tag{2.8}$$

The turbine efficiency is determined by measuring the total pressure and temperature at the inlet and outlet of the turbine according to Eq. (2.8). The maximum total-static isentropic efficiency of the turbine $\eta_T$ is normally between 65% and 70% at the design point of the turbine wheel.

## 2.3 Turbocharger Equations

The turbocharger consists of the turbine, compressor, and core unit (CHRA: center housing and rotating assembly) including the rotor and bearing system. Both turbine and compressor wheels are fixed in the rotor shaft that is supported on the bearing system of the radial and thrust bearings. The rotating shaft including the compressor wheel, turbine wheel, thrust rings, radial bearings, and seal rings is called the *rotor* of the turbocharger.

Due to expanding the exhaust gas of the engine in the turbine, it generates the turbine power that depends on the mass flow rate of the exhaust gas through the turbine and the isentropic enthalpy drop in the turbine. The effective turbine power results in

$$P_T = \eta_T \dot{m}_T \left| \Delta h_{sT} \right| \tag{2.9}$$

The isentropic enthalpy drop in the turbine stage is calculated by using some thermodynamic equations.

$$\left| \Delta h_{sT} \right| = c_{p,g} T_3 \left[ 1 - \left(\frac{p_4}{p_3}\right)^{\left(\frac{\kappa - 1}{\kappa}\right)_g} \right] \tag{2.10}$$

By inserting Eq. (2.10) in Eq. (2.9), one obtains the effective turbine power in a function of the mass flow rate, inlet temperature, and pressure ratio of the turbine.

$$P_T = \eta_T P_{T,ideal} \equiv \eta_T \dot{m}_T c_{p,g} T_3 \left[ 1 - \left( \frac{p_4}{p_3} \right)^{\left( \frac{\kappa-1}{\kappa} \right)_g} \right] \tag{2.11}$$

Due to the friction loss in the bearing system, the required compressor power equals the effective turbine power reduced by the mechanical efficiency $\eta_m$.

$$P_C = \eta_m P_T = \eta_m \eta_T \dot{m}_T c_{p,g} T_3 \left[ 1 - \left( \frac{p_4}{p_3} \right)^{\left( \frac{\kappa-1}{\kappa} \right)_g} \right] \tag{2.12}$$

Analogously, the required compressor power to compress the intake air is calculated from the ideal compressor power at the isentropic compression and compressor efficiency.

$$P_C = \frac{P_{C,ideal}}{\eta_C} \equiv \frac{\dot{m}_C \Delta h_{sC}}{\eta_C} \tag{2.13}$$

where
$\Delta h_{sC}$ is the increase of the isentropic enthalpy in the compressor.

Thus,

The required compressor power of the charge air is written as a function of the mass flow rate, inlet temperature, and pressure ratio of the compressor.

$$P_C = \frac{P_{C,ideal}}{\eta_C} \equiv \frac{\dot{m}_C c_{p,a} T_1}{\eta_C} \left[ \left( \frac{p_2}{p_1} \right)^{\left( \frac{\kappa-1}{\kappa} \right)_a} - 1 \right] \tag{2.14}$$

Having combined Eqs (2.12) and (2.14), one obtains the pressure ratio of the compressor $\pi_C$ in *the first turbocharger equation*.

$$\pi_C = \frac{p_2}{p_1} = \left( 1 + \left\langle \frac{\dot{m}_T}{\dot{m}_C} \frac{T_3}{T_1} \eta_{TC} \right\rangle \frac{c_{p,g}}{c_{p,a}} \left[ 1 - \left( \frac{p_3}{p_4} \right)^{-\left( \frac{\kappa-1}{\kappa} \right)_g} \right] \right)^{\left( \frac{\kappa}{\kappa-1} \right)_a} \tag{2.15}$$

within the overall efficiency of the turbocharger $\eta_{TC}$ is written as

$$\eta_{TC} = \eta_m \eta_T \eta_C \tag{2.16}$$

To achieve the high boost pressure of the charge air $p_2$, the compressor pressure ratio $\pi_C$ could be improved according to the first turbocharger equation (2.15) if

- the overall turbocharger efficiency $\eta_{TC}$ is high, especially a high mechanical efficiency of the bearing system in low-end torque;
- the exhaust gas temperature $T_3$ is high due to the large enthalpy. Hence, more turbine power is generated;
- the turbine pressure ratio $\pi_T$ (called turbine expansion ratio) is as high as possible;
- the inlet air temperature $T_1$ is as low as possible, so that the charge air temperature $T_2$ is low, leading to a high density of the charge air;
- the exhaust gas pressure $p_3$ is chosen at an optimal pressure in order to compromise between the turbine power and specific fuel consumption;
- the mass flow rate of the exhaust gas through the turbine is large.

The first turbocharger equation (2.15) shows the behavior of the pressure ratio $\pi_C$ ($\equiv p_2/p_1$) of the compressor versus the pressure ratio $\pi_T$ ($\equiv p_3/p_4$) of the turbine. In fact, the term $\delta$ in the angle brackets $\langle\ \rangle$ of Eq. (2.15) does not change so much along the full load curve of the compressor in the operating engine speed range. Therefore, the behavior of the pressure ratios of turbine and compressor can be displayed at various dimensionless parameters in the angle brackets $\langle\ \rangle$ of Eq. (2.15), as shown in Fig. 2.3.
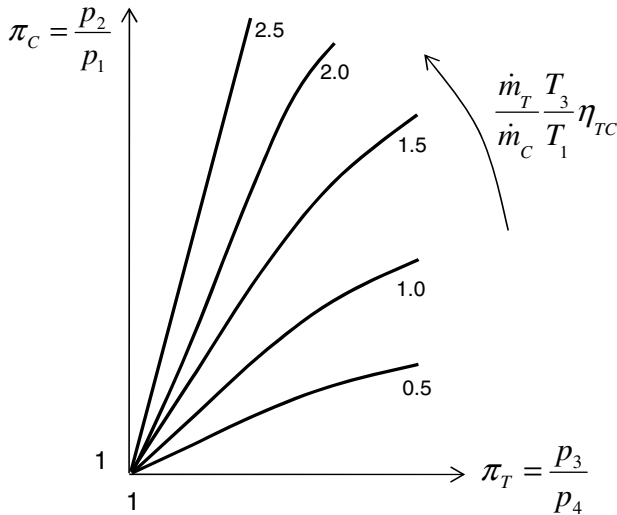


**Fig. 2.3** Behavior of the pressure ratios $\pi_C$ versus $\pi_T$

The exhaust gas flow in the turbine can be considered as the flow in a nozzle where the inlet and outlet pressures are $p_3$ and $p_4$, respectively. Based on the flow equation for compressible fluids in the nozzle, *the second turbocharger equation* describes the mass flow rate through the turbine in a function of the pressure, temperature at the turbine inlet, and the turbine expansion ratio.

$$\dot{m}_T = \mu A_T\, p_{3t} \sqrt{\frac{2}{R_g T_{3t}}} \sqrt{\left(\frac{\kappa}{\kappa-1}\right)_g \left[\left(\frac{p_{3t}}{p_4}\right)^{\frac{-2}{\kappa_g}} - \left(\frac{p_{3t}}{p_4}\right)^{-\left(\frac{\kappa+1}{\kappa}\right)_g}\right]} \qquad (2.17)$$

where
$\mu$ is the flow coefficient due friction and flow contraction at the nozzle outlet;
$A_T$ is the throttle cross-sectional area in the turbine wheel.

To eliminate the influences of $p_{3t}$ and $T_{3t}$ on the mass flow rate in the turbine shown in Eq. (2.17), the so-called corrected mass flow rate is defined as follows:

$$\dot{m}_{T,cor} \equiv \frac{\dot{m}_T \sqrt{T_{3t}}}{p_{3t}}$$

$$= \mu A_T \sqrt{\frac{2}{R_g}} \sqrt{\left(\frac{\kappa}{\kappa-1}\right)_g \left[\left(\frac{p_{3t}}{p_4}\right)^{\frac{-2}{\kappa_g}} - \left(\frac{p_{3t}}{p_4}\right)^{-\left(\frac{\kappa+1}{\kappa}\right)_g}\right]} = f\langle \pi_{T,ts}\rangle \qquad (2.18)$$

Eq. (2.18) indicates that the corrected mass flow rate of the turbine is independent of the inlet condition of the exhaust gas of $p_{3t}$ and $T_{3t}$; it depends only on the turbine expansion ratio $\pi_{T,ts}$.

The performance map of the turbine displays the corrected mass flow rate over the turbine expansion ratio $\pi_{T,ts}$ according to Eq. (2.18) at various rotor speeds in Fig. 2.4. From a turbine pressure ratio of approximately 3, the mass flow rate has no longer increased, even at higher rotor speeds. In this case, the flow in the turbine becomes a choke flow, where the exhaust gas speed at the throttle area has reached the sonic speed at Mach number Ma = 1. As a reason, the exhaust gas mass flow rate through the turbine corresponding to the nominal engine power must be smaller than the choke mass flow rate. Notice that the isentropic turbine efficiency at the choked flow condition is extremely low ($\eta_T < 60\%$) that is unusable in the turbochargers.

$$\dot{m}_{T,cor} = \frac{\dot{m}_T \sqrt{T_{3t}}}{p_{3t}}$$
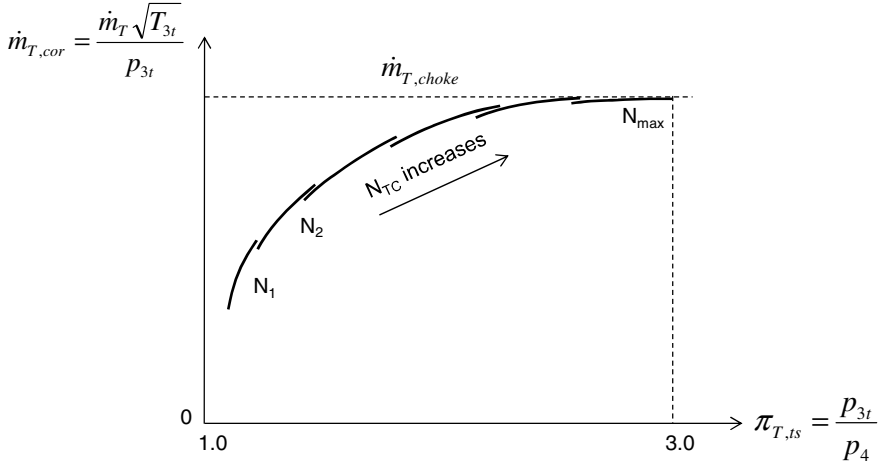


**Fig. 2.4** Performance map of the turbine

The mechanical efficiency of turbocharger induced by the bearing friction is re-sulted from Eq. (2.12).

$$\eta_m = \frac{P_C}{P_T} = \frac{\dot{m}_C c_{p,a}(T_2 - T_1)}{\eta_C \eta_T \dot{m}_T c_{p,g} T_3 \left[1 - \left(\dfrac{p_4}{p_3}\right)^{\left(\frac{\kappa-1}{\kappa}\right)_g}\right]} \tag{2.19}$$

Thus, the efficiency product of the mechanical and turbine efficiencies is written by using Eqs (2.14) and (2.19) in

$$\eta_m \eta_T = \frac{\dot{m}_C c_{p,a} T_1 \left[\left(\dfrac{p_2}{p_1}\right)^{\left(\frac{\kappa-1}{\kappa}\right)_a} - 1\right]}{\eta_C \dot{m}_T c_{p,g} T_3 \left[1 - \left(\dfrac{p_3}{p_4}\right)^{-\left(\frac{\kappa-1}{\kappa}\right)_g}\right]} \tag{2.20}$$

The efficiency $\eta_m \eta_T$ described in Eq. (2.20) is a key part in the overall efficiency of the turbocharger. It is determined by measuring the thermodynamic characteristics given in Eq. (2.20), such as the mass flow rates in the compressor and turbine, temperatures $T_1$ and $T_3$, compressor efficiency $\eta_C$, pressures at the compressor in- and outlet $p_1$ and $p_2$, and as well as pressures at the turbine in- and outlet $p_3$ and $p_4$. Figure 2.5 displays the efficiency $\eta_m \eta_T$ versus pressure ratio of turbine $\pi_{T,ts}$ at various speeds of the turbocharger.
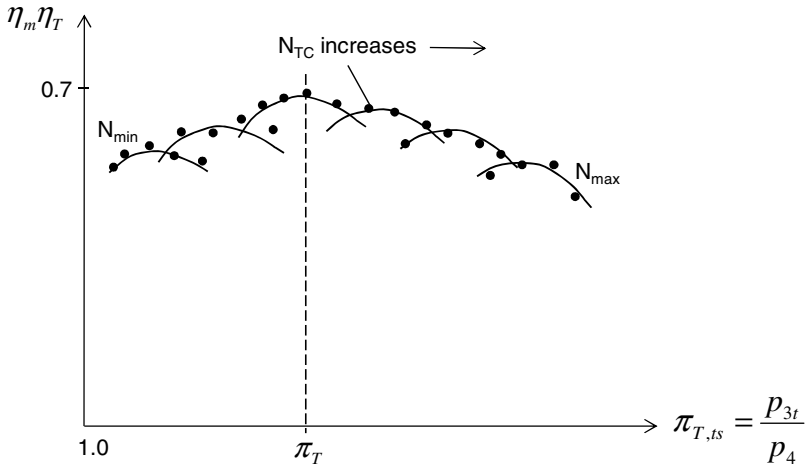
**Fig. 2.5** Efficiency $\eta_m\eta_T$ versus $\pi_{T,ts}$ at various speeds of the turbocharger

At low rotor speeds corresponding to the low-pressure ratios $\pi_T$, the mechanical efficiency is quite small due to large bearing friction at the low oil temperature in the bearings; additionally, the turbine efficiency is also small because of the aerodynamic working condition at the low rotor speed. Therefore, the resulting efficiency $\eta_m\eta_T$ remains low.

At the design point, the turbine efficiency is maximal while the mechanical efficiency of the bearings could increase a little bit due to the increased oil temperature in the bearings and high rotor speed at the same time. As a reason, the efficiency $\eta_m\eta_T$ reaches the maximum value at the turbine pressure ratio of the design point.

As the rotor speed further increases to the maximum speed, the turbine efficiency drops due to the aerodynamic working condition at the high speeds, and the mechanical efficiency decreases because the bearing friction increases at high rotor speeds. Hence, the efficiency $\eta_m\eta_T$ decreases with the turbine pressure ratio.

However, the efficiency $\eta_m\eta_T$ depends not only on the turbine pressure ratio but also on the position of VTG (variable turbine geometry), as shown in Fig. 2.6. Initially, the VTG is open at the min-flow condition for the minimum mass flow rate that is called 0% VTG (position 1) at the idle condition of the engine. The efficiency $\eta_m\eta_T$ increases with the turbine pressure ratio because the turbine efficiency becomes larger at high mass flow rates corresponding to the increased turbine pressure ratio. Then, the VTG is partly open at 30% VTG (position 2); at increasing the turbine pressure ratio, the corrected mass flow rate through the turbine rises, leading to the high turbine efficiency. Hence, the efficiency $\eta_m\eta_T$ increases since the turbine pressure ratio rises, as shown in Fig. 2.5. Hence, the efficiency $\eta_m\eta_T$ is higher than the efficiency at the position 1. At the further open position of 70% VTG (position 3), the turbine efficiency begins decreasing at the high mass flow rates corresponding to the large turbine pressure ratios. Finally, the VTG is fully open at 100% VTG (position 4); the mass flow rate
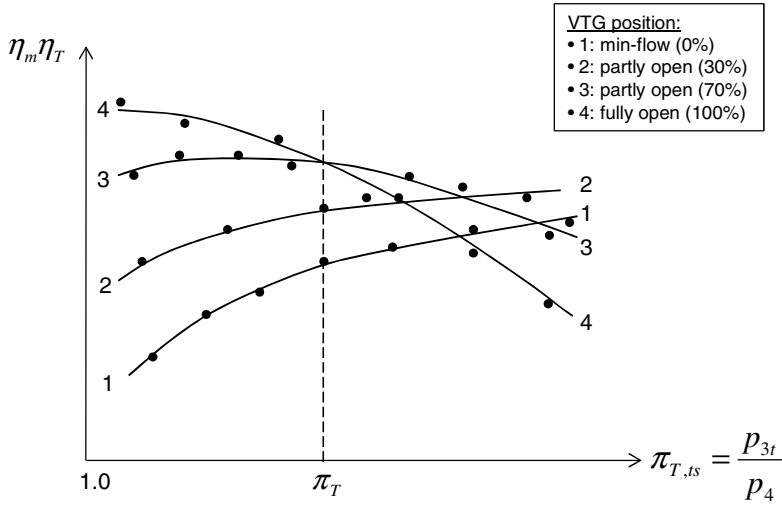
**Fig. 2.6** Efficiency $\eta_m\eta_T$ versus $\pi_{T,ts}$ at various VTG positions

significantly increases in the turbine at increasing the turbine pressure ratio, therefore the turbine efficiency reduces with the turbine-pressure ratio. As a result, the efficiency $\eta_m\eta_T$ drops with the turbine-pressure ratio, as illustrated in Fig. 2.6.

The performance map of the compressor shows the compressor ratio $\pi_C$ versus the corrected mass flow rate, as displayed in Figure 2.7.
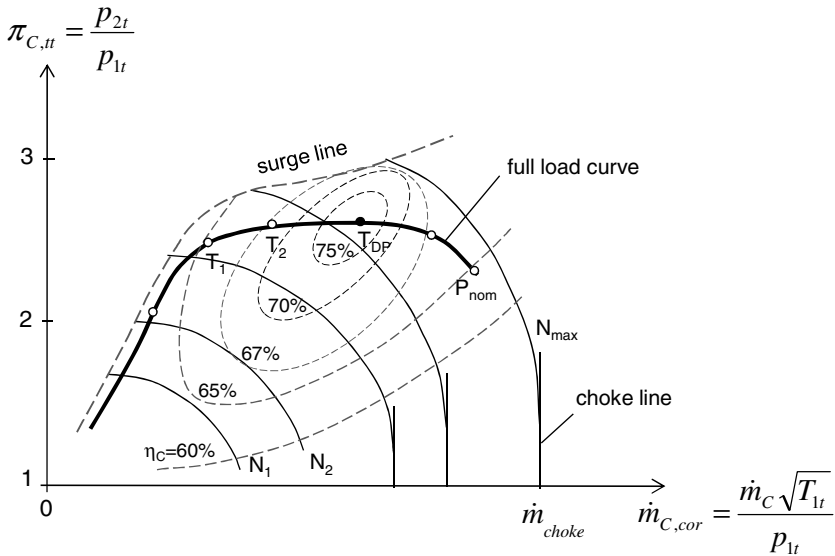


**Fig. 2.7** Performance map of the compressor

At low speeds of the turbocharger from about 30% of the maximum rotor speed $N_{max}$ at the idle condition, the pressure ratio relatively increases with a large pressure gradient to satisfy the requirement of a good transient response in low-end torque. At further increasing the rotor speed N to nearly 70% of $N_{max}$, the compressor pressure ratio increases to approximately 2.5, and the engine achieves the maximum torque $T_1$. Due to the reduced turbine efficiency at the high rotor speeds, in turn reducing the overall efficiency of the turbocharger, the compressor-pressure ratio decreases at the nominal engine power $P_{nom}$ in the full load curve according to the first turbocharger equation (2.15).

## 2.4  Response Time of Turbochargers

The response time is an important characteristic dealing with turbolag in the automotive turbochargers. The turbolag is the delayed time that the turbocharger needs to reach the maximum engine torque after speeding–up.

To characterize the turbolag of the turbocharger, the response time $\tau_{90}$ is defined as the time required to reach 90% of the maximum engine torque $T_1$ in low-end torque LET (s. Fig. 2.7). The response time $\tau_{90}$ is resulted from the effective turbine power and the polar mass inertia moment of the rotor.

The angular acceleration of the rotor is calculated from the turbocharger dynamics equation.

$$\eta_m P_T - P_C = I_p \ddot{\theta} \Omega \tag{2.21}$$

At acceleration in LET, the compressor power is relatively small compared to the turbine power. Therefore, the effective turbine power mostly accelerates the rotor to the angular rotor speed $\Omega$.

$$\eta_m P_T \approx I_p \ddot{\theta} \Omega \tag{2.22}$$

The rotor speed $N_{TC}$ of the turbocharger in LET is resulted from eq. (2.22).

$$N_{TC} = \frac{\Omega}{2\pi} \approx \frac{\eta_m P_T}{2\pi (I_p \ddot{\theta})} \tag{2.23}$$

By integrating the angular acceleration during the response time $\tau_{90}$, one obtains the average angular rotor velocity in LET

$$\Omega_{90} = \int_0^{\tau_{90}} \ddot{\theta}(t) dt \approx \bar{\bar{\theta}} \tau_{90} \tag{2.24}$$

where

$\bar{\bar{\theta}}$  is the average angular rotor acceleration in the response time.

Having substituted Eqs (2.22) and (2.24), and eliminated the average angular acceleration, the response time of the turbocharger results in

$$\tau_{90} \approx \frac{\Omega_{90}^2 I_p}{\eta_m P_T} \tag{2.25}$$

where

$I_p$ is the polar mass inertia moment of the rotor;

$P_T$ is the effective turbine power;

$\eta_m$ is the mechanical efficiency of the bearings.

To have a good transient response of the turbocharger, it is necessary to keep the response time $\tau_{90}$ as small as possible at the given rotor speed $\Omega_{90}$. Unfortunately, the effective turbine power $P_T$ is relatively small in the low-end torque (LET); therefore, the response time $\tau_{90}$ tends to become large, leading to the large turbo-lag. However, there are some improving measures according to Eq. (2.25):

1. The polar mass inertia moment $I_p$ of the rotor should be small. The turbine wheel plays a key role in the entire polar mass inertia moment of the rotor due to its heavy mass of Inconel 713C. The polar mass inertia moment of the turbine wheel is proportional to its mass m and wheel diameter squared ($D^2$); because of m ~ $\rho D^3$, the polar mass inertia moment of the turbine wheel is written in

$$I_{p,TW} \propto mD^2 \propto \rho D^5 \propto I_p \qquad (2.26)$$

Therefore, in order to reduce the inertia moment of the turbine wheel, there are some possibilities as follows:

- The turbine wheel should be lighter, such as using a light Titanium aluminide TiAl6V4 ($\rho$ = 4.45 g/cm³) instead of the heavy Inconel 713C ($\rho$ = 7.91 g/cm³);
- The turbine wheel is scalloped at the back face to reduce its mass; however, the turbine efficiency $\eta_T$ could be reduced by 2% to 3% due to the inappropriate aerodynamic flow condition at the scalloped back face, leading to reducing the effective turbine power $P_T$ according to Eq. (2.11);
- The turbine wheel diameter D should be reduced to decrease to the polar inertia moment, and to increase the turbine efficiency $\eta_T$ at low rotor speeds, leading to the increase of the effective turbine power $P_T$. However, the small turbine has some negative effects, such as low turbine efficiency $\eta_T$ at high rotor speeds and as well as small mass flow rate; in turn, reducing the nominal turbine power and having low turbine efficiency $\eta_T$ at the high rotor speeds.

2. The mechanical efficiency $\eta_m$ should be increased by using airfoil bearings, magnetic bearings, rolling element bearings, or rotating floating ring bearings with two oil films. Generally, the rolling-element bearings generate less friction power, especially in LET. Contrary to the ball bearings, oil-film bearings induce a little bit more friction power in LET because the effective oil viscosity in the bearing is relatively high at low rotor speeds. In fact, the ratio of the bearing friction to turbine power is relatively high due to the small effective turbine power $P_T$ generated in LET compared to the ratio at high rotor speeds. However, the discrepancy between the friction coefficients of the rolling element and rotating floating ring bearings is negligible at high rotor speeds. Note that the rolling element bearings cost nearly 10 times more than the oil-film bearings.

Therefore, it is recommended to carefully decide which material of the turbine wheel should be used, the suitable diameter of the turbine wheel, either scalloped

or unscalloped turbine wheel. In addition, which bearing system one applies to the turbochargers in compromise between the transient response and production cost.

## 2.5 Turbocharger Matching

In the following section, the procedure of turbocharger matching based on the engine characteristics, compressor performance map, first turbocharger equation, and turbine performance map is shown in Fig. 2.8.
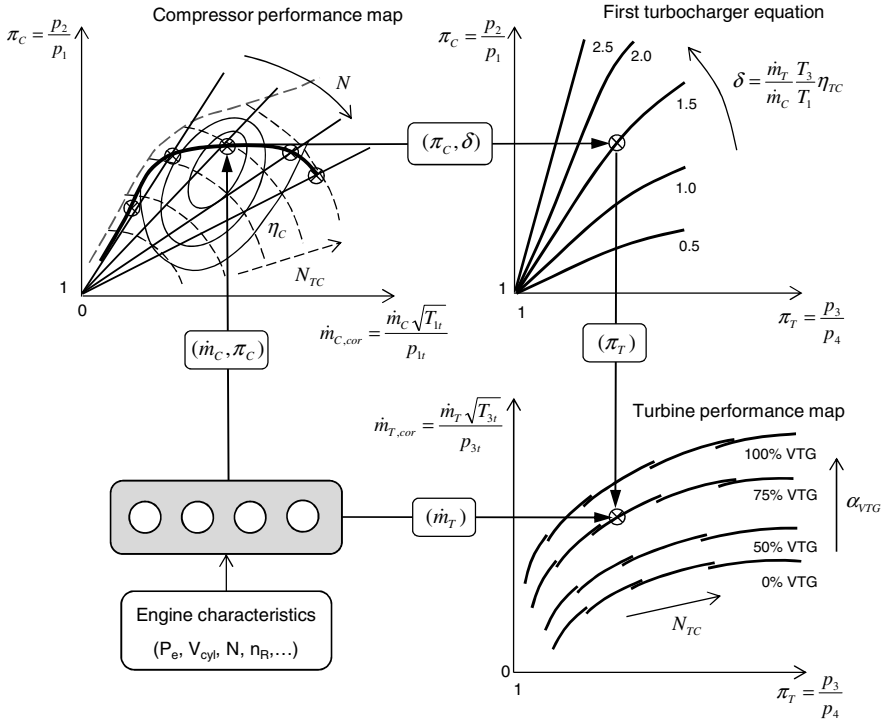


**Fig. 2.8** Procedure of turbocharger matching

The following steps are carried out in the procedure of turbocharger matching:

1) From the engine characteristics (s. Fig. 2.8 bottom left), the working area of the turbocharging in the compressor map is determined at the various operating points, such as low-end torque (LET), maximum torque, design point, and nominal power of the engine. At an operating point, the required mass flow rate of the charge air at the given turbocharger speed for the engine is resulted from the engine power according to equations (1.1) and (1.2). Then, the necessary charge air density for the engine is given by eq. (1.3); the compression ratio of the charge air without using the air intercooler is calculated from eq. (1.10).

Otherwise, by using the air intercooler after the compressor (s. Fig. 2.9), the charge air temperature $T_2$ is reduced at a lower temperature $T_{2*}$, leading to the increase of the charge air density $\rho_{2*}$.

The charge air temperature $T_{2*}$ after the intercooler is calculated from the compressed charge air temperature $T_2$ given in eq. (1.9), coolant inlet temperature $T_c$, and intercooler efficiency $\varepsilon_c$ (normally between 0.6 and 0.8) as follows:

$$T_{2*} = (1 - \varepsilon_c)T_2 + \varepsilon_c T_c < T_2 \tag{2.27}$$

Thus, the charge air temperature at using the air intercooler has decreased by

$$\Delta T_{2*} \equiv T_{2*} - T_2 = \varepsilon_c (T_c - T_2) < 0 \tag{2.28}$$

Therefore, the charge air density increases from $\rho_2$ to $\rho_{2*}$ at a small pressure drop in the intercooler. It is given by using the state equation of an ideal gas.

$$\rho_{2*} = \frac{p_{2*}}{R_a T_{2*}} = \frac{p_2 - \Delta p_c}{R_a T_{2*}} > \rho_2 \tag{2.29}$$

where $\Delta p_c$ is the pressure drop in the charge air intercooler.

Substituting eqs (1.9), (2.27), and (2.29) gives the compression ratio of the compressor with using the air intercooler. It is resulted by iteratively solving eq. (2.30).

$$\pi_C = \frac{p_2}{p_1} = \frac{p_{2*} + \Delta p_c}{p_1} = \frac{\rho_{2*} R_a T_{2*} + \Delta p_c}{p_1}$$

$$= \frac{\rho_{2*} R_a \left[ (1 - \varepsilon_c)T_1 \left( 1 + \frac{1}{\eta_C} \left( \pi_C^{\left(\frac{\kappa-1}{\kappa}\right)_a} - 1 \right) \right) + \varepsilon_c T_c \right] + \Delta p_c}{p_1} \tag{2.30}$$

where the charge air density $\rho_{2*}$ is given by the engine requirement, and $\kappa_a$ ($\approx 1.4$) is the isentropic exponent of the charge air.
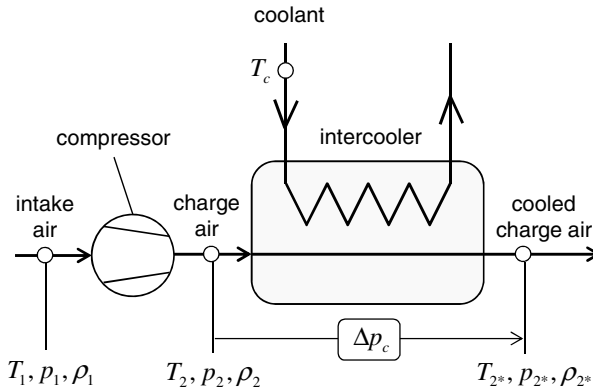


**Fig. 2.9** Compressor with the charge air intercooler

2) The operating point of the turbocharger is located in the compressor perfor-mance map (s. Fig. 2.8 top left) at the given mass flow rate and compression ratio of the charge air that we have just computed in the earlier step. The value δ in the diagram of the first turbocharger equation, as shown in Fig. 2.8 (top right), involves the mass flow rates of the charge air and exhaust gas, the tem-peratures of the exhaust gas and intake air, and the turbocharger efficiency. It is resulted from the working condition of the engine and the guessed or meas-ured efficiency of the turbocharger.

3) From the given compression ratio $\pi_c$ and value δ, the expansion ratio $\pi_T$ of the turbine corresponding to the operating point is determined in the diagram of the first turbocharger equation, as displayed in Fig. 2.8 (top right).

4) Both mass flow rate and expansion ratio of the turbine given by the steps 2 and 3 are used to determine the operating point of the turbocharger in the turbine performance map. The operating point gives the corresponding VTG angular position. Figure 2.8 (bottom right) shows the angular position of 75% VTG; i.e., the VTG opens at 75% of the maximum angle (100% VTG) from the min-flow position (0% VTG). Note that the mass flow rate of the exhaust gas, which is identical with the mass flow rate of the VTG turbine, equals the mass flow rates of the charge air and injected fuel in the cylinders based on the air-fuel ratio AFR defined in eq. (1.2). Therefore, the mass flow rate of the ex-haust gas is written in

$$\dot{m}_T = \dot{m}_a + \dot{m}_f = \dot{m}_a \left( \frac{AFR + 1}{AFR} \right) \tag{2.31}$$

By using the turbomachinery theory, the outlet diameter $D_2$ (exducer diameter) of the compressor wheel and the inlet diameter $D_3$ (inducer diameter) of the turbine wheel are computed at the given effective powers and mass flow rates of the com-pressor and turbine, mechanical efficiency, and turbocharger speed. The procedure of turbocharger matching is iterated until the guessed values, such as the efficien-cies of the compressor and turbine, efficiency of the air intercooler, etc. are con-verged. Furthermore, the computed values could be rematched with the measured efficiencies as soon as they are available.

# References

1.  Aungier, R.H.: Turbine Aerodynamics. ASME Press (2006)
2.  Baines, N.C.: Fundamentals of Turbocharging. Concepts ETI, Inc. (2005)
3.  Cumpsty, N.A.: Compressor Aerodynamics. Krieger Publishing Company (2004)
4.  Heywood, J.B.: Internal Combustion Engine Fundamentals. McGraw-Hill (1988)
5.  Japikse, D., Baines, N.C.: Introduction to Turbomachinery. Concepts ETI, Inc. (1994)
6.  Japikse, D., et al.: Axial and Radial Turbines. Concepts ETI Inc. (2003)
7.  Whitfield, A., Baines, N.C.: Design of Radial Turbomachines. Pearson Education, Longman Scientific and Technical (1990)

# Chapter 3
# Vibrations of Turbochargers

## 3.1  Introduction

Exhaust gas turbochargers used in the automobiles, such as passenger, on-road vehicles, and off-road engines have some discrepancies to the heavy turbomachines applied to the power plants and chemical industries. The first ones are much smaller and work at high rotor speeds in various operating conditions, such as variable rotor speeds, pressures, temperatures, and as well as mass flow rates. Contrary to the automotive turbochargers, the industrial turbomachines are bigger, heavier and mostly operate at a stationary working condition. Due to their large sizes of compressor and turbine wheels, the turbomachines only operate at low rotor speeds between 3,000 to 20,000 rpm. The maximum circumferential velocities of the turbine and compressor wheels used in the automotive turbochargers are approximately 530 and 560 m/s, respectively. The maximum circumferential velocities of the compressor and turbine wheels are determined by the durability of materials at various driving cycles. Their thermo-mechanical characteristics and lifetime depend on the using material, producing method, and as well as driving cycles.

The key issue of the discrepancies is the U2W ratio (called Unbalance to Weight) of the maximum unbalance force $F_U$ acting upon the rotor to the rotor weight $F_W$. In case of automotive turbochargers, the excited unbalance forces are much larger than their rotor weights due to the very high rotor speeds; hence, the U2W ratio is in the order of approximately 100. Contrary to turbochargers, the U2W ratio of the industrial turbomachines is in the order of about 1 because of their heavy weights and extremely low rotor speeds, as shown in Table 3.1.

**Table 3.1** U2W ratio of turbochargers and turbomachines

| Types | Rotor speed N (rpm) | Residual unbalance U (g.mm/plane) | Max. unbalance force $F_U$ (N) | Weight $F_W$ (N) | Ratio U2W |
|---|---|---|---|---|---|
| Automotive turbochargers | 150,000 to 300,000 | 0.1 to 1.0 | 200 to 500 | 1 to 5 | ≥ 100 |
| Industrial, aero. turbomachines | 3,000 to 20,000 | G2.5* | 550 to 1,000 | 1,000 to 10,000 | ≤ 1 |

* According to the balancing quality grade G2.5 (DIN-ISO 1940-1).

The U2W ratio shows different behaviors of the rotordynamics between the automotive turbochargers and industrial turbomachines. In case of the automotive turbochargers using the oil-film bearings, the journal initially lies nearly in the bearing center because of its small weight. After increasing the rotor speed, it moves from the bearing center outwards to the bearing wall due to the large unbalance force (nearly 100 times higher than its rotor weight at the high rotor speeds, U2W >> 1). After the rotor reaches the resonance, the journal turns backwards to the bearing center because of the self-centering of the rotor. It indicates that the journal of the turbochargers moves with the operating rotor speeds in the entire bearing clearance.

Contrary to the turbochargers, the journal of the industrial turbomachines is initially near the bearing bottom at low rotor speeds due to their heavy rotor weight. Because the excited unbalance force is much smaller than the rotor weight (U2W < 1), the journal cannot move far away from the equilibrium position; hence, the journal orbit is smaller and more stable compared to the turbocharger rotors. On the contrary, the orbit of the journal locus of turbochargers moves with the operating rotor speeds in a large range of the bearing clearance. Therefore, the bearing stiffness and damping coefficients of change nonlinearly with the rotor speeds. The larger the journal locus eccentricity, the higher the stiffness and damping coefficients of the oil-film bearing are. The response behavior of the bearing stiffness and damping coefficients versus the journal eccentricity $\varepsilon$ is displayed in Fig. 3.1. In the near of the bearing center ($\varepsilon = 0$), the bearing stiffness and damping coefficients have minimum values because the oil film thickness is maximum and nearly equals the radial bearing clearance. As the rotor journal moves near to the bearing wall ($\varepsilon = 1$), the oil film is squeezed due to the large eccentricity and the high whirl speed of the journal in the bearing, hence the bearing stiffness and damping coefficients increase drastically near the bearing wall.
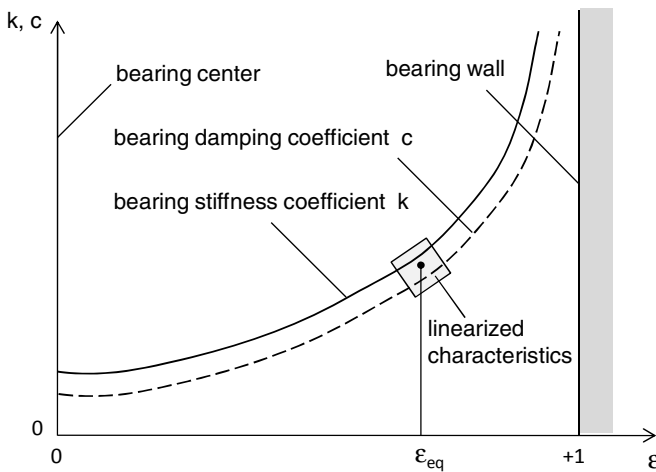


**Fig. 3.1** Stiffness and damping coefficients of the oil film bearings versus journal eccentricity $\varepsilon$

The stiffness and damping coefficients of the oil-film bearing obviously have a nonlinear characteristic versus the journal eccentricity, as shown in Fig. 3.1. As a reason, the induced bearing force acting upon the rotor is nonlinear as the journal locus moves in the entire bearing clearance. That is the case of the automotive turbochargers at U2W >> 1.

In the industrial turbomachines, the journal orbit does not move so far from the equilibrium position in the bearing clearance; i.e., in a small orbit of the journal locus. Therefore, the bearing stiffness and damping coefficients can be linearized at the vicinity of the equilibrium position of the journal $\varepsilon_{eq}$. In fact, rotordynamic behaviors of the industrial turbomachines supported by the oil-film bearings are normally quasi-linear.

## 3.2  Vibration Modes of Turbochargers

In the application of automotive turbochargers, the torsional vibration amplitudes of the rotor is relatively small compared to the lateral bending amplitudes caused by the rotor unbalance, especially at extremely high rotor speeds. Therefore, only degrees of freedom (DOF) in the lateral deflection of the rotor are taken into account in the rotordynamic analyses. The free vibration rotor responses of the linear system consist of many harmonic components with their eigenfrequencies and eigenmodes. On the contrary, the nonlinear vibration responses of turbochargers include not only the synchronous (harmonic) but also sub- and supersynchronous frequency components due to the nonlinear phenomena. Hence, the vibration modes of the nonlinear rotor responses have the shapes resulted from the combination of the modes of the synchronous and nonsynchronous vibrations.

Figure 3.2 shows the layout of a simplified rotor of turbochargers where the turbine and compressor wheels are mounted in the rotor shaft. The rotor is supported by two oil-film bearings located between the two wheels. After the low-speed balancing (called shop balancing), a residual unbalance $U_{TW}$ remains in the turbine shaft; a residual unbalance $U_{CW}$, in the compressor wheel after the high-speed balancing (called trim balancing). In case of both unbalance vectors have the same direction, the rotor unbalance is called the "in-phase couple" unbalance, and when the directions of the unbalance vectors are opposite to each other, the "out-of-phase couple" unbalance is resulted. The out-of-phase couple unbalance normally provides a good rotordynamic behavior because it leads to the smallest residual unbalance vector. In practice, after assembling the compressor wheel in the turbine shaft, the angle of the unbalance vectors is unknown between 0° and 180°.

The unbalance excites the rotor due to the centrifugal forces as the rotor speed $\Omega$ increases. The unbalance force equals the product of the unbalance U and rotor speed squared $\Omega^2$, hence $F_{Un} = U\Omega^2$ (s. Chapter 8). At the low rotor speeds, the unbalance force remains small, and the journal locates nearly at the bearing center due to small weight of the rotor. In this case, the bearing has a small stiffness coefficient, as shown in Fig. 3.1; therefore, the rotor behaves as a rigid rotor.
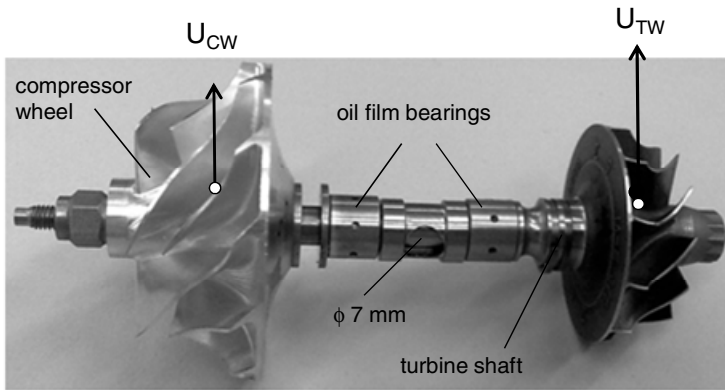
**Fig. 3.2** An unbalanced rotor supported by oil-film bearings

The vibration modes of the rotor are displayed in Fig. 3.3. At the low rotor speeds, the rotor is still rigid, the first mode has the cylindrical shape whirling inside the bearing clearance where both compressor and turbine wheels whirl in the same direction with a whirl velocity $\omega$ (called cylindrical mode). The second mode is the conical mode where the compressor wheel whirls opposite to the whirling direction of the turbine wheel (called conical mode). Finally, the third mode is the bending mode for further increasing the rotor speed where both wheels whirl in the same whirling direction again.

At the high rotor speeds, the unbalance force strongly increases with the rotor speed squared; thus, the journal moves outwards to the bearing wall. As a reason, the bearing stiffness coefficients become larger, as shown in Fig. 3.1, and the rotor deflects in the lateral direction due to excitation of the unbalance force. In this case, the rotor becomes flexible, and the first bending mode has a U-shape where both compressor and turbine wheels whirl in the same direction at a whirl velocity $\omega$. The first bending mode induces the first resonance of the rotor relating to the first eigenmode. At further increasing the rotor speed, the rotor traverses the second bending resonance relating to the second eigenmode with a S-shape where the compressor wheel whirls in the opposite whirling direction of the turbine wheel. Finally, the third bending mode with a W-shape relates to the third eigenmode where both wheels whirl in the same direction again.

The vibration modes of the rotor response in nonlinear rotordynamics are resulted from superimposing the modes of the synchronous and nonsynchronous frequency components. Their mode shapes depend on the current stiffness coefficients, damping ratios, and as well as the nonlinear characteristics of the rotor at various rotor speeds.
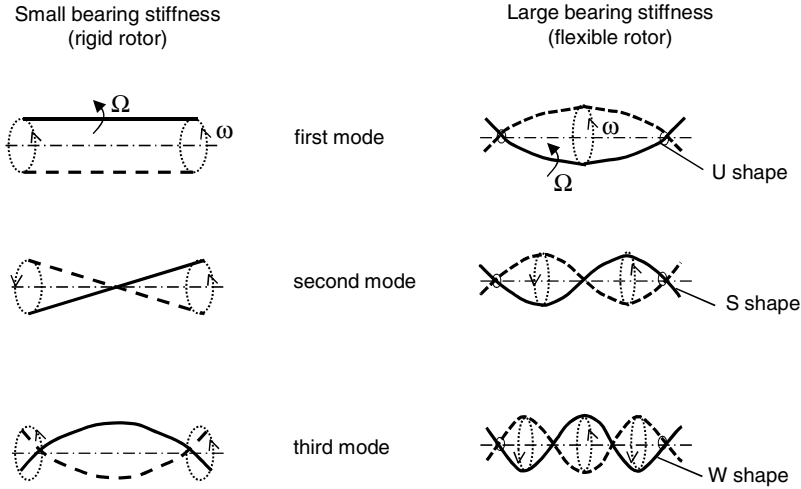
**Fig. 3.3** Shapes of the vibration eigenmodes

## 3.3 Vibration Characteristics of Turbochargers

In this section, the characteristics of vibrations are classified in the frequency and time domains, in which different kinds of vibrations are defined in each domain.

**a) In frequency domain**

- *Harmonic vibrations* have the same frequency of the rotor frequency $\Omega$. Their frequency orders are defined as 1X.

$$\omega = \Omega \qquad (3.1)$$

- *Subharmonics* have the whirl frequencies $\omega$ that are smaller than the rotor frequency $\Omega$. Their frequency orders equal a fractional integer 1/M.

$$\omega = \frac{1}{M}\Omega \qquad (3.2)$$

where M is an integer, such as M = 1,2,...,N.

- *Superharmonics* have the whirl frequencies that are larger than the rotor frequency. Their frequency orders equal a multiple integer M.

$$\omega = M\Omega \qquad (3.3)$$

where M is an integer, such as M = 1,2,...,N.

- *Subsynchronous vibrations* have the frequencies that are less than the rotor frequency. Their frequency orders equal an irrational order, such as 0.35X, or 0.47X.

- *Supersynchronous vibrations* have the frequencies that are larger than the rotor frequency. Their frequency orders equal a non-integer, such as 2.5X or 3.5X.

- *Forward whirls* are the rotor precessions whose velocities have the same direction of the rotor angular velocity.

- *Backward whirls* are the rotor precessions whose velocities have the direction opposite to the rotor angular velocity.

**b)  In Time Domain**

- *Harmonic vibrations* have a timely function of sine or cosine in a mathematical form

$$x(t) = A\sin(\Omega t + \varphi) \tag{3.4}$$

where

$x(t)$ is the timely amplitude of the vibration;
$A$ is the amplitude from the center to peak;
$\Omega$ is the rotor angular frequency in rad/s ($\Omega = 2\pi N$);
$N$ is the rotor speed in rps (round per second);
$\varphi$ is the phase in rad, the rotor angular position at the initial time ($t = 0$).

The excitation unbalance force is a harmonic vibration; its amplitude $A$ equals the unbalance amplitude of $U\Omega^2$.

- *Periodic vibrations* include the sub- and superharmonics. The frequency orders of the subharmonics equal a fraction of integer order, such as $(1/2)X$ and $(1/3)X$; the frequency orders of the superharmonics, a multiple integer order of $2X$ and $3X$. Therefore, they have the same amplitude after repeating of period $T$.

$$x(t) = x(t+T) \tag{3.5}$$

- *Quasi-periodic vibrations* consist of the sub- and supersynchronous vibrations; their frequency orders equal an irrational order, such as $0.37X$ or $0.45X$ (subsynchronous); $1.33X$ or $1.67X$ (supersynchronous). The quasi-periodic vibrations contain at least two incommensurate frequencies $\omega_1$ and $\omega_2$, in which the ratio $\omega_1/\omega_2$ is an irrational number. After repeating of period $T$, the amplitude at time ($t + T$) is not exactly the same amplitude at time $t$. The quasi-periodic vibrations often take place in nonlinear dynamics of the Neimark and Sacker bifurcation. After passing the bifurcation point, the periodic vibration with the frequency $\omega_1$ is bifurcated in another periodic vibration with the frequency $\omega_2$. The resulting quasi-periodic vibration consists of two incommensurate frequencies $\omega_1$ and $\omega_2$. Its quasi-periodic orbit wraps on the surface of a torus and does not intersect the Poincaré map at the same point at every period $T$ (s. Chapter 4).

$$x(t) \neq x(t+T) \tag{3.6}$$

- *Chaos vibrations* have no rule for their motions in which the unstable vibrations change from the quasi-periodic to chaos motions due to bifurcation.

- *Steady-state working conditions*
When the acceleration of the vibrations equals zero, the rotor vibrations are in a steady-state condition. This condition is considered when the rotor rotates with a constant angular speed at a certain interval of time.

*- Transient working conditions*

When the acceleration of the vibrations is taken into account, the vibrations are transient because the angular speed changes with time. At run-up or slowdown, the response behavior of the rotor is transient. In the transient condition, the amplitude and critical frequency of the rotor response strongly depend on the rotor acceleration compared to the steady-state working condition (s. Chapter 5).

*- Free vibration responses* are resulted from the rotordynamic system without excitation forces due to unbalance (homogeneous solution of the vibration equation). In a linear system, the free vibration response consists of the eigenvectors and eigenfrequencies of the rotor.

*- Forced vibration responses* are resulted from the rotordynamic system with excitation forces of the rotor unbalance (particular solution of the vibration equation). In a linear system, the unbalance forced vibration response is a harmonic vibration with the rotor frequency. On the contrary, the rotor forced vibration response is periodic or quasi-periodic vibrations including the synchronous and nonsynchronous whirl frequencies.

## 3.4   Linear and Nonlinear Vibrations of Turbochargers

In the following section, the discrepancies between the linear and nonlinear vibrations with synchronous and asynchronous frequencies are discussed. At first, the linear rotordynamic system deals with the unbalance excitation of the rotor. In case of a free vibration without unbalance excitation, the free vibration responses are the sum of the eigenvectors with the corresponding complex eigenvalues of the rotor. They are normally periodic vibrations with the relating eigenfrequencies. The eigenfrequencies of the linear system are the imaginary parts of the complex eigenvalues.

The unbalance response (also forced vibration response) traverses the resonances at the first, second, third, or higher critical speeds. The critical speeds are the rotational speeds of the rotor at which the rotor eigenfrequencies equal the rotor frequency. The unbalance responses are harmonic vibrations with the rotor frequency, having the frequency order of 1X.

The Campbell diagram (also whirl speed map) is only used in the linear rotordynamics to find the critical speeds where the rotor eigenfrequencies intersect the synchronous excitation frequency 1X. Each eigenfrequency of the free vibration response corresponds to an eigenmode of the vibration. The eigenmode of the flexible rotor has a U shape for the first, S shape for the second, and W shape for the third eigenfrequency.

In case of the linear rotordynamics, the modal analysis is applied to calculate the complex eigenvalues and eigenvectors of the rotor. The eigenfrequencies are the imaginary parts of the complex eigenvalues, in which the positive sign is for the forward whirl and the negative sign, for the backward whirl of the rotor. Similarly, the real parts of the complex eigenvalues show the behavior of the rotor stability that shall be discussed in the next section.

The stiffness and damping coefficients of the rotor are linear only at the small deflections of the well-balanced and damped rotor. As a reason, the vibration equation of the rotor is linear. Otherwise, the restoring forces of the rotor are nonlinear at the large rotor deflections; hence, the rotor vibration equation

becomes nonlinear. The nonlinear rotordynamic system is caused not only by the nonlinear characteristics of the stiffness and damping coefficients of the oil-film bearings but also by other characteristics, such as oil whirl, rotor misalignment, contact rub between the rotor and bearings, excessive unbalance, and as well as sidebands due to frequency modulations. Therefore, the rotor response of nonlinear rotordynamic systems is resulted from superimposing the unbalance excitation of the rotor on the nonsynchronous frequency components induced by the rotordynamic nonlinearity of the system.

The nonsynchronous frequency components contain the sub- and supersynchronous frequency components. The subsynchronous vibrations have frequencies smaller than the rotor frequencies with rational orders of (1/2)X and (1/3)X of the contact rub or irrational orders, such as  0.35X to 0.47X of the oil whirl. On the contrary, the supersynchronous vibrations have the frequencies higher than the rotor frequencies with integer orders of 2X, 3X, 4X, or non-integer orders of 2.5X and 3.5X in case of the frequency modulations. Both vibrations consist of the forward and backward whirls that are determined by on the sign of their eigenfrequencies.

As a result, the orbit of the rotor locus in a stable condition has mostly the Lissajous curves relating to the synchronous and nonsynchronous vibrations. The nonlinear vibration responses are normally the periodic or quasi-periodic vibrations. In case of the rotor instability, they could be changed from the periodic to quasi-periodic and chaos vibrations due to bifurcation.

Because of the rotor nonlinearity, the eigenfrequencies of the rotor vibration system have no longer existed. As a reason, the assumption that the vibration response is resulted from the eigenvectors and eigenvalues of the rotor, fails in nonlinear rotordynamics. Therefore, the modal analysis is not valid for analyzing the eigenfrequencies (also natural frequencies) of the nonlinear rotordynamic system. In this case, we do not use the Campbell diagram to study the eigenfrequencies and find the critical speeds of the rotor. Instead, the Waterfall diagram (also frequency spectrum diagram) is applied to analyze the whirl frequencies of the nonlinear rotor response. The frequency spectrum analysis in the Waterfall diagram shall be discussed more in detail in Chapter 7.

Some essential remarks of nonlinear rotordynamics of turbochargers are summarized:

1. In nonlinear rotordynamics, the vibration responses are not harmonic but periodic, quasi-periodic, and chaotic at the large rotor amplitudes. In fact, they contain not only the synchronous but also nonsynchronous vibrations, such as sub- and supersynchronous vibrations because of the nonlinear phenomena, such as excessive unbalance, misalignment, contact rub in the bearings, oil whirl, and sidebands as well.
2. The nonsynchronous frequencies of the vibration responses are induced by large rotor deflections and other nonlinear characteristics of the rotor and radial bearing forces.
3. The response amplitude of the rotor consists of not only the synchronous vibration amplitude of the unbalance but also the nonsynchronous vibration amplitudes depending on the rotor speed. In general, the amplitudes of the nonsynchronous vibrations are much larger than the harmonic unbalance response amplitude of 1X; therefore, the bending resonances do not obviously emerge in nonlinear rotordynamics. Instead, the rotor response amplitude is stabilized in the limit cycle (s. Chapters 4 and 7).

4. The bearing stiffness and damping coefficients strongly increase with the rotor deflections, leading to increase of the bearing forces. Due to the force balance between the bearing, unbalance, and other forces, the rotor response amplitude increases and reaches the equilibrium position. In fact, the unstable rotor orbit is restabilized in the limit cycle.

5. At an unbalance force acting upon the rotor, different rotor responses could occur in nonlinear rotordynamics due to bifurcation that shall be discussed in Chapter 4. These resulting responses generally depend on the initial conditions and other parameters, such as rotor speed, bearing clearances, oil inlet temperature and pressure.

6. Campbell diagram (whirl speed map) is used to analyze the eigenfrequencies in linear rotordynamics. However, it has not been applicable in nonlinear rotordynamics any longer; instead, Waterfall diagram (spectrogram) is applied to study the whirl frequencies and amplitudes of the rotor response versus the rotor speeds in nonlinear rotordynamics.

7. Hurwitz-Routh criterion is normally used to study the rotor stability in linear rotordynamics; Hopf bifurcation theory, in nonlinear rotordynamics.

## 3.5  Orbit of the Rotor Locus

**a) Basic Theory of the Eddy-Current Sensor**
To measure the locus of the certain point on the rotor, two eddy-current sensors are set up perpendicular to each other near this point. Figure 3.4 shows the contactless measure principle of the eddy-current sensor and explains how it works on the measurement of the rotor locus.
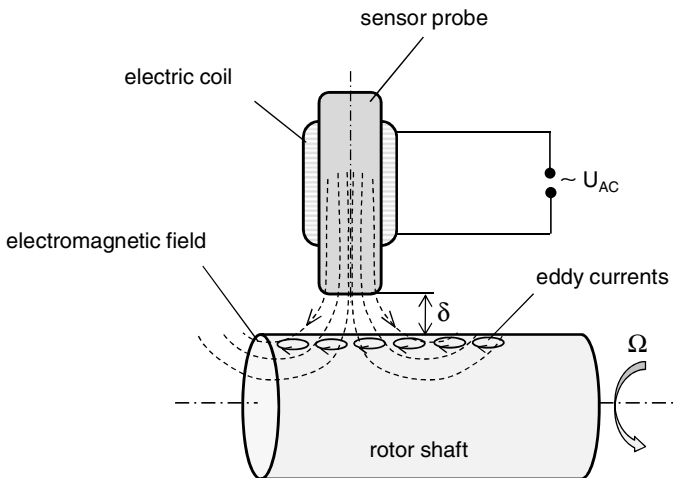


**Fig. 3.4** Working principle of the eddy-current sensor

The working principle of the eddy-current sensor is based on the electromagnetic induction. By means of using an alternating voltage $U_{AC}$ with a high frequency in the electric coil, a high-frequency alternating electromagnetic field is created at the end of the sensor probe according to the induction law. Having replaced the sensor probe near to the measured point on the rotor shaft with a distance $\delta$, the eddy-currents are induced in the target material of the rotor shaft. In turn, the eddy-currents create an electromagnetic field that reacts against the initial electromagnetic field of the sensor probe, leading to the timely change of the electric coil impedance. It varies with the current distance $\delta$ between the sensor probe and target material. Therefore, the timely change of the distance $\delta$ is determined by measuring the change of the electric coil impedance. To make sure that the measuring principle works, the target surface must be at least three times larger than the cross-sectional area of the sensor probe; the distance between the sensor probe and the rotor shaft is about $1 - 2$ mm.

### b) Measurement of the Rotor Locus

The automotive turbochargers are applied to high temperatures of the exhaust gases, such as 820 to 850°C in diesel engines, and 950 to 1050°C in gasoline engines. Therefore, it is not simple to measure the rotor locus at the turbine side because of very high temperatures of the exhaust gas. Additionally, there is difficulty in installing the sensors in the bearing casing to measure the orbit of the journal in the radial bearings. As a reason, one sets up the two eddy-current sensors are set up perpendicularly to each other at the compressor housing to measure the orbit of the shaft at the compressor inlet, as displayed in Figures 3.5 and 3.6. The measured orbit shows only the displacement of the shaft at this position but not the actual displacements of the journal inside the bearings or the rotor deflection between both radial bearings. However, analyzing the spectrum of the rotor frequencies and amplitudes at various rotor speeds in Waterfall diagram helps us to know the rotor response behavior. Additionally, the acceleration in the bearing casing near the radial bearings is also measured. Its acceleration spectrum in the Waterfall diagram
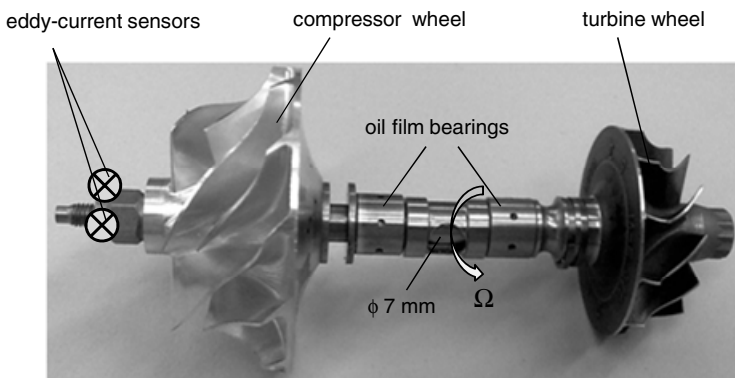


**Fig. 3.5** Position of the eddy-current sensors in the rotor

determines whether the contact rub between the rotor and bearings occurs. If the contact rub happens in the bearings, the large amplitudes of subsynchronous vibrations of (1/2)X or (1/3)X, and side band frequencies will appear in the Waterfall diagram, especially at the high rotor speeds. In addition, the computation of nonlinear rotordynamics provides all characteristics of the rotor response, like the rotor deflections, whirl frequencies, and vibration modes at any point of the rotor versus the rotor speeds at the run-up and slowdown simulation.

The eddy-current sensors are mounted perpendicularly to each other in the axes x and y on the compressor housing, as shown in Fig. 3.6. The distance of the sensors to the target is approximately 1 mm. The Bently keyphasor [1] located between the eddy-current sensors is used to indicate the rotor speed in the orbit. Each sensor measures the displacement of the rotor in each direction x and y. The orbit of the rotor has the form of Lissajous curve in the phase diagram x-y.

The orbit amplitude of the measured point of the rotor is resulted from its amplitude components in the directions x and y.

$$r(t) = \sqrt{x(t)^2 + y(t)^2} \tag{3.7}$$

where

x(t), y(t) are the measured vibration signals in the directions x and y, respectively.

The vibrations of the rotor response are measured by the eddy-current sensors in the directions x and y, as shown in Fig. 3.6. Its orbit is calculated according to eq. (3.7) and displayed in the phase plane x-y, as shown in Figures 3.7b, 3.8c, 3.9c, 3.10c, and 3.11c.
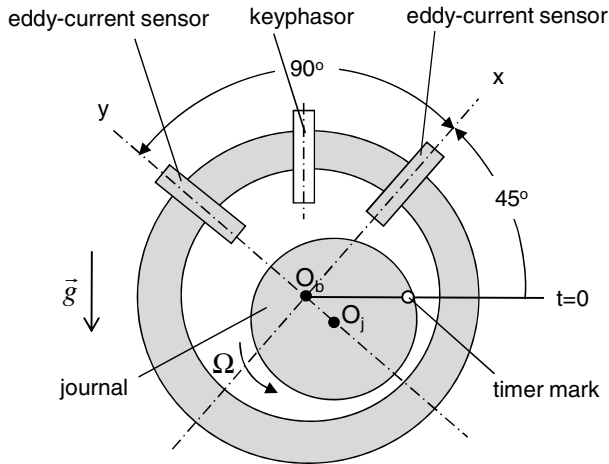


**Fig. 3.6** Layout of the eddy-current sensors

## c) Studying Cases of the Rotor Orbit

The vibration signals in the directions x and y are measured by the eddy-current sensors, as shown in Fig. 3.6. By means of the FFT spectra analyzer, the

corresponding frequencies are displayed in the spectrum diagram, and the orbit is computed and plotted in the phase diagram x-y.

Due to the nonlinearity, the harmonic vibration of the unbalance excitation is superimposed on the sub- and supersynchronous frequency components of the rotor; it results in the rotor vibration response. The vibration response of the rotor contains vibration components in the directions x and y and can be written in the complex formulation in the phase plane x-y (s. [6] and [8]).

$$r(t) = x(t) + jy(t) = \left( r_{fw}e^{j\Omega t} + r_{bw}e^{-j\Omega t} \right) + \sum_{k=1}^{K} \left( r_{k,fw}e^{j\omega_k t} + r_{k,bw}e^{-j\omega_k t} \right) \quad (3.8)$$

where

- the first term of the right hand side is the forward and backward unbalance harmonics with the rotor frequency $\Omega$;
- the second term is the asynchronous vibrations with the whirl frequencies $\omega_k = n_k\Omega$;
- K is the asynchronous frequency components of the nonlinear rotor.

Depending on the sub- or supersynchronous vibrations, the whirl frequency orders $n_k$ could be integer, fractional, and as well as irrational numbers ($n_k < 1$ or $n_k > 1$). The positive and negative signs of the whirl frequencies indicate forward and backward whirls, respectively.

## 3.6  Study of Case Histories

In the following section, some rotor orbits of the turbochargers are computed in which the rotor vibration response is resulted from the superimposition of the unbalance vibration (1X) on the nonsynchronous frequency components induced by the nonlinearity, such as the nonlinear bearing forces, excessive unbalance, rotor misalignment, and contact rub in the bearings.

In order to study the case histories, the frequencies and amplitudes of the vibration components are predetermined and illustrated in the frequency spectrum diagram. The timely vibrations in the directions x and y and the rotor response are plotted in the time domain; finally, the orbit of the rotor response is displayed in the phase plane x-y. These study cases aim to make the readers familiar with the nonlinear vibration responses that include various synchronous and asynchronous frequency components in nonlinear rotordynamics.

### Case History #1: Unbalanced Rotor

Anisotropic (orthotropic) radial bearings are defined when the bearing stiffness coefficients $K_x$ and $K_y$ in the directions x and y, respectively are different from each other. In other case, they are called isotropic bearings. Due to the different stiffness coefficients, the rotor deflection in the direction x is different from the rotor deflection in the direction y. As a result, the orbit shape of the rotor is elliptic where the maximal rotor deflection is in the direction with the lower stiffness coefficient of the bearing.

The rotor vibration response is resulted from superimposing the forward and backward whirls of the unbalanced rotor, its component

- in the direction x:

$$x(t) = r(K_x) \cos \Omega t + r_1(K_x) \cos(-\Omega t + \varphi_1)$$

- in the direction y:

$$y(t) = r(K_y) \sin \Omega t + r_1(K_y) \sin(-\Omega t + \varphi_1)$$

where

r is the forward vibration amplitude (peak amplitude, pk);
$r_1$ is the backward vibration amplitude (peak amplitude, pk); $r_1 = 0{,}5r$;
$\Omega$ is the rotor angular speed;
t is time.
$\varphi_1$ is the vibration phase (= $\pi/4$).

The frequency spectrum of the vibration components is displayed in Fig. 3.7a. The orbit of the rotor response is resulted from superimposing the vibration components, as displayed in Figure 3.7a. In case of $K_x < K_y$, the orbit is elliptical with the maximal deflection in the direction x. The whirl precession with the frequency $\omega = \Omega$ has the same rotating direction of the rotor velocity. In this case, the rotor orbit is a forward whirl because the forward amplitude is larger than the backward amplitude. Note that the whirling direction of the rotor follows the whirling direction of the vibration component with the larger amplitude. The rotor locus moves from the equilibrium position, nearly in the middle of the contact circle, forwards in an ellipse orbit. The contact circle is determined by manually moving and rotating the end of the compressor wheel at the screw-nut with a slight contact occurring somewhere between the rotor and bearings. However, the contact circle becomes larger in the operating condition of the turbocharger because the inner bearing clearance increases due to the thermal expansion of the bearing ring in the radial direction, and the flexible rotor deflects at the high rotor speeds.
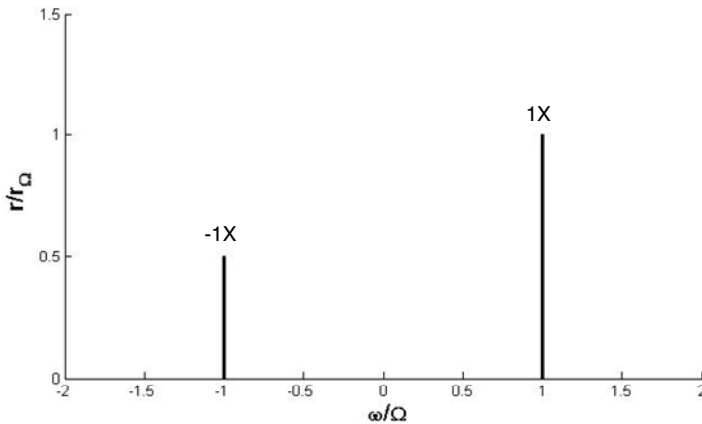


Fig. 3.7a Frequency spectrum of the unbalance vibration
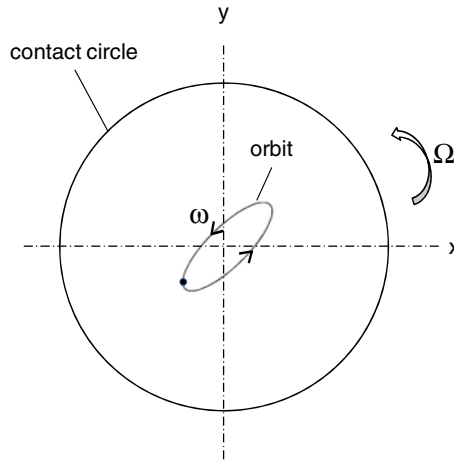
**Fig. 3.7b** Orbit of the rotor response (unbalance)

## Case History #2: Unbalanced Rotor with the Oil Whirl

In this case history, the unbalanced rotor working under influence of the oil whirl is studied. Oil whirl is a subsynchronous self-excited vibration acting upon the rotor with an irrational frequency order between 0.35X and 0.47X (called half-frequency whirl). The effect of the oil whirl is induced by the oil whirling in the bearing clearance that affects the rotor whirling with the oil whirl irrational frequency. Therefore, the oil whirl mostly occurs in the bearing clearance without the precondition of the rotor unbalance. Notice that the mass center eccentricity of the rotor causes the rotor unbalance; the oil whirling in the bearing clearance induces the oil whirl. Hence, both effects have nothing to do with each other.

In fact, the oil whirl does not take place as long as the damping in the bearing is large enough in order to keep the energy balance between the whirling kinetic energy induced by the destabilizing force and the dissipated damping energy in the bearing clearance. On the one hand, the damping coefficient of bearing decreases with the oil temperature. On the other hand, the cross-coupled stiffness coefficient of the bearing, causing the destabilizing force of the rotor, increases with the rotor speed. Therefore, the whirling kinetic energy of the rotor exceeds the reducing dissipated damping energy in the oil film because the oil film temperature increases with the rotor speed, leading to the oil whirl. Therefore, the oil whirl excites itself from a stable to unstable rotor response.

The rotor vibration response is resulted from the superimposition of the unbalance excitation and subsynchronous frequency component of the oil whirl, its component

- in the direction x:

$$x(t) = r \cos \Omega t + r_1 \cos( \omega_1 t + \varphi_1 )$$

- in the direction y:

$$y(t) = r \sin \Omega t + r_1 \sin(\omega_1 t + \varphi_1)$$

where

r is the harmonic vibration amplitude (peak amplitude, pk);
$r_1$ is the oil whirl vibration amplitude (peak amplitude, pk); $r_1 = r$;
$\Omega$ is the rotor frequency;
$\omega_1$ is the oil whirl frequency with an irrational frequency order 0.47X;
$\varphi_1$ is the vibration phase.

Figure 3.8b displays the superimposed vibrations in the directions x and y and the vibration response of the rotor. The phase difference between the vibrations in the directions x and y is 90° because the eddy-current sensors are perpendicular to each other (s. Fig. 3.6b). At the rotor speed of 200,000 rpm, the period $T_\Omega$ is about 0.3 ms; the period of the oil whirl vibration, $T_{\omega 1}$ nearly 0.64 ms.

The rotor orbit resulted from the periodic vibrations of the unbalance and self-excited oil whirl in the directions x and y are calculated at the rotor speed of 200,000 rpm and displayed in Fig. 3.8c. The rotor precession is a forward whirl having the same direction of the rotor speed. Due to the irrational frequency order of the oil whirl (0.47X), the rotor response is quasi-periodic, in which the orbits are not the same after repeat of period T. The timer marks taken by the keyphasor indicate the number of the revolutions of the rotor in one orbit cycle, which is called the convolution.

Having considered a single orbit of the rotor response, there are two timer marks on it; i.e., the orbit completes one convolution in every two revolutions of the rotor due to two timer marks. In other words, the oil whirl is a subsynchronous vibration having a frequency of nearly one-half of the rotor frequency ($\omega = 0.47\Omega$).
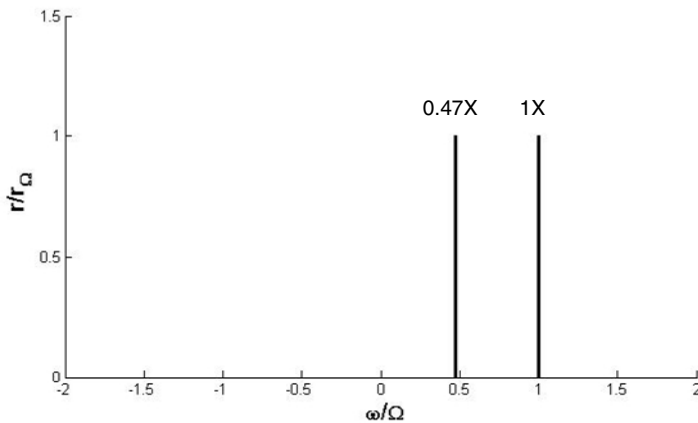


**Fig. 3.8a** Frequency spectrum of the vibration components
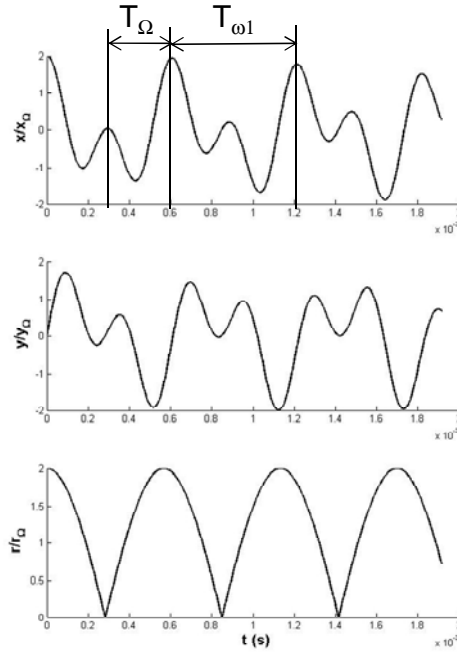
**Fig. 3.8b** Vibrations in the directions x and y and the rotor response at $N_{rotor} = 200,000$ rpm

Generally, in the subsynchronous frequency components with a frequency order of $(1/N)X$, the orbit of the rotor response completes one convolution in every N revolutions with N timer marks; in the supersynchronous components with a frequency order of NX, the rotor orbit completes N convolutions in one revolution of the rotor with one timer mark.

The asynchronous frequency components are summarized as follows:

- Subsynchronous frequency component $(1/N)X$ means N revolutions per convolution;
- Supersynchronous frequency component NX means N convolutions per revolution.

If the whirl orbit has N inner loops, it corresponds to a subsynchronous forward whirl with a frequency order of $1/(N+1)*X$. As a rule of thumb, the frequency order is the inversion of the number of loops (N+1). In case of the oil whirl with a forward whirl frequency order of $(1/2)X$, it results in one inner loop in the orbit, as shown in Fig. 3.8c. On the contrary, the backward whirls have N outer loops; the whirl frequency order is $1/(N-1)*X$.
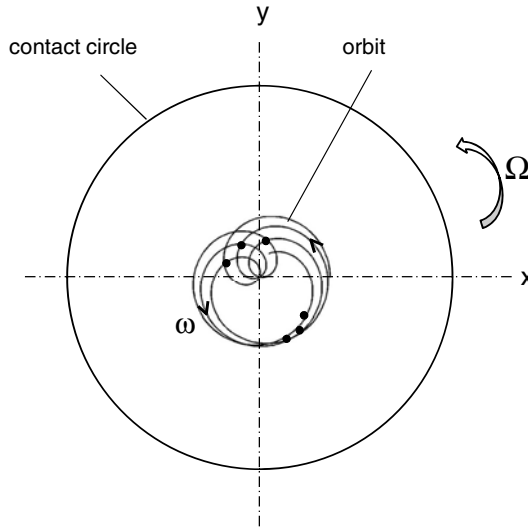
**Fig. 3.8c** Orbit of the rotor response (oil whirl)

## Case History #3:  Unbalanced Rotor with Inner and Outer Oil Whirls

To reduce the bearing friction, rotating floating ring bearings with two oil films have been usually applied to the automotive turbochargers. The rotor vibration response is resulted from superimposing the harmonic unbalance excitation on the subsynchronous components, the inner and outer oil whirl vibrations. The self-excited frequency components have irrational frequency orders from 0.25X to 0.70X for the inner oil whirl, from 0.1X to 0.3X for the outer oil whirl. The whirl frequency orders depend on the rotor speed and as well as the oil temperature.

The rotor vibration  response is resulted from superimposing the unbalance vibration on the subsynchronous frequency components of the oil whirls, its component

- in the direction x:

$$x(t) = r \cos \Omega t + r_1 \cos(\omega_1 t + \varphi_1) + r_2 \cos(\omega_2 t + \varphi_2)$$

- in the direction y:

$$y(t) = r \sin \Omega t + r_1 \sin(\omega_1 t + \varphi_1) + r_2 \sin(\omega_2 t + \varphi_2)$$

where

$r$ is the harmonic vibration amplitude (peak amplitude, pk);
$r_1$ is the vibration amplitude (peak amplitude, pk) of the inner oil whirl; $r_1 = 0.5r$;
$r_2$ is the vibration amplitude (peak amplitude, pk) of the outer oil whirl; $r_2 = 2r$;
$\Omega$ is the rotor frequency;
$\omega_1$ is the inner oil whirl frequency with an irrational frequency order 0.25X ;
$\omega_2$ is the outer oil whirl frequency with an irrational frequency order 0.1X;
$\varphi_1$, $\varphi_2$ are the vibration phases of the vibration components.

The frequency spectrum of the vibration components is displayed in Fig. 3.9a where the frequency components of the inner and outer oil whirls have frequency orders of 0.25X and 0.1X, respectively.
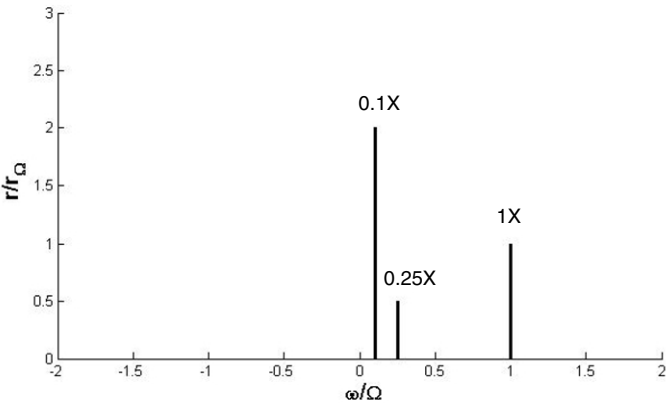


**Fig. 3.9a** Frequency spectrum of the vibrations
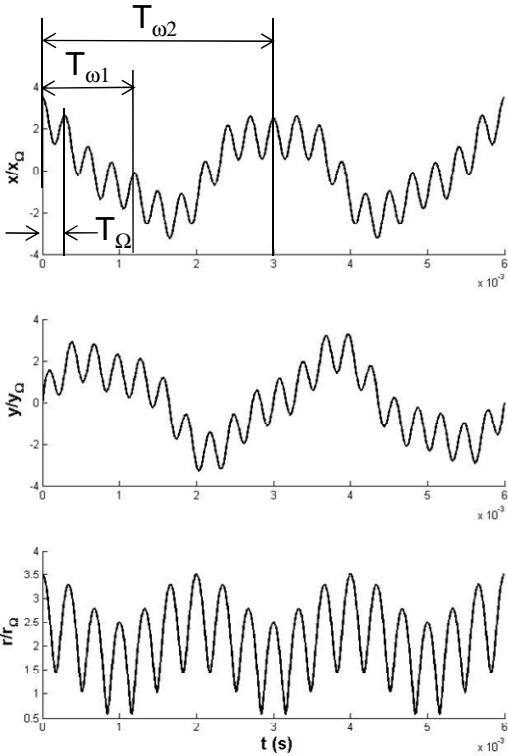


**Fig. 3.9b** Vibrations in the directions x and y and the rotor response at $N_{rotor} = 200,000$ rpm

The amplitude of the rotor vibration response consisting of the unbalance, inner, and outer oil whirls at the rotor speed of 200,000 rpm is calculated according to eqs (3.7) and (3.8), as shown in Figure 3.9b. The vibration response is a periodic or quasi-periodic vibration because their subsynchronous whirls have irrational frequency orders. In case of the quasi-periodic response, the amplitudes after repeat of period T are not always the same amplitude. Its response orbit shown in Fig. 3.9c does not have the same orbit at times (t + nT). In Fig. 3.9b the period of the rotor $T_\Omega$ is found at 0.3 ms at 200,000 rpm; the period of the inner oil whirl $T_{\omega 1}$ nearly 1.2 ms; the period of the outer oil whirl $T_{\omega 2}$, approximately 3 ms.

At the high rotor speeds, the temperature of the inner oil film becomes higher than the temperature of the outer oil film due to the smaller inner bearing clearance. As a reason, the ring speed of the bearing decreases with the rotor speed, and the frequency of the inner oil whirl reduces to nearly 25% of the rotor frequency (0.25X) at the high rotor speeds. The frequency of the outer oil whirl is lower than the inner oil whirl. It is assumed approximately 10% of the rotor frequency (0.1X).

The rotor orbit resulted from the periodic vibrations of the unbalance and self-excited inner and outer oil whirls in the directions x and y are calculated and displayed in Fig. 3.9c. The inner loops of the rotor orbit indicate that the rotor precession is a forward whirl having the same direction of the rotor speed. The envelope of the rotor orbit is called the limit cycle, in which the rotor locus stabilizes. Note that the limit cycle is different to the contact circle of the rotor.
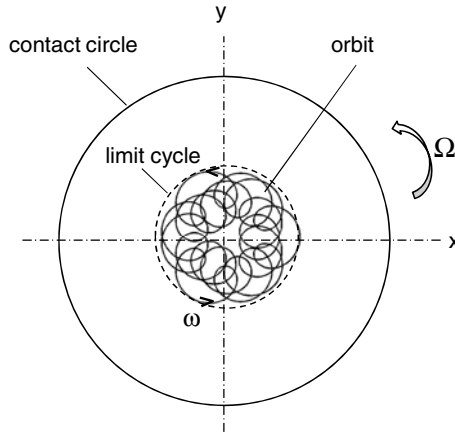


**Fig. 3.9c** Orbit of the rotor response (inner and outer oil whirls)

## Case History #4:  Heavy Rub in the Bearings

In a heavy rub at normal tight condition in the bearings, the unbalance forces excite the subsynchronous frequency components of the nonlinear rotor induced by heavy rub; it results in the rotor vibration response. At the heavy rub in the bearings, the rub subsynchronous frequency components have fractional frequency orders like (1/2)X, (1/3)X, or (1/4)X, and high harmonic orders, such as 2X, 3X.

The rotor vibration  response is resulted from superimposing the unbalance vibration on the subsynchronous frequency component of the heavy rub, its component

- in the direction x:

$$x(t) = r \cos \Omega t + r_{bw} \cos(-\Omega t) + r_1 \cos(\omega_1 t + \varphi_1)$$

- in the direction y:

$$y(t) = r \sin \Omega t + r_{bw} \sin(-\Omega t) + r_1 \sin(\omega_1 t + \varphi_1)$$

where

r is the harmonic vibration amplitude (peak amplitude, pk);
$r_{bw}$ is the backward harmonic vibration amplitude (peak amplitude, pk); $r_{bw} = 0.5r$;
$r_1$ is the vibration amplitude (peak amplitude, pk); $r_1 = 1.5r$;
$\Omega$ is the rotor frequency;
$\omega_1$ is the rub-related frequency with a fractional frequency order (1/2)X;
$\varphi_1$ is the vibration phase.

The frequency spectrum of the vibrations is displayed in Fig. 3.10a where the rub frequency component has a fractional frequency order of (1/2)X.
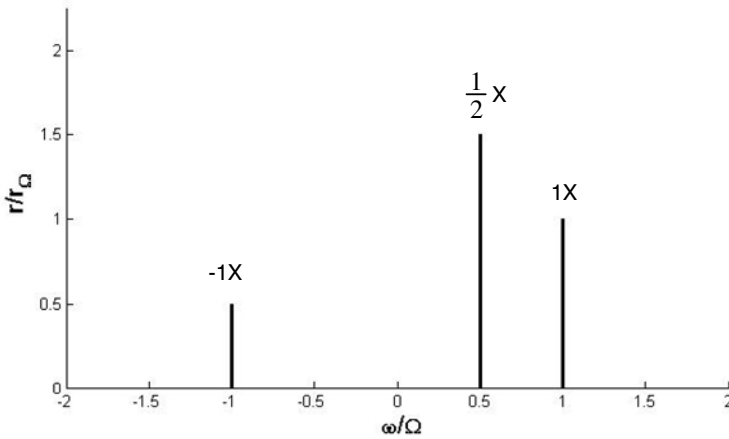


**Fig. 3.10a** Frequency spectrum of the vibrations

The amplitude of the rotor vibration response consisting of the unbalance and subsynchronous whirl of heavy rub at the rotor speed of 200,000 rpm is calculated according to eqs (3.7) and (3.8), as illustrated in Figure 3.10b. The rotor vibration response is periodic because the subsynchronous whirl has a fractional frequency order of (1/2)X. In Fig. 3.10b, the period of the rotor $T_\Omega$ is found at 0.3 ms at 200,000 rpm; the period of the contact rub whirl $T_{\omega 1}$ nearly 0.6 ms.

The rotor orbit resulted from the periodic vibrations of the unbalance harmonics and rub subsynchronous whirl in the directions x and y are calculated at the rotor speed of 200,000 rpm and plotted in Fig. 3.10c. The rotor response is a forward
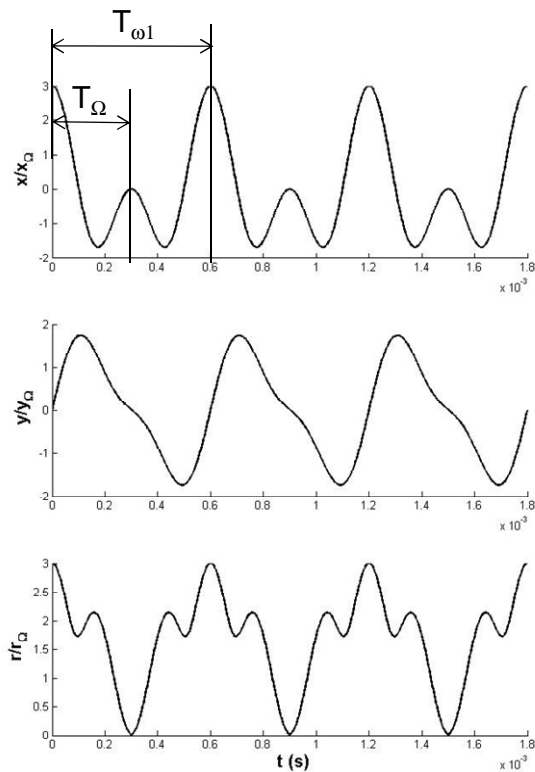
**Fig. 3.10b** Vibrations in the directions x and y and the rotor response at $N_{rotor} = 200,000$ rpm
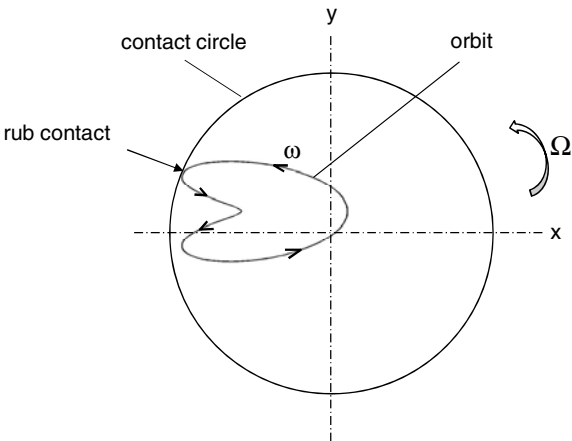


**Fig. 3.10c** Orbit of the rotor response (heavy rub)

whirl with a fractional frequency component of (1/2)X. It indicates that the rub contact of the rotor to the bearing occurs once in every two revolutions of the rotor. After contacting the bearing wall, the rotor bounces back; the rub contact takes place again after the rotor rotates two revolutions, as shown in Fig. 3.10c.

## Case History #5:  High Radial Loads due to Misalignment

The rotor misalignment induces high radial loads on the bearings because the journal eccentricity increases. As a result, the oil film in the bearing clearance is squeezed, so that the rotordynamic behavior of the system becomes strongly nonlinear at the high journal eccentricities. In fact, the unbalance forces excite the supersynchronous frequency components at high radial bearing loads, resulting in the rotor vibration response. The supersynchronous frequency components normally have integer frequency orders of 2X and 3X at high radial loads due to misalignment.

The rotor vibration response is resulted from superimposing the unbalance vibration on the supersynchronous frequency component of the rotor misalignment, its component

• in the direction x:

$$x(t) = r \cos\Omega t + r_{1,fw} \cos(\omega_1 t + \varphi_1) + r_{1,bw} \cos(-\omega_1 t + \varphi_1)$$

• in the direction y:

$$y(t) = r \sin\Omega t + r_{1,fw} \sin(\omega_1 t + \varphi_1) + r_{1,bw} \sin(-\omega_1 t + \varphi_1)$$

where

r is the harmonic vibration amplitude (peak amplitude, pk);
$r_{1,fw}$ is the forward vibration amplitude 2X (peak amplitude, pk); $r_{1,fw} = 0.6r$;
$r_{1,bw}$ is the backward vibration amplitude -2X (peak amplitude, pk); $r_{1,bw} = 0.4r$;
$\Omega$ is the rotor frequency;
$\omega_1$ is the whirl frequency 2X;
$\varphi_1$ is the vibration phase.

The frequency spectrum of the vibrations is displayed in Fig. 3.11a in which the supersynchronous frequency components have an integer frequency order of 2X of the misalignment or extremely large radial load; the unbalance excitation frequency has an order of 1X.

The amplitude of the rotor vibration response consisting of the unbalance harmonics and misalignment supersynchronous whirl at the rotor speed of 200,000 rpm is calculated according to eqs (3.7) and (3.8) and displayed in Figure 3.11b. The vibration response is periodic because the supersynchronous whirl has an integer frequency order of 2X.

In Fig. 3.11b, the period of the rotor $T_\Omega$ is found at 0.3 ms at 200,000 rpm; the period of the misalignment frequency whirl $T_{\omega 1}$, nearly 0.15 ms. The response orbit resulted from the superimposition of the unbalance harmonics and misalignment supersynchronous whirls in the directions x and y is calculated at the rotor speed of 200,000 rpm and plotted in Fig. 3.11c.
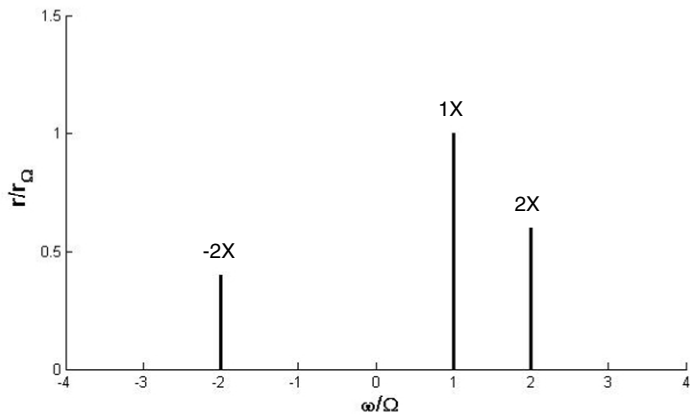
**Fig. 3.11a** Frequency spectrum of the vibrations
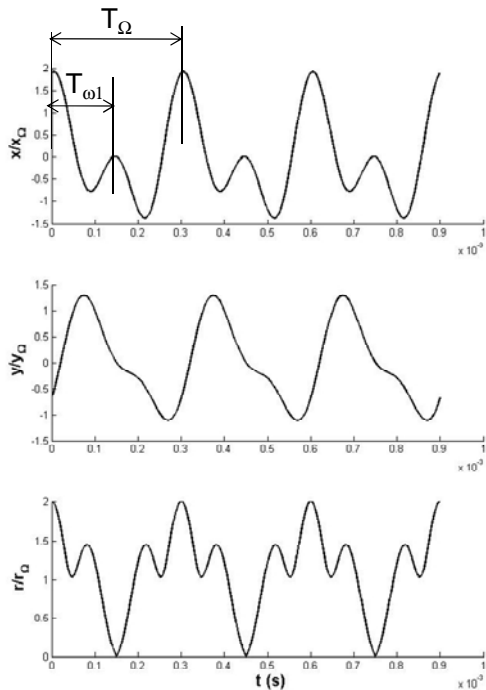


**Fig. 3.11b** Vibrations in the directions x and y and the rotor response at $N_{rotor} = 200,000$ rpm
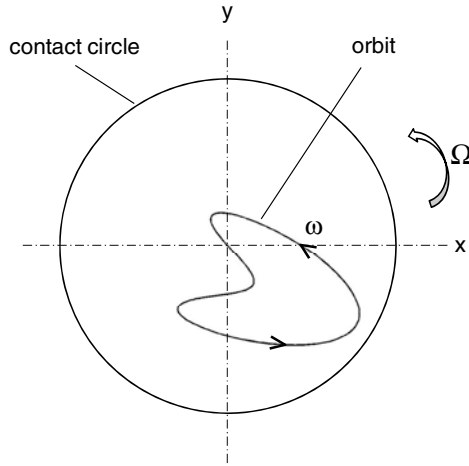
**Fig. 3.11c** Orbit of the rotor response (banana shape)
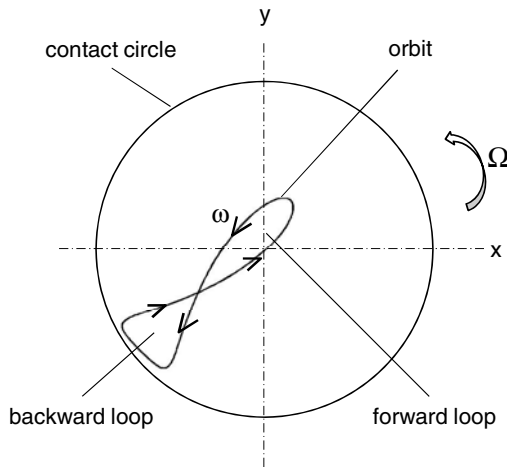


**Fig. 3.11d** Orbit of the rotor response (lying eight shape)

At increasing the radial bearing load due to a strong misalignment, the response orbit changes from the "banana" shape, as shown in Fig. 3.11c, to the "lying eight" shape. The banana orbit shape is a forward whirl and bounces back as it comes close to the bearing wall. In case of very high radial loads on the bearings, the orbit of the rotor response turns into the lying eight shape, as displayed in Fig. 3.11d. Contrary to the banana shape, the lying eight shape has forward and backward loops. The journal bounces in the backward loop. Far away from the bearing wall, the radial load is decreased; hence, the rotor whirls in the forward loop again, having the same whirl direction of the rotor speed, as illustrated in Fig. 3.11d.

The rotor misalignment with an extremely high radial load or the excessively unbalanced rotor could cause the contact rub between the journal and bearing. The frequencies have multiple harmonic frequency orders of 2X, 3X, or higher, and as well as fractional frequency orders of (1/2)X, (1/3)X, as discussed in the case history #4.

# References

1. Bently, D.E., Hatch, C.: Fundamentals of Rotating Machinery Diagnostics. Bently Pressurized Bearing Press (2002)
2. Ehrich, F.: Handbook of Rotordynamics. Krieger Publishing Company (2004)
3. Gasch, R., Nordmann, R., Pfuetzner, H.: Rotordynamik, vol. 2. Auflage, Springer (2006)
4. Kraemer, E.: Rotordynamics of Rotors and Foundations. Springer, Heidelberg (1993)
5. Newland, D.E.: Mechanical Vibration Analysis and Computation. Dover Publications Inc. (2006)
6. Schmidt, G., Tondl, A.: Nonlinear Vibrations. Cambridge University Press (2009)
7. Vance, J.: Rotordynamics of Turbomachinery. J. Wiley and Sons Inc. (1988)
8. Tondl, A.: Some problems of Rotor Dynamics. Chapman & Hall (1965)

# Chapter 4
# Stability Analysis of Rotordynamic Behaviors

## 4.1 Introduction

Two important issues of the automotive turbochargers in the rotordynamics are resonance and instability of the rotor. Both have a common harmful effect that causes damages of the turbochargers during the operation. However, there is a big difference between the resonance and instability if we take a close look on them.

At the resonance, the rotor reaches maximum deflection at the critical frequencies depending on the rotor characteristics, such as mass, mass inertia moments, stiffness, and damping coefficients. The excitation unbalance force is proportional to the rotor speed squared. The unbalanced force is balanced by the inertia force, bearing force, stiffness, and damping forces acting on the rotor at any time t. The more the rotor deflects, the larger the stiffness force acts upon the rotor. In case of lacking or small damping effect, the deflection of the rotor extremely increases at the resonance, so that the normal stress of the shaft exceeds the ultimate tensile stress, or the contact between the journal and bearings occurs. Therefore, the rotor could be damaged at the critical frequency. Due to self-centering effect of the rotor, the maximum deflection amplitude will be reduced at once when the rotor speed passes the critical speed.

Contrary to the resonance, the rotor amplitude in unstable condition extremely increases with time, even at a constant rotor speed. As soon as the rotor speed exceeds the onset of instability (threshold of instability), the rotor becomes unstable at which the rotor amplitude increases with time without limit; it is not reduced at further raising the rotor speed. In case of using the oil-film bearings, oil whirl takes place when the dissipative damping force is quite small compared to the destabilizing force induced by the cross-coupled bearing stiffness coefficient. The oil whirl is a kind of the self-excitation instability where the rotor amplitude increases without precondition of unbalance. When the oil whirl frequency reaches the bending critical frequency, mostly the first-order critical frequency, the oil whirl turns to oil whip. At the oil–whip, the rotor becomes a real instability where the rotor deflection continuously increases, and the journal eccentricity exceeds the bearing clearance, leading to damage of the radial bearings and turbochargers as well.

In order to avoid the damage of the turbochargers due to rotor instability, all rotor characteristics including compressor, turbine wheels, shaft, sealing, and fluid film bearings must be studied at the beginning of rotordynamic design. There are

two common methods to look into the stability analysis of the turbochargers: first, eigenvalues analysis with the Routh-Hurwitz criterion for linear rotordynamics; second, bifurcation method with the Hopf theory for nonlinear rotordynamics.

## 4.2 Stability Analysis of Linear Rotordynamics

### 4.2.1 Eigenvalues of the Free Vibration Response

The eigenvalues analysis is based on the free vibration response of the linear rotordynamic system. The free vibration response is resulted by superimposing the harmonic components of the rotor without excitation of the rotor unbalance. In fact, the free vibration response is exact the homogeneous solutions of the vibration equations of the rotor. Each harmonic component has a complex eigenvalue in which the imaginary part is the eigenfrequency of the rotor (also called natural frequency), and the real part indicates the stability characteristic of the rotor.

The free vibration response of the rotor is written in

$$r(t) = \sum_{i=1}^{N} r_i e^{\lambda_i t} \qquad (4.1)$$

where
$r_i$ is the rotor amplitude corresponding to the eigenvalue;
$\lambda_i$ is the complex eigenvalue of the eigenmode i;
N is the number of degrees of freedom (DOF) of the rotor.

The complex eigenvalue consists of the real and imaginary parts

$$\lambda = \alpha \pm j\omega_d \qquad (4.2)$$

within
$\alpha$ is the real part of the eigenvalue, called the growth/decay rate;
$\omega_d$ is the imaginary part of the complex eigenvalue (eigenfrequency or damped natural frequency).

Substituting $\lambda$ into eq. (4.1), one obtains the rotor free response by applying Euler's theorem.

$$
\begin{aligned}
r(t) &= \sum_{i=1}^{N} r_{i,fw} e^{\alpha_i t} e^{j\omega_i t} + \sum_{i=1}^{N} r_{i,bw} e^{\alpha_i t} e^{-j\omega_i t} \\
&= \sum_{i=1}^{N} r_{i,fw} e^{\alpha_i t} \left[\cos(\omega_i t) + j\sin(\omega_i t)\right] + \sum_{i=1}^{N} r_{i,bw} e^{\alpha_i t} \left[\cos(-\omega_i t) + j\sin(-\omega_i t)\right] \\
&\equiv x(t) + jy(t)
\end{aligned}
$$

$$(4.3)$$

The parts in the square brackets [ ] in eq. (4.3) are the harmonic vibrations with the eigenfrequencies of the forward and backward frequency components. Hence, the maximal amplitude is limited to one at any time t. On the contrary, the terms

before the square brackets [ ] containing an exponential function exp($\alpha_i$t) change with time. The amplitude of the rotor response depends on the growth/decay rate $\alpha_i$. If the rate $\alpha_i$ is positive, the rotor amplitude increases with time without limit. The rotor response is unstable at any positive rate $\alpha$; therefore, $\alpha$ is the key parameter for the stability analysis of the rotor in linear rotordynamics.

Cases of the growth/decay rate $\alpha$ for the rotor response behavior:

- $\alpha < 0$: stability;
- $\alpha = 0$: onset of instability (threshold of instability);
- $\alpha > 0$: instability.

The stability behaviors depending on the growth/decay rates are displayed in Figures 4.1a, b, and c. At a decay rate ($\alpha < 0$), the vibration amplitude with the frequency $\omega$ diminishes in a short time. The envelope of the vibration is the exponential function $r_0.\exp(\alpha t)$ that begins from the initial position $r_0$ at time t = 0 and decreases with time to zero. The corresponding forward orbit decays from the initial position $r_0$ to zero as t $\rightarrow$ $\infty$. In this case, the free vibration is stable or unconditionally stable, as displayed in Fig.4.1a.

On the contrary, at a growth rate ($\alpha > 0$), the vibration begins at the initial position and increases with time exponentially; therefore, the vibration is unstable, as shown in Fig. 4.1c.

At the rate of $\alpha = 0$, the vibration amplitude is unchanged with time, neither decreasing nor increasing with time because the amplitude of the function $r_0.\exp(\alpha t)$ always remains constant at $r_0$ at any time t, as shown in Fig. 4.1b. The rotor vibration moves in a circular orbit that is called limit cycle, which occurs in the Hopf bifurcation. The vibration is at the threshold of instability (onset of instability).

To study the rotor stability, the complex eigenvalues $\lambda$ are analyzed in the $\lambda$ plane, as shown in Fig. 4.2. The complex eigenvalue and its conjugated eigenvalue have the common real part and opposite imaginary part with positive and negative signs that correspond to forward and backward damped natural frequencies. If both these eigenvalues lie in the half-left plane ($\alpha < 0$), the rotor behavior is stable; on the half-right plane ($\alpha > 0$), it is unstable. In case of the threshold of instability ($\alpha = 0$), the rotor vibration moves with the damped natural frequency $\omega_d$ at the constant amplitude, neither decreasing nor increasing with time.

In order to maintain the rotor in a stable condition, all eigenvalues of the rotor must lie on the left-half plane, so that the growth/decay rates are always negative.

In this case, there are two possibilities:

- When they locate in the upper left-half plane, the vibration response is a stable forward whirl and decays with time from the initial position to zero, as shown in Fig. 4.1a;
- When they locate in the lower left-half plane, the vibration response is a stable backward whirl and decays with time from the initial position to zero, similar to Fig. 4.1a, but the whirl direction is opposite to the forward whirl.
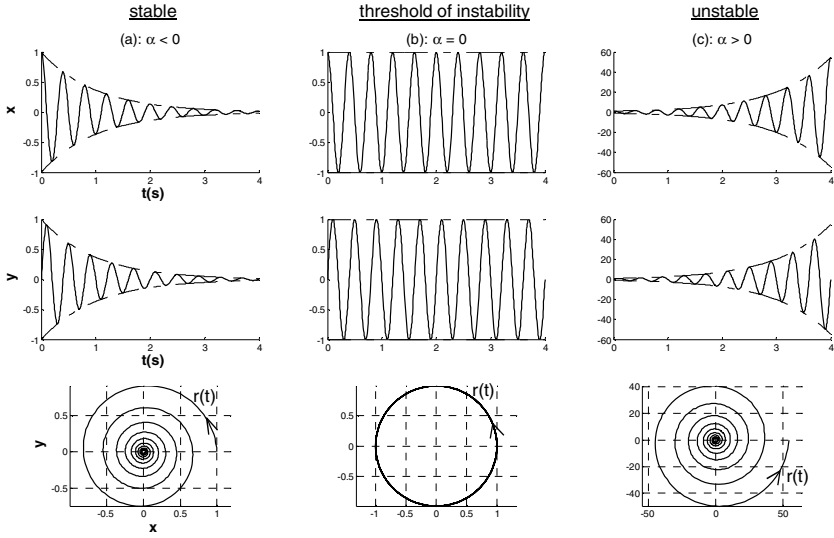
**Fig. 4.1** a; b; c: Cases of the growth/decay rates $\alpha$ in the phase plane x-y
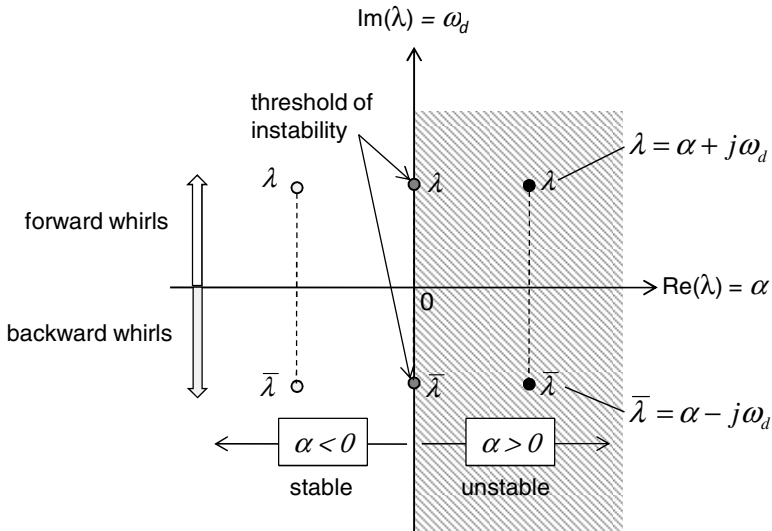


**Fig. 4.2** Stability analysis in the $\lambda$ plane

## 4.2.2  A Study Case of Calculating the Eigenvalues

In the following section, a very simple model of the Jeffcott rotor is chosen to demonstrate the principle of calculating the eigenvalues of the rotor. The key issue is preferred to understand the physical meaning of the problem, rather than to

show off the complicated mathematical calculations. Therefore, a simple Jeffcott rotor is used for the study case in which the gyroscopic effect of the wheel is not taken into account. Figure 4.3 shows the simulated Jeffcott rotor that consists of the wheel, rotor shaft, and two orthotropic bearings. The wheel with mass m is located in the middle of the shaft that is supported by the orthotropic bearings ($K_1 \neq K_2$) at the ends of the shaft. The rotor is excited by the unbalance force $F_{Un}$, which is proportional to the rotor speed squared.
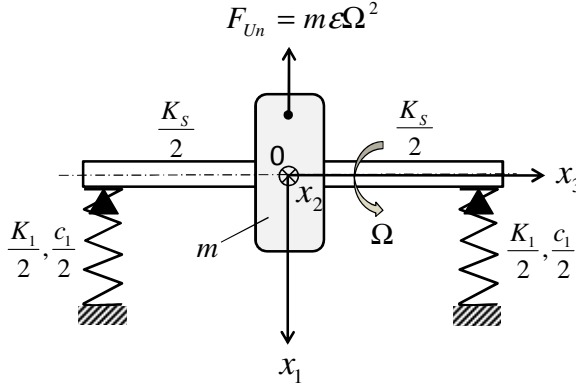


**Fig. 4.3** Simulation model of the Jeffcott rotor

The bearing stiffness coefficients are $K_1$ and $K_2$; bearing damping coefficients, $c_1$ and $c_2$ in the directions $x_1$ and $x_2$, respectively. The shaft has its own stiffness coefficient $K_S$. The impedance method is used to calculate the equivalent stiffness coefficient acting upon the rotor. The equivalent stiffness coefficient of the rotor is resulted from the shaft and bearing stiffness coefficients in each direction.
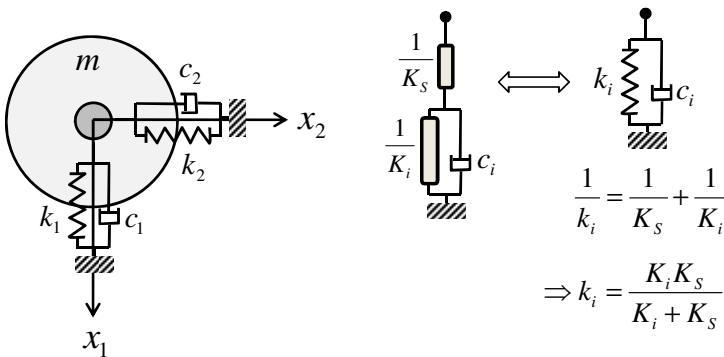


**Fig. 4.4** Equivalent stiffness coefficient $k_i$

The equivalent impedances acting upon the rotor $1/k_1$ and $1/k_2$ in the directions $x_1$ and $x_2$ are calculated.

$$\frac{1}{k_i} = \frac{1}{K_S} + \frac{1}{K_i}, \quad i = 1, 2 \tag{4.4}$$

Therefore, the equivalent stiffness coefficient of the rotor becomes

$$k_i = \frac{K_i K_S}{K_i + K_S}, \quad i = 1, 2 \tag{4.5}$$

Having applied the Newton's second law to the rotor, the vibration equations without the gyroscopic effect of the 2-DOF rotor are written in

$$\begin{cases} m\ddot{x}_1 + c_1 \dot{x}_1 + k_1 x_1 = m\varepsilon\Omega^2 \cos \Omega t \\ m\ddot{x}_2 + c_2 \dot{x}_2 + k_2 x_2 = m\varepsilon\Omega^2 \sin \Omega t \end{cases} \tag{4.6}$$

The homogeneous equations are taken into account in studying the rotor stability

$$\begin{cases} m\ddot{x}_1 + c_1 \dot{x}_1 + k_1 x_1 = 0 \\ m\ddot{x}_2 + c_2 \dot{x}_2 + k_2 x_2 = 0 \end{cases} \tag{4.7}$$

Eq. (4.7) is formulated in the matrix form

$$\begin{bmatrix} m & 0 \\ 0 & m \end{bmatrix} \cdot \begin{bmatrix} \ddot{x}_1 \\ \ddot{x}_2 \end{bmatrix} + \begin{bmatrix} c_1 & 0 \\ 0 & c_2 \end{bmatrix} \cdot \begin{bmatrix} \dot{x}_1 \\ \dot{x}_2 \end{bmatrix} + \begin{bmatrix} k_1 & 0 \\ 0 & k_2 \end{bmatrix} \cdot \begin{bmatrix} x_1 \\ x_2 \end{bmatrix} = \begin{bmatrix} 0 \\ 0 \end{bmatrix} \tag{4.8}$$

The free vibration solutions of eq. (4.8) are assumed

$$\begin{bmatrix} x_1 \\ x_2 \end{bmatrix} = \begin{bmatrix} X_1 e^{\lambda t} \\ X_2 e^{\lambda t} \end{bmatrix} \tag{4.9}$$

where
$X_1$ and $X_2$ are the amplitudes of $x_1$ and $x_2$, respectively;
$\lambda$ is the complex eigenvalue, $\lambda = \alpha \pm j\omega_d$.

Inserting eq. (4.9) and its first and second order derivatives in eq. (4.8), one obtains

$$\begin{bmatrix} m\lambda^2 + c_1\lambda + k_1 & 0 \\ 0 & m\lambda^2 + c_2\lambda + k_2 \end{bmatrix} \begin{bmatrix} X_1 e^{\lambda t} \\ X_2 e^{\lambda t} \end{bmatrix} = \begin{bmatrix} 0 \\ 0 \end{bmatrix} \tag{4.10}$$

For nontrivial solutions $x_1$ and $x_2$, the determinant of the first matrix must be equal to zero.

$$\begin{vmatrix} m\lambda^2 + c_1\lambda + k_1 & 0 \\ 0 & m\lambda^2 + c_2\lambda + k_2 \end{vmatrix} = 0 \tag{4.11}$$

Thus,

$$(m\lambda^2 + c_1\lambda + k_1).(m\lambda^2 + c_2\lambda + k_2) = 0 \tag{4.12}$$

Equation (4.12) is called the characteristic equation of the rotor with fourth order of $\lambda$. It is resulted from twice degrees of freedom (2*DOF) of the rotor due to forward and backward whirls. In this case, the number of DOF ($x_1$ and $x_2$) equals 2; hence, the characteristic equation is in the fourth order of $\lambda$. Notice that DOF of the rotor is the number of the independent spatial coordinates that describe the rotor vibration behavior at any time. Therefore, it equals the number of the ordinary differential equations (ODE) of the rotor vibration; hence, DOF = 2, as shown in eq. (4.6).

Roots of the characteristic equation $D(\lambda)$ are the eigenvalues of the system that are generally complex numbers. Eq. (4.12) can be written in two homogeneous equations

$$m\lambda^2 + c_i\lambda + k_i = 0; \; i = 1, 2 \tag{4.13}$$

Eq. (4.13) can be transformed with dropping the index i into

$$\lambda^2 + 2\omega_n\zeta\lambda + \omega_n^2 = 0 \tag{4.14}$$

where
$\zeta$ is the damping ratio
$\omega_n$ is the undamped natural frequency.

The undamped natural frequency is defined as

$$\omega_n = \sqrt{\frac{k}{m}} \tag{4.15}$$

The dimensionless damping ratio is defined as

$$\zeta \equiv \frac{c}{2m\omega_n} = \frac{c}{2\sqrt{km}} \tag{4.16}$$

The eigenvalues are obtained by solving eq. (4.14)

$$\lambda = -\omega_n\zeta \pm j\omega_n\sqrt{1-\zeta^2} = -\frac{c}{2m} \pm j\omega_n\sqrt{1-\zeta^2} \equiv \alpha \pm j\omega_d \tag{4.17}$$

Resulting from eq. (4.17), there are four eigenvalues $\lambda_i$ of the characteristic equation:

$$\lambda_i = \alpha_i \pm j\omega_{d,i}; \; i = 1, 2 \tag{4.18}$$

within

$$\alpha_i = -\frac{c_i}{2m} = -\omega_{n,i}\zeta_i \text{ is the growth/decay rate (1/s);} \tag{4.19}$$

$$\omega_{d,i} = \omega_{n,i}\sqrt{1-\zeta_i^2} \text{ is the damped natural frequency (1/s).} \qquad (4.20)$$

To keep the rotor stable in any working condition, the growth/decay rate must be always negative, as discussed earlier. According to eq. (4.19), the rotor is stable when the damping coefficient c is positive; otherwise, the rotor is unstable at the negative damping coefficient, e.g. in case of suction in the damping absorber.

The damped natural frequency $\omega_d$ is normally a little bit smaller than the undamped frequency $\omega_n$ depending on the damping ratio according to eq. (4.20).

There are three cases of the dimensionless damping ratio $\zeta$:

- $\zeta < 1$: the vibration response is underdamped or subcritically damped with the underdamped frequency $\omega_d < \omega_n$. The rotor orbit is stable, and its amplitude decreases with time. In this case, the growth/decay rate results in

$$\alpha = -\omega_n\zeta \qquad (4.21)$$

- $\zeta = 1$: the vibration response is critically damped, $\omega_d = 0$. There is no vibration, and its amplitude decreases much more quickly to zero without oscillation. In this case, the growth/decay rate is opposite to the undamped natural frequency.

$$\alpha = -\omega_n \qquad (4.22)$$

- $\zeta > 1$: the vibration response is overdamped or supercritically damped, $\omega_d = 0$. There is no vibration, and its amplitude decreases quickly to zero without oscillation. In this case, the growth/decay rate is written in

$$\alpha = -\omega_n(\zeta \pm \sqrt{\zeta^2 - 1}) \qquad (4.23)$$

The decay rate with the plus sign in eq. (4.23) is much larger than the decay rate with the minus sign; therefore, its response amplitude decays much faster than the amplitude with the minus sign. In fact, the decay rate with the minus sign dominates the response amplitude in the long-term motion.

The influence of the damping ratio $\zeta$ on the growth/decay rate $\alpha$ is displayed in Fig. 4.5. First, at the undamped condition ($\zeta < 1$), the growth/decay rate linearly decreases with $\zeta$. Second, at the critically damped condition ($\zeta = 1$), the rate $\alpha$ equals to $-\omega_n$ according to eq. (4.22). Third, at the overdamped condition ($\zeta > 1$), the decay rate with minus sign decreases from $\omega_n$ to zero (long-term motion $\zeta^- > 1$), and the decay rate with the plus sign increases from $\omega_n$ to $\infty$ (short-term motion $\zeta^+ > 1$) as the damping ratio $\zeta$ increases to $\infty$.

The behaviors of the vibration response at various damping ratios are illustrated in Fig. 4.6. The underdamped vibration response ($\zeta < 1$) with a damped natural frequency $\omega_d$ decays much more slowly than the critically and overdamped vibration responses because of its small decay rate $\alpha$, as shown in Fig. 4.5.

**Fig. 4.5** Growth/decay rate α at various damping ratios ζ



**Fig. 4.6** Response amplitudes at various damping ratios ζ

## 4.2.3 *Stability Analysis by Routh-Hurwitz Criterion*

In the earlier section, a simple model of the Jeffcott rotor without the gyroscopic effect has been studied. In fact, the computed model of turbochargers is much more complex than the Jeffcott rotor model. In the computed turbocharger model, the gyroscopic effect of the compressor and turbine wheels are taken into account,

orthotropic oil film bearings must be also considered. In this case, the numbers of degree of freedom N are very large, such as 15, 20, or more; the eigenvalues result in two times of DOF (= 2N). Therefore, it is very difficult to solve the 2N-order characteristic equation of $\lambda$ analytically.

The vibration equations of the rotordynamic model of turbochargers are described in the matrix form

$$\mathbf{M\ddot{x} + C\dot{x} + Kx = f}(t) \tag{4.24}$$

where
$\mathbf{M}$ = (N x N) mass matrix containing the mass and inertia moments of the rotor;
$\mathbf{C}$ = (N x N) damping coefficient matrix containing the diagonal and cross-coupled damping coefficients;
$\mathbf{K}$ = (N x N) stiffness matrix containing the diagonal and cross-coupled stiffness coefficients;
$\mathbf{x(t)}$ = (N x 1) vibration response vector;
$\mathbf{f(t)}$ = (N x 1) external forces vector.

In order to reduce the second to first order equation set, a (2N x 1) new vector $\mathbf{z}$ of the vibration response is defined.

$$\mathbf{z} \equiv \begin{bmatrix} \mathbf{x} \\ \mathbf{y} \end{bmatrix} = \begin{bmatrix} \mathbf{x} \\ \mathbf{\dot{x}} \end{bmatrix} \Rightarrow \mathbf{\dot{z}} = \begin{bmatrix} \mathbf{\dot{x}} \\ \mathbf{\ddot{x}} \end{bmatrix} = \begin{bmatrix} \mathbf{y} \\ \mathbf{\dot{y}} \end{bmatrix} \tag{4.25}$$

where $\mathbf{y} = \mathbf{\dot{x}}; \quad \mathbf{\dot{y}} = \mathbf{\ddot{x}}$.

By substituting the vector $\mathbf{z}$ into eq. (4.24), one obtains 2N first order vibration equations of the rotor.

$$\begin{bmatrix} \mathbf{\dot{x}} \\ \mathbf{\ddot{x}} \end{bmatrix} = \begin{bmatrix} \mathbf{0} & \mathbf{I} \\ -\mathbf{M^{-1}K} & -\mathbf{M^{-1}C} \end{bmatrix} \cdot \begin{bmatrix} \mathbf{x} \\ \mathbf{\dot{x}} \end{bmatrix} + \begin{bmatrix} \mathbf{0} \\ \mathbf{M^{-1}f}(t) \end{bmatrix}$$

$$\mathbf{\dot{z}} = \begin{bmatrix} \mathbf{0} & \mathbf{I} \\ -\mathbf{M^{-1}K} & -\mathbf{M^{-1}C} \end{bmatrix} \cdot \mathbf{z} + \begin{bmatrix} \mathbf{0} \\ \mathbf{M^{-1}f}(t) \end{bmatrix} \tag{4.26}$$

$$= \mathbf{Az} + \mathbf{b}(t)$$

To analyze the dynamic stability, only the homogeneous equations of eq. (4.26) are considered where the excitation force $\mathbf{f}(t)$ equals zero; hence, $\mathbf{b}(t) = 0$.

$$\mathbf{\dot{z}} = \mathbf{Az} \tag{4.27}$$

where
$\mathbf{z}$ = (2N x 1) vector, the vibration response vector;
$\mathbf{A}$ = (2N x 2N) matrix of the rotor;
N = degrees of freedom of the rotor (DOF).

One assumes the free vibration response vector as

$$\mathbf{z} = \mathbf{\hat{z}}e^{\lambda t} \tag{4.28}$$

within $\mathbf{\hat{Z}}$ is the ( 2N x 1) eigenvector.

Substituting the response vector $\mathbf{z}$ and its first order derivative into eq. (4.27), one obtains

$$(\mathbf{A} - \lambda \mathbf{I})\hat{\mathbf{z}}e^{\lambda t} = 0 \tag{4.29}$$

The characteristic equation of the eigenvalues is derived from eq. (4.29).

$$\det(\mathbf{A} - \lambda \mathbf{I}) = 0 \tag{4.30}$$

Because $\mathbf{A}$ has the order of a (2N x 2N) matrix, the characteristic equation is a polynomial equation of 2N order.

$$D(\lambda) = a_n \lambda^n + a_{n-1}\lambda^{n-1} + ... + a_2\lambda^2 + a_1\lambda + a_0 = 0 \tag{4.31}$$

where
$\lambda$ are the complex eigenvalues with $\lambda = \alpha + j\omega_d$;
$a_i$ is the equation coefficients, i = 0, 1, 2,…, n;
n is the polynomial exponent that equals twice DOF (n = 2N).

Having used the Gauss theorem, eq. (4.31) can be written in the polynomial with the n order of $\lambda$ where $\lambda_i$ are the roots of $D(\lambda)$.

$$D(\lambda) = a_n(\lambda - \lambda_1)(\lambda - \lambda_2)...(\lambda - \lambda_{n-1})(\lambda - \lambda_n) \tag{4.32}$$

Finding the roots $\lambda_i$ of the polynomial $D(\lambda)$ in eq. (4.31) is quite difficult, especially at a large number of DOF. In fact, it need not know the exact values of the roots $\lambda_i$, but only the real parts $\alpha$ of the eigenvalues are necessary for the stability analysis. In this case, the Routh-Hurwitz stability criterion is applied to analyze the eigenvalues in linear rotordynamics.

According to the Routh-Hurwitz criterion, the vibration response is stable when the two following conditions are satisfied:

1. All coefficients $a_i$ in the characteristic equation (4.31) must be nonzero and have the same positive or negative signs.

2. Hurwitz determinant $D_{n-1}$, and its diagonal determinants $D_i$ for i = 1, 2,…, n-2 must be positive.

$$D_{n-1} = \begin{vmatrix} a_{n-1} & a_{n-3} & a_{n-5} & . & ... & . & 0 \\ a_n & a_{n-2} & a_{n-4} & . & ... & . & 0 \\ 0 & a_{n-1} & a_{n-3} & a_{n-5} & ... & . & . \\ 0 & a_n & a_{n-2} & a_{n-4} & ... & . & . \\ 0 & 0 & . & . & ... & a_1 & 0 \\ 0 & 0 & . & . & ... & a_2 & a_0 \\ 0 & 0 & . & . & a_5 & a_3 & a_1 \end{vmatrix} > 0 \tag{4.33}$$

where the coefficients $a_{n-i}$ equal zero at all negative indices (n-i) for i = 0, 1,..., n.

The Hurwitz determinant $D_{n-1}$ and diagonal determinants $D_i$ for the characteristic equation $D(\lambda)$ of n order (n = 2 DOF) can be written in

$$D_1 = |a_{n-1}| > 0;$$

$$D_2 = \begin{vmatrix} a_{n-1} & a_{n-3} \\ a_n & a_{n-2} \end{vmatrix} > 0;$$

$$D_3 = \begin{vmatrix} a_{n-1} & a_{n-3} & a_{n-5} \\ a_n & a_{n-2} & a_{n-4} \\ 0 & a_{n-1} & a_{n-3} \end{vmatrix} > 0...$$

$$D_{n-2} = \begin{vmatrix} a_{n-1} & a_{n-3} & a_{n-5} & ... & . & 0 \\ a_n & a_{n-2} & a_{n-4} & ... & . & 0 \\ 0 & a_{n-1} & a_{n-3} & ... & . & 0 \\ 0 & a_n & a_{n-2} & ... & . & a_0 \\ 0 & 0 & . & ... & a_3 & a_1 \\ 0 & 0 & . & ... & a_4 & a_2 \end{vmatrix} > 0.$$

The Routh-Hurwitz criterion is applied to the Jeffcott rotor, as shown in Fig. 4.3 to analyze the rotor stability of the vibration equations with the fourth order of $\lambda$. The characteristic equation of the rotor vibration is written in

$$(m\lambda^2 + c_1\lambda + k_1).(m\lambda^2 + c_2\lambda + k_2) =$$
$$m^2\lambda^4 + m(c_1 + c_2)\lambda^3 + (mk_1 + mk_2 + c_1c_2)\lambda^2 + (c_1k_2 + c_2k_1)\lambda + k_1k_2 = 0 \tag{4.34}$$

Checking stability conditions of eq. (4.34):
- the first condition is satisfied because all coefficients are positive and nonzero;
- the second condition of $D_1$, $D_2$, and $D_3$ has to be checked whether they are positive.

The Hurwitz determinant and diagonal determinants are calculated.

$$D_1 = |m(c_1 + c_2)| = m(c_1 + c_2)$$

$$D_2 = \begin{vmatrix} m(c_1 + c_2) & (c_1k_2 + c_2k_1) \\ m^2 & (mk_1 + mk_2 + c_1c_2) \end{vmatrix} = m^2(c_1k_1 + c_2k_2) + mc_1c_2(c_1 + c_2)$$

$$D_3 = \begin{vmatrix} m(c_1 + c_2) & (c_1k_2 + c_2k_1) & 0 \\ m^2 & (mk_1 + mk_2 + c_1c_2) & k_1k_2 \\ 0 & m(c_1 + c_2) & (c_1k_2 + c_2k_1) \end{vmatrix}$$

The determinant $D_3$ results in after a few calculating steps

$$D_3 = mc_1c_2\left(m(k_1 - k_2)^2 + (c_1 + c_2)(c_1k_2 + c_2k_1)\right)$$

All determinants $D_1$, $D_2$, and $D_3$ are positive due to positive damping coefficients $c_1$ and $c_2$; hence, the vibration response is stable. Otherwise, the rotor response is unstable when the damping coefficients are negative at a suction damper.

## 4.3   Stability Analysis of Nonlinear Rotordynamics

The eigenvalues have not existed any longer in nonlinear rotordynamics; therefore, the eigenvalues analysis is not valid in this case. Instead, the bifurcation theory is normally used to analyze the stability of nonlinear rotordynamics. The nonlinearity is mainly caused by the nonlinear characteristic of the oil-film bearings. The nonlinear bearing forces acting upon the rotor contain two parts, the rotation and damping forces. According to the bearing dynamics, the bearing rotation forces are nonlinear to the journal eccentricity and angular position of the journal locus. The bearing damping forces are nonlinear not only to the journal eccentricity and its angular position but also to the eccentricity velocity and whirl velocity of the journal in the bearing clearance. As a reason, the vibration equations are generally nonlinear in the rotordynamics of the automotive turbochargers.

### 4.3.1   Vibration Equations in the Autonomous Systems

Having used the Newton's second law for the nonlinear rotor of N degrees of freedom (DOF), one obtains the vibration equations of the rotor in the matrix second-order equations.

$$\begin{bmatrix} \dot{\mathbf{x}} \\ \ddot{\mathbf{x}} \end{bmatrix} = \begin{bmatrix} \mathbf{0} & \mathbf{I} \\ -\mathbf{M}^{-1}\mathbf{K}_S & \mathbf{0} \end{bmatrix} \cdot \begin{bmatrix} \mathbf{x} \\ \dot{\mathbf{x}} \end{bmatrix} + \begin{bmatrix} \mathbf{0} \\ \mathbf{M}^{-1}\mathbf{F}_{Un}(t) + \mathbf{M}^{-1}\mathbf{F}_B(\mathbf{x}, \dot{\mathbf{x}}) \end{bmatrix} \tag{4.35}$$

where
$\mathbf{M}$ = (N x N) diagonal matrix containing mass and mass inertia moments;
$\mathbf{K}_S$ = (N x N) shaft stiffness coefficient matrix;
$\mathbf{I}$ = (N x N) unit matrix;
$\mathbf{x}$ = (N x 1) DOF vector including all degrees of freedom of the system;
$\mathbf{F}_{Un}$ = (N x 1) unbalance force vector;
$\mathbf{F}_B$ = (N x 1) bearing force vector consisting of the rotation and damping forces;
N = degrees of freedom (DOF).

By substitution of the new vector $\mathbf{z}$ into eq. (4.35), the vibration equations become

$$
\begin{aligned}
\dot{\mathbf{z}} &= \begin{bmatrix} \mathbf{0} & \mathbf{I} \\ -\mathbf{M}^{-1}\mathbf{K}_S & \mathbf{0} \end{bmatrix} \cdot \mathbf{z} + \begin{bmatrix} \mathbf{0} \\ \mathbf{M}^{-1}\mathbf{F}_{\mathbf{Un}}(t) + \mathbf{M}^{-1}\mathbf{F}_{\mathbf{B}}(\mathbf{z}, \Omega) \end{bmatrix} \\
&= \mathbf{A}\mathbf{z} + \mathbf{b}(\mathbf{z}, \Omega, t)
\end{aligned}
\tag{4.36}
$$

within

$$
\mathbf{z} \equiv \begin{bmatrix} \mathbf{x} \\ \mathbf{y} \end{bmatrix} = \begin{bmatrix} \mathbf{x} \\ \dot{\mathbf{x}} \end{bmatrix} \text{ is the (2N x 1) vector of DOF}
$$

with

$$
\mathbf{x} = (x_1 \ x_2 ... x_N)^T ; \ \mathbf{y} = (y_1 \ y_2 ... y_N)^T ;
$$

$$
\mathbf{A} = \begin{bmatrix} \mathbf{0} & \mathbf{I} \\ -\mathbf{M}^{-1}\mathbf{K}_S & \mathbf{0} \end{bmatrix} \text{ is the (2N x 2N) stiffness matrix of the shaft;}
$$

$$
\mathbf{b} = \begin{bmatrix} \mathbf{0} \\ \mathbf{M}^{-1}\mathbf{F}_{\mathbf{Un}}(t) + \mathbf{M}^{-1}\mathbf{F}_{\mathbf{B}}(\mathbf{z}, \Omega) \end{bmatrix}
$$

is the (2N x 1) vector including the unbalance excitation force and bearing forces acting upon the rotor.

The system is called autonomous when it is explicitly independent of time t explicitly. For simplicity of using the bifurcation theory, we transform the non-autonomous nonlinear system into the autonomous nonlinear system. Hence, the vibration equations in eq. (4.36) become the autonomous equation system of

$$
\dot{\mathbf{u}} = \mathbf{A}^*\mathbf{u} + \mathbf{b}^*(\mathbf{u}, \theta, \Omega)
\tag{4.37}
$$

where the external force vector $\mathbf{b}^*$ is explicitly is independent of time t. Equation (4.37) is the 2N+1 first-order differential equations with an additional equation ($\dot{\theta}=1$) that only depend on the rotor speed $\Omega$, which is chosen as a bifurcation parameter of the vibration equation system at the given rotor and bearing characteristics. To study the interactive bifurcation analysis of dynamic systems, the software package MATCONT [4] based on the MATLAB code is recommended.

## 4.3.2  Stability Analysis by Bifurcation Theory

The bifurcation occurs when the quantitative characteristic of the vibrations change from the steady state at the equilibrium to the unsteady-state condition (periodic motions) as the bifurcation parameter μ reaches the critical threshold value $\mu_0$, which is called bifurcation point. At the bifurcation point, the dynamic behavior of the system is transferred from the steady-state to periodic or quasi-periodic vibrations, from the stable to unstable dynamic behaviors, and from the regular to irregular and as well as to chaotic motions. Hopf bifurcation is a special kind of the bifurcation that connects the equilibrium to the periodic oscillation at the bifurcation point (s. [7], [9], and [10]).

The loss of stability at Hopf bifurcation takes place as the eigenvalue $\lambda(\mu_0)$ and its conjugated eigenvalue cross the imaginary axis at the points $\pm\omega_0$ where the bifurcation parameter arrives at the critical value $\mu_0$ that depends on the given characteristic of the system, such as the rotor unbalance, bearing clearances and geometries, and oil working condition (oil temperature and pressure). At the bifurcation point, the dynamic behavior changes from the equilibrium to periodic oscillations with the initial frequency $\omega_0$. The orbit of the rotor locus is limited in the limit cycle at the studied bifurcation parameter, such as the rotor speed.
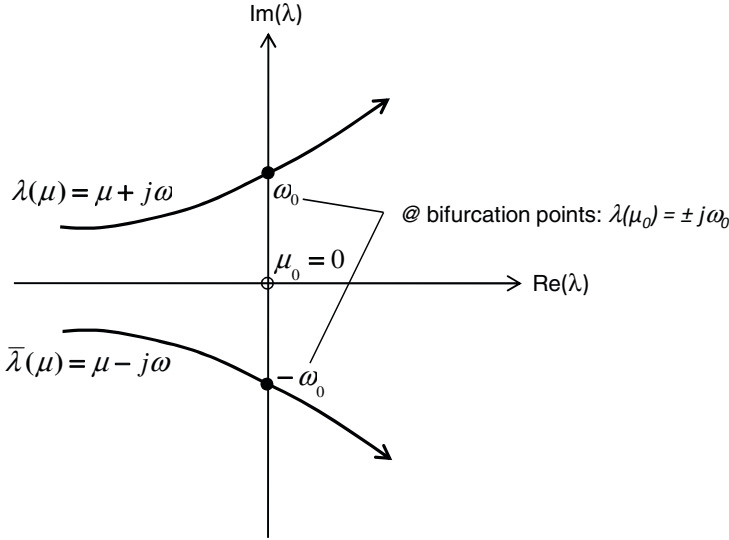


**Fig. 4.7** Hopf bifurcation in the $\lambda$ plane

### 4.3.3 Characteristics of Hopf Bifurcation Theory

#### a) Equilibrium points
Equilibrium points are defined as the state vectors $\mathbf{u}^*$ where the system is in a steady-state condition. They are found by setting the vibration equation (4.37) equal zero.

$$\dot{\mathbf{u}}^* = \mathbf{A}^*\mathbf{u}^* + \mathbf{b}^*(\mathbf{u}^*, \theta, \Omega) \equiv \mathbf{f}(\mathbf{u}^*, \theta, \Omega) = \mathbf{0} \qquad (4.38)$$

where $\Omega$ is chosen as the bifurcation parameter ($\Omega \equiv \mu$). The system state changes from the equilibrium to periodic vibrations with the initial frequency $\omega_0$ at the bifurcation point $\mu_0 = \Omega_0$. The equilibrium points are also called fixed or singular points.

#### b) Bifurcation point
Bifurcation point $\mu_0 \equiv \Omega_0$ is the intersection of the trivial branch and nontrivial half-branches; their solutions correspond to the equilibrium points. At this point,

the loss of stability takes place, and the vibration response of the system changes
from the equilibrium state to periodic vibrations (s. Fig. 4.8).

## c) Node and focus

- Node has no oscillation ($\omega = 0$) where the stable trajectories approach the stable
node, and the unstable trajectories move away from the unstable node (s. Fig. 4.9a).
- Focus contains a vibration with a non-zero frequency $\omega$ where the spirals ap-
proach the stable focus with time. They are called stable spirals whose speeds
are negative. At the unstable focus, the spirals move away from it, as shown in
Fig. 4.9b. Hence, the spirals are unstable; their speeds are positive; i.e., the spiral
amplitudes increase with time.
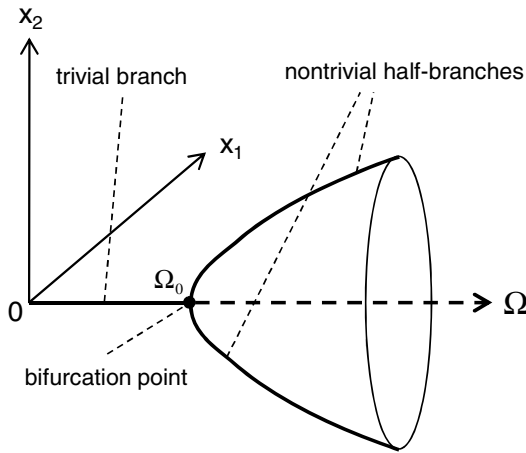


**Fig. 4.8** Bifurcation point in the bifurcation plane
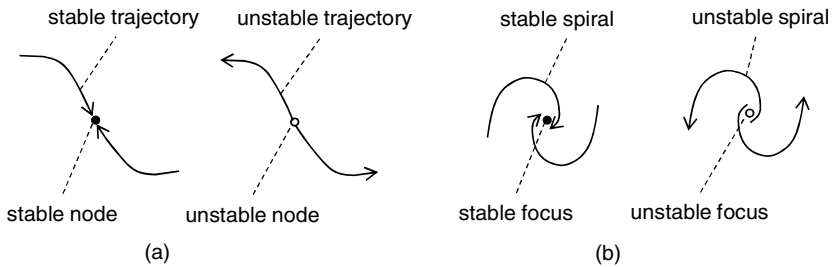


**Fig. 4.9** a,b: Node and focus in the phase plane

## d) Limit cycles

Limit cycle is a closed orbit that the trajectories asymptotically move to (stable
spirals) or away from (unstable spirals). Generally, the limit cycle has an ellipse
shape. There are three kinds of the limit cycle in nonlinear rotordynamics.

- Stable limit cycle encircles an unstable focus that the inner unstable spiral moves away from and approaches the stable limit cycle. The outer stable spiral moves from outside towards the limit cycle. The focus is also called spiral point (s. Fig. 4.10a).
- Unstable limit cycle encircles a stable focus that the inner stable spiral moves away from the limit cycle towards. The outer unstable spiral moves away from the limit cycle outwards (s. Fig. 4.10b).
- Half-stable limit cycle encircles a stable focus that the inner stable spiral moves away from the limit cycle towards, and the outer stable spiral moves from outside towards the limit cycle, as shown in Fig. 4.11a or vice versa in Fig. 4.11b.
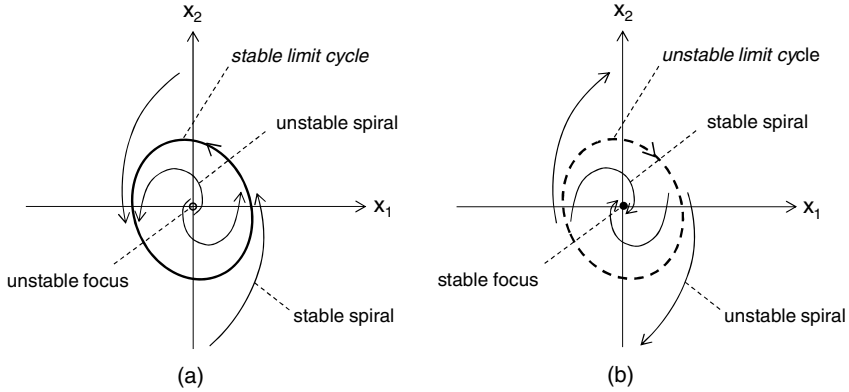


**Fig. 4.10** a,b: Stable and unstable limit cycles in the phase plane
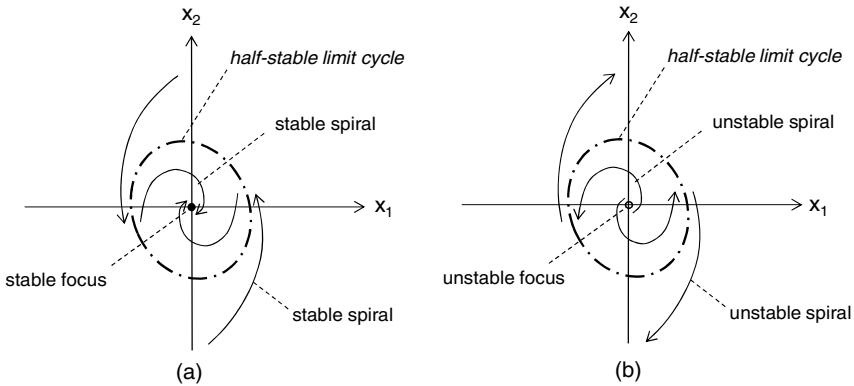


**Fig. 4.11** a,b: Half-stable limit cycles in the phase plane

### e) Stability definitions

- The dynamic behavior is asymptotically stable to the equilibrium $\mathbf{u}^*$ when the perturbation $\boldsymbol{\varepsilon}$ reaches zero as time t goes to infinity.

$$\lim_{t \to \infty} \mathbf{u}(t) = \lim_{t \to \infty} (\mathbf{u}^* + \boldsymbol{\varepsilon}) = \mathbf{u}^*; \qquad |\boldsymbol{\varepsilon}| = 0$$

- The dynamic behavior is stable at $\mathbf{u}^*$ when the perturbation $\boldsymbol{\varepsilon}$ remains smaller than the limit value $\varepsilon_0$ as time t goes to infinity.

$$\lim_{t \to \infty} \mathbf{u}(t) = \lim_{t \to \infty}(\mathbf{u}^* + \boldsymbol{\varepsilon}) = \mathbf{u}^* + \boldsymbol{\varepsilon}; \quad |\boldsymbol{\varepsilon}| < \varepsilon_0$$

- The dynamic behavior is unstable at $\mathbf{u}^*$ when the perturbation $\boldsymbol{\varepsilon}$ increases to $\boldsymbol{\delta}$ that is larger than the limit value $\varepsilon_0$ as time t goes to infinity.

$$\lim_{t \to \infty} \mathbf{u}(t) = \lim_{t \to \infty}(\mathbf{u}^* + \boldsymbol{\varepsilon}) = \mathbf{u}^* + \boldsymbol{\delta}; \quad |\boldsymbol{\delta}| > \varepsilon_0$$

### 4.3.4  Classifications of Hopf Bifurcation

There are three kinds of Hopf bifurcation, as shown in Fig. 4.12.

**a) Transcritical bifurcation**
The loss of stability on the trivial branch occurs when the bifurcation parameter $\Omega$ arrives at the critical value $\mu_0$ at the bifurcation point.

**b) Supercritical pitchfork bifurcation**
Two stable nontrivial half-branches encircle the unstable trivial branch beginning from the bifurcation point. The supercritical bifurcations are called subtle bifurcations because the amplitude of the periodic vibrations is limited in the limit cycle after the soft loss of stability at the bifurcation point $\mu_0$ (s. Fig. 4.10a). As long as the limit cycle remains within the bearing clearance, they are harmless and not dangerous for the bearings.



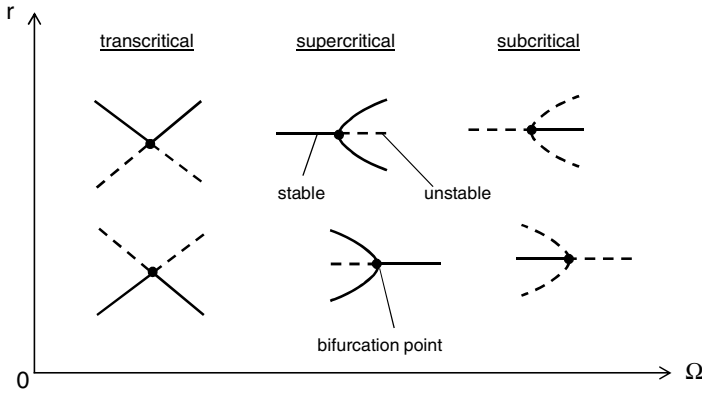**Fig. 4.12** Classification of Hopf bifurcations

**c) Subcritical pitchfork bifurcation**
Two unstable nontrivial half-branches encircle the stable trivial branch beginning from the bifurcation point. The subcritical bifurcations are much more dangerous and harmful than the supercritical bifurcations because the amplitude of the periodic vibrations moves away from the unstable limit cycle outwards (s. Fig. 4.10b).

They are called the hard loss of stability at the bifurcation point $\mu_0$. Such jumps to higher amplitudes could often happen near the bifurcation point where the rotor behavior changes from the equilibrium state to periodic vibrations. In this case, bearing wears and damages could occur when the journal amplitude exceeds the bearing clearance.

The bifurcations are classified into the transcritical bifurcations when the quantitative characteristics change along the trivial branch, into the supercritical bifurcations when two stable nontrivial branches encircle the unstable trivial branch, and into the subcritical bifurcations when two unstable nontrivial branches encircle the stable trivial branch.

### 4.3.5   Coordinates Transformation in the Bifurcation

Having studied the vibration equations at the given rotor and bearing characteristics, the right-hand side of eq. (4.37) is defined as a vector $\mathbf{f(u,\theta,\Omega)}$.

$$\dot{\mathbf{u}}(t) = \mathbf{A}^*\mathbf{u} + \mathbf{b}^*(\mathbf{u},\theta,\Omega) \equiv \mathbf{f(u,\theta,\Omega)} \tag{4.39}$$

For simplicity, the vector $\mathbf{u}(t)$ is considered in the two dimensions of $x_1(t)$ and $x_2(t)$. The coordinate transformation of $(x_1,x_2)$ in the polar coordinate system $(r, \theta)$ is written down as follows:

$$\begin{cases} x_1(t) = r(t)\cos\theta(t) \\ x_2(t) = r(t)\sin\theta(t) \end{cases} \tag{4.40}$$

Thus,

$$\dot{\mathbf{u}}(t) \equiv \mathbf{f(u,\theta,\Omega)} \rightarrow \begin{cases} \dot{r}(t) = g(r,\theta,\Omega) \\ \dot{\theta}(t) = 1 \rightarrow \theta = t \end{cases} \tag{4.41}$$

The bifurcation in the polar coordinate system of eq. (4.39) is displayed in the bifurcation plane, as shown in Fig. 4.13. The coordinates $(x_1,x_2)$ are transformed to the polar coordinates $(r, \theta)$ where r is the radius and $\theta$ is the angular position of the rotor locus. The supercritical pitchfork bifurcation is demonstrated in the following example.

Having varied the bifurcation parameter of the rotor speed $\Omega$, Hopf bifurcation takes place when this parameter arrives at the critical value $\Omega_0$. From the bifurcation point, the rotor vibration is transferred from the steady-state equilibrium to the periodic vibrations, as shown in Fig. 4.14. At the given rotor speed of $\Omega_k$ after the bifurcation point, the periodic vibration is limited in the limit cycle that encircles the unstable focus. The soft loss of stability causes the unstable spiral of the rotor locus moving away from the unstable focus towards the stable limit cycle. The response amplitude r(t) and the rotor orbit of the periodic vibration at the rotor speed $\Omega_k$ are plotted in the phase plane $x_1x_2$, as displayed in Fig. 4.14. The rotor orbit stabilizes in the limit cycle that corresponds to both nontrivial half-branches. Obviously, the radius of the limit cycle changes with the rotor speed.
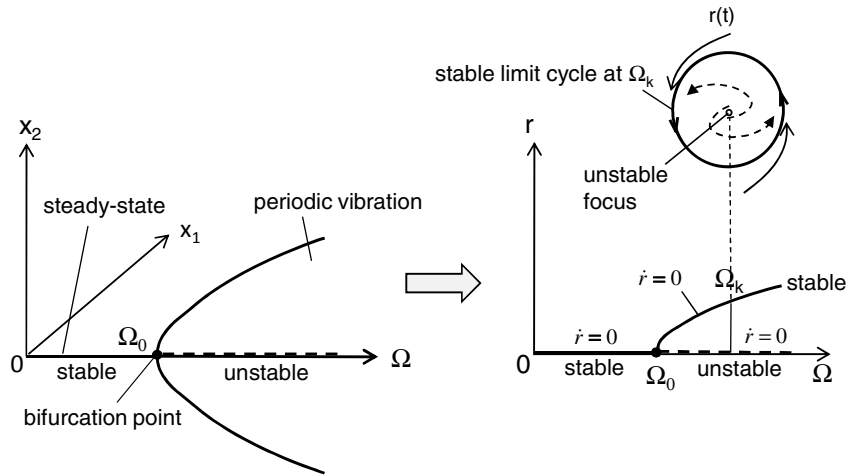
**Fig. 4.13** Coordinate transformation in the bifurcation plane
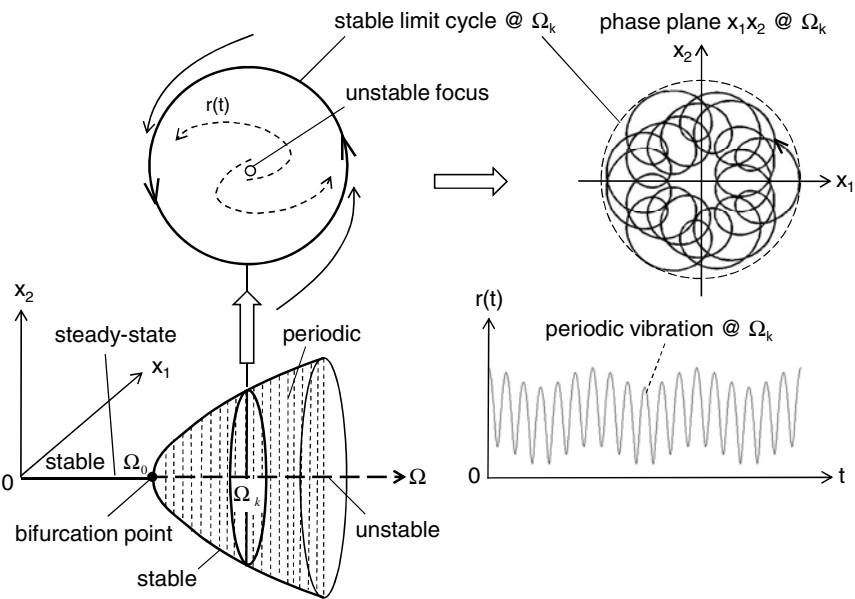


**Fig. 4.14** Limit cycle of the periodic vibration in Hopf bifurcation

### 4.3.6  Jacobian Matrix of the Vibration Equations

In order to find the eigenvalues of the equilibrium points (singular points), the Jacobian matrix is necessary. The Jacobian matrix $\mathbf{J}$ is calculated from the first partial derivatives of the vibration equations (4.39) and written as

$$
\mathbf{J} \equiv
\begin{bmatrix}
\frac{\partial f_1}{\partial x_1} & \frac{\partial f_1}{\partial x_2} & \cdot & \cdot & \frac{\partial f_1}{\partial x_n} \\
\frac{\partial f_2}{\partial x_1} & \frac{\partial f_2}{\partial x_2} & \cdot & \cdot & \frac{\partial f_2}{\partial x_n} \\
\cdot & \cdot & \cdot & \cdot & \cdot \\
\cdot & \cdot & \cdot & \cdot & \cdot \\
\frac{\partial f_n}{\partial x_1} & \frac{\partial f_n}{\partial x_2} & \cdot & \cdot & \frac{\partial f_n}{\partial x_n}
\end{bmatrix}
\tag{4.42}
$$

The singular point-related eigenvalue is resulted by setting the characteristic determinant D of the matrix $(\mathbf{J} - \lambda_i\mathbf{I})$ at the corresponding singular point $x_i^*$ to zero, where $\mathbf{I}$ is the unit matrix. Hence, the determinant D at the singular point is written as follows:

$$
D =
\begin{vmatrix}
(\frac{\partial f_1}{\partial x_1} - \lambda_i) & \frac{\partial f_1}{\partial x_2} & \cdot & \cdot & \frac{\partial f_1}{\partial x_n} \\
\frac{\partial f_2}{\partial x_1} & (\frac{\partial f_2}{\partial x_2} - \lambda_i) & \cdot & \cdot & \frac{\partial f_2}{\partial x_n} \\
\cdot & \cdot & \cdot & \cdot & \cdot \\
\cdot & \cdot & \cdot & \cdot & \cdot \\
\frac{\partial f_n}{\partial x_1} & \frac{\partial f_n}{\partial x_2} & \cdot & \cdot & (\frac{\partial f_n}{\partial x_n} - \lambda_i)
\end{vmatrix}_{x = x_i^*}
= 0 \tag{4.43}
$$

Eq. (4.43) is in fact the characteristic equation of the vibration system. If the real part of the complex eigenvalue $\lambda_i$ is negative, the solutions of the rotor response are stable. Hence, the trivial branch and nontrivial half-branches are stable in the supercritical bifurcations. Otherwise, the rotor responses are unstable with positive real parts of $\lambda_i$ at the trivial branch and nontrivial half-branches in the subcritical bifurcations, as displayed in Fig. 4.12.

### 4.3.7  A Study Case of the Subcritical Hopf Bifurcation

Having considered a rotor with two DOF of $x_1$ and $x_2$, the vibration equations are written in

$$
\begin{cases}
\dot{x}_1 = -x_2 + x_1\left[\mu + (x_1^2 + x_2^2)\right] \\
\dot{x}_2 = +x_1 + x_2\left[\mu + (x_1^2 + x_2^2)\right]
\end{cases}
\tag{4.44}
$$

By using the polar coordinate transformation in eq. (4.40), one obtains the vibration equations in the polar coordinate system $(r, \theta)$ after a few calculating steps.

$$
\begin{cases}
\dot{r} \equiv f(r) = r(\mu + r^2) \\
\dot{\theta} = 1 \rightarrow \theta = t
\end{cases}
\tag{4.45}
$$

where $\mu$ is the bifurcation parameter; r(t) the radius; $\theta$(t) the polar angle.

## a) Finding the equilibrium points

By setting the first part of eq. (4.45) equal zero, three equilibrium points are given.

$$\begin{cases} r_1^* = 0 & for\ \forall\mu \\ r_{2,3}^* = \pm\sqrt{-\mu} & for\ \forall\mu < 0 \end{cases} \tag{4.46}$$

## b) Finding the corresponding eigenvalues

The eigenvalues are resulted from setting determinant D equals zero, at the equilibrium points in eq. (4.43).
Thus,

$$D = \det(\mathbf{J} - \lambda\mathbf{I}) = (3r^2 + \mu - \lambda_i)_{r_i^*} = 0 \tag{4.47}$$

Thus, the eigenvalues are found.

$$\begin{cases} \lambda_1 = \mu \leq 0 \ \ or\ > 0\ \ at\ r_1^* = 0,\ \forall\mu \\ \lambda_{2,3} = -2\mu > 0\ \ at\ r_{2,3}^* = \pm\sqrt{-\mu},\ \forall\mu < 0 \end{cases} \tag{4.48}$$

## c) Bifurcation plane ($\mu$, $x_i$)

The first eigenvalue has only a real part $\mu$ that can be negative or positive depending on the bifurcation parameter $\mu$. In case of $\mu < 0$, one has the stable trivial branch; otherwise, the unstable trivial branch. The second and third eigenvalues have also only a real part of -2$\mu$ that is always positive because the bifurcation parameter $\mu$ must be negative at the singular solutions in eq. (4.46). Hence, the two nontrivial half-branches are unstable in the bifurcation plane, as displayed in Fig. 4.15.

## d) Studying behavior of stability

The speeds of the inner and outer spirals are calculated from eq. (4.45) for various radii r depending on the bifurcation parameter $\mu$.

$$\begin{cases} \dot{r}(t) \leq 0 & for\ \ 0 < r \leq \sqrt{-\mu},\ \forall\mu < 0 \\ \dot{r}(t) > 0 & for\ \ r > \sqrt{-\mu},\ \forall\mu < 0 \end{cases} \tag{4.49}$$

The behavior of the rotor stability in the subcritical Hopf bifurcation is shown in Fig. 4.16. As long as the rotor locus is inside the limit cycle, the rotor behavior is always stable and tends to move to the stable focus due to the negative speed. The stable focus corresponds to the stable trivial branch at $\mu < 0$.

When the rotor locus exceeds the limit cycle, the response behavior becomes unstable; the rotor locus moves from the limit cycle outwards while the response amplitude with the positive speed increases with time. In this case, the limit cycle corresponds to the unstable non-trivial half-branches at $\mu < 0$, as displayed in Fig. 4.15. Such unstable response causing jump in the amplitude from the unstable limit cycle; the jump amplitude exceeds the bearing clearance, leading to damage of the radial bearings.

$$r_2^* = +\sqrt{-\mu}$$

unstable

stable
$$r_1^* = 0$$

0

unstable
$$r_1^* = 0$$

$\mu$

$x_1$

$x_2$

bifurcation point

unstable

$$r_3^* = -\sqrt{-\mu}$$
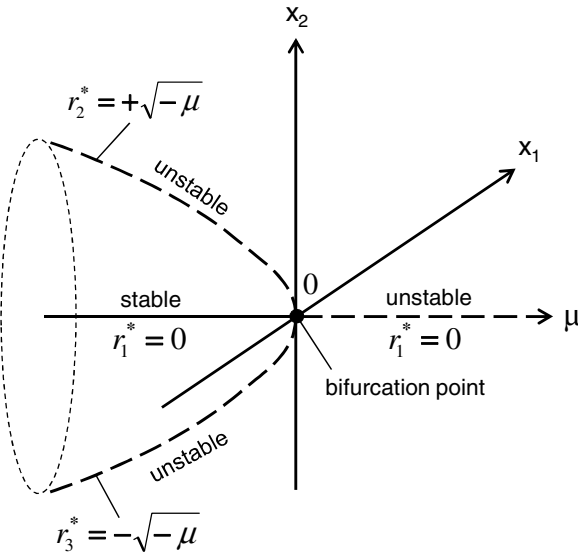
**Fig. 4.15** Subcritical pitchfork Hopf bifurcation

$x_2$

*unstable limit cycle*

$\dot{r} > 0$

$\sqrt{-\mu}$

stable spiral

$\dot{r} < 0$

$\sqrt{-\mu}$

$x_1$

stable focus

unstable spiral
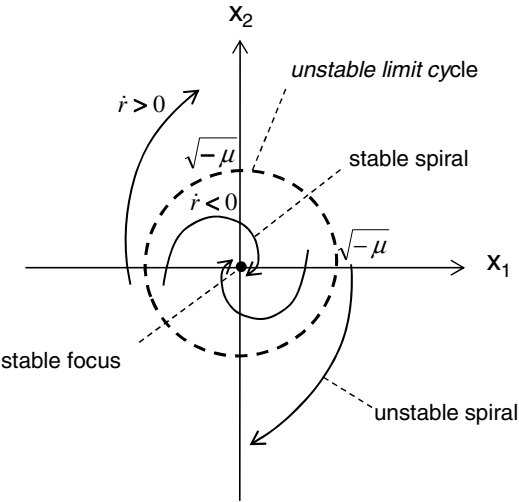
**Fig. 4.16** Behavior of the rotor locus at $\mu < 0$

## 4.3.8   Stability with Neimark-Sacker Torus Bifurcations

### a) Classification of Neimark-Sacker bifurcations

Hopf bifurcation occurs when the dynamic behavior changes from the equilibrium state to periodic vibrations and loses its stability at the first bifurcation point $\Omega_{0,1}$. On the contrary, to the Hopf bifurcation, the periodic vibrations at the Neimark-Sacker bifurcation lose their stabilities to the torus at the second bifurcation point $\Omega_{0,2}$. Therefore, it is a kind of the secondary Hopf bifurcation or generalized Hopf bifurcation [7]. The torus can be attractive or repelling with the periodic vibrations. In case of attractive torus (stable torus), the trajectories move towards the torus; in case of repelling torus (unstable torus), the trajectories move away from it. The first one is called supercritical torus bifurcation; the latter, the subcritical torus bifurcation. The periodic or quasi-periodic vibration amplitudes are limited on the limit torus surface in the Neimark-Sacker bifurcation that is called torus bifurcations; their quasi-periodic vibrations often occur at the beginning of the chaotic vibrations.

Figures 4.17 and 4.19 display the super- and subcritical Neimark-Sacker bifurcations. In the supercritical torus bifurcation, the trajectories with periodic with frequency $\omega_2$ or quasi-periodic vibrations move on the limit surface of the attractive torus. The resulting vibrations of the Neimark-Sacker bifurcation with two incommensurate frequencies of $\omega_1$ and $\omega_2$ are quasi-periodic and on the verge of becoming chaos (s. Fig. 4.17).

Having taken a close look at the supercritical torus bifurcation in the Poincaré map, the vibration response consists of two frequencies $\omega_1$ and $\omega_2$ in the longitudinal and latitudinal directions, respectively [7]. Depending on the frequency ratio, the vibration is quasi-periodic if the ratio is irrational (i.e. incommensurate $\omega_1$ and $\omega_2$). The orbit of the quasi-periodic vibration response that wraps on the torus surface intersects the Poincaré map at the point P that is in the invariant curve C. Because of quasi-periodicity, the orbit never cuts the Poincaré section at the same point P after repeat of period T at time $t = T, 2T, ..., nT$, instead at different points P', P'',…, $P^n$ in the invariant curve C. Therefore, the Poincaré map is usually applied to study the periodic vibrations, especially of non-autonomous systems. The quantitative change of stability in the Neimark-Sacker bifurcation can be investigated in the Poincaré map [7], as shown in Fig. 4.18.

Contrary to the supercritical torus bifurcation, the trajectories of the subcritical torus bifurcation are repelled from the repelling inner torus, as shown in Fig. 4.19. Just before the second bifurcation point $\Omega_{0,2}$, the jump-up of the periodic vibrations with the frequency $\omega_2$ takes place from the inner (repelling) to outer (attractive) torus directly; shortly after the turning point $\Omega_T$ between the inner and outer tori, the response amplitude jumps from the turning point to the center of the inner torus. Between the second bifurcation and turning point, the outer trajectories are repelled from the inner torus surface to the outer torus surface; the inner trajectories, from the inner torus surface to the nontrivial half-branches of the Hopf bifurcation.

Supercritical torus bifurcation
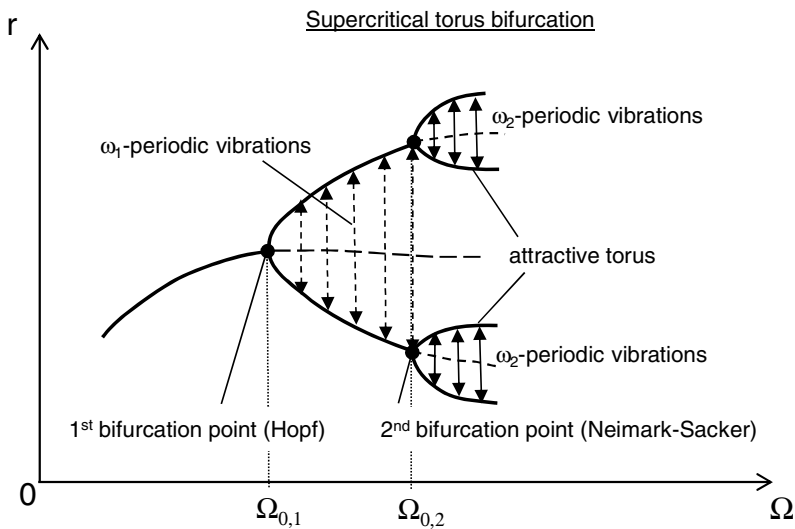


**Fig. 4.17** Supercritical Neimark-Sacker bifurcation
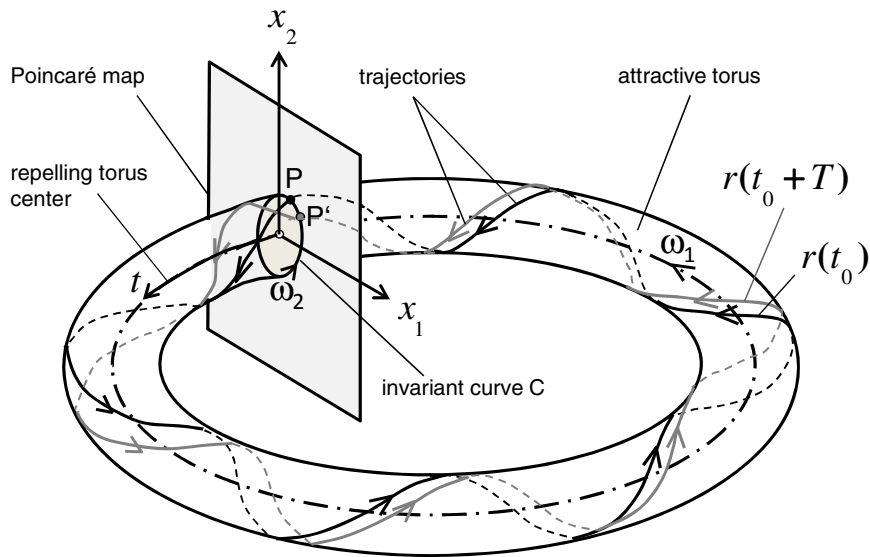


**Fig. 4.18** Supercritical Neimark-Sacker bifurcation in the attractive torus

Subcritical torus bifurcation
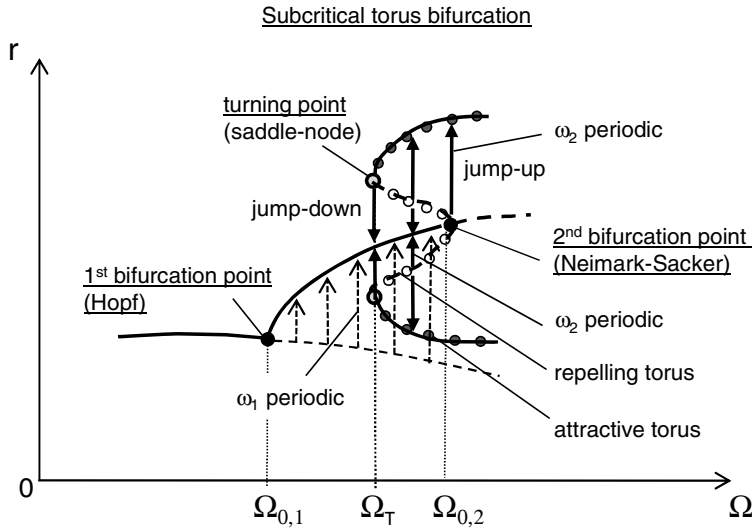


**Fig. 4.19** Subcritical Neimark-Sacker bifurcation

These vibrations in the tori that are superimposed by the periodic vibrations with the frequency $\omega_1$ of the Hopf bifurcation and the periodic vibrations with the frequency $\omega_2$ of the Neimark-Sacker bifurcation could contain other periodic or quasi-periodic vibrations with the rational and irrational frequencies, respectively. In case of the irrational frequency ratio; i.e., both $\omega_1$ and $\omega_2$ are incommensurate, the vibrations could change from the periodic vibration of the Hopf bifurcation to the quasi-periodic and eventually chaotic vibration in the Neimark-Sacker bifurcation. Such sudden jumps of the journal in the radial bearings at large response amplitudes are dangerous and harmful for the radial bearings and destructively damage them.

## b) Stability in Neimark-Sacker bifurcations
In the following section, the stability of a two-DOF problem in the Neimark-Sacker bifurcation is studied in the $\lambda$ plane [10]. Having developed the Taylor series at the vicinity of the equilibrium point x*, one obtains the vibration solutions in the first order at the time iteration step i+1.

$$\begin{cases} x_{1,i+1} = x_1^* + \varepsilon_{1,i+1} \\ x_{2,i+1} = x_2^* + \varepsilon_{2,i+1} \end{cases} \tag{4.50}$$

where $\varepsilon_1, \varepsilon_2$ are the disturbances of $x_1$ and $x_2$, respectively.

At small disturbances, they can be written in terms ε of the earlier time step i.

$$\begin{cases} \varepsilon_{1,i+1} \approx a\varepsilon_{1,i} + b\varepsilon_{2,i} \\ \varepsilon_{2,i+1} \approx c\varepsilon_{1,i} + d\varepsilon_{2,i} \end{cases} \tag{4.51}$$

where a, b, c, and d are the coefficients.

According to [10], the disturbances in eq. (4.51) can be transformed to the new coordinates of $u_1$ and $u_2$.

$$\begin{cases} u_{1,i+1} = \alpha u_{1,i} - \beta u_{2,i} \\ u_{2,i+1} \approx \alpha u_{1,i} + \beta u_{2,i} \end{cases} \tag{4.52}$$

where α and β are the real and imaginary parts of the eigenvalues λ, respectively.

Equation (4.52) is further transformed to the polar coordinate system (r, θ) with using the relation of α and β with the complex eigenvalues of $\lambda_1$ and $\lambda_2$.

$$\begin{cases} u_{1,i} = r_i \cos\theta_i \\ u_{2,i} = r_i \sin\theta_i \end{cases} \tag{4.53}$$

and

$$\begin{cases} \lambda_1 = \alpha + j\beta = \rho e^{j\phi} = \rho\cos\phi + j\rho\sin\phi \\ \lambda_2 = \alpha - j\beta = \rho e^{-j\phi} = \rho\cos\phi - j\rho\sin\phi \end{cases} \tag{4.54}$$

Thus,

$$\begin{cases} \alpha = \rho\cos\phi \\ \beta = \rho\sin\phi \end{cases} \tag{4.55}$$

Substituting of eqs (4.53), (4.52), and (4.55), the vibration solutions at time step i+1 are written in

$$\begin{cases} r_{i+1} \cos\theta_{i+1} = \rho r_i \cos(\theta_i + \phi) \\ r_{i+1} \sin\theta_{i+1} = \rho r_i \sin(\theta_i + \phi) \end{cases} \tag{4.56}$$

Therefore,

$$\begin{cases} r_{i+1} = \rho r_i \\ \theta_{i+1} = \theta_i + \phi \end{cases} \quad for \quad \forall i = 0, 1, 2,..., n. \tag{4.57}$$

- Setting i = 0 into eq. (4.57), it gives:

$$\begin{cases} r_1 = \rho r_0 \\ \theta_1 = \theta_0 + \phi \end{cases}$$

- Analogously, i = 1:

$$\begin{cases} r_2 = \rho r_1 = \rho^2 r_0 \\ \theta_2 = \theta_0 + 2\phi \end{cases}$$

- Analogously, further i = $n > 0$:

$$\begin{cases} r_n = \rho^n r_o \\ \theta_n = \theta_0 + n\phi \end{cases} \tag{4.58}$$

The solution r(t) in eq. (4.58) is stable if the radius $\rho < 1$ for increasing n. Hence, the stability condition is written as

$$\lim_{\substack{n \to \infty \\ \rho < 1}} r_n = \rho^n r_0 = 0 \tag{4.59}$$

where the eigenvalues are

$$\lambda_{1,2} = \alpha \pm j\beta = \rho e^{\pm j\phi}.$$

The stability behavior is shown in Fig. 4.20 where the dynamic behavior is stable within the unit circle; unstable, at outside the unit circle, according to eq. (4.59).
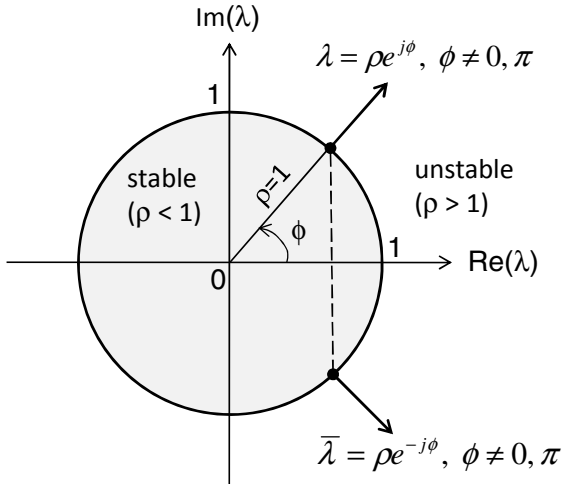


**Fig. 4.20** Stability of the Neimark-Sacker bifurcation

### 4.3.9  *Vibration Equations of the Non-autonomous Systems*

The vibration system is called non-autonomous when its solutions depend on time t explicitly. Hence, the vibration equations (4.36) with the bifurcation parameter $\Omega$ become

$$\dot{\mathbf{z}} = \mathbf{A}\mathbf{z} + \mathbf{b}(\mathbf{z}, t, \Omega) \tag{4.60}$$

The non-autonomous first-order ODE with two DOF of $x_1$ and $x_2$ in eq. (4.60) can be converted into the autonomous first-order ODE of $x_1$ and $x_2$ and one ODE of time t.

$$\begin{cases} \dot{x}_1 = f_1(x_1, x_2, \Omega) \\ \dot{x}_2 = f_2(x_1, x_2, \Omega) \\ \dot{t} = 1 \end{cases} \tag{4.61}$$

Suppose that $x_1(t)$ and $x_2(t)$ are converged, the initial solutions of the equations are $x_{1,0}$ and $x_{2,0}$ at $t_0 = 0$ at the starting point $P_0$ in the phase plane $x_1x_2$.

The Poincaré mapping M is applied to the transformation from $P_0$ to $P_1$, $P_1 - P_2$, and successively to $P_k$. Finally, one can write the relation of $P_k$ at time $t_k$ in $P_0$ by successively iterating the mapping function M in k times [10].

$$P_k = M^k P_0$$
$$at \ \ t_k = kT; k = 0, 1, 2, ..., m \tag{4.62}$$

where $T$ is the period.

The vibration responses $x_1(t)$ and $x_2(t)$ consist of many periodic frequency components due to nonlinearity. The result from superimposing sub- and super-synchronous vibrations on the excitation harmonics; hence, the vibration responses are periodic or quasi-periodic vibrations. In case of subsynchronous frequency components of a frequency order $(1/N)X$, one has N cutting points in the Poincaré map in every convolution in which the whirl orbit completes a cycle in the time interval of N times T. Because of the quasi-periodicity, the Poincaré points are never the same points after repeat of period T at time t = 0, T, 2T, ..., mT [10] as shown in Fig. 4.21. Therefore, the transient vibrations will appear rather in scattered dots in the Poincaré map, as shown in Figure 4.22.

For a vibration equation system of two DOF ($x_1$ and $x_2$), the transient solutions are quasi-periodic vibrations containing the unbalance harmonic frequency of 1X and subsynchronous frequency component with the frequency order of nearly $(1/2)X$ (oil whirl with 0.47X). They intersect the Poincaré map at two points $P_{k,1}$ and $P_{k,2}$ (called Poincaré point) at time $t_k = kT$ with k = 0,1,...,m after repeat of k times period T. Their transient response orbits at the various times $t_k$ are demonstrated in Figure 4.22.
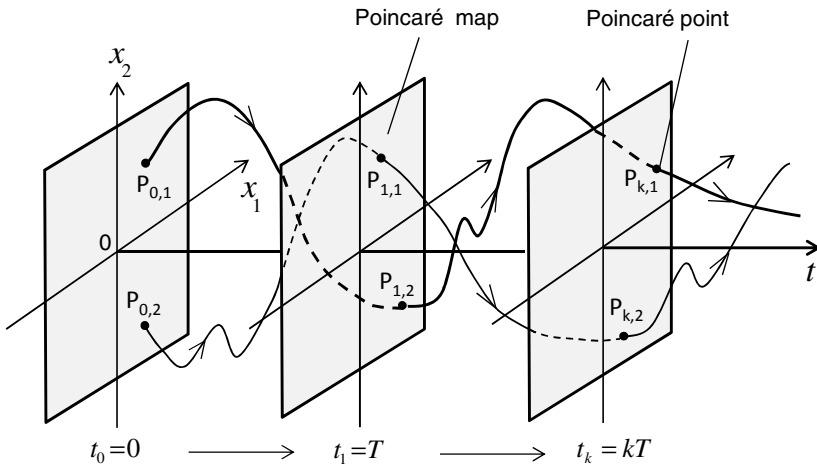
**Fig. 4.21** Poincaré points in the Poincaré map at various times
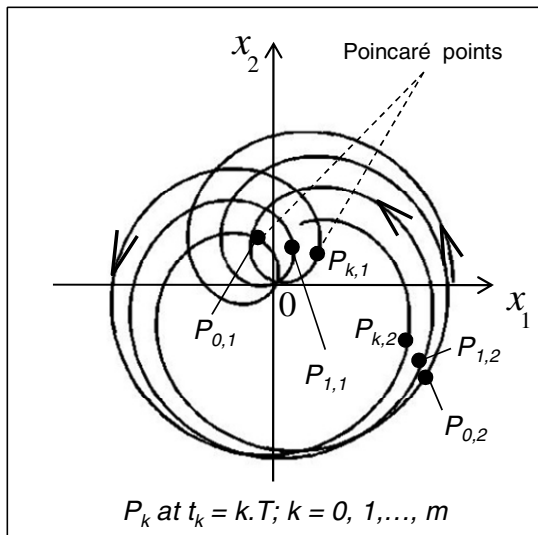


**Fig. 4.22** Response orbits at various times in the Poincaré map

# References

1. Bently, D.E., Hatch, C.: Fundamentals of Rotating Machinery Diagnostics. Bently Pressurized Bearing Press (2002)
2. Ehrich, F.: Handbook of Rotordynamics. Krieger Publishing Company (2004)
3. Kraemer, E.: Rotordynamics of Rotors and Foundations. Springer, Heidelberg (1993)

4.  Govaerts, W., et al.: MATCONT: Program of Bifurcation Analysis of Dynamical Systems (2006)
5.  Newland, D.E.: Mechanical Vibration Analysis and Computation. Dover Publications Inc. (2006)
6.  Randall, R.B.: Vibration-based Condition Monitoring: Industrial, Aerospace and Automotive Applications. John Wiley and Sons (2011)
7.  Seydel, R.: Practical Bifurcation and Stability Analysis, 3rd edn. Springer, Heidelberg (2010)
8.  Schmidt, G., Tondl, A.: Nonlinear Vibrations. Cambridge University Press (2009)
9.  Strogatz, S.H.: Nonlinear Dynamics and Chaos. Westview (1994)
10. Thompson, J.M.T., Stewart, H.B.: Nonlinear Dynamics and Chaos. J. Wiley and Sons Inc. (1986)

# Chapter 5
# Linear Rotordynamics of Turbochargers

## 5.1 Introduction

We have thoroughly discussed the rotordynamic stability in Chapter 4. In this chapter, it deals with the resonance that is a harmful effect causing damages to the turbochargers. When the rotor angular frequency equals its eigenfrequency (undamped natural frequency), the resonance occurs at the critical speed at which the rotor arrives at the maximum deflection amplitude.

The unbalance force $F_{Un}$ acting upon the rotor, which is proportional to the rotor speed squared, induces the rotor deflection r. That means, the higher the rotor speed, the larger the unbalance force acts on the rotor. During the operation of turbochargers, the unbalance force deflects the rotor outwards in the lateral direction, against the stiffness force of the rotor shaft and the damping force. The larger the rotor amplitude, the higher the stiffness force acts on the rotor, and the larger the restoring potential energy generated in the vibration rotor. Additionally, the damping force is proportional to the deflection velocity of the shaft. In other words, the rotor is kept in balance from the inertia, stiffness, damping, and unbalance forces of the rotor at any rotor speed according to Newton's second law.

At subcritical rotor speeds ($\Omega \ll \Omega_{cr}$), both the inertia and damping forces are small; hence, only the stiffness force balances the unbalance force. The deflection direction is nearly the same direction of the unbalance force; thus, the rotor deflection further increases during speed-up, leading to increasing the phase angle of the vibration $\phi > 0°$, as displayed in Fig. 5.1.

At the critical speed ($\Omega = \Omega_{cr}$), the direction of the unbalance force is perpendicular to the deflection direction, leading to a phase angle $\phi = 90°$. At the resonance, the stiffness force balances the inertia force that becomes larger; hence, only the damping force keeps the unbalance force in balance. Therefore, the resonance amplitude is proportional to the inversion of the damping ratio $\zeta$, as shown in eq. (5.17) at $\eta = 1$. Note that the larger the damping ratio, the smaller the resonance amplitude.

At supercritical speeds ($\Omega > \Omega_{cr}$), the vibration phase angle $\phi$ is larger than 90° due to the self-centering of the rotor where the deflection direction is nearly opposite to the unbalance force of the rotor. As a result, the rotor amplitude continuously reduces to the unbalance radius as the rotor speed passes the critical speed. At the very high rotor speeds (hypercritical speeds, $\Omega \gg \Omega_{cr}$), the stiffness and

damping forces become smaller; therefore, only the inertia force balances the un-
balance force.  The rotor mass center tends to approach the bearing center at the
vibration phase angle of $\phi \approx 180°$, as shown in Figs 5.1 and 5.5.

From the point of view of energy consideration, the resonance amplitude of the
rotor is determined by the energy balance between the total kinetic energy of the
rotor (translation and rotation), the total potential energy of the rotor stiffness
(translation and rotation), and the dissipated damping energy of the bearings act-
ing upon the rotor. The rotor damping energy dissipates the kinetic energy of the
rotor during the deflection. The higher the rotor speed, the larger the dissipation
energy induced in the rotor. Increasing the rotor speed increases the potential and
dissipation energies in order to balance the kinetic energy of the rotor. When the
rotor arrives at the equilibrium of the energy balance, the resonance takes place at
the maximum rotor deflection.

Obviously, the larger the damping force, the smaller the resonance amplitude
becomes. In case of small damping ratios, the rotor deflection increases extremely
large at the resonance, so that the normal stress of the shaft exceeds the ultimate
tensile stress, leading to fracture of the rotor. Therefore, the rotor could be dam-
aged at the critical frequency due to contact between the journal and bearings or
rotor fracture.
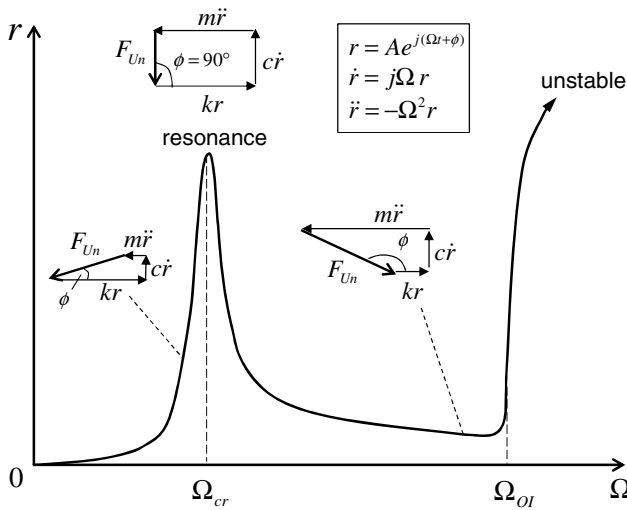


**Fig. 5.1** Rotor response behavior versus rotor speed

After traversing the resonance at the critical speed $\Omega_{cr}$, the rotor speed increases
at speed-up of the turbocharger and reaches the onset of instability $\Omega_{OI}$ at which
the rotor behavior becomes unstable; therefore, the amplitude sharply increases
with time and becomes very large because of oil whip, a self-excitation instability
in nonlinear rotordynamics. Due to the subsynchronous self-excited vibration
of the oil whip, the speed at the onset of instability is much higher than the first

critical speed. Therefore, at designing the rotordynamic system of the turbocharg-
ers, the critical speed should be as high as possible, so that the rotor speed at the
onset of instability occurs outside the working speed range of the turbochargers. It
would be very comfortable and ideal if the working speed range lay between the
first resonance and the onset of instability. In fact, automotive turbochargers work
on a wide speed range in the resonance region that varies from small to very large
rotor speeds. In order to avoid damages of the turbochargers, a large damping ratio
in the bearings is required to reduce the rotor deflection at the resonance in case of
linear rotordynamics; and to keep the limit cycle as small as possible in case of
nonlinear rotordynamics. However, the large bearing damping forces could induce
more friction in the bearings, leading to a low efficiency of the turbochargers, es-
pecially in low-end torque. Hence, the bearing damping force should be as large as
required, but not larger than necessary to compromise among the resonance ampli-
tude, bearing friction, and reducing noises.

## 5.2  Vibration Response of the Linear Rotordynamic System

Vibration response of the linear rotordynamic system is resulted by the excitation
force of the rotor unbalance. The rotor response results in the product of the sys-
tem transfer impedance and unbalance excitation force, as shown in Fig. 5.2. The
transfer impedance Z of the linear system is defined as the inversion of the com-
plex dynamic stiffness coefficient $K_S$ that contains the stiffness and damping coef-
ficients of the rotor, rotor mass, and rotor speed as well ([2], [5]).

Excitation                    Linear system                    Response

$$F_U = m\varepsilon\Omega^2 e^{j\Omega t} \implies Z(\Omega) \equiv \frac{1}{K_S(\Omega)} \implies r(t) = Z(\Omega).F_U(t)$$
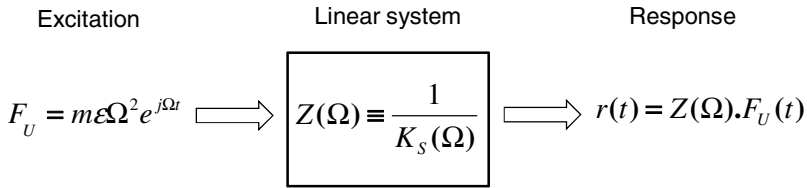
**Fig. 5.2** Vibration response of a linear rotordynamic system

In the linear rotordynamic system, the rotor unbalance response vector is the
sum of the responses of N degrees of freedom (DOF).

$$\mathbf{r}(t) = \sum_{i=1}^{N=DOF}\mathbf{r_i}(t) = \sum_{i=1}^{N=DOF}\mathbf{Z}_i(\Omega)F_{U,i}(t) \equiv \sum_{i=1}^{N=DOF}\mathbf{K}_{S,i}^{-1}(\Omega)F_{U,i}(t) \qquad (5.1)$$

The linear rotordynamic system is only valid in small response amplitudes with
low rotor unbalances. Otherwise, at large amplitudes in case of high unbalances,
the rotor response becomes nonlinear because the stiffness and damping forces of
the radial bearings have not been linear any longer.

According to Eq. (5.1), the vibration response is resulted from the complex dynamic stiffness and excitation unbalance force of the rotor. For the sake of simplicity, the Jeffcott rotor with the isotropic bearings is used to calculate the rotor response in linear rotordynamics, as displayed in Fig. 5.3.
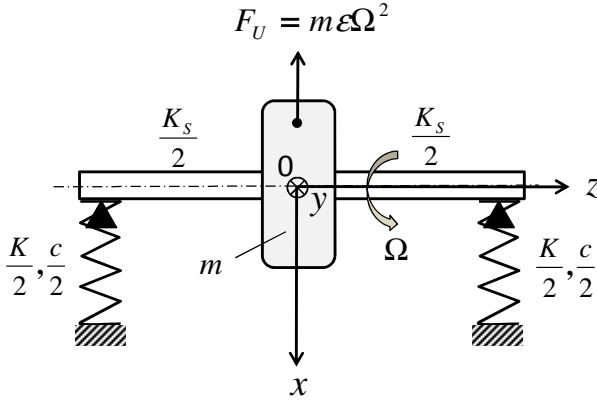


**Fig. 5.3** Jeffcott rotor with isotropic bearings

In case of isotropic bearings (i.e. $k_1 = k_2 \equiv k$; $c_1 = c_2 \equiv c$), the vibration equations of the rotor are written in

$$\begin{cases} m\ddot{x} + c\dot{x} + kx = m\varepsilon\Omega^2 \cos\Omega t \\ m\ddot{y} + c\dot{y} + ky = m\varepsilon\Omega^2 \sin\Omega t \end{cases} \tag{5.2}$$

where

k is the equivalent stiffness coefficient of the rotor resulted from K and $K_S$, as given in Eq. (4.5);
c is the damping coefficient of the rotor.

Note that both degrees of freedom x and y (DOF = 2) could be combined in one degree of freedom r (DOF = 1) only if the isotropic bearings have the same bearing characteristics in the directions x and y, e.g. the bearing stiffness and damping coefficients have the same values in both directions.

Having used the complex coordinate (r, $\phi$) with

$$\begin{cases} \mathbf{r} = x + jy \\ \phi = \arctan\left(\dfrac{y}{x}\right) \end{cases} \tag{5.3}$$

Eq. (5.2) is written in the complex coordinate

$$m\ddot{\mathbf{r}} + c\dot{\mathbf{r}} + k\mathbf{r} = m\varepsilon\Omega^2 e^{j\Omega t} \tag{5.4}$$

The rotor response $\mathbf{r}(t)$ of the linear ordinary differential Equation (5.4) consists of the free and forced vibration responses that are the homogeneous and particular solutions of Eq. (5.4), respectively.

$$\mathbf{r}(t) = \mathbf{r_h}(t) + \mathbf{r_u}(t) \tag{5.5}$$

where

$\mathbf{r_h}(t)$ is the free vibration response (homogeneous solution),

$\mathbf{r_u}(t)$ is the forced vibration response (unbalance response or particular solution).

The generalized free vibration response of the homogeneous equation (5.4) is expressed in

$$\mathbf{r_h}(t) = \sum_{i=1}^{N=DOF} \boldsymbol{\varphi}_i \left( r_i e^{\lambda_i t} \right)$$
$$= \sum_{i=1}^{N=DOF} \boldsymbol{\varphi}_i \left( r_{i,fw} e^{(\alpha_i + j\omega_i)t} + r_{i,bw} e^{(\alpha_i - j\omega_i)t} \right) \tag{5.6}$$

within the (N x N) modal matrix $\boldsymbol{\Phi}$ of the (N x 1) eigenvectors $\boldsymbol{\varphi}_i$

$$\boldsymbol{\Phi} = \left( \boldsymbol{\varphi}_1 \quad \boldsymbol{\varphi}_2 \quad ... \quad \boldsymbol{\varphi}_N \right)$$

where

N is the degrees of freedom (DOF) of the rotor;
$\lambda_i$ is the eigenvalue corresponding to the eigenfrequency $\omega_i$;
$\boldsymbol{\varphi}_i$ is the eigenvector corresponding to the eigenvalue $\lambda_i$;
$r_i$ is the vibration amplitude of the DOF i, and forward (fw); backward (bw).

The generalized unbalance vibration response of Eq. (5.4) is written as

$$\mathbf{r_u}(t) = \sum_{i=1}^{N=DOF} \boldsymbol{\varphi}_i p_i e^{j\Omega t} \tag{5.7}$$

where

N is the degrees of freedom (DOF) of the rotor;
$\boldsymbol{\varphi}_i$ is the eigenvector corresponding to the eigenvalue $\lambda_i$;
$p_i$ is the vibration amplitude of the DOF i; forward (fw) and backward (bw);
$\Omega$ is the rotor speed.

For a stable rotor response, the free vibration response $\mathbf{r_h}(t)$ diminishes in a short time (called short-term response), as discussed in Section 4.2. Notice that the free vibration response (homogeneous solution) is responsible for the rotor stability; the forced vibration response (unbalance response or particular solution), for the rotor resonance.

Therefore, the rotor response $\mathbf{r}(t)$ approaches the unbalance response $\mathbf{r_u}(t)$ of the (N x 1) vector in the long-term response.

$$\mathbf{r}(t) \rightarrow \mathbf{r_u}(t) = \mathbf{\Phi p_u}(t) \tag{5.8}$$

where

the (N x N) modal matrix $\mathbf{\Phi}$ of the (N x 1) eigenvectors $\mathbf{\varphi}_i$

$$\mathbf{\Phi} = \begin{pmatrix} \mathbf{\varphi}_1 & \mathbf{\varphi}_2 & ... & \mathbf{\varphi}_N \end{pmatrix} \tag{5.9}$$

and the (N x 1) modal response vector $\mathbf{p_u}$ with

$$\mathbf{p_u} = \begin{pmatrix} p_1 \\ p_2 \\ ... \\ p_N \end{pmatrix} \cdot e^{j\Omega t} \tag{5.10}$$

Now, we turn back to the simple Jeffcott rotor with the vibration equation (5.4), the unbalance response becomes after a short time

$$r_u(t) = A(\Omega)e^{j\Omega t} \tag{5.11}$$

Inserting $r_u$, its first, and second derivatives in eq. (5.4), one obtains the complex response amplitude

$$A(\Omega) = \frac{m\varepsilon\Omega^2}{(k - m\Omega^2) + jc\Omega} = \left(\frac{m\varepsilon\Omega^2}{(k - m\Omega^2)^2 + (c\Omega)^2}\right)\left[(k - m\Omega^2) - jc\Omega\right] \tag{5.12}$$

within the complex dynamic stiffness coefficient $K_S$ of the rotor as given in

$$K_S(\Omega) = (k - m\Omega^2) + jc\Omega \tag{5.13}$$

The amplitude of the rotor response A is calculated from Eq. (5.12)

$$|A| = \frac{m\varepsilon\Omega^2}{\sqrt{(k - m\Omega^2)^2 + (c\Omega)^2}} \tag{5.14}$$

and the phase angle $\phi$ of the rotor response results in

$$\phi = \arctan\left(\frac{-c\Omega}{k - m\Omega^2}\right) \tag{5.15}$$

Thus,

$$r_u(t) = A(\Omega)e^{j\Omega t} = |A|e^{j\phi}e^{j\Omega t} = |A|e^{j(\Omega t + \phi)} \tag{5.16}$$

Having used Eqs (5.14) and (5.15), the amplitude and phase angle of the rotor response are written in the unbalance radius, speed, and damping ratio.

$$\begin{cases} |A| = \dfrac{\varepsilon \eta^2}{\sqrt{(1-\eta^2)^2 + 4\zeta^2 \eta^2}} \\ \phi = \arctan\left(\dfrac{-2\zeta\eta}{1-\eta^2}\right) \end{cases} \tag{5.17}$$

where

$\varepsilon$ is the unbalance radius,
$\zeta$ is the damping ratio defined in Eq. (4.16),
$\eta$ is the speed ratio of the rotor to critical speed ($\eta \equiv \Omega/\Omega_{cr}$).

The amplitude of the vibration response relative to the unbalance radius versus speed ratio $\eta$ is plotted in Fig. 5.4.

At a given damping ratio $\zeta$, the rotor amplitude reaches the resonance amplitude of $\varepsilon/(2\zeta)$ according to Eq. (5.17) since the denominator reaches the minimum of $2\zeta$ at the speed ratio $\eta=1$. In case of the critically damped vibration at $\zeta = 1$, the rotor critical amplitude equals $\varepsilon/2$, even lower than the unbalance radius $\varepsilon$. The pikes of the resonance amplitudes at various damping ratios are located in the curve $A_{max}$ lying on the right-hand side of the critical speed ratio $\eta = 1$. Obviously, the resonance amplitudes change inversely related to $\zeta$, as shown in Fig. 5.4.
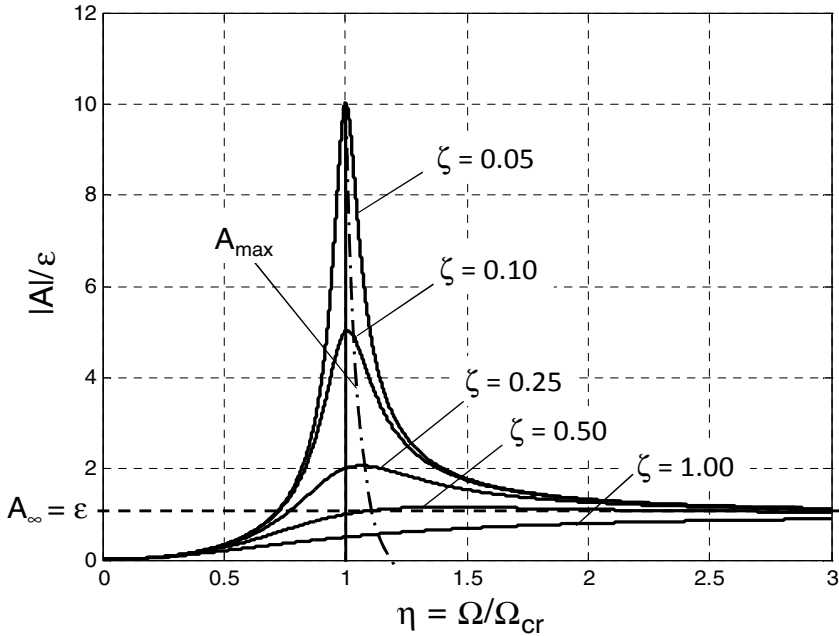


**Fig. 5.4** Relative rotor amplitude $|A|/\varepsilon$ of the vibration response

Applying the L´Hôpital´s rule to Eq. (5.17), the rotor amplitude asymptotically approaches the unbalance radius ε at hypercritical speeds (η >> 1).

$$|A_\infty| = \lim_{\eta \to \infty} \frac{\varepsilon \eta^2}{\sqrt{(1-\eta^2)^2 + 4\zeta^2 \eta^2}} = \lim_{\eta \to \infty} \frac{2\varepsilon \eta}{2\eta} = \varepsilon \qquad (5.18)$$

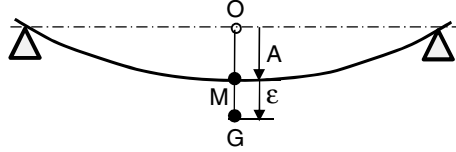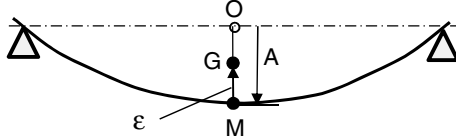η < 1: subcritical

η > 1: supercritical
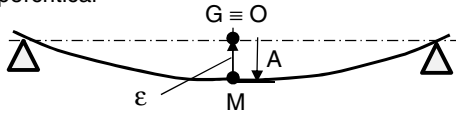
η >> 1: hypercritical

**Fig. 5.5** Self-centering of the rotor at super- and hypercritical speeds
(O: bearing center; M: rotor geometric center; G: rotor mass center;
ε: unbalance radius)

Figure 5.5 shows the self-centering effect of the rotor where the rotor mass center G moves toward the bearing center O at supercritical rotor speeds (η > 1); at hypercritical rotor speeds of about $3\Omega_{cr}$ (η ≈ 3), the rotor mass center nearly approaches the bearing center (G→O) according to Eq. (5.18), as shown in Fig. 5.4.

The phase angle of the vibration response versus the speed ratio is drawn in Fig. 5.6 (a). According to Eq. (5.17), the phase angle begins nearly from zero at subcritical rotor speeds (η << 1), decreases to -90° at the critical speed (η = 1), and changes from -90° to -180° at supercritical speeds (η >> 1).

Similarly, the deflection amplitude of the rotor is displayed in the polar coordinate system (r,φ) in Fig. 5.6 (b). At the small rotor speeds, the deflection direction is in nearly the same direction as the unbalance force locating at the heavy spot (HS), which is identical to the point G shown in Fig. 5.5. This behavior is useful during the balancing of the rotor that shall be discussed later. The deflection direction lags behind the unbalance force direction with a phase lag φ that grows when increasing the rotor speed Ω. The amplitude of the response vector reaches the maximum at the resonance with a phase lag of 90° where the rotor deflects perpendicularly to the

unbalance force at the critical speed $\Omega_{cr}$. For hypercritical speeds, the rotor ampli-
tude decreases and the rotor deflection changes its direction opposite to the unbal-
ance force with a phase lag larger than 90°. At very large hypercritical speeds ($\Omega \to \infty$), the phase lag approaches 180° opposite to the unbalance force, as shown in Fig.
5.6(b), and the rotor amplitude converges to the unbalance radius $\varepsilon$ (s. Fig. 5.4).
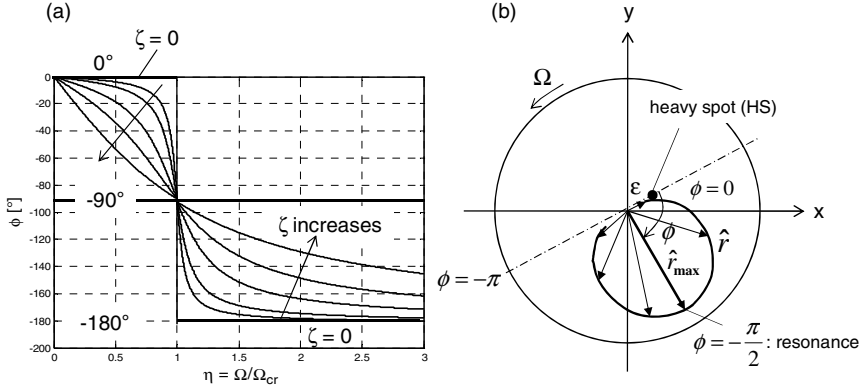


**Fig. 5.6 (a)** Phase angle of the vibration response; (b) Response vector

## 5.3 Bearing Force Acting on the Flexible Rotor

The bearing force $F_B$ acting on the rotor in Fig. 5.7 at the steady-state condition
will be studied. Having considered the shaft with the rotor effective stiffness coef-
ficient k resulted from the shaft and bearings coefficients, as given in Eq. (4.5), the
bearing force is proportional to the rotor deflection.

$$F_B = kr_M \tag{5.19}$$

Using the relation among k, m, and the critical speed $\Omega_{cr}$, one obtains

$$F_B = m\Omega_{cr}^2 r_M \tag{5.20}$$

With further relations of $\eta$ and $r_M$ in eq. (5.17) with

$$\begin{cases} \eta = \dfrac{\Omega}{\Omega_{cr}} \to \Omega_{cr} = \dfrac{\Omega}{\eta} \\[4mm] r_M = \dfrac{\varepsilon\eta^2}{\sqrt{(1-\eta^2)^2 + 4\zeta^2\eta^2}} \end{cases} \tag{5.21}$$

the bearing force acting on the flexible damped rotor becomes

$$F_{B,flex} = \frac{m\varepsilon\Omega^2}{\sqrt{(1-\eta^2)^2 + 4\zeta^2\eta^2}} = m\varepsilon\Omega_{cr}^2\left(\frac{\eta^2}{\sqrt{(1-\eta^2)^2 + 4\zeta^2\eta^2}}\right) \tag{5.22}$$

In the rigid rotor, the bearing force equals the unbalance force because the rotor stiffness coefficient k is very large ($k \to \infty$).

$$F_{B,rigid} = m\varepsilon\,\Omega^2 = m\varepsilon\,\Omega_{cr}^2\eta^2 \tag{5.23}$$
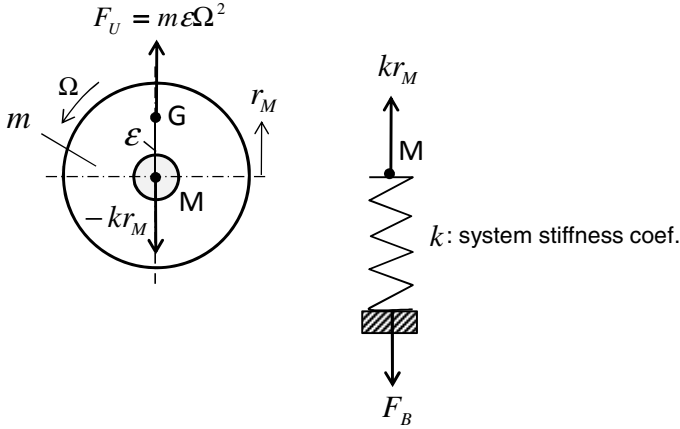


**Fig. 5.7** Bearing force acting on a flexible rotor

The relative bearing force in Eq. (5.22) versus the speed ratio with various damping ratios is plotted in Fig. 5.8. Contrary to the rigid rotor, the bearing force of the flexible rotor reduces after the resonance in supercritical speeds. According to the L'Hôpital's rule, at a very high rotor speed, the bearing force approaches the limit value of

$$F_{B,flex,\infty} = \lim_{\eta \to \infty} m\varepsilon\Omega_{cr}^2 \left( \frac{\eta^2}{\sqrt{(1-\eta^2)^2 + 4\zeta^2\eta^2}} \right) = m\varepsilon\Omega_{cr}^2 \tag{5.24}$$

According to Eq. (5.23), the bearing force of the rigid rotor increases without limit at large hypercritical speeds($\eta \gg 1$), as shown in Fig. 5.8. The bearing forces of both cases are relatively small up to the rotor speed ratio of 0.5 because the deflection of the rotor is quite small in this speed range. After that, the bearing force of the underdamped and flexible rotor increases very fast to the resonance and reaches the critical force depending on the damping ratio $\zeta$ according to eq. (5.22)

$$F_{B,flex,cr} = \frac{m\varepsilon\Omega_{cr}^2}{2\zeta}. \tag{5.25}$$

With a very low damping ratio $\zeta$, the bearing force becomes too large enough to damage the rotor and bearings. At a damping ratio of 5%, the bearing force of the flexible rotor at the critical speed is 10 times higher than the asymptote unbalance force at $\eta \gg 1$, as shown in Fig. 5.8.
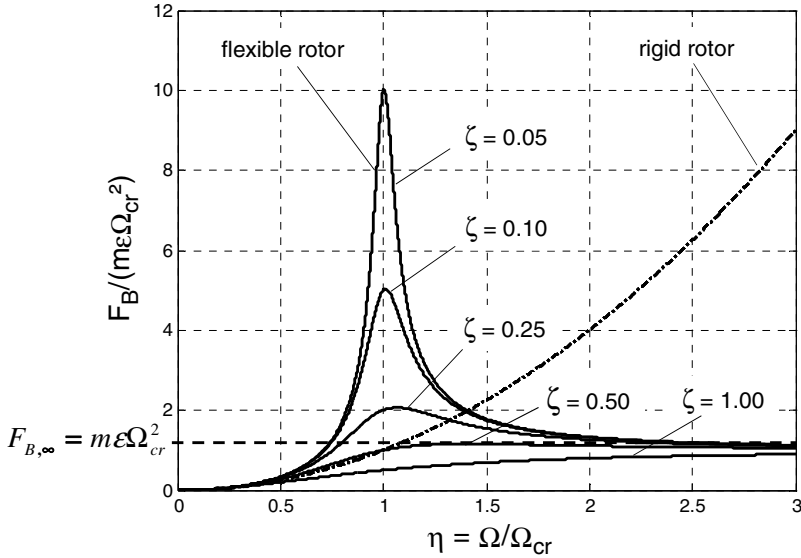


**Fig. 5.8** Bearing forces acting on a rigid and flexible rotor

According to Eq. (5.22), the bearing force depends on two key parameters: the unbalance radius $\varepsilon$ and damping ratio $\zeta$. In fact, the high-speed balancing (called trim balancing) could be carried out at a high balancing speed to about maximum 1.5 times of the first critical speed and not further higher because the turbine wheel is generally driven by the cool air at the balancing, instead of the high temperature of exhaust gas (large enthalpy). Therefore, the residual unbalance remains high at the operational condition in the supercritical speeds. Normally, the maximal speed of the automotive turbochargers is about 2.5 times of the critical speed. Hence, the bearing force in the working condition of the speed ratios $\eta$ between 1.5 and 2.5 is relatively large. In this speed range, more damping in the bearings is required to reduce the bearing force. Generally, the damping ratio should be large enough to prevent bearing defects and to reduce airborne noises. Fortunately, the engine noise is loud enough in the speed ratios between 1.5 and 2.5 to suppress the unbalance whistle.

## 5.4 Gyroscopic Effect of the Rotor System

Gyroscopic effect of the large compressor and turbine wheels becomes more important at high rotor speeds in the rotor. The gyroscopic effect is proportional to

the rotor speed and the polar mass inertia moment of the wheel, which is proportional to the mass and radius squared. In the turbochargers, the compressor and turbine wheel diameters are much larger than the rotor shaft diameter, as shown in Fig. 5.9. Therefore, their gyroscopic effects must be taken into account in the rotordynamic computation of the rotor.
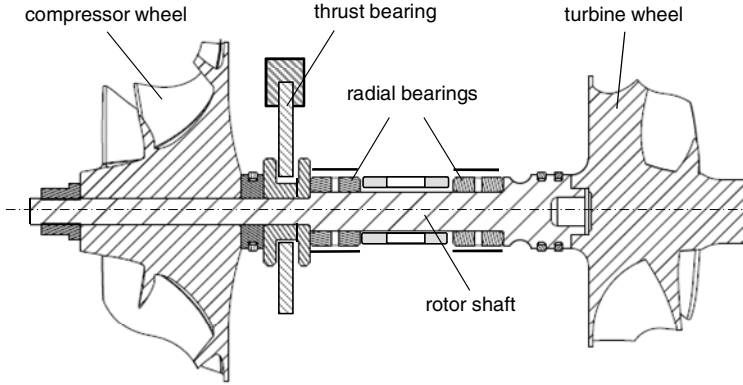


**Fig. 5.9** Rotor of a small automotive turbocharger

The gyroscopic effect of the rotor is based on the angular momentum theorem. It indicates that the timely change of the angular momentum equals all external moments acting upon the rotor.

$$\mathbf{M}_P = \left(\frac{d\mathbf{L}}{dt}\right)_P \tag{5.26}$$

where
$\mathbf{M}_P$ is the external resulting moment vector at a reference point P in the rotor;
$\mathbf{L}_P$ is the angular momentum vector at the point P.

Having used the product rule of differentiation in the transport theorem in analytical dynamics between the stationary and rotating coordinate systems (x,y,z) and (x',y',z'), the timely change of the angular momentum is formulated in the Euler's equation [15].

$$\mathbf{M} = \frac{d\mathbf{L}}{dt} = \left(\frac{\partial\mathbf{L}}{\partial t}\right)_{rot} + (\boldsymbol{\omega} \times \mathbf{L}) \tag{5.27}$$

where $\boldsymbol{\omega}$ is the angular velocity of the rotating coordinate system (x',y',z') due to the gyroscopic effect and results in

$$\boldsymbol{\omega} = \dot{\theta}_x \mathbf{i}' + \dot{\theta}_y \mathbf{j}' \tag{5.28}$$

The angular momentum of the wheel in Fig. 5.10 is calculated in the rotating coordinate system (x',y',z') with the unit vectors **i', j', k'**

$$\mathbf{L} = I_{t,x}\dot{\theta}_x\mathbf{i}' + I_{t,y}\dot{\theta}_y\mathbf{j}' + I_p\Omega\mathbf{k}' \tag{5.29}$$

where

I_{t,x}, I_{t,y} are the transverse mass inertia moments in the directions of x' and y';

$I_p$ is the polar mass inertia moment in the direction z';

$\dot{\theta}_x, \dot{\theta}_y$ are the angular velocities of the wheel in the directions x', y', respectively;

$\Omega$ is the rotor speed ($\Omega$ = const).



$$\boxed{I_{t,x} = I_{t,y} \equiv I_t}$$
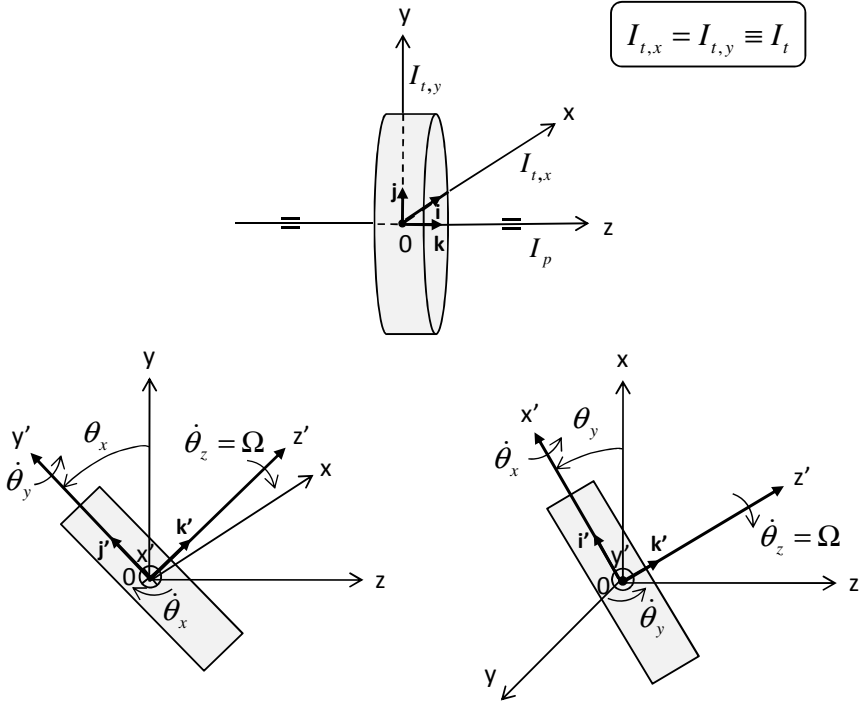
**Fig. 5.10** Gyroscopic effect of the rigid rotor wheel

The timely derivative of the angular momentum in the rotating coordinate system is derived by differentiating Eq. (5.29).

$$\left(\frac{\partial \mathbf{L}}{\partial t}\right)_{rot} = I_{t,x}\ddot{\theta}_x\mathbf{i}' + I_{t,y}\ddot{\theta}_y\mathbf{j}' \tag{5.30}$$

The vector cross product of ($\boldsymbol{\omega}\times\mathbf{L}$) in Eq. (5.27) is calculated.

$$(\boldsymbol{\omega}\times\mathbf{L}) = \left(\dot{\theta}_x\mathbf{i}' + \dot{\theta}_y\mathbf{j}'\right) \times \left(I_{t,x}\dot{\theta}_x\mathbf{i}' + I_{t,y}\dot{\theta}_y\mathbf{j}' + I_p\Omega\mathbf{k}'\right)$$
$$= I_p\dot{\theta}_y\Omega\mathbf{i}' - I_p\dot{\theta}_x\Omega\mathbf{j}' \tag{5.31}$$

The resulting moment **M** on the rotor consists of two parts in the rotating coordinate system: the timely change of the angular momentum given in Eq. (5.30) and the timely change of the unit vectors **i'**, **j'**, and **k'** in Eq. (5.31), and is resulted according to Eq. (5.27) in

$$\mathbf{M} = \left(I_t \ddot{\theta}_x + I_p \Omega \dot{\theta}_y\right)\mathbf{i}' + \left(I_t \ddot{\theta}_y - I_p \Omega \dot{\theta}_x\right)\mathbf{j}' \tag{5.32}$$

The unit vectors **i'** and **j'** of the rotating coordinate system (x',y',z') with the angular velocity **ω** become very small angles $\theta_x$, $\theta_y \ll 1$ (s. Appendix A).

$$\begin{cases} \mathbf{i}' \approx \mathbf{i} - \theta_y \mathbf{k} \approx \mathbf{i} \\ \mathbf{j}' \approx \mathbf{j} + \theta_x \mathbf{k} \approx \mathbf{j} \end{cases}$$

Hence, the resulting moment **M** in the stationary coordinate system (x,y,z) is written in

$$\begin{cases} M_x = I_t \ddot{\theta}_x + I_p \Omega \dot{\theta}_y \rightarrow \sum M_x = I_t \ddot{\theta}_x = M_x - I_p \Omega \dot{\theta}_y \\ M_y = I_t \ddot{\theta}_y - I_p \Omega \dot{\theta}_x \rightarrow \sum M_y = I_t \ddot{\theta}_y = M_y + I_p \Omega \dot{\theta}_x \end{cases} \tag{5.33}$$

The fictitious gyroscopic moment additionally acting upon the rotor is defined in Eq. (5.33) and written in the stationary coordinate system (x,y,z).

$$\begin{aligned} \mathbf{M_G} &= M_{G,x}\mathbf{i} + M_{G,y}\mathbf{j} \\ &= \left(-I_p \Omega \dot{\theta}_y\right)\mathbf{i} + \left(I_p \Omega \dot{\theta}_x\right)\mathbf{j} \end{aligned} \tag{5.34}$$

The gyroscopic moment stiffens the rotor stiffness of the forward whirls and de-stiffens the rotor stiffness of the backward whirls when increasing the rotor speeds. As a result, the forward whirl eigenfrequencies increase with the rotor speed; the backward whirl eigenfrequencies, decrease with the rotor speed, as shown in the Campbell diagram (s. Section 5.7). Hence, the critical speeds of the turbochargers are higher than the critical speeds of the rotor without consideration of the gyroscopic effect.

## 5.5  Vibration Equations of Turbochargers

To create the vibration equations of the turbochargers, two methods are most applied: the momentum theorems and Lagrange's equations.

**a) Momentum approaches**

**Lateral vibrations**
Based on the impulse momentum theorem, the vibration equation is written at the rotor mass center G.

$$\mathbf{F_M} = m\ddot{\mathbf{r}}_\mathbf{G} \tag{5.35}$$

where

$\mathbf{F_M}$ is the external forces acting upon the rotor geometric center M;
$\mathbf{r_G}$ is the vector of the rotor mass center G.

The mass center vector of the rotor is calculated from the vectors of the rotor geometric center and unbalance radius (s. Fig. 5.11).

$$\mathbf{r_G} = \mathbf{r_M} + \mathbf{r_\varepsilon} \tag{5.36}$$

with

$$\mathbf{r_\varepsilon} = \varepsilon\, e^{j(\Omega t + \beta)} \rightarrow \ddot{\mathbf{r}}_\varepsilon = -\varepsilon\,\Omega^2 e^{j(\Omega t + \beta)} \tag{5.37}$$

Setting the external forces acting at the rotor center M containing the stiffness and damping forces in Eq. (5.35), one obtains the vibration equation at the rotor center M.

$$m\ddot{\mathbf{r}}_M + c\dot{\mathbf{r}}_M + k\mathbf{r}_M = m\,\varepsilon\Omega^2 e^{j(\Omega t + \beta)} \tag{5.38}$$

where

$\mathbf{r_M}$ is the vibration response of the rotor;
rhs term is the excitation unbalance force.
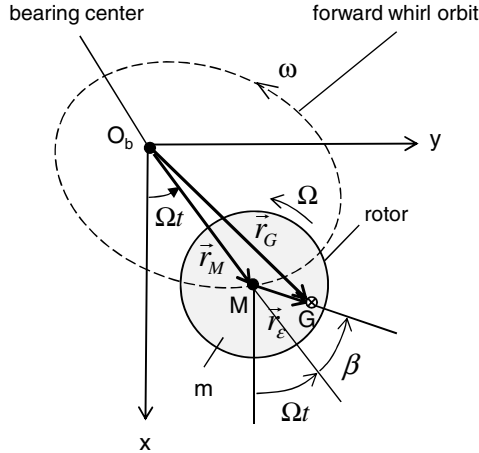


**Fig. 5.11** Response vector $r_M$ of the unbalanced rotor

- **Rotational vibrations**

The rotational vibration equations are derived from the angular momentum theorem at a reference point P in the rotor.

$$\mathbf{M_P} = \left(\frac{d\mathbf{L}}{dt}\right)_P \tag{5.39}$$

where

$\mathbf{M_P}$ are the external torques acting upon the rotor;

$\mathbf{L}$ is the angular momentum defined in Eq. (5.29). Its time derivative is written as

$$\left(\frac{d\mathbf{L}}{dt}\right)_{\mathbf{P}} = \begin{pmatrix} I_t\ddot{\theta}_x + I_p\Omega\dot{\theta}_y \\ I_t\ddot{\theta}_y - I_p\Omega\dot{\theta}_x \end{pmatrix}$$

The external torques $\mathbf{M_P}$ contain the circulant damping, stiffness moments, as well as the unbalance moment in which

- the circulant damping moment is described

$$\mathbf{M_c} = -(c_{r,x}\dot{\theta}_x\mathbf{i} + c_{r,y}\dot{\theta}_y\mathbf{j}) \tag{5.40}$$

- the circulant and interaction stiffness moment results in

$$\mathbf{M}_k = -(k_{r,x}\theta_x + K_{tr}x)\mathbf{i} - (k_{r,y}\theta_y + K_{tr}y)\mathbf{j} \tag{5.41}$$

- the unbalance moment $\mathbf{M_U}$ caused by the misalignment between the wheel and rotation axis due to the couple unbalance is derived in Eq. (5.49).

$$\mathbf{M}_U = \begin{bmatrix} (I_t - I_p)\alpha\Omega^2\cos\Omega t \\ (I_t - I_p)\alpha\Omega^2\sin\Omega t \end{bmatrix} \tag{5.42}$$

where

$I_t$, $I_p$ are the transverse and polar mass inertia moments at the mass center G;
$\alpha$ is the amplitude of the couple unbalance;
$\Omega$ is the rotor speed.
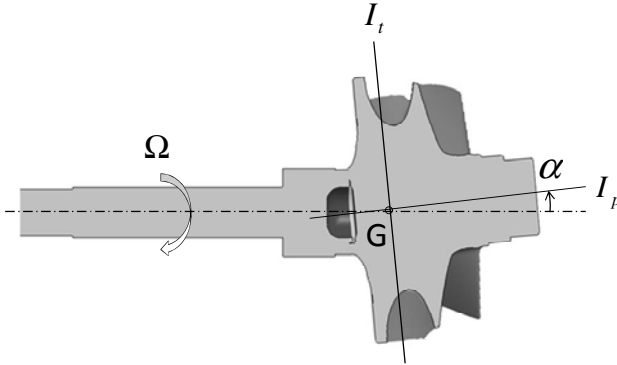


**Fig. 5.12** Couple unbalance with a misalignment angle $\alpha$

## b) Calculating the moment $\mathbf{M_U}$ of the couple unbalance

By production process, the geometric axis of the turbine wheel is misaligned with the rotational axis of the shaft at an angle $\alpha$, as shown in Fig. 5.12, leading to the couple unbalance that induces the unbalance moment acting on the rotor. This un-

balance moment excites the rotor by an excitation moment, similar to the excitation unbalance force. Both excitations cause large response amplitudes of the rotor in the cylindrical and conical modes at the resonance.

Having used the angular momentum theorem and the product rule of differentiation in the transport theorem of analytical dynamics according to the Euler's equation, one derives the unbalance moment $\mathbf{M}_U$ induced by the dynamic unbalance in the timely change of the angular momentum like the gyroscopic moment.

$$\mathbf{M} = \frac{d\mathbf{L}}{dt} + \mathbf{M}_U = \left[ \left( \frac{\partial \mathbf{L}}{\partial t} \right)_{(x',y',z')} + (\boldsymbol{\omega} \times \mathbf{L}) \right] + \mathbf{M}_U = 0$$

$$\mathbf{M}_U = -\left[ \left( \frac{\partial \mathbf{L}}{\partial t} \right)_{(x',y',z')} + (\boldsymbol{\omega} \times \mathbf{L}) \right]$$

(5.43)

where

$$\boldsymbol{\omega} = \Omega \mathbf{i} \qquad\qquad (5.44)$$

$\boldsymbol{\omega}$ is the angular velocity of the rotating coordinate system (x',y',z');
$\mathbf{L}$ is the angular momentum of the rotor.

The angular momentum vector of the turbine wheel is written in the rotating coordinate system (x',y',z'), as shown in Fig. 5.13.

$$\mathbf{L} = \left( I_p \Omega \cos\alpha \right)\mathbf{i}' - \left( I_t \Omega \sin\alpha \right)\mathbf{j}' \qquad\qquad (5.45)$$
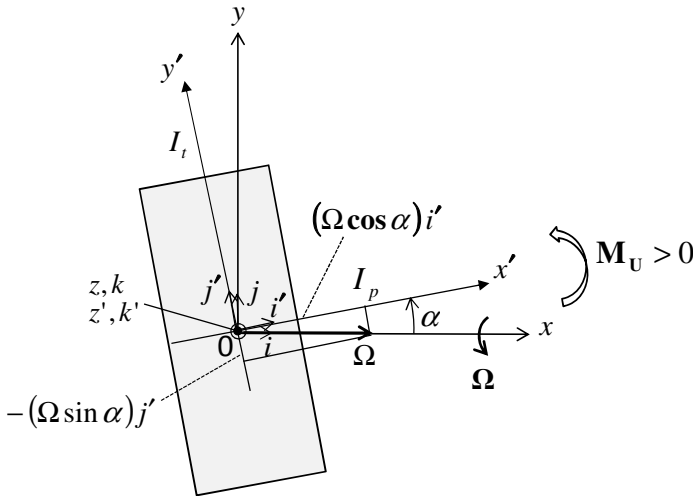


Fig. 5.13 Unbalance moment of a misaligned rotor

Using the relations between the unit vectors **i**, **j**, **i'**, **j'** of two coordinate systems

$$\begin{cases} \mathbf{i}' = (\cos\alpha)\mathbf{i} + (\sin\alpha)\mathbf{j} \\ \mathbf{j}' = (-\sin\alpha)\mathbf{i} + (\cos\alpha)\mathbf{j} \end{cases} \tag{5.46}$$

the angular velocity **ω** can be written in the rotating coordinate system (x',y',z') as

$$\boldsymbol{\omega} = \Omega\,\mathbf{i} = \Omega\cos\alpha\,\mathbf{i}' - \Omega\sin\alpha\,\mathbf{j}' \tag{5.47}$$

Substituting Eqs (5.45) and (5.47) into Eq. (5.43), one obtains the unbalance moment vector in the stationary coordinate system (x,y,z) with k = k'.

$$\mathbf{M_U} = -(\boldsymbol{\omega}\times\mathbf{L}) = (I_t - I_p)\Omega^2\,\sin\alpha\cos\alpha\,\mathbf{k} \tag{5.48}$$

within

$$\left(\frac{\partial\mathbf{L}}{\partial t}\right)_{(x',y',z')} = \mathbf{0} \quad \text{because } \Omega \text{ and } \alpha \text{ are constant, as given in Eq. (5.45).}$$

The misalignment angle $\alpha$ of the couple unbalance is generally very small ($\alpha \ll 1$); hence, Eq. (5.48) can be written in $\alpha$ (radian).

$$\mathbf{M_U} \approx (I_t - I_p)\alpha\,\Omega^2\,\mathbf{k} = U_\alpha\Omega^2\mathbf{k} \tag{5.49}$$

The unbalance moment vector $\mathbf{M_U}$ acting upon the rotor in the direction z is caused by the moment unbalance of

$$U_\alpha = \alpha(I_t - I_p) \tag{5.50}$$

In the automotive turbochargers, the transverse mass inertia moment $I_t$ of the entire rotor is mostly larger than the polar inertia moment $I_p$ ($I_t \gg I_p$). Therefore, according to Eq. (5.49), the direction of the unbalance moment $\mathbf{M_U}$ is positive in case of a positive misalignment angle $\alpha$, as shown in Fig. 5.13. During the rotation, the misalignment angle takes turns changing from the positive to negative direction and vice versa; hence, the unbalance moment direction is changed in the same direction of $\alpha$. Therefore, the unbalance moment $\mathbf{M_U}$ excites the rotor in the third and fourth equations of eq. (5.52). As a result, the rotor amplitude of the conical vibration mode is strongly amplified (s. Fig. 5.14), leading to wear in the bearings by rubbing and damages them in the worst case.

Note that the misalignment angle due to the couple unbalance cannot be removed by the low-speed balancing (called shop balancing). Moreover, it is very difficult to balance the unbalance moment $\mathbf{M_U}$ of the turbine shaft at the shop balancing in case of $I_t \gg I_p$ and a large misalignment angle $\alpha$. The useful way to reduce this unbalance moment is trying to produce a good turbine shaft by well centering and setting the shaft possibly perpendicular to the turbine wheel at welding and grinding. As a result, it could provide the rotor with a small misalignment angle (small dynamic unbalance) and a low eccentricity (low static unbalance) in order to prevent the rotor from the vibration excitations induced by the unbalance moments and forces, as shown in Eq. (5.52).
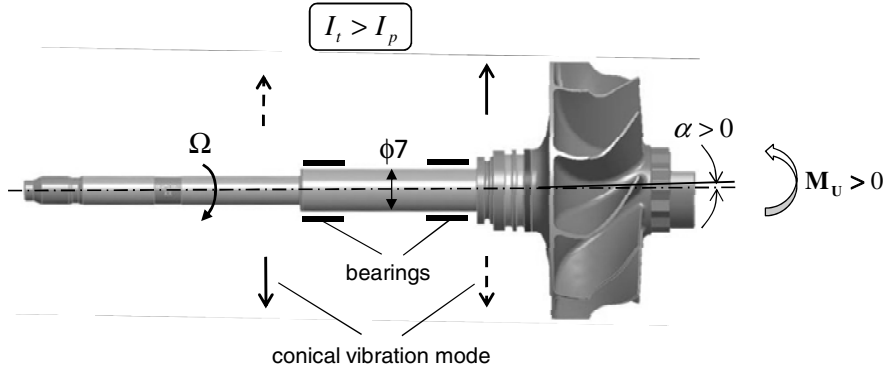
**Fig. 5.14** Influence of the unbalance moment on the turbine shaft

The vibration equations of the linear rotordynamic turbocharger with N degrees of freedom (DOF) resulted from the lateral and rotational vibrations are written in

$$\mathbf{M}\ddot{\mathbf{q}} + (\mathbf{C} + \mathbf{G})\dot{\mathbf{q}} + \mathbf{K}\mathbf{q} = \mathbf{Q}(t) \tag{5.51}$$

where
N = degrees of freedom of the turbocharger;
$\mathbf{M}$ = (N x N) diagonal mass and inertia moment matrix;
$\mathbf{C}$ = (N x N) lateral and circulant damping matrix;
$\mathbf{G}$ = (N x N) gyroscopic moment matrix;
$\mathbf{K}$ = (N x N) lateral and circulant stiffness matrix;
$\mathbf{q}$ = (N x 1) DOF vector;
$\mathbf{Q}(t)$ = (N x 1) unbalance force and moment vector.

An application of Eq. (5.51) to the Jeffcott rotor with 4 DOFs is demonstrated in Fig. 5.15. The vibration equations for the Jeffcott rotor are derived in the coordinate system (x,y,z) by means of the momentum approach where the gyroscopic effect is taken into account in the vibration equations.

$$\begin{cases} m\ddot{x} + c_{l,x}\dot{x} + k_{l,x}x + K_{tr}\theta_x = m\varepsilon\Omega^2\cos\Omega t \\ m\ddot{y} + c_{l,y}\dot{y} + k_{l,y}y + K_{tr}\theta_y = m\varepsilon\Omega^2\sin\Omega t \\ I_t\ddot{\theta}_x + I_p\Omega\dot{\theta}_y + c_{r,x}\dot{\theta}_x + K_{tr}x + k_{r,x}\theta_x = (I_t - I_p)\alpha\,\Omega^2\cos\Omega t \\ I_t\ddot{\theta}_y - I_p\Omega\dot{\theta}_x + c_{r,y}\dot{\theta}_y + K_{tr}y + k_{r,y}\theta_y = (I_t - I_p)\alpha\,\Omega^2\sin\Omega t \end{cases} \tag{5.52}$$

where
$k_l$, $k_r$ are the lateral and circulant system stiffness coefficients;
$K_{tr}$ is the interaction stiffness coefficient of lateral and circulant vibrations;
$c_l$, $c_r$ are the lateral and circulant system damping coefficients;
$\varepsilon$ is the unbalance radius of the rotor;

$\alpha$ is the misalignment angle.
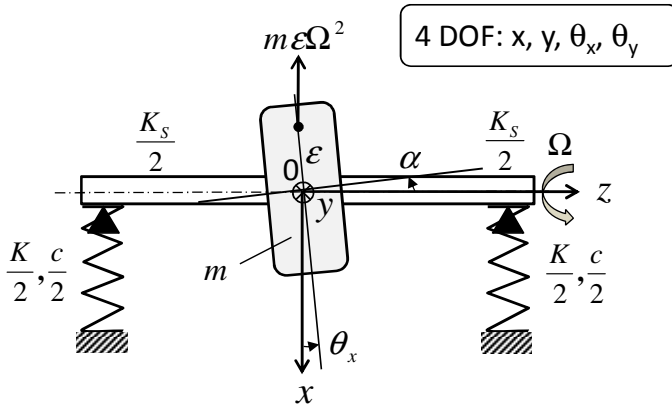


**Fig. 5.15** Jeffcott rotor with 4 DOFs

Vibration equations (5.52) are written in the matrix form as follows:

$$
\begin{bmatrix} m & 0 & 0 & 0 \\ 0 & m & 0 & 0 \\ 0 & 0 & I_t & 0 \\ 0 & 0 & 0 & I_t \end{bmatrix} \cdot \begin{bmatrix} \ddot{x} \\ \ddot{y} \\ \ddot{\theta}_x \\ \ddot{\theta}_y \end{bmatrix} + \begin{bmatrix} c_{l,x} & 0 & 0 & 0 \\ 0 & c_{l,x} & 0 & 0 \\ 0 & 0 & c_{r,x} & I_p\Omega \\ 0 & 0 & -I_p\Omega & c_{r,y} \end{bmatrix} \cdot \begin{bmatrix} \dot{x} \\ \dot{y} \\ \dot{\theta}_x \\ \dot{\theta}_y \end{bmatrix} +
$$

$$
\begin{bmatrix} k_{l,x} & 0 & K_{tr} & 0 \\ 0 & k_{l,y} & 0 & K_{tr} \\ K_{tr} & 0 & k_{r,x} & 0 \\ 0 & K_{tr} & 0 & k_{r,y} \end{bmatrix} \cdot \begin{bmatrix} x \\ y \\ \theta_x \\ \theta_y \end{bmatrix} = \begin{bmatrix} m\varepsilon\Omega^2 \cos \Omega t \\ m\varepsilon\Omega^2 \sin \Omega t \\ (I_t - I_p)\alpha\Omega^2 \cos \Omega t \\ (I_t - I_p)\alpha\Omega^2 \sin \Omega t \end{bmatrix}
$$

$$(5.53)$$

**c) Lagrange's approach**

The vibration equations can be derived from the Lagrange's approach based on the kinetic and potential energies of the rotor with N degrees of freedom (DOF=4).

- The kinetic energy $T_{rotor}$ consists of the lateral and rotational parts,

$$
T_{rotor} = \tfrac{1}{2} m\dot{\mathbf{r}}^2 + \tfrac{1}{2} I\dot{\boldsymbol{\theta}}^2 \tag{5.54}
$$

where

$$
T_l = \tfrac{1}{2} m\dot{\mathbf{r}}^2 = \tfrac{1}{2} \sum_{i=1}^{N} m_i \dot{x}_i^2 \quad \text{is the lateral kinetic energy;}
$$

$$T_r = \tfrac{1}{2} I \dot{\boldsymbol{\theta}}^2 = \tfrac{1}{2} \sum_{i=1}^{N} I_i \dot{\theta}_i^2 \text{ is the rotational kinetic energy;}$$

within $I$ are the transverse and polar mass inertia moments.

- The potential energy $V_{rotor}$ consists of the lateral and rotational parts,

$$V_{rotor} = \tfrac{1}{2} k_l \mathbf{r}^2 + \tfrac{1}{2} k_r \boldsymbol{\theta}^2 \tag{5.55}$$

where

$$V_l = \tfrac{1}{2} k_l \mathbf{r}^2 = \tfrac{1}{2} \sum_{i=1}^{N} k_{l,i} x_i^2 \text{ is the lateral potential energy;}$$

$$V_r = \tfrac{1}{2} k_r \boldsymbol{\theta}^2 = \tfrac{1}{2} \sum_{i=1}^{N} k_{r,i} \theta_i^2 \text{ is the rotational potential energy;}$$

within
$k_l$, $k_r$ are the lateral and circulant stiffness coefficients, respectively;
$\mathbf{r}$ is the lateral vector;
$\boldsymbol{\theta}$ is the angle vector.

Having defined the Lagrange function $L$ of the rotor,

$$L \equiv T_{rotor} - V_{rotor} \tag{5.56}$$

the vibration equations of the rotor with N degrees of freedom are written in the Lagrange equation.

$$\frac{d}{dt}\left(\frac{\partial L}{\partial \dot{q}_i}\right) - \frac{\partial L}{\partial q_i} + \frac{\partial F}{\partial \dot{q}_i} = Q_i; \; i = 1, 2, ..., N \tag{5.57}$$

where
$q_i$ are the Lagrangian coordinates of DOF;
$Q_i$ are the non-conservative generalized forces and moments, such as friction forces and moments;

$F$ is the Rayleigh dissipation function defined as [17]

$$F = \tfrac{1}{2} c_l \dot{\mathbf{r}}^2 + \tfrac{1}{2} c_r \dot{\boldsymbol{\theta}}^2 = \tfrac{1}{2} \sum_{i=1}^{N} \left( c_{l,i} \dot{x}_i^2 + c_{r,i} \dot{\theta}_i^2 \right) \tag{5.58}$$

where
$c_l$, $c_r$ are the lateral and circulant damping coefficients, respectively.

## 5.6  Transient Response at the Run-Up

In the run-up, the rotor with an angular acceleration, the transient rotor response will be studied on a Jeffcott rotor with two DOFs of x and y, as demonstrated in Fig. 5.15.

The coordinates of the mass center G of the rotor are written in the coordinate system (x,y).

$$\mathbf{r_G} = \mathbf{r_M} + \mathbf{r_\varepsilon}$$
$$= [x + \varepsilon \cos(\varphi + \beta)]\mathbf{i} + [y + \varepsilon \sin(\varphi + \beta)]\mathbf{j} \tag{5.59}$$

where
$\varphi$ is the rotation angle of the rotor.

The rotor speed is resulted from

$$\dot{\varphi} = \ddot{\varphi}t \equiv a_\varphi t \tag{5.60}$$

where
$a_\varphi$ is the constant angular acceleration of the rotor.

The rotation angle of the rotor is resulted by integrating Eq. (5.60).

$$\varphi = \int \dot{\varphi} \, dt = \int a_\varphi t \, dt = \tfrac{1}{2} a_\varphi t^2 \tag{5.61}$$
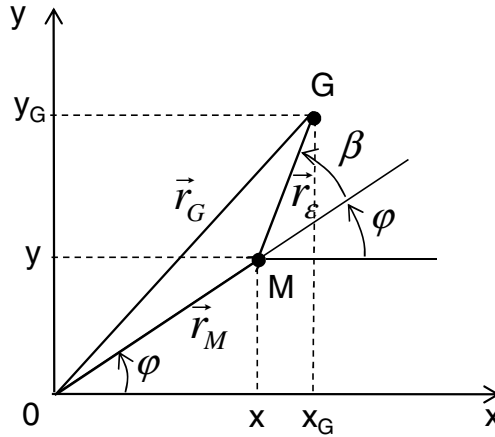


Fig. 5.16 Coordinates of the geometric and mass center of the rotor

After twice differentiating Eq. (5.59), one obtains the acceleration of the mass center G

$$\begin{cases} \ddot{x}_G = \ddot{x} - \varepsilon \left[ \dot{\varphi}^2 \cos(\varphi + \beta) + \ddot{\varphi} \sin(\varphi + \beta) \right] \\ \ddot{y}_G = \ddot{y} - \varepsilon \left[ \dot{\varphi}^2 \sin(\varphi + \beta) - \ddot{\varphi} \cos(\varphi + \beta) \right] \end{cases} \tag{5.62}$$

The first term in the square brackets in Eq. (5.62) is much larger than the second term with increasing time t since

$$\frac{\left|\dot{\varphi}^2\cos(\varphi+\beta)\right|}{\left|\ddot{\varphi}\sin(\varphi+\beta)\right|}=\frac{\left|\dot{\varphi}^2\right|}{\left|\ddot{\varphi}\right|}=\left|a_\varphi\right|t^2\gg1 \tag{5.63}$$

Thus,

$$\begin{cases}\ddot{x}_G=\ddot{x}-\varepsilon\dot{\varphi}^2\cos(\varphi+\beta)\\\ddot{y}_G=\ddot{y}-\varepsilon\dot{\varphi}^2\sin(\varphi+\beta)\end{cases} \tag{5.64}$$

The vibration equations of the two-DOF Jeffcott rotor with anisotropic bearings, as shown in Fig. 5.17, are written at the rotor center M (x,y) with $\beta=0$.

$$\begin{cases}m\ddot{x}+c_{22}\dot{x}+k_{22}x=m\varepsilon\dot{\varphi}^2(t)\cos\varphi\\m\ddot{y}+c_{33}\dot{y}+k_{33}y=m\varepsilon\dot{\varphi}^2(t)\sin\varphi\end{cases} \tag{5.65}$$

where
$c_{22}$, $c_{33}$ are the diagonal damping coefficients in the directions x and y;
$k_{22}$, $k_{33}$ are the diagonal stiffness coefficients in the directions x and y.
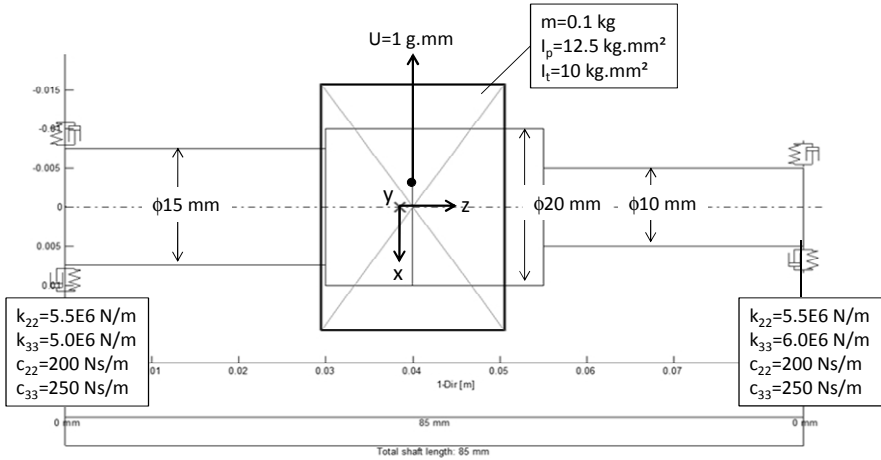


**Fig. 5.17** Computed model of the Jeffcott rotor

The Jeffcott rotor has a mass of m = 0.1 kg, the polar and transverse mass inertia moments of $I_p$ = 12.5 kg.mm² and $I_t$ = 10 kg.mm², respectively. The total length of the rotor is about l = 85 mm and its various lengths and diameters are given in Fig. 5.17. The residual unbalance U = 1 g.mm lies at the mass center of the wheel and induces the excitation unbalance force acting on the rotor. The rotor rotates with accelerated rotational speeds Ω in the direction z and deflects in the directions x and y due to the unbalance force. In the computation, it is assumed that the anisotropic bearings are located at each end of the rotor with the constant stiffness and damping coefficients in Fig. 5.17.

To compute the rotor vibration response of Eq. (5.65), the computational program of rotordynamics MADYN 2000 [9] based on the finite element method is applied at a steady-state working condition and various accelerations during the speed-up. At steady state ($a_\varphi = 0$), the rotor deflection versus the rotor speed is displayed in Fig. 5.18. Owing to the unbalance force, the rotor deflects at increasing rotor speeds and reaches the resonance at the critical speed of nearly 59,100 rpm. The maximum rotor deflection at the resonance is about 27 µm.

After passing the resonance, the rotor amplitude continuously decreases to the unbalance radius ε of approximately 5 µm because of self-centering effect of the rotor at the supercritical speeds, as discussed in Section 5.2.

At the run-up, the rotor speed is accelerated with an acceleration $a_\varphi$; therefore, the unbalance force is also increased with time according to Eqs (5.60) and (5.65). Figure 5.19a shows a time interval Δt that is needed to run-up the rotor from 5 to 100% of the maximum rotor speed $N_{max}$. Note that the shorter the time interval, the higher the acceleration at which the rotor speeds up. At the acceleration with time interval of 0.1 s, the resonance at $a_\varphi = 0.158 \, N_{max}/s$ occurs at 64,700 rpm higher than the steady-state critical speed, but the resonance amplitude is reduced from 27 to 12 µm, as shown in Fig. 5.19c. For further increasing accelerations with a time interval of 0.05 s, the resonance at $a_\varphi = 0.317 \, N_{max}/s$ takes place much later at the critical speed of about 69,750 rpm where the resonance amplitude of 11 µm is smaller than the earlier case, but the critical speed is higher (s. Fig. 5.19d). Contrary to the stationary working condition, the rotor deflection at the run-up vibrates with reducing amplitudes.
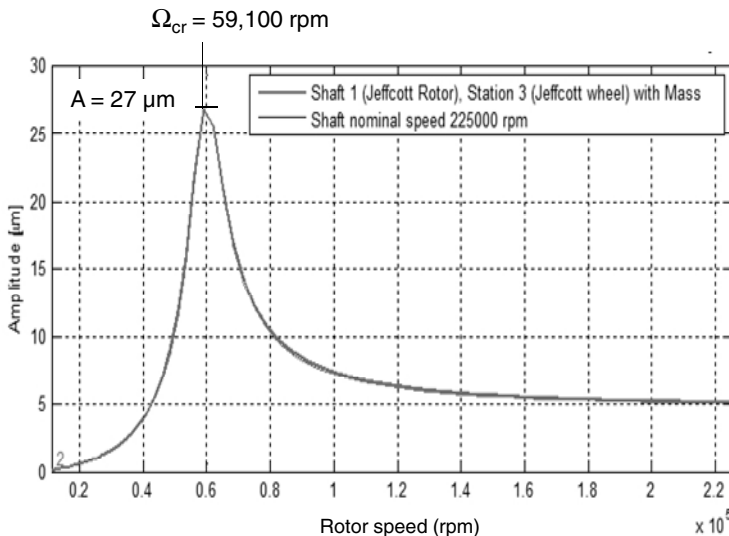


**Fig. 5.18** Deflection rotor amplitude vs. rotor speed at steady state
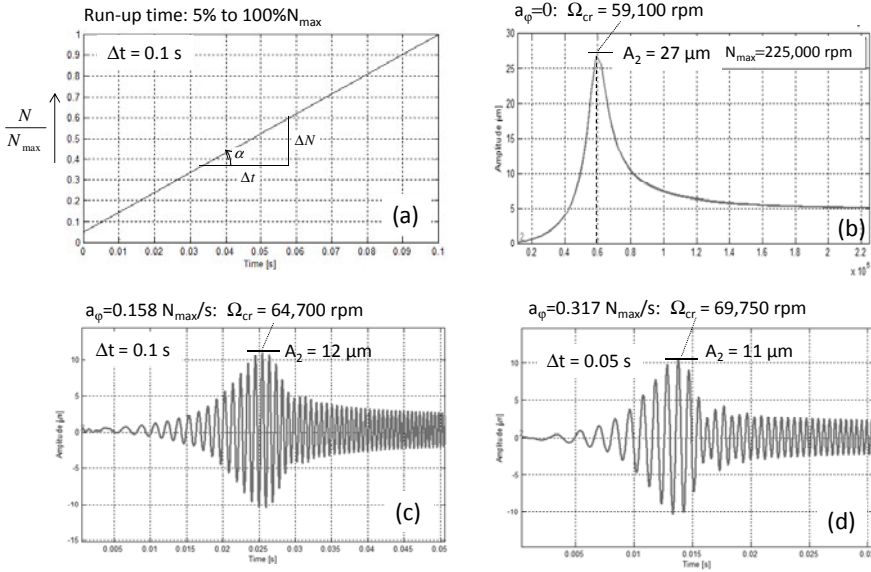
**Fig. 5.19** a, b, c, d: Rotor responses at various run-up accelerations

The computing results in Fig. 5.19 show that the critical speeds increase with the run-up acceleration compared to the critical speed at $a_\varphi = 0$. However, the resonance amplitudes decrease with the acceleration. Therefore, it is usually to speed-up the rotor over the critical speeds at high accelerations in order to avoid the resonance damage, especially in turbomachines of the power plants.

## 5.7  Frequency Analysis in Campbell Diagram

In linear rotordynamics, only the resonance response of the rotor has been studied. The characteristics of the rotor system are designed in such a way that the resonances are possible to occur outside the operating speed range of the rotor. However, the resonance cannot always be outside the operating speed range, such as in the automotive turbochargers. In this case, more damping is necessary to keep the resonance rotor amplitude as small as possible, and therefore to prevent the bearings from fatal damages.

According to Eq. (5.17), the resonance amplitude increases dramatically when the rotor speeds equal the eigenfrequencies (called natural frequencies) of the rotor in case of small damping ratio. In fact, it is not easy to calculate the natural frequencies depending on many rotor characteristics like gyroscopic effects by analytically solving the nonlinear equation of the rotor eigenfrequencies and rotor speed.

$$\omega_n(m, I_t, I_p, \Omega, k, c) = \Omega \qquad (5.66)$$

However, Eq. (5.66) can be graphically solved in the Campbell diagram (called whirl speed diagram) by means of the intersections between the eigenfrequencies

and the synchronous excitation line 1X where $\omega_n$ equals $\Omega$. The critical speeds are resulted from the cutting points in the Campbell diagram. The gyroscopic effect stiffens the rotor eigenfrequencies of the forward whirls and destiffens the rotor eigenfrequencies of the backward whirls with increasing rotor speeds, as shown in Fig. 5.20a. Therefore, the critical speeds of the forward whirls are higher than those without the gyroscopic effect.

The rotational kinetic energy of the rotor excites only the forward whirls because both have the same rotational direction; therefore, the amplitudes are strongly amplified at the resonance. On the contrary, the backward whirl direction is opposite to the rotational direction of the rotor; hence, the rotational kinetic energy of the rotor is dissipated, instead exciting the backward whirls at the resonance. As a result, the unbalance forces normally excite only the forward whirls at the resonances. However, the unbalance force could excite the backward whirls in case of asymmetric rotors or oscillating rotor speeds. Therefore, the intersections between the eigenfrequencies of the forward whirls and the synchronous excitation line 1X determine the critical speeds in the Campbell diagram.

The first forward whirl eigenfrequency $\omega_1$ cuts the synchronous excitation line 1X at the first bending resonance; the maximum amplitude A takes place at the critical speed $\Omega_{cr,1}$ ($\omega_1 = \Omega_{cr,1}$). Any point in the excitation line 1X satisfies eq. (5.66) with $\omega = \Omega$. The eigenfrequency $\omega_2$ may cut the excitation line 1X at
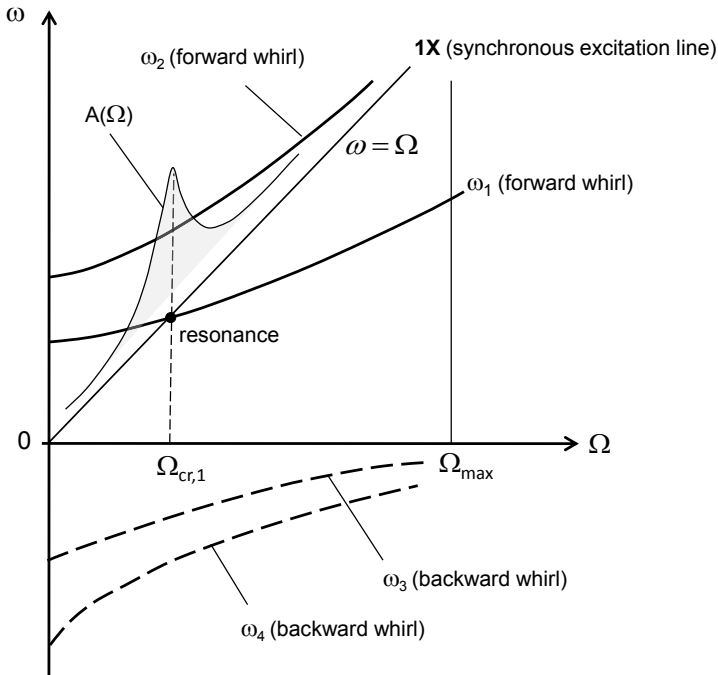


**Fig. 5.20a** Campbell diagram of the eigenfrequencies versus rotor speed
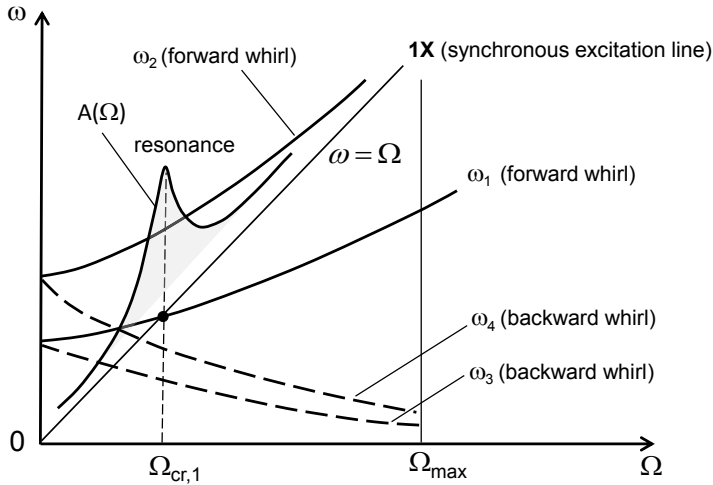
**Fig. 5.20b** Simplified Campbell diagram

a higher rotor speed that is outside the operating speed range. The backward whirls $\omega_3$ and $\omega_4$ have not been normally excited by the unbalance force, and therefore they do not cause resonances at the symmetric rotor.

In the turbochargers, it has to design the rotor having its first bending critical speed as high as possible, so that the onset of instability speed at the oil whip is outside the operating speed range of the turbochargers. Moreover, the rotor unbalance induces the unbalance whistle, one of the unwanted airborne noises in the automotive turbochargers. The unbalance whistle has the same frequency as the rotor and disturbs the driver and passengers during driving. However, the unbalance whistle induced at high critical speeds is generally suppressed by the engine noise at high motor speeds. That is a second reason that the first critical frequency should be as high as possible.

For simplicity, the Campbell diagram is sometimes displayed as in Fig. 5.20b where the backward whirls (dash lines) are in the same side as the forward whirls (solid lines). While the eigenfrequencies of the forward whirls increase with the rotor speed, the backward whirls eigenfrequencies decrease to zero. Even the backward whirls frequencies cut the excitation line 1X, however the resonances do not occur in the backward whirls.

In the following section, the eigenmodes of the rigid rotor of Fig. 5.21 are computed, as shown in the Campbell diagram. The rotor is supported at each end by two isotropic bearings with an effective stiffness coefficient $k/2$ of the rotor. The rigid rotor has a translatory vibration in the directions x and y, and a conical vibration in the directions $\theta_x$ and $\theta_y$, as shown in Fig. 5.21. The rotor is assumed as a full cylinder with a radius r and length l. In case of $l^2 < 3r^2$, the polar mass inertia moment is larger than the transverse inertia moment ($I_p > I_t$) for the short, thick rotor; if $l^2 > 3r^2$, $I_p$ is smaller than $I_t$ ($I_p < I_t$) for the long, slender rotor.

The free vibration equations of the rigid rotor with 4 DOFs of x, y, $\theta_x$, and $\theta_y$ are written in

$$\begin{cases} m\ddot{x} + kx + k_\delta\theta_x = 0 \\ m\ddot{y} + ky + k_\delta\theta_y = 0 \\ I_t\ddot{\theta}_x + I_p\Omega\dot{\theta}_y + k_\theta\theta_x + k_\delta x = 0 \\ I_t\ddot{\theta}_y - I_p\Omega\dot{\theta}_x + k_\theta\theta_y + k_\delta y = 0 \end{cases} \tag{5.67}$$

where

k, $k_\theta$ are the lateral and circulant bearing stiffness coefficients;
$k_\delta$ is the coupling stiffness coefficient of DOF.

Having inserted the free vibration response

$$r = \hat{r}e^{j\omega t} \rightarrow \dot{r} = j\omega\, r \quad and \quad \ddot{r} = -\omega^2 r$$
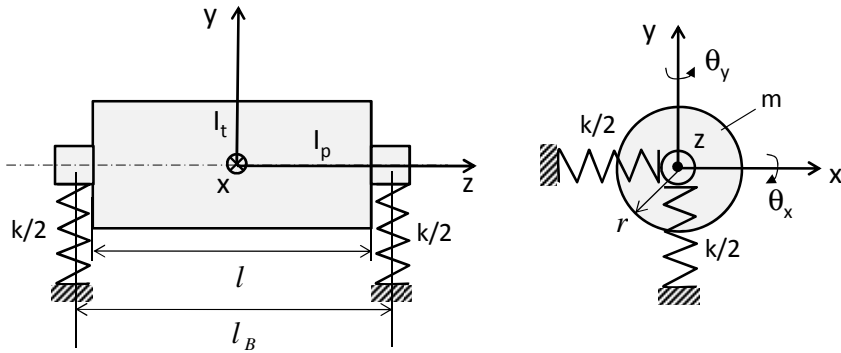


**Fig. 5.21** Case history of the rigid rotor

in Eq. (5.67), one obtains the characteristic equation

$$D(\omega) = (k - m\omega^2).(k_\theta + I_p\Omega\omega - I_t\omega^2) - k_\delta^2 = 0 \tag{5.68}$$

The eigenfrequencies are resulted from the roots of Eq. (5.68) which are in a function of the rotor speed $\Omega$ because of the gyroscopic effect. They can be numerically computed at various rotor speeds and are plotted in Figs 5.22a and 5.22b. However, one can analytically calculate their responses depending on the rotor speeds.

The rotor speed is derived from the characteristic Equation (5.68) and written in the rotor eigenfrequency.

$$\Omega = \frac{mI_t\omega^4 - (kI_t + k_\theta m)\omega^2 + (kk_\theta - k_\delta^2)}{mI_p\omega\left(\omega^2 - \dfrac{k}{m}\right)} \tag{5.69}$$

- At $\Omega = 0$, the numerator of Eq. (5.69) equals zero; hence, four natural frequencies $\omega_{1,0}$, $\omega_{2,0}$, $\omega_{3,0}$, and $\omega_{4,0}$ are determined.
- As $\Omega$ goes to $\infty$, the denominator converges to zero; one gets

$$\omega_{2;4,\infty} = \pm\sqrt{\frac{k}{m}}; \quad \omega_{3,\infty} \to 0 \tag{5.70}$$

- As $\omega$ goes to $\infty$, it gives the asymptotic relation between $\Omega$ and $\omega$ according to the L'Hôpital's rule.

$$\Omega = \lim_{\omega \to \infty} \left( \frac{mI_t\omega^4 - \left(kI_t + k_\theta m\right)\omega^2 + \left(kk_\theta - k_\delta^2\right)}{mI_p\omega\left(\omega^2 - \dfrac{k}{m}\right)} \right) = \frac{I_t\omega}{I_p} \tag{5.71}$$

Thus,

$$\omega = \frac{I_p\Omega}{I_t} \tag{5.72}$$

where

- $I_p < I_t$ gives $\omega/\Omega < 1$; its gradient is smaller than 1X ($\omega = \Omega$);
- $I_p > I_t$ gives $\omega/\Omega > 1$; its gradient is larger than 1X ($\omega = \Omega$).

The behaviors of the eigenfrequencies can be plotted by such asymptotic methods in Figs (5.22a) and (5.22b). In case of $I_p < I_t$, the gradient of the asymptote $\omega_1$ in Eq. (5.72) is less than 1; there are two critical speeds $\Omega_{c,1}$ and $\Omega_{c,2}$ in the synchronous excitation line 1X, as shown in Fig. 5.22a. On the contrary, if $I_p > I_t$, there is only one critical speed $\Omega_{c,2}$ because the gradient of the asymptote $\omega_1$ is larger than 1. Therefore, the eigenfrequency of the forward whirl $\omega_1$ never cuts the excitation line 1X at $I_p > I_t$ (s. Fig. 5.22b).

To investigate the eigenmodes of the eigenfrequencies $\omega_1$ and $\omega_2$, the ratio of critical speeds is used. The critical speed ratio $\xi$ for the symmetric rotor with overhung ends is defined [14], as shown in Fig. 5.21.

$$\xi \equiv \left(\frac{\Omega_{c,1}}{\Omega_{c,2}}\right)^2 = \frac{4(I_t - I_p)}{ml_B^2} = \left(\frac{l - 3r^2}{3l_B^2}\right) \tag{5.73}$$

where
l is the length of the rotor;
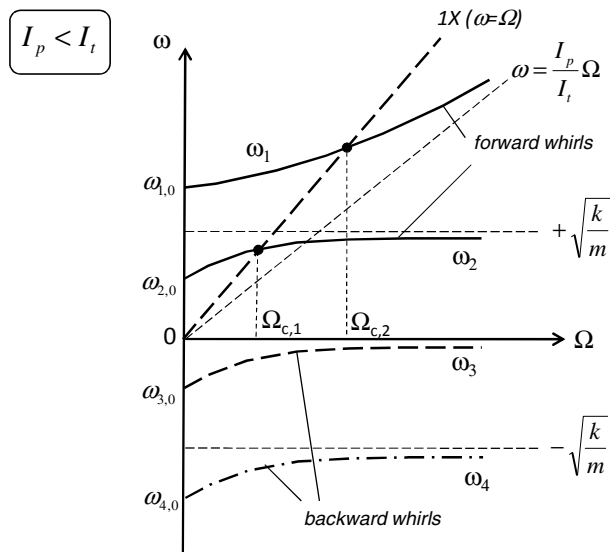r is the rotor radius;
$l_B$ is the bearing span.
There are two cases of $\xi$:

- $\xi < 1$ at $(1 - 3r^2) < 3l_B^2$, the cylindrical mode occurs at the lower frequency.
- $\xi > 1$ at $(1 - 3r^2) > 3l_B^2$, the conical mode occurs at the lower frequency.

$I_p < I_t$



**Fig. 5.22a** Campbell diagram in case of $I_p < I_t$
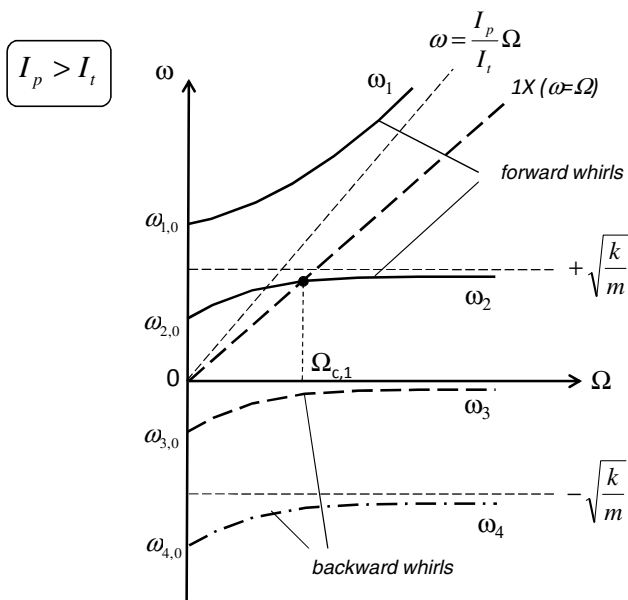
$I_p > I_t$



**Fig. 5.22b** Campbell diagram in case of $I_p > I_t$

## 5.8  Computations of Linear Rotordynamics

Automotive turbochargers mostly use rotating floating ring bearings (RFRB) with two oil films which have some nonlinear characteristics of the bearing stiffness and damping coefficients: Therefore, the nonlinear rotordynamic effects of sub-synchronous whirls, such as oil whirls and supersynchronous whirls like excessively high unbalance forces, rotor misalignment, contact rubs, and frequency modulations must be taken into account in the computations. To compute the rotordynamic behavior of the turbocharger some commercial codes such as Adams, SimPack, MADYN 2000, etc. are used. Unfortunately, the nonlinear characteristics of the oil-film bearings have not been well simulated yet for nonlinear rotordynamics because all mutual effects between the fluid-, thermo-, and rotor-dynamics in the oil films are quite difficult to simulate numerically.

However, some characteristics of turbochargers have been carried out at first by the computation of linear rotordynamics with the program MADYN 2000 in order to study the modal analysis. In this case, the anisotropic bearings are assumed to have constant stiffness and damping coefficients in each direction, instead of the nonlinear bearing forces acting upon the rotor. Nevertheless, the results of the linear rotordynamic computation can provide the critical speeds of the rotor in the Campbell diagram and the rotor eigenmodes of the harmonic vibrations induced by the unbalance excitation forces as well as moments.

The rotor of the turbocharger displayed in Fig. 5.23 consists of the compressor and turbine wheels, and two rotating floating ring bearings. The computed rotor model is transformed to the finite element model where the wheels, shaft, and bearings with all necessary degrees of freedom (DOF) are taken into account in the computation. Each wheel has 4 DOFs of $x_2$, $x_3$, $\theta_2$, and $\theta_3$ in the inertial coordinate system (1,2,3); the shaft element and bearings have 2 DOFs of $x_2$ and $x_3$. The rotor velocity $\Omega$ aligns with the axial direction 1, as shown in Fig. 5.23.

The bearings have the stiffness coefficients $k_{22}$=2.0E3 N/m; $k_{33}$=2.25E3 N/m and the small damping coefficients $c_{22}$=50 Ns/m; $c_{33}$=55 Ns/m, which are used in the computation of the modal analysis. The total mass of the small turbocharger rotor is about 95 g. The polar and transverse mass inertia moments at the mass center G result in $I_p$=6.4E-6 kg.m² and $I_t$=107E-6 kg.m², respectively, as shown in Fig. 5.23.

The first bending resonance is found at the first critical speed of nearly 131,900 rpm in the Campbell diagram (s. Fig. 5.24) in which the forward whirl eigenfrequency $\omega_4$ with the eigenmode #4 cuts the synchronous excitation line 1X. Three forward whirls with the eigenmodes #2, #4, and #6 in the frequency range up to 6,000 Hz appear in the Campbell diagram; however, three backward whirls with the eigenmodes #1, #3, and #5 do not excite the rotor at the resonances. The second resonance of the eigenmode #6 occurs outside the operating rotor speed of 285,000 rpm.
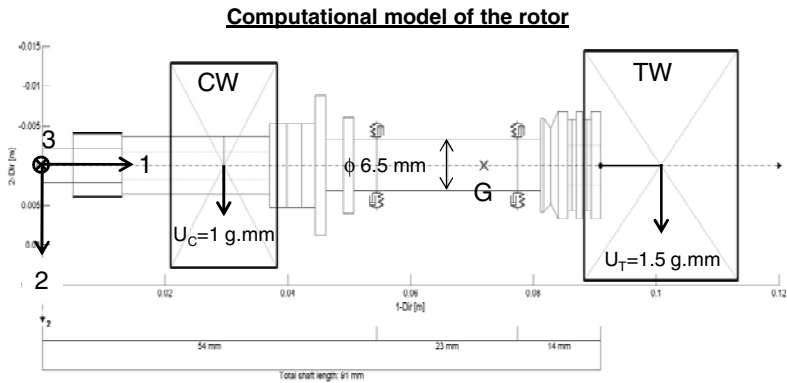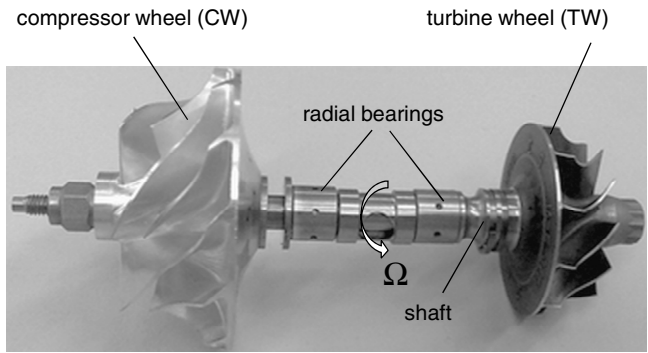
**Fig. 5.23** Computational model of the turbocharger rotor
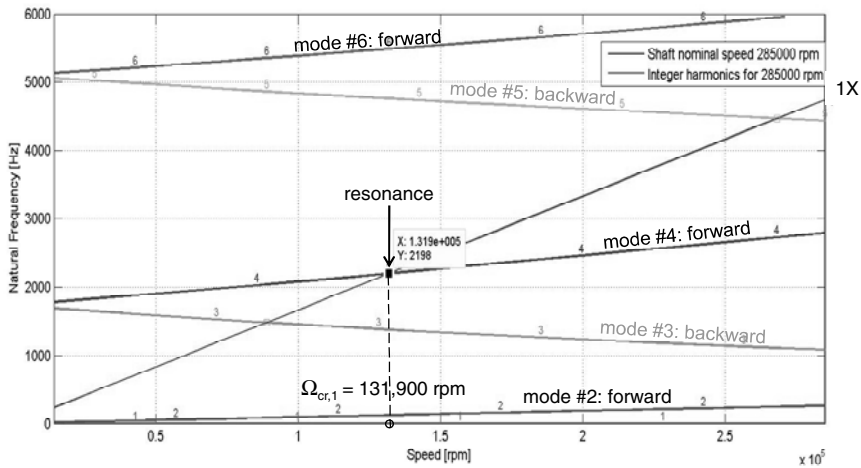


**Fig. 5.24** Campbell diagram of the turbocharger rotor
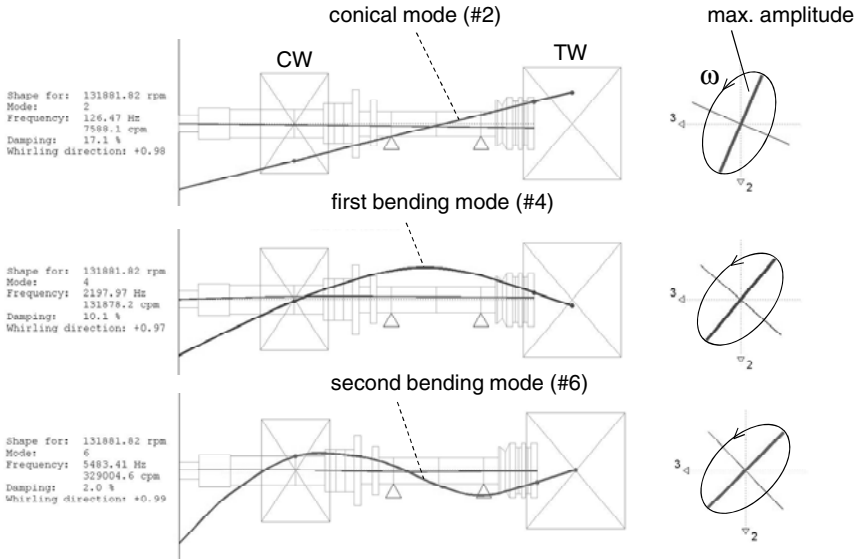
**Fig. 5.25** Vibration eigenmodes of the rotor near the resonance

The vibration shapes of the eigenmodes of the rotor were already discussed in Chapter 3. At a low rotor speed of about 7,588 rpm, the rotor is still rigid and its transverse mass inertia moment $I_t$ = 107E-6 kg.m² is larger than the polar inertia moment $I_p$ = 6.4E-6 kg.m². In this case, the critical speed ratio ξ in Eq. (5.73) is much larger than 1 (ξ >> 1); therefore, the conical mode (eigenmode #2) takes place at the low frequency, as shown in Fig. 5.25. Obviously, a long and slender rigid rotor ($I_t$ >> $I_p$) tends to tumble with the conical mode shape at low rotor speeds rather than with the cylindrical one. In the conical mode, the displacements of the compressor (CW) and turbine wheels (TW) go out of phase; i.e., their deflection directions are opposite to each other with a phase lag of 180°.

The rotor amplitude of the conical mode is normally larger than the amplitude of the cylindrical because it is amplified by the long arm of the rotor from the rotation point of the conical mode. On the contrary, the rotor amplitude of the cylindrical mode is limited by the small bearing clearance. At large, the shorter, and thicker rigid rotor ($I_t$ << $I_p$) is more stable than the long, and slender rotor ($I_t$ >> $I_p$) at low rotor speeds since the forward whirl eigenmode is a cylindrical mode. In this case, the displacements of the compressor (CW) and turbine wheels (TW) go in phase and their amplitudes are limited in the bearing clearance. The whirl orbits of the rotor eigenmodes are illustrated in the phase plane 2-3, in which the amplitude and direction of the minimal and maximal rotor deflections are indicated for each vibration mode (s. Fig. 5.25).
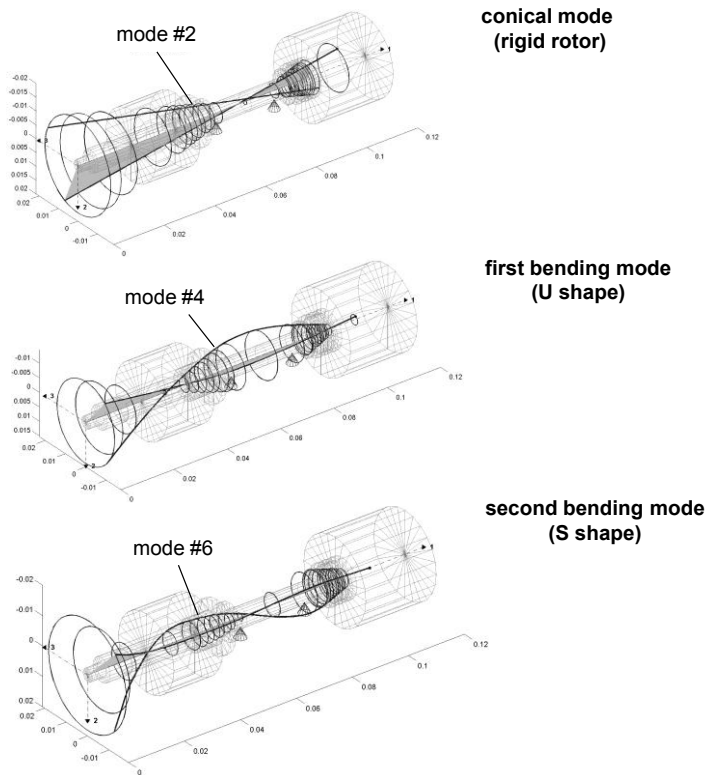
**Fig. 5.26** Vibration eigenmodes of the rotor near $\Omega_{cr}$ = 132,000 rpm

The rotor becomes flexible at increasing its speed. It begins to deflect itself due to unbalance and arrives at the maximum deflection at the first resonance with $\Omega_{cr}$ = 131,900 rpm. The forward whirl eigenmode #4 of the flexible rotor has a U mode shape where the deflections of the wheels are in phase. At high supercritical speeds, the bending shape of the forward whirl eigenmode #6 changes from the U to S shape and approaches the second resonance at a second critical speed outside the rotor speed range, as shown in the Campbell diagram (s. Fig. 5.24). The deflection directions of the wheels are opposite to each other in the S shape of the eigenmode #6. Unless the second resonance is far away from the maximum rotor speed, the rotor amplitude will increase again shortly after the self-centering of the first resonance.

Figure 5.26 displays the shapes of the eigenmodes #2, #4, and #6 of the forward whirls. The elliptic whirl orbit of the rotor has the maximum amplitude whose direction locates in the phase plane 2-3, as shown in Fig. 5.25. In order to measure the rotor eigenmode, four eddy-current sensors should be installed at the ends of the rotor at the compressor and turbine wheels. If the vibration responses at the rotor ends take turns moving in the opposite direction with a phase lag of 180°, the rotor vibration is out of phase, either the conical (rigid

rotor) or the second bending mode with a S shape (flexible rotor) depending on the rotor speed is possible. Otherwise, the rotor vibration is in phase, either the cylindrical (rigid rotor) or the first bending mode with a U shape (flexible rotor) depending on the rotor speed could be the case. However, it is very difficult to measure the rotor deflection at the turbine side due to high temperatures of the exhaust gase at 850°C  in diesel engines and 1,050°C in gasoline engines.

# References

1.  Adams Jr., M.L.: Rotating Machinery Vibration. CRC, Taylor and Francis (2001)
2.  Bently, D.E., Hatch, C.: Fundamentals of Rotating Machinery Diagnostics. Bently Pressurized Bearing Press (2002)
3.  Childs, D.: Turbomachinery Rotordynamics. J. Wiley and Sons Inc. (1993)
4.  Ehrich, F.: Handbook of Rotordynamics. Krieger Publishing Company (2004)
5.  Funakawa, Tatara: Stability criterion of an elastic rotor in journal bearings. Trans. JSME 30(218) (1964)
6.  Gasch, R., Nordmann, R., Pfuetzner, H.: Rotordynamik, vol. 2. Auflage, Springer (2006)
7.  Genta, G.: Dynamics of Rotating Systems. Springer, Heidelberg (2005)
8.  Kraemer, E.: Rotordynamics of Rotors and Foundations. Springer, Heidelberg (1993)
9.  MADYN 2000: Program of Computational Rotordynamics. Delta JS (2011)
10. Muszýnska, A.: Rotordynamics. CRC, Taylor and Francis (2005)
11. Newland, D.E.: An Introduction to Random Vibrations, Spectral & Wavelet Analysis, 3rd edn. Dover Publications Inc. (2005)
12. Rao, J.S.: Rotordynamics, 3rd edn. New Age Intl. Publishers (2007)
13. Rieger, N.F.: Rotordynamics 2 - Problems in Turbomachinery. CISM Courses and Lectures No. 297 (1988)
14. Rieger, N.F.: Balancing of Rigid and Flexible Rotors. U.S. DoD (1986)
15. Taylor, J.R.: Classical Mechanics. University Science Books (2005)
16. Vance, J.: Rotordynamics of Turbomachinery. J. Wiley and Sons Inc. (1988)
17. Yamamoto, T., Ishida, Y.: Linear and Nonlinear Rotordynamics. J. Wiley and Sons Inc. (2001)

# Chapter 6
# Bearing Dynamics of Turbochargers

## 6.1 Introduction

To support the rotor in the operation, the bearing system including the thrust and radial bearings is necessary for turbochargers. The impulse forces of fluids in the wheels and pressures acting on the compressor and turbine wheels cause the axial thrust on the rotor that depends on different working conditions. Hence, the axial thrust is balanced by the thrust bearing to keep the rotor stable in the axial direction. On the contrary, the radial bearings induce the bearing forces to balance the unbalance forces acting upon the rotor in the radial direction.

Figure 6.1 displays the layout of the bearing system in the core unit (CHRA: center housing and rotating assembly) that includes the rotor shaft, turbine and compressor wheels, thrust rings, and radial bearings. The thrust bearing is mounted and fixed in the bearing housing, not rotating with the rotor; it is in the middle between the thrust rings that are fixed in the shaft, rotating with the rotor. The reacting force of the thrust bearing acts upon one of thrust rings to keep the rotor in balance against the axial thrust. The thrust bearing force is induced by squeezing of the oil film between the bearing and thrust rings; hence, the oil-film thickness determines the reacting force of the thrust bearing. Note that the smaller the oil-film thickness, the larger the thrust bearing force induces, and vice versa.

Radial bearings rotate and float in the inner and outer oil films, called the rotating floating ring bearings (RFRB). These bearings are applied to the automotive turbochargers in order to reduce the bearing friction compared to the semi-floating ring bearings, especially in low-end torque (LET). As a reason, the response behavior of turbochargers (turbolag) improves at low rotor speeds. Normally, two kinds of radial bearings are used in the automotive turbochargers: hydrodynamic fluid-film bearings and rolling-element bearings. The latter reduces much more bearing friction at low rotor speeds; therefore, they are sometimes applied to some automotive turbochargers in order to keep $CO_2$ emission low according to the current emission law or to improve the transient behavior further. At high rotor speeds, the difference of the bearing friction between the fluid-film and rolling-element bearings is quite small because the oil temperature increases; hence, the oil viscosity reduces, leading to reduction of the bearing friction of the oil-film bearings.

The rotor is supported on the bearing system rotating and floating in the bearing housing, as displayed in Fig. 6.2. The bearing system is supplied with pressurized oil at the oil inlet. The oil channels in the bearing housing provide the thrust and radial bearings with the pressurized oil, which has two main functions. Firstly, the bearing

forces that are generated by the oil hydrodynamic effect keep the rotor stable in the axial and radial directions, and damp the rotor vibration to prevent its response from large amplitude at the resonance. Secondly, fresh supply oil removes the induced heating flow in the bearings by the convection in the axial direction, and by the conduction between two oil-films in the radial direction through the bearing ring. This cooling function keeps the effective oil temperature in the bearings as low as possible, and therefore maintains the bearing stiffness and damping coefficients large at the high rotor speeds, in turn large stiffness and damping forces of the bearings.
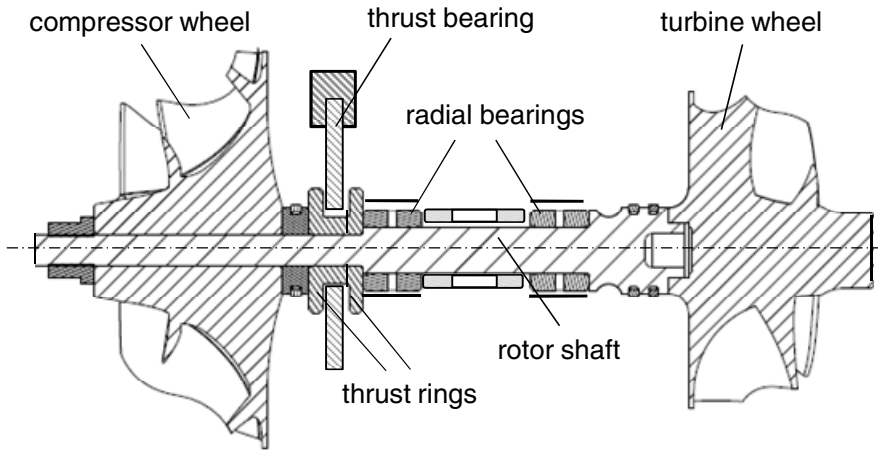
**Fig. 6.1** Layout of the bearing system in a turbocharger
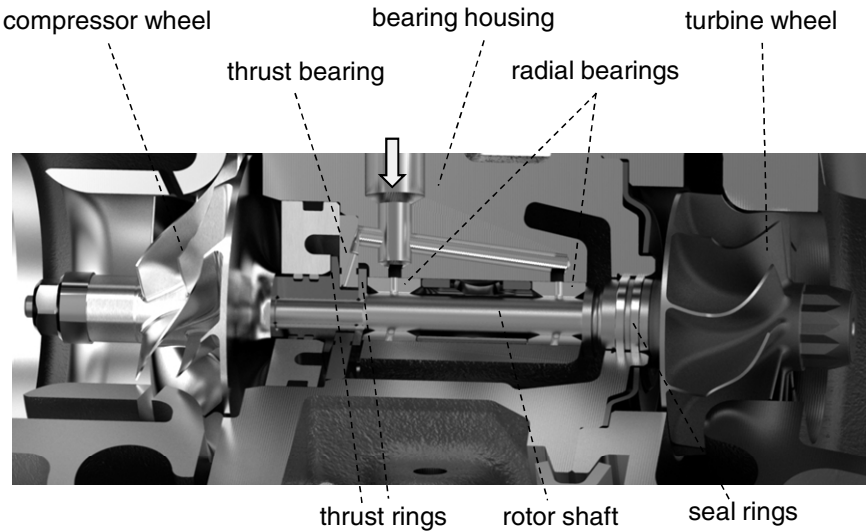
**Fig. 6.2** CHRA (center housing and rotating assembly) of a wastegated turbocharger (Courtesy BMTS)

In the following section, Table 6.1 compares the characteristics between the fluid-film and rolling-element bearings. Despite many disadvantages, the rolling-element bearings have only one main advantage of the small bearing friction at low rotor speeds, especially in low-end torque. As shown in Tab. 6.1, the friction coefficient of the ball bearings is in the order of 10 times lower than the oil-film bearings at low rotor speeds. However, the friction coefficients of both bearings are nearly equal at the high rotor speeds since the effective oil temperature in the bearings has been already high, leading to low oil viscosity and low bearing friction at these rotor speeds. However, the bearing efficiency only plays a secondary role at the high rotor speeds because the turbine power is much larger than the bearing friction power at these high rotor speeds.

The main disadvantage of the rolling-element bearings is very loud. Besides the unbalance whistle (1X), the typical induced noises of the ball bearings are highly-harmonic noises (2X, 3X, or higher frequency order), defected-bearing-related noises, and side-band noises induced by the frequency modulations of the unbalance whistle, highly harmonic noises, and defected-bearing-related noises. Compared to the oil-film bearings, the so-called constant tone (subsynchronous noise) due to oil whirl does not occur in the ball bearings. However, the ball bearings cost nearly 10 times more than the oil-film bearings. When the monetary penalty for exceeding the allowable limit of $CO_2$ emission is quite high, or the transient behavior is significantly improved at the low-end torque, the ball bearings are reasonable to apply to the automotive turbochargers.

**Table 6.1** Comparison of bearing characteristics between the oil-film and rolling-element bearings of turbochargers

| Characteristics | Oil-film bearings (rotating floating ring bearings) | Rolling-element bearings (combined thrust and radial bearings) |
|---|---|---|
| Functionality | separate radial and thrust bearings | combined radial and thrust bearings |
| Load direction | radial and axial | radial and axial |
| Volumetric size | small outer diameter of radial bearings | outer diameter: 2x larger |
| Friction coefficient | • in LET: <u>large</u> → $\mu = 10^{-2}...10^{-1}$<br>• at high speeds: small → $\mu = 10^{-3}$ | • in LET: <u>small</u><br>→ $\mu = 10^{-3}... 10^{-2}$<br>• at high speeds: small<br>→ $\mu = 10^{-3}$ |
| Damping coefficient (bearing/rotor) | 2x larger because of two oil films: inner bearing clearance (20 μm); outer bearing clearance (70 μm) | very small, clearance between balls/race (< 0.5 μm); 1x oil-film damper (50...80 μm) |
| Noise | less noisy: unbalance whistle; constant tone (inner oil whirl) | noisy: unbalance whistle, high harmonics, defected bearing frequencies, sidebands due to frequency modulation |
| Oil volumetric flow rate | small | nearly 2x larger |
| Lifetime | unlimited | limited by high cycle fatigue (HCF) |
| Damage | possibly damaged by oil whip (self-excited instability); less or no wear (normal condition) | ball contacting at high speeds; more wear |
| Cost | low | very high |

## 6.2 Reynolds Lubrication Equation

The Reynolds lubrication equation is used to compute the bearing forces of the oil-film bearings. While the Navier-Stokes equations deal with the highly large convection terms at high Reynolds numbers, the Reynolds equations, with the insignificantly small convection terms at low Reynolds numbers. The flows in the oil-film bearings of the automotive turbochargers are normally laminar with low Reynolds numbers between 100 and 200; therefore, the convection terms are quite small. As a reason, the Reynolds equations are used in the oil-film bearings instead of the more complex Navier-Stokes equations.

Figure 6.3 shows the hydrodynamic characteristic of the oil film in the bearing in which the journal moves with a circumferential velocity $U_2$; the bearing rotates in case of the rotating floating ring bearing with a circumferential velocity $U_1$.
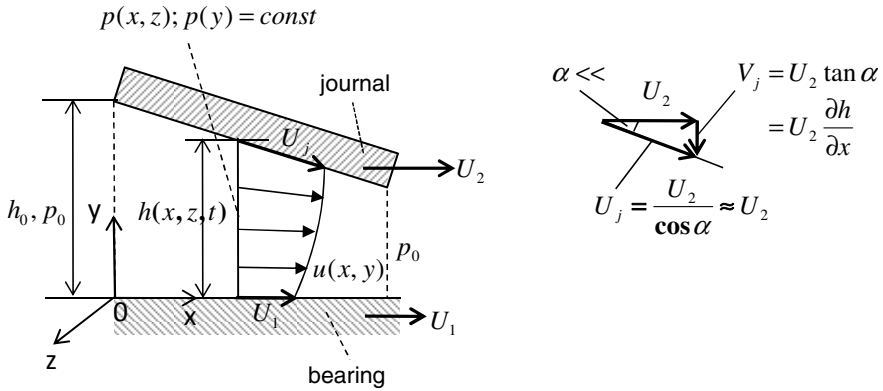


**Fig. 6.3** Hydrodynamic oil film in the radial bearing

The oil film can be simplified as a fluid wedge that is surrounded by the bearing and journal moving with the velocities $U_1$ and $U_2$, respectively (s. Fig. 6.3). Due to the moving journal and bearing, lubricating oil is drawn into the wedge from the inlet with the pressure $p_0$ and flows with a velocity $u(x,y)$ through the wedge. The oil film is squeezed inside the wedge because of the wedge and squeeze effects in the oil film. Hence, the oil-film pressure $p(x,z)$ increases in the directions x and z from the oil inlet to the middle of the fluid wedge; it remains unchanged in the direction y since the oil-film thickness is very small. The Reynolds number of the oil flow in the wedge is very low; therefore, the flow of the oil film is laminar, and its velocity has a parabolic profile.

The velocity of the journal $U_2$ contains two components: $U_j$ parallel to the journal surface and $V_j$ perpendicular to the moving direction of $U_2$. The first one is nearly equal to the moving velocity $U_2$ because the inclination angle $\alpha$ between the journal and bearing is very small ($U_2 \approx U_j$). The second one is derived from $U_2$ and $\alpha$ and written in

$$V_j = U_2 \tan \alpha = U_2 \frac{\partial h}{\partial x} < 0 \tag{6.1}$$

The direction of $V_j$ is negative, acting perpendicular to the oil film. Therefore, the incompressible oil is squeezed; the oil-film pressure increases correspondingly.

Having applied the Reynolds and continuity equations to the incompressible oil film of the wedge, the pressure distribution in the oil film is given by the Reynolds lubrication equation [5].

$$\frac{\partial}{\partial x}\left(h^3 \frac{\partial p}{\partial x}\right) + \frac{\partial}{\partial z}\left(h^3 \frac{\partial p}{\partial z}\right) = 6\eta\left[(U_1 - U_2)\frac{\partial h}{\partial x} + 2\left(V_j + \frac{\partial h}{\partial t}\right)\right] \tag{6.2}$$

where
h(x,z,t) is the thickness of the oil film;
p(x,z) is the oil-film pressure;
$\eta$ is the oil dynamic viscosity.

By setting Eq. (6.1) into Eq. (6.2), the Reynolds lubrication equation becomes

$$\frac{\partial}{\partial x}\left(h^3 \frac{\partial p}{\partial x}\right) + \frac{\partial}{\partial z}\left(h^3 \frac{\partial p}{\partial z}\right) = 6\eta\left[(U_1 + U_2)\frac{\partial h}{\partial x} + 2\frac{\partial h}{\partial t}\right] \tag{6.3a}$$

In a non-rotating radial bearings with $U_1 = 0$, Eq. (6.3a) is rewritten as

$$\frac{\partial}{\partial x}\left(h^3 \frac{\partial p}{\partial x}\right) + \frac{\partial}{\partial z}\left(h^3 \frac{\partial p}{\partial z}\right) = 6\eta U_2 \frac{\partial h}{\partial x} + 12\eta \frac{\partial h}{\partial t} \tag{6.3b}$$

Both first terms in the right-hand side of eq. (6.3a) are induced by the rotor velocity and wedge effect (called the wedge-velocity term); the third term, by the squeeze-film effect (called the squeeze-film term). Due to the converged wedge geometry, the change of the oil-film thickness h in the direction x is always negative; therefore, the wedge-velocity term is also negative.

The oil-film thickness h in the radial bearing results in

$$h + e = c_0 \tag{6.4}$$

where
e is the journal displacement inside the bearing clearance;
$c_0$ the radial bearing clearance (= const).

Thus,

$$\frac{\partial h}{\partial t} = -\frac{\partial e}{\partial t} \tag{6.5}$$

In case of the journal moves from the bearing center outwards due to unbalance; i.e., the timely rate change of e is positive. According to Eq. (6.5), the timely change of the oil-film thickness is negative; i.e., the squeeze-film term is also negative. All terms in the right-hand side in Eqs (6.3a) and (6.3b) are negative.

Obviously, the pressure terms in the left-hand side of Eqs (6.3a) and (6.3b) are negative. Notice that this term is the second-order derivatives of the oil-film pressure. So, the oil-film pressure p(x,z) has a paraboloid shape with the maximum pressure inside the wedge, as shown in Fig. 6.4. On the one hand, the wedge-velocity terms in Eqs (6.3a) and (6.3b) raise the bearing stiffness coefficients due to the rotation of the bearing with the velocity $U_1$, and the journal with the velocity $U_2$ where the oil is pumped into the wedge, and compressed by the rotating kinetic energy. On the other hand, the squeeze-film term induces the bearing damping coefficients by means of the timely change of the oil-film thickness.
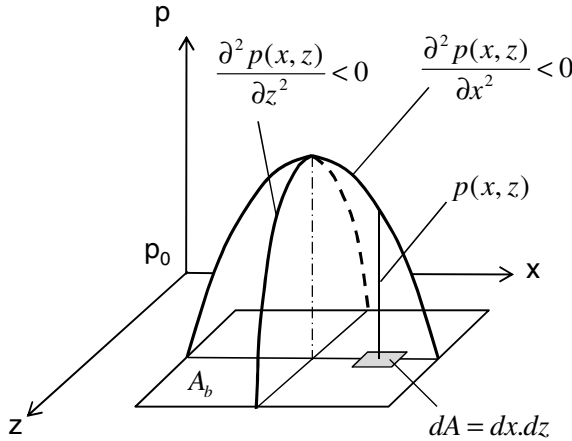


**Fig. 6.4** Pressure distribution p(x,z) of the oil film

By solving Eq. (6.3a) or (6.3b) with the boundary conditions, one obtains the pressure distribution of the oil film in the bearing clearance. The total bearing force is resulted by integrating the pressure of the oil film over the bearing surface.

$$F_B = \oint_{A_b} p(x,z)\, dA = \int_{z_0}^{z_b} \int_{x_0}^{x_b} p(x,z)\, dx\, dz \tag{6.6}$$

where $A_b$ is the pressure surface of the bearing.

## 6.3 Lubrication Regimes in the Stribeck Curve

Two rough surfaces 1 and 2 lubricated by the oil film move to each other where the friction force $F_t$ acts on the moving surface 2. Figure 6.5 displays three general lubrication regions of the boundary, mixed, and hydrodynamic lubrications in the tribology. We begin to study the lubrication regimes in the Stribeck curve, from the right-hand to the left-hand side in Fig. 6.5. The hydrodynamic lubrication

occurs when the surfaces are completely separated by the lubricated oil film; i.e., no contact of materials takes place between two surfaces in this regime. In the hydrodynamic lubrication region (full oil film), the friction coefficient μ is proportional to the Hersey dimensionless number according to Eq. (6.11).

The Hersey number is defined as

$$He \equiv \frac{\eta N}{p} \tag{6.7}$$

where
η is the oil dynamic viscosity (Pa.s);
N is the rotor speed (rps);
p is the oil-film pressure between two surfaces (Pa).

The friction force in the hydrodynamic lubrication is calculated

$$F_t = \tau A_t = \eta \left( \frac{\partial u}{\partial h} \right) A_t \approx \eta \left( \frac{U_2}{h} \right) A_t \tag{6.8}$$

The oil velocity $U_2$ is calculated from the shaft rotational speed and its diameter.

$$U_2 = \Omega R = \pi N D$$

Thus, Eq. (6.8) becomes

$$F_t = \eta \left( \frac{\pi N D}{h} \right) A_t = \left( \frac{\pi D}{h} \right) A_t \eta N \tag{6.9}$$

where
D is the shaft diameter;
h is the oil film thickness between the surfaces;
$A_t$ is the oil lubricated surface area;
η is the oil viscosity;
N is the rotor speed (rps).

The normal force at the contact surface is calculated as

$$F_n = p A_t \tag{6.10}$$

The friction coefficient is defined as the ratio of the friction to the normal force of Eqs (6.9) and (6.10).

$$\mu \equiv \frac{F_t}{F_n} = \left( \frac{\pi D}{h} \right) \frac{\eta N}{p} = k \left( \frac{\eta N}{p} \right) = k.He \tag{6.11}$$

Equation (6.11) indicates that the friction coefficient is proportional to the Hersey number in the hydrodynamic lubrication, as shown in Fig. 6.5. It is straightforward

that the higher the rotor speed, the larger the friction force induces in the oil film at a constant bearing load.

When the oil-film thickness becomes smaller, the micro-contact at the asperities between the surfaces takes place. This lubrication regime is now called the mixed lubrication where the adhesion friction mainly causes the friction at the asperities of the surfaces.

The friction force is derived from the shear stress of the softer material at the asperities and contact surface.

$$F_t = \tau A_t \tag{6.12}$$

The normal force is derived from the normal stress at the asperities and contact surface.

$$F_n = \sigma_n A_t \tag{6.13}$$

where $\sigma_n$ is the plastic normal stress .

Therefore, the friction coefficient in the mixed lubrication is resulted from Eqs (6.12) and (6.13).

$$\mu \equiv \frac{F_t}{F_n} = \frac{\tau}{\sigma_n} \tag{6.14}$$

The plastic deformation takes place at the vicinity of the contact asperities rather than the elastic deformation that occurs far away from the contact zone. At the plastic deformation, the atoms near the contact zone in the surface slide and move to each other in the form of slip planes and dislocations that correct the errors in the crystal structures of the surfaces. This process is called the work hardening or strain hardening in which the shear stress, normal stress, and hardness of the surface material are strengthened as the plastic deformation continues. Hence, the surface material at the contact zone is hardened by increasing the strength of the plastic shear and normal stress. According to [9], the plastic shear stress increases faster than the plastic normal stress. Therefore, the friction coefficient $\mu$, as given in Eq. (6.14) increases in the mixed lubrication region at reducing the Hersey number. In this region, the plastic deformation occurs at the asperities of the surfaces.

In the boundary lubrication, the surfaces are only lubricated by oil additives connected by the oil molecules in the point of view in the nanotribology [9]. In this case, the friction coefficient is nearly unchanged at small Hersey numbers in this regime. At increasing load, the Hersey number reduces because the pressure p in the contact zone becomes larger. By further increasing load or oil temperature, the oil-molecule chains break, and therefore the surfaces are now non-lubricating seized. As a reason, the friction coefficient jumps up, leading to the seizure of the surfaces, as shown in the Stribeck curve at very small Hersey numbers (s. Fig. 6.5).
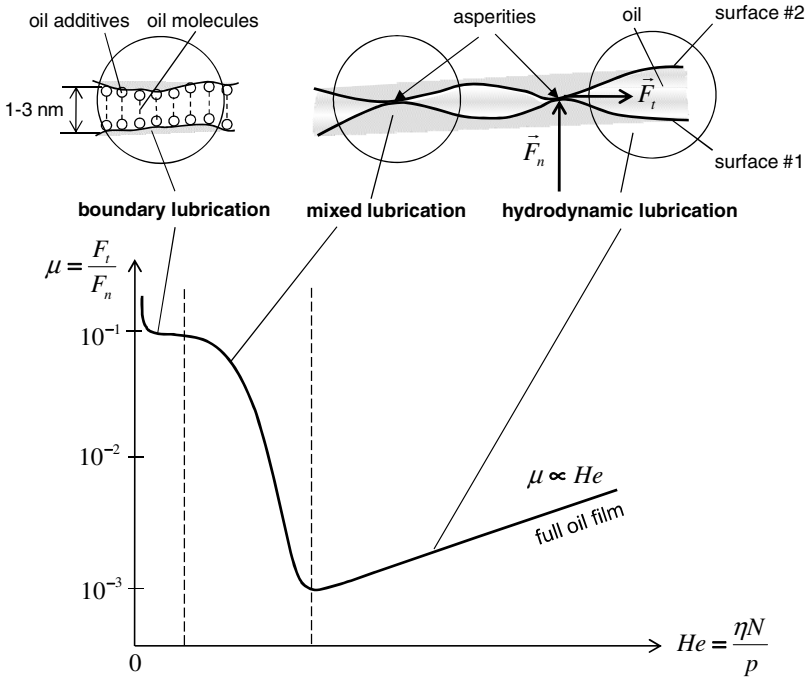
**Fig. 6.5** Stribeck curve of the oil lubricated journal bearing

## 6.4 Thrust Bearings

### 6.4.1 Working Principle

The working principle of thrust bearings, as shown in Fig. 6.6 is based on the hydrodynamic effect of the lubricating oil described by the Reynolds lubrication equation. The thrust rings fixed to the rotor shaft rotates with the same rotor speed $\Omega$ and its circumferential velocity U at the mean diameter $D_m$ of the bearing segment (s. Fig. 6.7). The bearing segment including the tapered land, flat plateau, and oil groove is mounted and fixed in the bearing housing, and therefore the thrust ring moves relatively to the thrust bearing with the rotor speed $\Omega$. Due to the wedge and squeeze-film effects, the oil-film pressure is generated on the thrust ring to keep the rotor in balance, against the axial thrust acting upon the rotor.

In this case, the wedge velocity $U_2 = 0$ and the bearing velocity $U_1 = U$, as indicated in Figure 6.3 where U is the thrust-ring's velocity. Therefore, the Reynolds lubrication Equation (6.3a) for the thrust bearing becomes

$$\frac{\partial}{\partial x}\left(h^3 \frac{\partial p}{\partial x}\right) + \frac{\partial}{\partial z}\left(h^3 \frac{\partial p}{\partial z}\right) = 6\eta U \frac{\partial h}{\partial x} + 12\eta \frac{\partial h}{\partial t} \tag{6.15}$$

where
p(x,z) is the induced pressure in the bearing;
h(x,z) is the oil film thickness in the bearing;
$\eta$ is the oil dynamic viscosity;
U is the circumferential velocity at the mean diameter $D_m$.
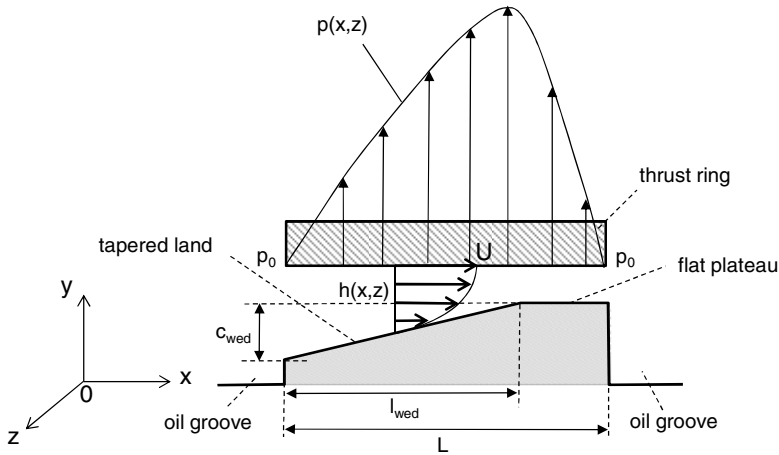


**Fig. 6.6** Working principle of a thrust bearing
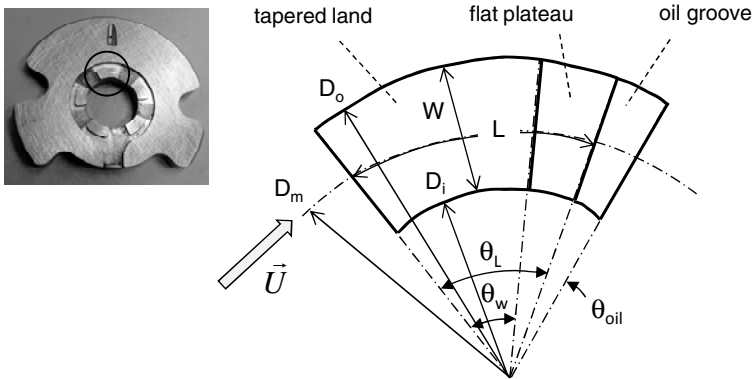


**Fig. 6.7** Geometry of a segment of the thrust bearing

On the one hand, the thrust ring with the velocity U pumps oil into the wedge and squeezes it in the bearing due to the wedge effect. Hence, the oil pressure increases strongly because of its incompressibility. On the other hand, at increasing the axial thrust, the timely change of the oil film thickness is negative, leading to the increase of pressure induced by the squeeze-film effect.

By integrating the pressure p(x,z) over the bearing surface $A_b$ of all bearing segments, one obtains the bearing force acting opposite to the axial thrust. At equilibrium position, the bearing force equals the axial thrust where the oil film thickness between the thrust ring and bearing segment is determined. The oil film thickness must be larger than the required minimum oil-film thickness, as given in Eq. (6.32) depending on the surface roughness, to prevent the bearing wear in the mixed lubrication and the seizure of the bearing in the boundary zone.

## 6.4.2 Calculation of the Axial Thrust on the Rotor

To design a thrust bearing that is used in the automotive turbochargers, the axial thrust must be determined at first. The axial thrust is caused by the different pressures acting upon the compressor and turbine wheels and as well as the impulse force induced by the flows in the wheels in the axial direction. Since the turbochargers work at various speeds in the run-up, slowdown at different traffic situations, the axial thrust depends on the rotor speed; its acting direction could change from one direction to the opposite one.

There are two usual ways to compute the axial thrust: either using CFD (computational fluid dynamics) or applying the Newton's second law. The first one provides a precise result but requires a huge computing effort at all working conditions of turbochargers including the mesh generation of the entire turbocharger, computing time (CPU), and post processing of the computational results. On the contrary, using the Newton's second law to compute the axial force is quite simple, but some thermodynamics and turbomachinery backgrounds are required. However, its analytical result is quite good, compared to the CFD numerical results. The discrepancy between them is less than 10% according to our test computation by using both methods at an automotive turbocharger. Moreover, using the Newton's second law needs much less computing time to carry out the task for all working conditions; the result discrepancy between both methods is smaller than the safety tolerance range of the axial thrust at the bearing design. As a reason, the Newton's second law is usually applied to computing the axial thrust in automotive turbochargers.

The thrust force $\vec{F}_T$ opposite to the reaction force $\vec{F}_R$ is derived from the second law applied to the control volume (CV). The fluid flows through the control volume with a mass flow rate $\dot{m}$, as shown in Fig. 6.8.

The fluid flow is assumed as steady state and the viscous friction at the wall of the control volume (CV) to be negligibly small. According to the Newton's second law, the acting forces on the control volume (CV) are written at the steady state condition.

$$\sum \vec{F} = \sum_j \left( \vec{F}_{p,j} + \vec{F}_{J,j} \right) + \vec{F}_R = m\vec{a} = \vec{0} \qquad (6.16)$$

where

$\vec{F}_p$ is the pressure force;

$\vec{F}_J$ is the impulse force;
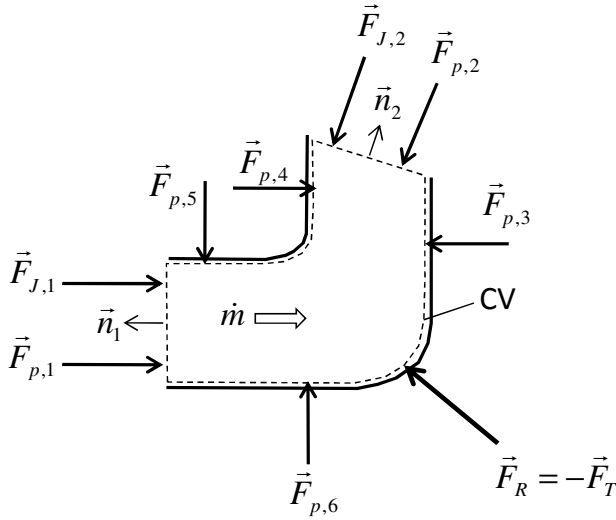
**Fig. 6.8** Forces acting upon a control volume (CV)

$\vec{F}_R$ is the reaction force acting upon the control volume;
$\vec{a}$ is the flow acceleration.

By integrating pressure p over surface A, the pressure force results in

$$\vec{F}_p \;=\; -\oint_A p\,\vec{n}\,dA \;=\; -\,\overline{p}\,A\,\vec{n} \tag{6.17}$$

where
$\vec{n}$ is the normal vector at the surface;
$\overline{p}$ is the average pressure at the surface.

The momentum force is calculated by the momentum theorem.

$$\vec{F}_J \;=\; -\oint_A \rho\,\vec{v}\,.(\vec{v}\,,\vec{n}\,)dA \;=\; -\,\rho\,\overline{v}^{\,2}\,A\,\vec{n} \;=\; -\,\dot{m}\,\overline{v}\,\vec{n} \tag{6.18}$$

where
$\dot{m}$ is the mass flow rate through the control volume;
$\vec{v}$ is the fluid velocity vector perpendicular to the surface;
$\rho$ is the fluid density at the surface;
$\overline{v}$ is the fluid average velocity at the inlet and outlet flow areas.

Substitution of Eqs (6.16), (6.17), and (6.18) gives the axial thrust acting on the rotor at the steady state.

$$\vec{F}_T \;=\; -\vec{F}_R \;=\; \sum_j \left(\vec{F}_{p,j} + \vec{F}_{J,j}\right) = -\sum_j \left(\overline{p}_j A_j + \dot{m}\,\overline{v}_j\right)\vec{n}_j \tag{6.19}$$
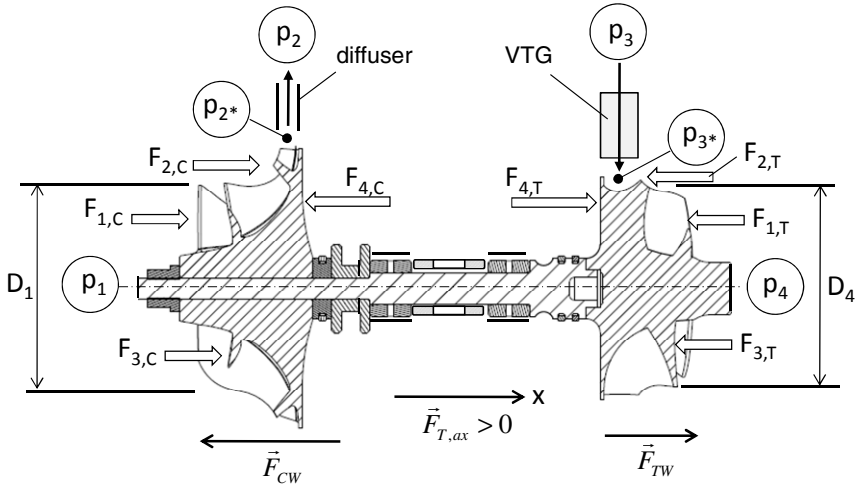
**Fig. 6.9** Acting forces on the rotor of a turbocharger

Eq. (6.19) is the fundamental equation that is used to compute the axial thrust of the thrust bearing. Due to the rotor symmetry, the resulting force on the rotor is acting in the axial direction x, which is called the axial thrust $F_{T,ax}$, as displayed in Fig. 6.9.

The axial thrust $F_{T,ax}$ acting upon the rotor is resulted from all forces of the compressor and turbine wheels that are indicated in Fig. 6.9. On the compressor wheel (left) $F_{1,C}$ is the pressure force at the compressor inlet surface; $F_{2,C}$ the pressure force at the shroud surface; $F_{3,C}$ the impulse force in the compressor wheel; $F_{4,C}$ the pressure force at the back face. Similarly, the acting forces at the turbine wheel (right) are $F_{1,T}$, $F_{2,T}$, $F_{3,T}$, and $F_{4,T}$.

The pressure force $F_{1,C}$ is calculated according to Eq. (6.17).

$$F_{1,C} = A_1 p_1 = \frac{\pi D_1^2}{4} p_1 \tag{6.20}$$

where
$D_1$ is the inlet diameter of the compressor;
$p_1$ is the inlet pressure of the ambient air.

The pressure force $F_{2,C}$ is resulted by using the mean pressure $p_m$ of the inlet and outlet pressures of the compressor wheel.

$$F_{2,C} = A_S p_m = A_S \left( \frac{p_1 + p_{2*}}{2} \right) \tag{6.21}$$

where
$A_S$ is the projected area in the direction x of the shroud surface;
$p_1$ is the inlet pressure at the compressor wheel;
$p_{2*}$ is the outlet pressure at the compressor wheel.

The impulse force $F_{3,C}$ is resulted from Eq. (6.18) by using the ideal gas equation.

$$F_{3,C} = \dot{m}_C c_{m,1} = \dot{m}_C \left( \frac{\dot{m}_C}{\rho_1 A_{in}} \right) = \frac{\dot{m}_C^2 R_a T_1}{p_1 A_{in}} \tag{6.22}$$

where

$\dot{m}_C$ is the air mass flow rate through the compressor wheel;
$c_{m,1}$ is the meridional component of air velocity at the compressor inlet;
$R_a$ is the gas constant of air;
$T_1$ is the inlet temperature of air;
$p_1$ is the inlet pressure of air;
$A_{in}$ is the cross-sectional area at the inlet of the compressor wheel.

The air pressure at the back face of the compressor wheel is nearly unchanged when the gap between the bearing housing and the back face of the compressor wheel is as large as about 1 mm according to the CFD results. Hence, the pressure force $F_{4,C}$ at the back face is computed with a constant pressure $p_{2*}$ like Eq. (6.17).

$$F_{4,C} = A_{bf,C} p_{2*} \tag{6.23}$$

where
$A_{bf,C}$ is the acting pressure surface of the back face of the compressor wheel;
$p_{2*}$ is the outlet pressure at the compressor wheel.

The resulting force on the compressor wheel (CW) is computed from Eqs (6.20) to (6.23).

$$F_{CW} = F_{1,C} + F_{2,C} + F_{3,C} - F_{4,C} \tag{6.24}$$

Analogous to Eq. (6.24) one obtains the resulting on the turbine wheel (TW).

$$F_{TW} = -F_{1,T} - F_{2,T} - F_{3,T} + F_{4,T} \tag{6.25}$$

Therefore, the axial thrust acting upon the rotor becomes

$$F_{T,ax} = F_{CW} + F_{TW} \tag{6.26}$$

Normally, the acting force on the compressor wheel is higher than the one on the turbine wheel because the compressor wheel diameter is generally larger than the turbine wheel diameter. As a reason, the resulting axial thrust is normally acting in the direction to the compressor wheel; it defines the negative axial thrust with the direction from the turbine to compressor wheel ($F_{T,ax} < 0$). At the compressor surge, the axial thrust takes turns changing its direction from the turbine to compressor wheel ($F_{T,ax} < 0$) and vice versa ($F_{T,ax} > 0$) with a very high frequency, as displayed in Fig. 6.9.

The inlet and outlet pressures, temperatures, and mass flow rates of the compressor and turbine are computed by the turbocharged engine processing. However, the pressure $p_{2*}$ at the outlet of the compressor wheel in front of the diffuser, and $p_{3*}$ at the inlet of the turbine wheel after the variable turbine geometry (VTG)

have been unknown. It is very difficult to determine them by means of measurement. Therefore, they are estimated by using the reaction degrees of the compressor and turbine.

The reaction degree $r_C$ of the compressor is defined as the ratio of the enthalpy increase in the compressor wheel to the enthalpy increase of the compressor stage.

$$r_C = \frac{\Delta h_C}{\Delta h_{St}} = \frac{1 - \left(\dfrac{p_{2*}}{p_1}\right)^{\frac{\kappa_a - 1}{\kappa_a}}}{1 - \left(\dfrac{p_2}{p_1}\right)^{\frac{\kappa_a - 1}{\kappa_a}}} \tag{6.27}$$

where $\kappa_a$ is the isentropic exponent of the charge air.

Having solved Eq. (6.27), the pressure $p_{2*}$ is given.

$$p_{2*} = p_1 \left[ 1 + r_C \left( \left(\frac{p_2}{p_1}\right)^{\frac{\kappa_a - 1}{\kappa_a}} - 1 \right) \right]^{\frac{\kappa_a}{\kappa_a - 1}} \tag{6.28}$$

where the reaction degree $r_C$ of the compressor is normally between about 55% and 60% for all working conditions.

Analogously, the reaction degree $r_T$ of the turbine is defined as the ratio of the enthalpy decrease in the turbine wheel to the enthalpy increase of the turbine stage.

$$r_T = \frac{\Delta h_T}{\Delta h_{St}} = \frac{1 - \left(\dfrac{p_4}{p_{3*}}\right)^{\frac{\kappa_g - 1}{\kappa_g}}}{1 - \left(\dfrac{p_4}{p_3}\right)^{\frac{\kappa_g - 1}{\kappa_g}}} \tag{6.29}$$

where
$\kappa_g$ is the isentropic exponent of exhaust gas.

The pressure $p_{3*}$ is resulted from Eq. (6.29) in

$$p_{3*} = p_4 \left[ 1 + r_T \left( \left(\frac{p_3}{p_4}\right)^{-\left(\frac{\kappa_g - 1}{\kappa_g}\right)} - 1 \right) \right]^{\frac{-\kappa_g}{\kappa_g - 1}} \tag{6.30}$$

where the reaction degree $r_T$ of the turbine is varied from about 20% to 90% depending on the position of the variable turbine geometry (VTG); nearly 50% at wastegated turbochargers for all positions of the waste gate. The reaction degrees

of the compressor and turbine are the key factor to compute the axial thrust. They should be determined by measurement at the similar type of the designed turbocharger in order to choose an appropriate reaction degree at the first design.

The axial thrust acting upon the rotor has been computed by the program CAF (Computing Axial Force) for turbochargers in [10] for turbochargers. The results of the axial thrust versus rotor speed are demonstrated in Fig. 6.10.
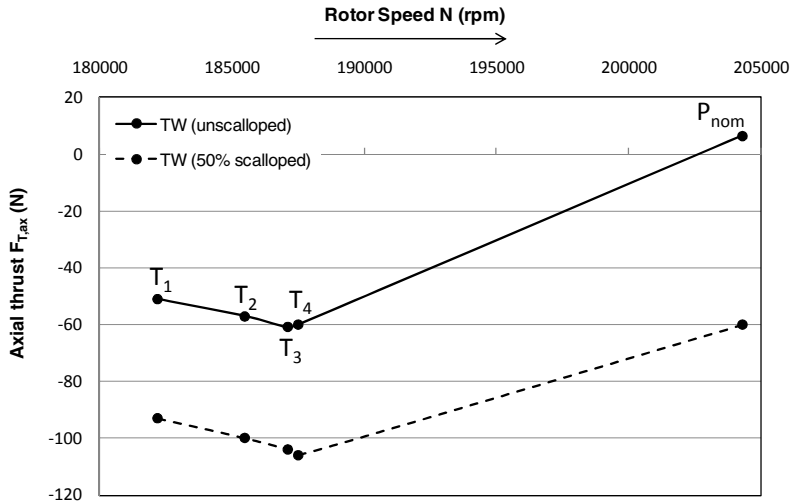


Fig. 6.10 Computed axial thrusts vs. rotor speed of a small turbocharger

Figure 6.10 shows the characteristic of the axial thrust over the rotor speeds in a small turbocharger with an unscalloped and a 50%-scalloped turbine wheel (TW). In case of the unscalloped turbine wheel, the negative axial thrust is nearly 50N in the low-end torque $T_1$ at a rotor speed of 182,000 rpm; its negative thrust direction is acting to the compressor wheel. At increasing the rotor speed to approximately 188,000 rpm, the turbocharger provides various engine torques $T_2$, $T_3$, and $T_4$ in the full load curve, in which the corresponding axial thrusts increase from 50 N to 60 N in the negative thrust direction. After that, the negative axial thrust reduces at $T_4$ from 60 N to the positive axial thrust of nearly 10 N at the nominal power $P_{nom}$. Shortly before reaching the nominal power, the negative thrust turns to the positive direction because the acting force on the turbine wheel becomes larger than the acting force on the compressor wheel; hence, the axial thrust direction changes from the compressor to the turbine wheel (s. Fig. 6.9).

To improve the response behavior of the turbocharger, the turbine wheel is scalloped by 50%; i.e., the possibly scalloped area of the back face reduces by 50%. Therefore, the axial thrust $F_{TW}$ on the turbine wheel is strongly reduced while the axial thrust $F_{CW}$ on the compressor wheel remains unchanged. As a reason, the resulting axial thrust $F_{T,ax}$ increases at $T_1$ from 50 N to 90 N; at $T_4$ from 60 N to about 105 N; at $P_{nom}$ from 10 N to 60 N in the negative thrust direction. In

this case, only negative axial thrust ($F_{T,ax} < 0$) acts on the rotor in the negative thrust direction from the turbine to compressor wheel, as indicated in Fig. 6.10.

### 6.4.3  Design of Thrust Bearings

Before designing the geometry of thrust bearings for the automotive turbochargers, one has to decide which concept should be applied. Either each thrust bearing for the tailored turbocharger of each application or one thrust bearing for all turbochargers used in various applications. The former offers customers an optimal performance in terms of bearing loads and friction as well because the bearing is tailored for this individual application. However, it is not economical for the turbocharger producers to make each thrust bearing for each individual application. On the contrary, the latter concept is very economical for the turbocharger producers, but the bearing friction is huge at most applications because the over-dimensioned bearing has to be designed at the maximum thrust load of the largest turbocharger in the platform. To make compromise between both extremes, at least two types of thrust bearings are normally designed for each platform of the turbochargers; the platform is based on the diameter of the rotor shaft. Each platform contains many combinations of various sizes of the compressor and turbine wheels for different nominal powers of the engines.

In case of only one type of thrust bearings is designed for the platform, the bearing friction is quite large at small turbochargers in the platform because the thrust load is based on the largest turbocharger. Therefore, it is recommended that at least two types of thrust bearings should be used in each platform: the small one is applied to the range of the smallest to the middle turbocharger, and the large one for the middle to the largest turbocharger. For an application range in a platform, the maximum thrust load is determined at the combination of the largest compressor wheel and the smallest turbine wheel at the maximum pressure ratio of the compressor; it has been computed in Section 6.4.2 with a safety factor. If the safety factor is chosen too high, the thrust bearing is overdesigned and therefore quite robust against the bearing wear. However, the bearing friction increases; the response behavior of the turbocharger is worse. In case of a small safety factor, the bearing friction reduces, and the response behavior of the turbocharger is improved. However, the bearing could be worn or damaged at some working conditions in the mixed or boundary lubrication region; in turn, the bearing friction increases significantly. As a reason, one should think twice at deciding how large the safety factor should be selected.

Figure 6.7 shows the typical geometry of a thrust bearing that is derived by experience. At a given thrust load, the minimum oil-film thickness of the thrust bearing geometry is computed at the various working conditions, such as the highest oil inlet temperature, corresponding to rotor speeds by using the program TBD [11] based on DIN 31653 [1], so that it satisfies the limit oil-film thickness to avoid the mixed lubrication region. Figure 6.11 gives the required minimum oil-film thickness that is based on the combined conjunction mean roughness depth of the bearing and thrust ring surfaces surrounded by the oil film (s. Table 6.2).

**Table 6.2** Conjunction mean roughness depths of the various finishing surfaces

| Conjunct. roughness $R_z$ (μm) | Finishing methods | Limit oil-film thickness $h_{lim}$ (μm) |
|---|---|---|
| 0.8 – 1.6 | grind, lap, honing, polishing | depends on Rz and the bearing segment mean diameter Dm, as given in Fig. 6.11. |
| 1.6 – 4.0 | grind and lap, honing | |
| 4.0 – 8.0 | grind and lap | |
| 8.0 – 18.0 | grind, precision mill, and fine turning | |

The conjunction mean roughness depth combined the surfaces of the bearing and thrust ring is defined as

$$R_z = \sqrt{R_{z,bearing}^2 + R_{z,disk}^2} \tag{6.31}$$

According to DIN 31653 [1], the limit oil-film thickness $h_{lim}$ that depends on the surface roughness $R_z$ and segment mean diameter $D_m$, is empirically determined.

$$h_{min} \geq h_{lim} = 1.25 \sqrt{\frac{D_m R_z}{3.10^3}} \tag{6.32}$$

where
$D_m$ is the mean diameter of the bearing segment in meter;
$R_z$ is the combined conjunction mean roughness depth in meter.

To prevent the working condition of the thrust bearing from the mixed lubrication region, the oil-film thickness should be larger than the limit film thickness, as displayed in Fig. 6.11; otherwise, the thrust bearing works in the mixed or boundary lubrication regions. In this case, the bearing pressure surface has to be enlarged, so that the minimum oil-film thickness $h_{min}$ fulfills the requirement given in Eq. (6.32) for all operational conditions.

In the following section, the minimum oil-film thickness, oil volumetric flow rate, friction power of the bearing, and effective oil temperature inside the thrust bearing are computed at the various rotor speeds, oil inlet temperatures, and as well as oil types for an application of the automotive turbochargers by the program TBD [11].

The dimensionless load number in the hydrodynamic lubrication region is defined as

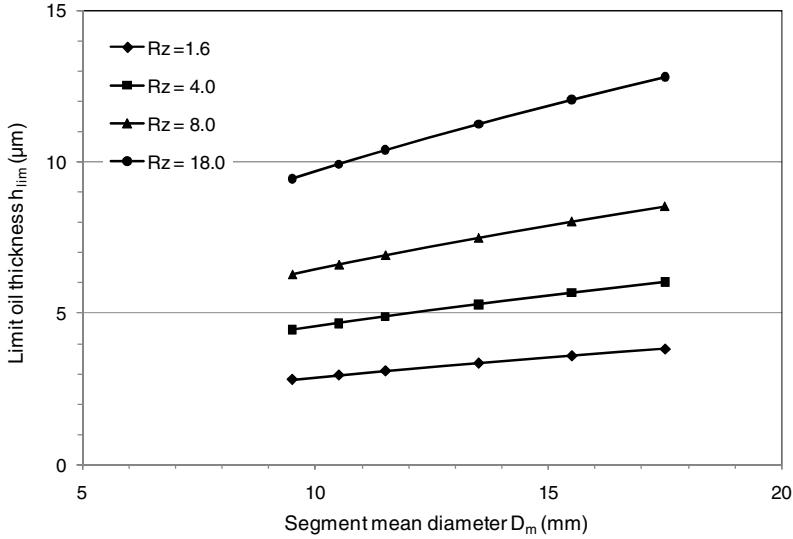$$F^* \equiv \frac{F\left(\dfrac{h_{min}}{L}\right)}{F_f} \tag{6.33}$$

where
F is the bearing load;
$F_f$ is the friction force in the bearing;
$h_{min}$ is the minimum oil-film thickness;
L is the bearing segment (pad) length (s. Fig. 6.7).



**Fig. 6.11** Limit oil-film thickness vs. segment mean diameter $D_m$ and $R_z$

The friction force is resulted from the bearing theoretical friction power $P_{f,th}$.

$$F_f \equiv \frac{P_{f,th}}{U} = \eta_{eff} \frac{U}{h_{min}} LWZ \qquad (6.34)$$

where
$\eta_{eff}$ is the effective oil dynamic viscosity;
U is the circumferential velocity at the mean diameter of bearing;
W is the width of bearing (s. Fig. 6.7);
Z is the number of bearing segments.

The dimensionless load number $F_B^*$ for a thrust bearing is resulted from $F^*$

$$F_B^* \equiv F^* \left( \frac{c_{wed}}{h_{min}} \right)^2 = \frac{F c_{wed}^2}{\eta_{eff} U L^2 WZ} = F_B^* \left\langle \frac{h_{min}}{c_{wed}}, \frac{W}{L} \right\rangle \qquad (6.35)$$

where

$c_{wed}$ is the wedge height, as shown in Fig. 6.6.

The dimensionless load number $F_B{}^*$ is a function of $h_{min}/c_{wed}$ and W/L given in Eq. (6.35) that is computed by solving the Reynolds lubrication equation [1]. At the given bearing geometry and boundary conditions, such as the axial bearing load F, bearing mean velocity U, the minimum oil-film thickness $h_{min}$ is calculated from $F_B{}^*$ at the initial oil viscosity with the guessed effective oil temperature $T_{eff}$. The effective oil temperature is computed by the iterative method based on the balance of heat flows in the thrust bearing. The effective oil temperature is converged when the absolute relative change of the oil temperature is smaller than the given convergence value of $10^{-6}$.

Similar to Eqs (6.33) and (6.35), the dimensionless friction number of the thrust bearing is the basics of computing the effective oil temperature at each iteration step.

$$f_B^* \equiv f^* \left( \frac{c_{wed}}{h_{min}} \right) = \frac{P_f}{P_{f,th}} \left( \frac{c_{wed}}{h_{min}} \right)$$

$$= \frac{P_f c_{wed}}{\eta_{eff} U^2 LWZ} = f_B^* \left\langle c_{wed}, l_{wed}, L, W, h_{min} \right\rangle \tag{6.36}$$

where

$P_f$ is the real bearing friction power derived from Eq. (6.36).

$$P_f = \frac{f_B^* \eta_{eff} U^2 LWZ}{c_{wed}} \tag{6.37}$$

The dimensionless friction number $f_B{}^*$ depends on the bearing geometries and oil film thickness and is resulted by solving the Reynolds lubrication equation [1]. Hence, the real bearing friction power $P_f$ is determined at the effective oil viscosity relating to the iterated oil temperature $T_{eff}$ in the bearing at each iteration step. The oil volumetric flow rates and oil temperature distribution in the bearing are displayed in Figure 6.12.

Due to the bearing friction, the oil temperature in the bearing increases by a temperature difference

$$\Delta T_2 \equiv (T_2 - T_1) = \frac{P_f}{\rho c_p \left( Q_2 + \dfrac{Q_3}{2} \right)} = \frac{P_f}{\rho c_p \left( Q_1 - \dfrac{Q_3}{2} \right)} \tag{6.38}$$

The volumetric in- and outflow rates of $Q_1$ and $Q_3$ are calculated by the Reynolds equation depending on the bearing geometries, rotor velocity, and iterated effective oil viscosity; therefore, the temperature increase $\Delta T_2$ in the bearing is computed at every iteration step according to Eq. (6.38).

To remove the friction power induced in the bearing, fresh oil with a volumetric flow rate Q with the inlet temperature $T_{in}$ is partly mixed with the oil outflow rate $Q_3$ from the bearing segment.

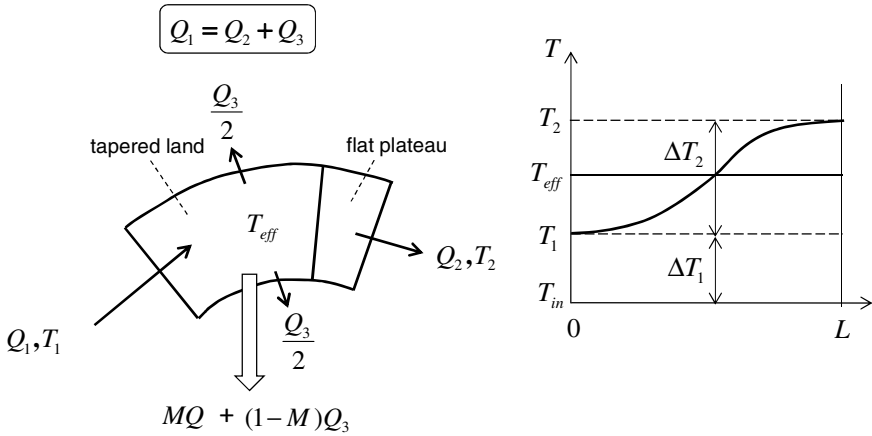$$\rho c_p \left(MQ + (1-M)Q_3\right)\Delta T_1 = \rho c_p Q_2 \Delta T_2 \tag{6.39}$$

where
M is the mixing factor ($0 \le M \le 1$) of the fresh oil (common value 0.5);
$\Delta T_1 = T_1 - T_{in}$, the temperature increase after the oil mixing;
$\Delta T_2 = T_2 - T_1$, the temperature increase in the bearing segments;
$\rho$ is the oil density;
$c_p$ is the heat capacity at constant pressure.



**Fig. 6.12** Volumetric flow rates and oil temperatures in a thrust bearing

The temperature increase of the fresh oil due to mixing with the high-temperature outflow oil from the bearing segment results from Eq. (6.39) in

$$\Delta T_1 \equiv (T_1 - T_{in}) = \frac{Q_2 \Delta T_2}{MQ + (1-M)Q_3} \tag{6.40}$$

The required fresh oil flow rate Q is calculated from the bearing friction power.

$$Q = \frac{P_f}{\rho c_p (T_{out} - T_{in})} \tag{6.41}$$

The effective oil temperature is defined as the average temperature of $T_1$ and $T_2$.

$$T_{eff} \equiv \frac{T_1 + T_2}{2} = T_{in} + \Delta T_1 + \frac{\Delta T_2}{2} \tag{6.42}$$

The effective bearing temperature in Eq. (6.42) has to be iterated so long that the convergence criterion is reached.

$$\frac{\left| T_{eff}^{i} - T_{eff}^{i-1} \right|}{T_{eff}^{i-1}} \leq \varepsilon \qquad (6.43)$$

where

$T_{eff}^{i}$ is the effective temperature at iteration step i;

$T_{eff}^{i-1}$ is the effective temperature at iteration step (i-1);

$\varepsilon$ is the convergence radius (common value $10^{-6}$).

One computes the effective oil dynamic viscosity $\eta_{eff}$ by using the Cameron and Vogel equation at the effective temperature $T_{eff}^{i}$ at the iteration step i.

$$\eta_{eff}^{i} = a \exp\left( \frac{b}{T_{eff}^{i} - c} \right) \qquad (6.44)$$

where

a, b, and c are the coefficients determined by three reference points $(\eta_1, T_1)$, $(\eta_2, T_2)$, and $(\eta_3, T_3)$ of the oil type.

By solving the equation system at the reference points, one obtains the coefficients a, b, and c as follows:

$$c = \frac{\beta T_3 - T_2}{\beta - 1} \qquad (6.44a)$$

within

$$\beta = \frac{\left( \dfrac{T_1 - T_2}{T_1 - T_3} \right) \ln\left( \dfrac{\eta_3}{\eta_1} \right)}{\ln\left( \dfrac{\eta_2}{\eta_1} \right)}$$

$$b = \frac{(T_1 - c)(T_2 - c) \ln\left( \dfrac{\eta_2}{\eta_1} \right)}{(T_1 - T_2)} \qquad (6.44b)$$

$$a = \frac{\eta_1}{\exp\left( \dfrac{b}{T_1 - c} \right)} \qquad (6.44c)$$

where
a is in N.s/m² (Pa.s);
b, c, and T are in Kelvin (K);
β is dimensionless.

The computed dynamic viscosity η of SAE 5W30 oil versus oil temperature T is
displayed in Fig. 6.13. The effective oil temperature in the bearing generally lies
between 30°C and 50°C above the inlet temperature. The temperature increase
caused by the bearing friction depends on many parameters, such as the bearing
geometries, oil inlet temperature, rotor speed, minimum oil-film thickness. In any
cases the effective oil temperature should not exceed the oil coking temperature of
about 210°C for SAE 5W30 oil. When it exceeds the coking temperature, oil will
be burnt (coked) in the bearing. To avoid coked oil in the bearing, the geometry of
the bearing segment must be optimized, so that the effective oil temperature de-
creases below the oil coking temperature.

   The thrust bearing with many segments (pads) is mostly made of brass, a yel-
lowish alloy of copper and zinc including small amounts of manganese and alumi-
num (CuZnX-MnAl; X is the percentage of zinc). The bearing material of brass
has not only an excellent tribological characteristics but also high thermal conduc-
tivity that reduces wear and removes the heat flow caused by the bearing friction.
Therefore, it decreases the effective oil temperature and increases the oil-film
thickness (s. Fig. 6.14).



Oil ISO VG 100 (SAE 30)

$$\eta(T) = a\,\mathbf{exp}\left(\frac{b}{T(K)-c}\right)$$
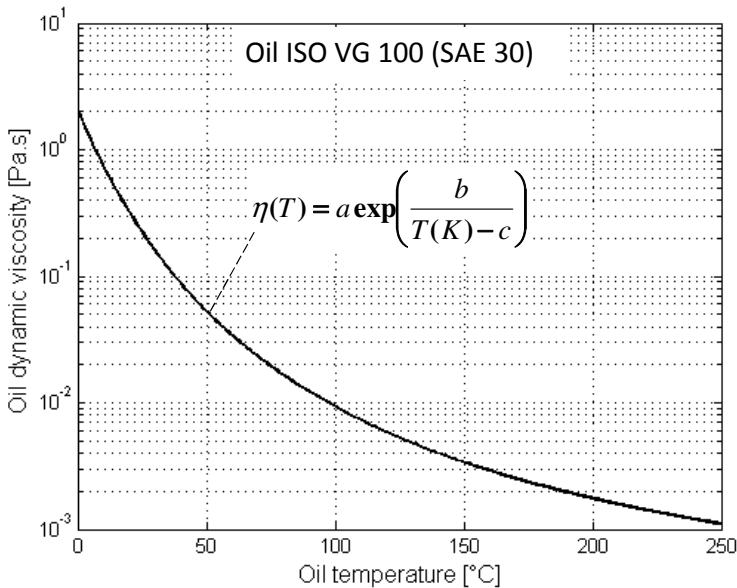
**Fig. 6.13** Computed oil dynamic viscosity versus temperature
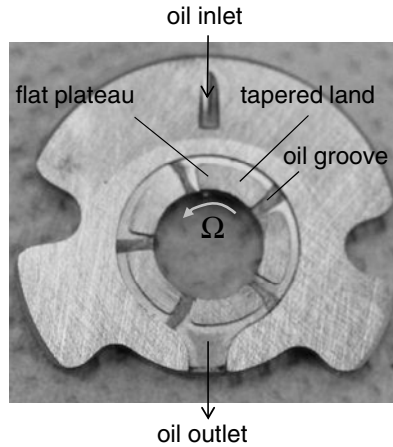
**Fig. 6.14** Thrust bearing with five segments (Courtesy BMTS)

Figure 6.15 displays the computed axial load versus the minimum oil-film thickness at various oil inlet temperatures. The minimum oil-film thickness in the thrust bearing is found at the axial thrust of 70 N with the rotor speed of 190,000 rpm and the oil inlet temperatures from 50°C, 90°C, 120°C, and 150°C. Obviously, the oil-film thickness decreases with the axial load and oil inlet temperature. The bearing geometry must be designed at the worst case with the maximum oil inlet temperature of 150°C and largest thrust load in the turbocharger. The resulting oil-film thickness for this case is about 5 µm (case d) that satisfies the limit oil-film thickness with the conjunction surface roughness $R_z$ between 1.6 µm and 4 µm, as given in Fig. 6.11 according to DIN 31653 [1].

Notice that the limit oil thickness is only a recommended value that should be validated by experiments for each application. It is very difficult to predict at which oil-film thickness the mixed lubrication occurs in the bearing. In practice, the contaminants in oil cause more wear in form of deep cuts or scratches than wear in the mixed lubrication (s. Chapter 9). By reducing the oil inlet temperature from 150°C to 120°C, 90°C, and 50°C, the oil-film thickness increases from 5 µm to approximately 6.5 µm, 8.5 µm, and 14 µm, as displayed in Fig. 6.15 in cases c, b, and a.

The computed bearing friction power versus the oil inlet temperature at the thrust load of 70 N and rotor speed of 190,000 rpm is shown in Fig. 6.16. By reducing the oil inlet temperature, the minimum oil-film thickness increases; hence, the velocity gradient $U/h_{min}$ of the oil film reduces. At the same time, the effective oil viscosity at low temperatures increases faster than the velocity-gradient drop; therefore, the bearing friction power increases at reducing the oil inlet temperatures. However, the bearing friction power decreases as the oil inlet temperature increases up to about 135°C, then the friction power increases a little bit as the oil inlet temperature further increases to 150°C. The reason for this increase could be that the velocity gradient of the oil film is higher than the decrease of the oil viscosity in the high temperature due to strongly reducing the oil-film thickness.
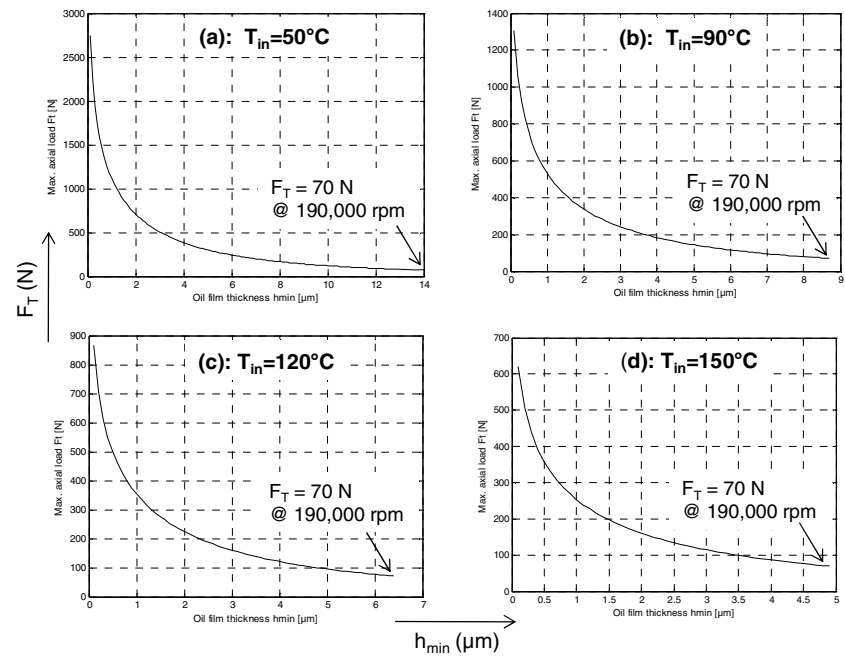
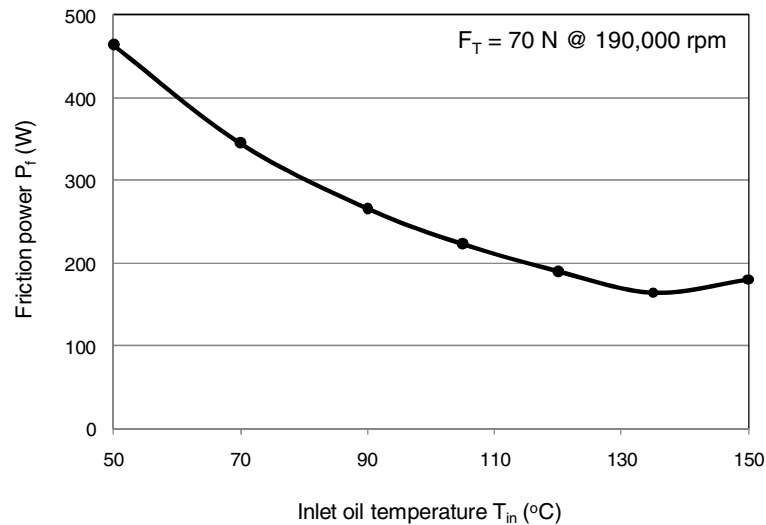Fig. 6.15 Thrust loads versus oil-film thickness at different $T_{in}$



Fig. 6.16 Computed thrust bearing friction power versus oil inlet temperature

### 6.4.4  Influential Parameters of Thrust Bearings

To optimize the bearing design in terms of bearing friction, effective temperature in the bearing, and maximum bearing load, some influential parameters should be considered. They are the ratios $W/L$, $l_{wed}/L$, $c_{wed}/l_{wed}$, and $D_m$, as displayed in Fig. 6.17.

- **Ratio W/L**

The ratio of the segment width to its length of the bearing should be between 0.5 and 2. On the one hand, at a long bearing segment with the length L much larger than its width W ($W/L \ll 1$) the effective oil film is overheated and the bearing temperature increases due to the long wedge; therefore, the oil viscosity reduces; in turn, the oil-film thickness decreases, so that the mixed lubrication takes place. On the other hand, at the narrow bearing segment with $W/L \gg 1$ the oil-film pressure does not have enough time to build up because of the short wedge; hence, the oil-film thickness is reduced. Moreover, the side oil outflow $Q_3$ in the radial direction is smaller due to large flow resistance. It induces an increase of the effective oil temperature in the bearing segment, and in turn the reduction of the oil-film thickness. In order to compromise of both extremes of $W/L$, and to optimize the bearing friction the square bearing segment ($W/L = 1$) shows an optimum for the oil-film thickness and maximum thrust load by experience.

Therefore, the optimum value for the segment ratio $W/L$ equals one at the square bearing segment ($W = L$). However, it is very difficult in practice to design a thrust bearing with square segments that fulfills many predetermined parameters, such as the given bearing outer diameter, given bearing pressure surface, an acceptable number of segments for a small mean diameter, mass-producing tolerance. In fact, the ratio of $W/L$ between 0.75 and 1 is normally used for a well-designed thrust bearing of the turbochargers.
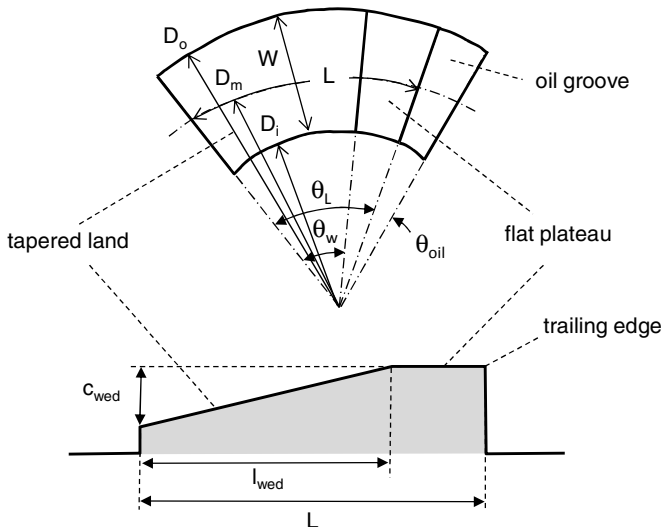


**Fig. 6.17** Geometrical parameters of a thrust bearing

- **Ratio $l_{wed}$/L**

The ratio should vary between 0.7 and 0.8 where the optimum value is at 0.75 for the maximum bearing load capacity. If the wedge length $l_{wed}$ is so small that the oil-film pressure does not build up enough to balance the thrust load because the hydrodynamic wedge effect is too small. In consequence, the oil-film thickness reduces, the bearing friction increases, the effective oil temperature becomes higher, leading to the bearing wear and possibly to the seizure of the bearing and thrust rings. In the other case, at $l_{wed} \gg L$ the oil-film pressure increases due to large wedge effect; hence, the oil thickness becomes larger and in turn more oil flow rate is required. However, the maximum induced pressure begins dropping in front of the trailing edge sooner than in the normal case at the ratio of 0.75 due to the very small flat plateau. The early pressure drop is not optimal for the load capacity of the bearing. In order to optimize the load capacity, oil flow rate, oil-film thickness, and friction power of the bearing, the ratio $l_{wed}$/L should be chosen nearly 0.75 for the bearing segments.

• **Ratio $c_{wed}$/$l_{wed}$**

This ratio indicates the slope of bearing wedge. At a small slope, the oil-film pressure is not increased strongly; therefore, the oil-film thickness decreases, and the effective oil temperature in the bearing segment becomes higher. On the contrary, the oil pressure increases faster due to the large wedge effect. As a reason, the oil-film thickness increases, but much more oil flow rate is necessary.

At small thrust bearings, the bearing slope $c_{wed}$/$l_{wed}$ varies from 1:75 to 1:150; at large thrust bearings, flatter bearing slopes from 1:200 to 1:400 are usually applied to designing thrust bearings. The reason of using the flatter bearing slopes is to avoid a large pressing force required by producing thrust bearings. On the contrary, steep bearing slopes can be used at small thrust bearings at which the pressing force is still small.

• **Mean diameter $D_m$**

The bearing friction power is proportional to the mean velocity squared at the mean diameter of the bearing segment, as shown in Eq. (6.37).

$$P_f \propto \frac{\eta_{eff} U^2 LWZ}{c_{wed}} \qquad (6.45)$$

with the mean velocity at the mean diameter $D_m$

$$U = \Omega \frac{D_m}{2} = \pi N D_m \qquad (6.46)$$

where N is the rotor speed in rps.

In order to reduce the bearing friction, the segment mean diameter should be as small as possible, but one has to check whether

- the minimum oil-film thickness is less than the limit oil-film thickness;
- the effective oil temperature in the bearing is higher than the oil coking temperature;

- the maximum induced oil pressure in the bearing is higher than the ultimate tensile stress of the bearing material, leading to the plastic deformation in the bearing.

The influential parameters of thrust bearings are summarized in Table 6.3.

**Table 6.3** Influential parameters of thrust bearings

| Influential parameters | Normal values | Optimum value |
|---|---|---|
| W/L | 0.5 ... 2.0 | 1.0 |
| $l_{wed}/L$ | 0.70 ... 0.80 | 0.75 |
| $c_{wed}/l_{wed}$ | 1:75 ... 1:150 (small bearings) | - |
| | 1:200 ... 1:400 (large bearings) | - |
| $D_m$ | possibly small | - |

## 6.5  Fluid-Film Radial Bearings

Some points of view on designing radial bearings for turbochargers are taken into account, as shown in Fig. 6.18. First, the main function of the radial bearings is to keep the rotor stable (rotordynamic stability) at all operating conditions of the turbocharger. Second, the rotor must be well balanced with high-speed balancing, so that the residual unbalance is small enough to reduce the unbalance force acting on the bearing and unbalance whistle. Additionally, radial bearings must have enough damping effect to keep the rotor stable and to suppress noises induced by the unbalance excitation (unbalance whistle) and inner oil whirl (constant tone). The latter can be reduced by a suitable geometry of the bearing and bearing clearances. Third, the bearing friction should be reduced as much as possible to improve the transient response of the turbocharger or to reduce $CO_2$ and $NO_x$ emission, especially in low-end torque. Fourth, radial bearings should work in a long lifetime with minimum or without wear. Fifth, they should be produced at an economical producing cost with the best quality and functionality for a long lifetime.

However, there is no patent remedy on how to 100% fulfill all five challenging targets perfectly. Therefore, the best solution is compromising of them and setting priority of the targets. One has to take the compromise between the need to satisfy the customer wishes and the need to gain profit. However, the customers would accept to pay a little bit more for innovative products that the competitors have not yet brought in the market. Note that the early bird catches the worm but just for a short time because the enemies never sleep. Therefore, do not enjoy yourself too long after the winning; instead, go back to hard work as soon as possible for the next battle.
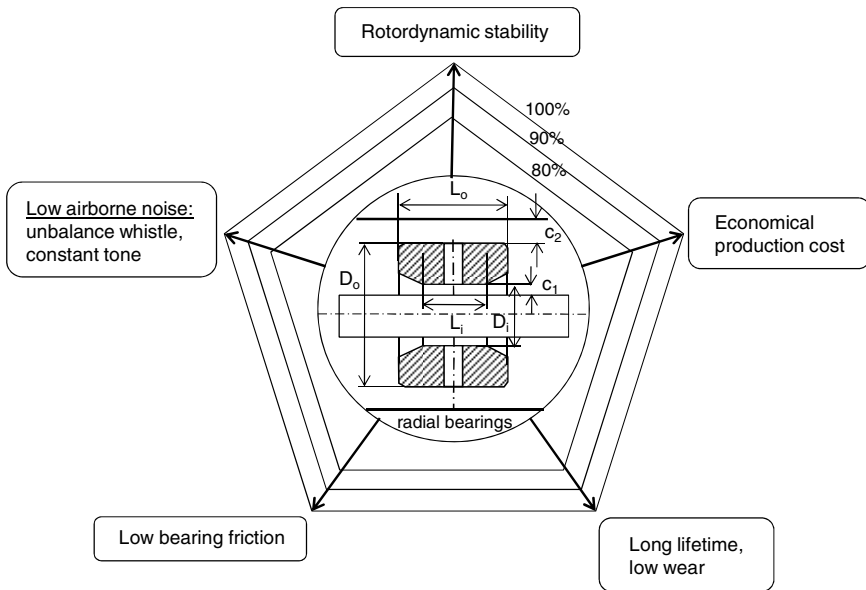
**Fig. 6.18** Strategy to design radial bearings for turbochargers

In the technical point of view the producing tolerance for the nominal diametral bearing clearance of 20 µm is normally ±6 µm due to saving producing costs. It is resulted from tolerances of the diameters of the bearing and journal. Bearing clearances with large tolerances mostly cause rotor instabilities at high rotor speeds and bearing wear. When the diametral bearing clearance is the minimum of 14 µm, the bearing friction becomes larger; the oil temperature in the bearing increases (coked oil); the oil-film thickness reduces (mixed or boundary lubrication); therefore, wear and seizure could occur in the bearing. On the contrary, when the bearing clearance is the maximum of 26 µm, the bearing stiffness and damping coefficients reduce; the rotor instability takes place at some working conditions (oil whirl or oil whip). Such rotor instabilities cause wear and damage of the rotor and bearings. That is just only one of many technical difficulties at the bearing design, and the goal is always to keep the producing cost as low as possible; hence, the profit as high as possible. In order to save costs of development, testing, and production, only one type of radial bearings is used in each platform to that different compressor and turbine wheels belong. Hence, we have to design one type of radial bearings for different rotors that consist of different diameters of the compressor and turbine wheels operating on various conditions. All of these are a big challenge for the rotordynamic engineers who have to cope with the bearing design in the industry of turbochargers.

### 6.5.1 Theory of Fluid Film Bearings

The working principle of the radial bearings, as shown in Fig. 6.19 is based on the hydrodynamic effect described by the Reynolds lubrication equation. The pressure

of the oil film is induced by the wedge contour between the bearing and journal whose velocities are $U_b$ and $U_j$, respectively.

Lubricating oil is squeezed in the converged wedge by the rotation of the journal and bearing. Therefore, the oil pressure increases and reaches the maximum pressure in the wedge in front of $\theta = \pi$, as displayed in Fig. 6.20. At the minimum oil-film thickness ($\theta = \pi$), the oil velocity arrives at the maximum, and the lowest pressure occurs shortly behind the minimum bearing gap $h_{min}$ at the high rotor speeds. Due to the pressure drop, air releasing and cavitation could take place there, and the gas bubbles continue moving in the diverged bearing wedge ($\pi < \theta \leq 2\pi$). The induced pressure of the oil film in the converged wedge generates the bearing forces acting upon the journal to keep the rotor stable in the radial direction.
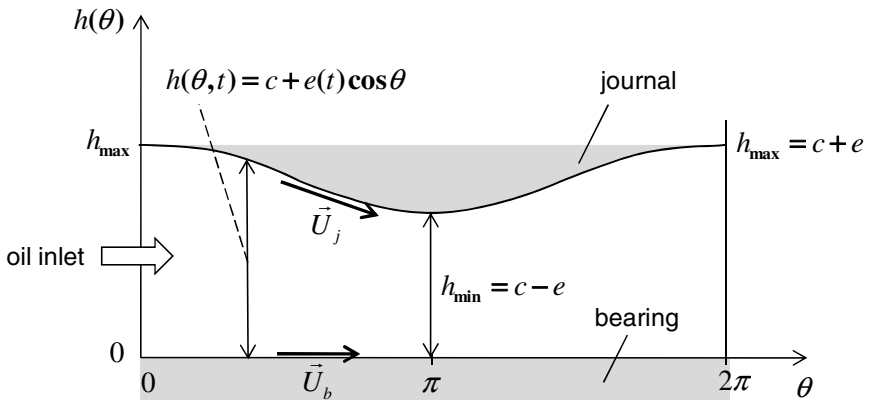


**Fig. 6.19** Working principle of the radial bearing

The Reynolds lubrication equation for radial bearings is derived from Eq. (6.3a) and rewritten as

$$\frac{\partial}{\partial x}\left(h^3 \frac{\partial p}{\partial x}\right) + \frac{\partial}{\partial z}\left(h^3 \frac{\partial p}{\partial z}\right) = 6\eta\left[\left(U_j + U_b\right)\frac{\partial h}{\partial x} + 2\frac{\partial h}{\partial t}\right] \qquad (6.47)$$

where
$U_j$ is the journal velocity;
$U_b$ is the bearing ring velocity;
$h$ is the oil-film thickness.
$x$ is the circumferential direction ($x = R\theta$);
$z$ is the axial direction.

At the non-rotating floating ring bearings, the bearing velocity $U_b$ equals zero, and the Reynolds lubrication equation is the same equation for thrust bearings, as shown in Eq. (6.15) where U is the journal velocity instead of the velocity of the thrust ring.

Figure 6.20 shows the bearing force induced in the wedge, and the pressure distribution in the bearing clearance. To balance the external force $F_J$ acting upon the rotor, the bearing force $F_B$ is resulted at the attitude angle $\alpha$, acting on the journal in the opposite direction of the external force. At the equilibrium position, the minimum oil-film thickness at $\theta = \pi$ is determined by the hydrodynamic Reynolds lubrication equation, as shown in Fig. 6.20.
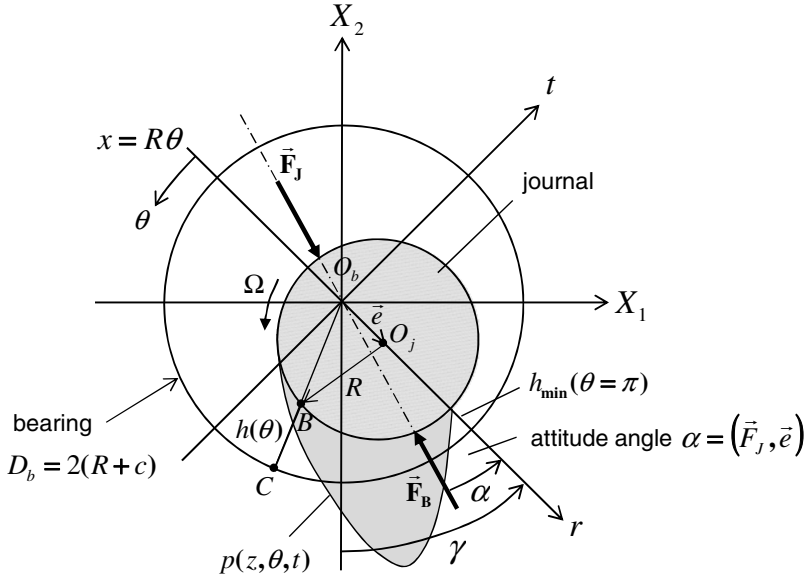


**Fig. 6.20** Bearing force vector $\vec{F}_B$ acting upon the journal

The bearing force $F_B$ is resulted from integrating the pressure distribution over the journal surface in the bearing clearance. The relation between the angular position, journal eccentricity, and bearing clearance allows calculating the oil-film thickness in the bearing, as shown in Fig. 6.21.

After a few calculating steps, one obtains the oil-film thickness in a function of the position angle $\theta$ and time t.

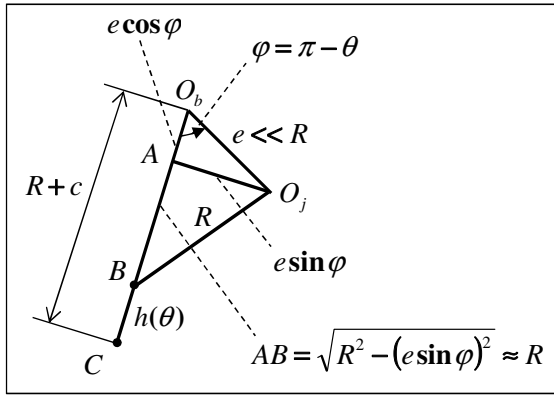$$h(\theta, t) = c - e(t)\cos\varphi = c + e(t)\cos\theta \tag{6.48}$$

where
c is the radial bearing clearance;
e is the journal eccentricity changed with time t ($\varepsilon = e/c$).

According to Eq. (6.48), the maximum and minimum oil-film thicknesses are given at $\theta = 0; 2\pi$ and $\theta = \pi$, respectively.

$$\begin{cases} h_{max} = c + e \quad at \quad \theta = 0; 2\pi \\ h_{min} = c - e \quad at \quad \theta = \pi \end{cases} \tag{6.49}$$

**Fig. 6.21** Geometric relation of the oil-film thickness

Having used the geometric relations given in Figs 6.20 and 6.21,

$$\begin{cases} x = R\theta, \\ h = c + e\cos\theta \rightarrow \partial h/\partial t = \dot{e}\cos\theta = c\dot{\varepsilon}\cos\theta \end{cases}$$

the Reynolds lubrication Equation (6.47) is written in the cylindrical coordinates.

$$\frac{\partial}{\partial\theta}\left((1+\varepsilon\cos\theta)^3\frac{\partial p}{\partial\theta}\right) + R^2\frac{\partial}{\partial z}\left((1+\varepsilon\cos\theta)^3\frac{\partial p}{\partial z}\right)$$

$$= -6\eta\left(\frac{R}{c}\right)^2\left[(\Omega - 2\dot{\gamma})\varepsilon\sin\theta - 2\dot{\varepsilon}\cos\theta\right]$$

(6.50)

where
p is the induced pressure in the oil film;
R is the journal radius (= D/2);
$\Omega$ is the angular velocity of the rotor;
$\dot{\gamma}$ is the whirl velocity;
$\varepsilon$ is the journal relative eccentricity;
$\dot{\varepsilon}$ is the timely change of the journal relative eccentricity;
$\eta$ is the oil dynamic viscosity.

The boundary conditions (BCs) for the Equation (6.50) at the

- inlet:   $p(\theta=0, z) = p(\theta=2\pi, z) = p_i$;                                    (6.50a)

- outlet: $p(\theta, z= +L/2) = p(\theta, z= -L/2) = p_o$                              (6.50b)

where
$p_i$ is the oil inlet pressure;
$p_o$ is the oil outlet pressure;
L is the bearing width.

## 1. Pressure distribution for long bearings (L/D > 1)

In the long bearings, the pressure gradient in the circumferential direction θ is much larger than in the axial direction z; therefore, the second term at the right-hand-side of Eq. (6.50) is omitted. The Reynolds equation becomes obviously

$$\frac{\partial}{\partial\theta}\left((1+\varepsilon\cos\theta)^3\frac{\partial p}{\partial\theta}\right)=-6\eta\left(\frac{R}{c}\right)^2\left[(\Omega-2\dot\gamma)\varepsilon\sin\theta-2\dot\varepsilon\cos\theta\right] \quad (6.51)$$

By solving Eq. (6.51) with the given boundary conditions, one obtains the pressure distribution p(θ) in the bearing [16].

$$p(\theta)=p_i+6\eta\left(\frac{R}{c}\right)^2\left[\begin{array}{c}(\Omega-2\dot\gamma)\dfrac{\varepsilon(2+\varepsilon\cos\theta)\sin\theta}{(2+\varepsilon^2)(1+\varepsilon\cos\theta)^2}\\[2mm]+\dfrac{\dot\varepsilon}{\varepsilon}\left(\dfrac{1}{(1+\varepsilon\cos\theta)^2}+\dfrac{1}{(1+\varepsilon)^2}\right)\end{array}\right] \quad (6.52)$$

The bearing forces of the non-cavitating oil film are resulted by integrating the pressure distribution over the journal surface in the radial and tangential directions [5].

$$\begin{cases}F_r=6\eta\left(\dfrac{R}{c}\right)^2RL\left[\dfrac{2\varepsilon^2(\Omega-2\dot\gamma)}{(2+\varepsilon^2)(1-\varepsilon^2)}+\dfrac{2\dot\varepsilon}{(1-\varepsilon^2)^{3/2}}\left(\dfrac{\pi}{2}-\dfrac{8}{\pi(2+\varepsilon^2)}\right)\right]\\[4mm]F_t=6\eta\left(\dfrac{R}{c}\right)^2RL\left[\dfrac{\pi\varepsilon(\Omega-2\dot\gamma)}{(2+\varepsilon^2)(1-\varepsilon^2)^{1/2}}+\dfrac{4\varepsilon\dot\varepsilon}{(2+\varepsilon^2)(1-\varepsilon^2)^{1/2}}\right]\end{cases} \quad (6.53)$$

## 2. Pressure distribution for short bearings (L/D ≤ 1)

In the short bearings, the pressure gradient in the circumferential direction θ is much smaller than in the axial direction z; therefore, the first term at the right-hand-side of Eq. (6.50) is omitted. The Reynolds equation becomes straightforwardly

$$\frac{\partial}{\partial z}\left((1+\varepsilon\cos\theta)^3\frac{\partial p}{\partial z}\right)=\frac{-6\eta}{c^2}\left[(\Omega-2\dot\gamma)\varepsilon\sin\theta-2\dot\varepsilon\cos\theta\right] \quad (6.54)$$

By solving Eq. (6.54) with the given boundary conditions, one obtains the pressure distribution p(θ, z) on the journal surface [8].

$$p(\theta, z) = p_0 + \frac{3\eta}{c^2(1+\varepsilon\cos\theta)^3}\left((\Omega-2\dot\gamma)\varepsilon\sin\theta - 2\dot\varepsilon\cos\theta\right)\left(\frac{L^2}{4} - z^2\right)$$

$$(6.55)$$

Similarly, the bearing forces of the non-cavitating oil film are resulted by integrating the pressure distribution over the journal surface in the bearing clearance in the radial and tangential directions [14].

$$\begin{cases} F_r = \dfrac{\eta}{2}\left(\dfrac{R}{c}\right)^2 \dfrac{L^3}{R}\left[\dfrac{2\varepsilon^2(\Omega-2\dot\gamma)}{(1-\varepsilon^2)^2} + \dfrac{\pi\dot\varepsilon(1+2\varepsilon^2)}{(1-\varepsilon^2)^{5/2}}\right] \\[4mm] F_t = \dfrac{\eta}{2}\left(\dfrac{R}{c}\right)^2 \dfrac{L^3}{R}\left[\dfrac{\pi\varepsilon(\Omega-2\dot\gamma)}{2(1-\varepsilon^2)^{3/2}} + \dfrac{4\varepsilon\dot\varepsilon}{(1-\varepsilon^2)^2}\right] \end{cases}$$

$$(6.56)$$

The attitude angle $\alpha$ between the external force and journal eccentricity is calculated from the radial and tangential force components of Eq. (6.56).

$$\alpha = \arctan\left|\frac{-F_t}{F_r}\right| = f(\Omega, \varepsilon, \dot\varepsilon, \dot\gamma)$$

$$(6.57)$$

where $\dot\gamma$ is the whirl velocity of the journal ($\dot\gamma \equiv \omega$).

## 6.5.2 Nonlinear Bearing Forces on the Rotor

The bearing forces $F_r$ and $F_t$ are based on the rotating coordinate system (r,t) in the journal. In fact, the bearing forces acting upon the journal in the inertial coordinate system $(X_1, X_2)$ are required for the rotordynamic vibration equations. Therefore, the coordinate transformation from the rotating to inertial coordinate system is necessary to compute the bearing forces in the inertial coordinate system $(X_1, X_2)$.

The nonlinear bearing force is transformed to the inertial coordinate system $(X_1, X_2)$.

$$\vec{F}_B = \begin{pmatrix} F_1 \\ F_2 \end{pmatrix} = \begin{pmatrix} \sin\gamma & \cos\gamma \\ -\cos\gamma & \sin\gamma \end{pmatrix}\begin{pmatrix} F_r \\ F_t \end{pmatrix}$$
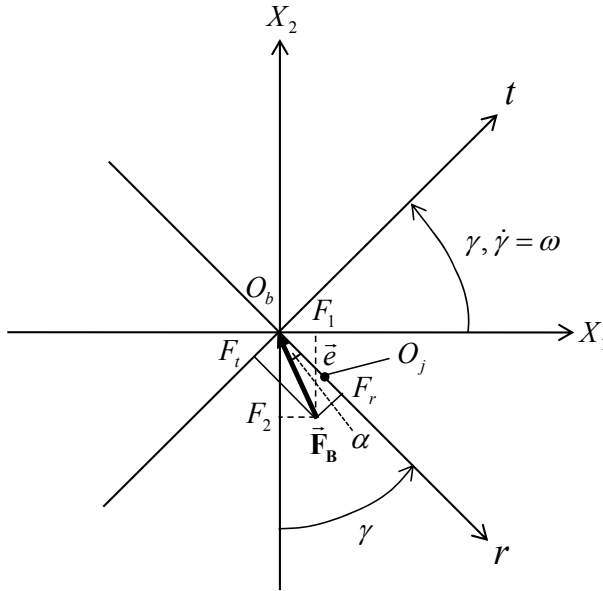
$$(6.58)$$

where
$F_1$, $F_2$ are the force components in the inertial coordinates $X_1$ and $X_2$;
$F_r$, $F_t$ are the force components in the rotating coordinates r and t.

Thus,

$$\begin{cases} F_1 = +F_r\sin\gamma + F_t\cos\gamma \equiv f_1(\varepsilon, \dot\varepsilon, \gamma, \dot\gamma, \Omega) \\ F_2 = -F_r\cos\gamma + F_t\sin\gamma \equiv f_2(\varepsilon, \dot\varepsilon, \gamma, \dot\gamma, \Omega) \end{cases}$$

$$(6.59)$$

where $\gamma$ is the angular position of the journal (s. Fig. 6.22).

**Fig. 6.22** Transformation between the coordinate systems (r, t) and ($X_1$, $X_2$)

For a large displacement $\varepsilon$ and high whirl velocity $\dot{\gamma}$ of the journal, the bearing force depends on $\varepsilon, \dot{\varepsilon}, \gamma, \dot{\gamma},$ and $\Omega$ nonlinearly, as given in Eqs (6.56) and (6.59). They cannot be separated into the stiffness and damping bearing forces like in the linear rotordynamics. As a reason, the vibration equation system of the rotor becomes nonlinear due to the nonlinear bearing forces. They change with time, depending on the journal eccentricity $\varepsilon$, its velocity $\dot{\varepsilon}$ , the journal angular position $\gamma$, the whirl velocity $\dot{\gamma}$ , and the rotor speed $\Omega$.

The bearing force given in Eq. (6.56) is valid only for the short bearings of non-cavitating flows. In fact, the radial bearings used in the turbochargers are neither short nor long bearing type, and cavitating flows could occur in the oil film at the high rotor speeds. Hence, two-phase flows must be taken into account in the rotordynamic computation due to cavitation and air releasing [13].

Solving the Reynolds lubrication equation for two-phase cavitating flow of the oil film, one obtains the nonlinear bearing forces for any bearing ratio L/D. At a given journal eccentricity $\varepsilon$ and angular journal position $\gamma$, the bearing forces $F_r$ and $F_t$ are in functions of $\varepsilon, \dot{\varepsilon}, \gamma, \dot{\gamma}$, and the Sommerfeld number So.

By using the coordinate transformation in Eq. (6.59), one achieves the bearing forces $F_1$ and $F_2$ in the inertial coordinate system ($X_1$, $X_2$). To reduce computing time, the transient nonlinear bearing forces are computed by the impedance method, instead of solving the Reynolds lubrication equations at each iteration time step. As a reason, the transient bearing forces are linearized at each iteration time

step by applying the Taylor's series to the computed bearing forces at the journal equilibrium position of ε, γ, and So.

Having used the Taylor's series, the bearing forces in the inertial coordinate system $(X_1, X_2)$ are linearized at the journal equilibrium position.

$$\begin{cases} F_1 \approx F_{0,1} + \left( \dfrac{\partial f_1}{\partial x_1} x_1 + \dfrac{\partial f_1}{\partial x_2} x_2 + \dfrac{\partial f_1}{\partial \dot{x}_1} \dot{x}_1 + \dfrac{\partial f_1}{\partial \dot{x}_2} \dot{x}_2 \right) \equiv F_{0,1} + \Delta F_1 \\[3mm] F_2 \approx F_{0,2} + \left( \dfrac{\partial f_2}{\partial x_1} x_1 + \dfrac{\partial f_2}{\partial x_2} x_2 + \dfrac{\partial f_2}{\partial \dot{x}_1} \dot{x}_1 + \dfrac{\partial f_2}{\partial \dot{x}_2} \dot{x}_2 \right) \equiv F_{0,2} + \Delta F_2 \end{cases}$$

$$(6.60)$$

where

$F_{0,1}, F_{0,2}$ are the static loads acting upon the bearing given in Eq. (6.64);

$\dfrac{\partial f_i}{\partial x_k}$ is the bearing stiffness coefficients; i, k = 1, 2;

$\dfrac{\partial f_i}{\partial \dot{x}_k}$ is the bearing damping coefficients; i, k = 1, 2.

The static load $F_0$ acting on the short bearing is resulted by substituting $\dot{\varepsilon} = \dot{\gamma} = 0$ into Eq. (6.56).

$$\vec{F}_0 = F_{0,r} \vec{e}_r + F_{0,t} \vec{e}_t \tag{6.61}$$

within

$\vec{e}_r, \vec{e}_t$ are the unit vectors in the coordinate system (r,t);

and the force components

$$F_{0,r} = -\frac{\eta}{2} \left( \frac{R}{c} \right)^2 \frac{L^3}{R} \left[ \frac{2\varepsilon^2 \Omega}{(1-\varepsilon^2)^2} \right]; \tag{6.61a}$$

$$F_{0,t} = \frac{\eta}{2} \left( \frac{R}{c} \right)^2 \frac{L^3}{R} \left[ \frac{\pi \varepsilon \Omega}{2(1-\varepsilon^2)^{3/2}} \right] \tag{6.61b}$$

The magnitude of the static load vector $F_0$ results in

$$\begin{aligned} F_0 &= \sqrt{F_{0,r}^2 + F_{0,t}^2} \\ &= \frac{\eta \Omega}{2} \left( \frac{R}{c} \right)^2 \frac{L^3}{R} \left[ \frac{\pi \varepsilon}{2(1-\varepsilon^2)^2} \sqrt{1 - \varepsilon^2 + \left( \frac{4\varepsilon}{\pi} \right)^2} \right] \equiv F_\eta A \end{aligned} \tag{6.62}$$

within
the reference force $F_\eta$ in Eq. (6.62) is defined as

$$F_\eta \equiv \frac{\eta\Omega}{2}\left(\frac{R}{c}\right)^2\frac{L^3}{R} \tag{6.63}$$

Therefore,

$$\begin{cases} F_{0,1} = F_{0,r}\sin\gamma + F_{0,t}\cos\gamma = f_{0,1}(\varepsilon,\gamma,\Omega) \\ F_{0,2} = -F_{0,r}\cos\gamma + F_{0,t}\sin\gamma = f_{0,2}(\varepsilon,\gamma,\Omega) \end{cases} \tag{6.64}$$

The attitude angle $\alpha$ at the equilibrium condition is derived from Eq. (6.64).

$$\tan\alpha = -\frac{F_{0,t}}{F_{0,r}} = \frac{\pi\sqrt{1-\varepsilon^2}}{4\varepsilon} \tag{6.65}$$

The static load curve on which the journal center $O_j$ locates at the equilibrium position is displayed in Fig. 6.23. According to Eq. (6.65), the attitude angle $\alpha$ goes to $\pi/2$ (So $\to \infty$) at very small journal eccentricities ($\varepsilon \to 0$).; $\alpha$ approaches zero (So = 0) at the maximum eccentricity ($\varepsilon \to 1$). Under the static load $F_0$, the journal center locates at the relative eccentricity $\varepsilon$ and attitude angle $\alpha$. At increasing the bearing load, the journal center moves downwards along the static load curve to the new equilibrium position, locating at the larger eccentricity and smaller attitude angle, and vice versa.

At a constant rotor speed $\Omega$, the journal center $O_j$ occurs near the bearing center $O_b$ under a low static load $F_0$. As the static load increases, the journal center moves



**Fig. 6.23** Static load curve of the oil-film bearing

downwards with increasing eccentricity and decreasing attitude angle along the load curve to the bearing wall $W_b$ at the contact circle $\varepsilon = 1$ (So = 0). On the contrary, the journal is loaded by a constant large load $F_0$: at first, its center lies near the bearing wall $W_b$ at a low rotor speed $\Omega$. Then, as the rotor speed increases, the journal center begins moving upwards with decreasing eccentricity and increasing attitude angle along the load curve to the bearing center $O_b$ at $\varepsilon = 0$ (So $\rightarrow \infty$).

**Sommerfeld number.** So is defined according to the English convention\*. It describes the relation between the bearing geometry, average load pressure, rotor speed, and oil viscosity in one dimensionless number.

$$So \equiv \frac{\eta N}{\overline{p}}\left(\frac{R}{c}\right)^2 \tag{6.66}$$

where
R is the shaft radius;
c is the radial bearing clearance;
$\eta$ is the oil dynamic viscosity;
N is the rotor speed (rps) with $N = \Omega/(2\pi)$;
$\overline{p}$ is the average load pressure on the bearing.

\*) In the German convention, the **Sommerfeld number** So\* is defined as

$$So^* \equiv \frac{\overline{p}}{\eta\Omega}\left(\frac{c}{R}\right)^2 = \frac{1}{2\pi \, So}$$

Note that we use the Sommerfeld number So according to the English convention in this book.

The average load pressure in the bearing is defined as

$$\overline{p} \equiv \frac{F_0}{DL} \tag{6.67}$$

where
$F_0$ is the static load on the bearing at equilibrium (s. Fig. 6.23);
D is the bearing inner diameter;
L is the bearing inner length.

Inserting the average load pressure and rotor speed in Eq. (6.66), the Sommerfeld number becomes

$$So \equiv \frac{\eta\Omega}{2\pi}\frac{DL}{F_0}\left(\frac{R}{c}\right)^2 \tag{6.68}$$

Having substituted $F_0$ of Eq. (6.62) into Eq. (6.68), one obtains Sommerfeld number for short bearings in the relative journal eccentricity $\varepsilon$.

$$So = \cfrac{\cfrac{1}{2\pi\beta^2}}{\cfrac{\pi\varepsilon}{2(1-\varepsilon^2)^2}\sqrt{1-\varepsilon^2+\left(\cfrac{4\varepsilon}{\pi}\right)^2}} \equiv \cfrac{\cfrac{1}{2\pi\beta^2}}{A} \qquad (6.69)$$

where

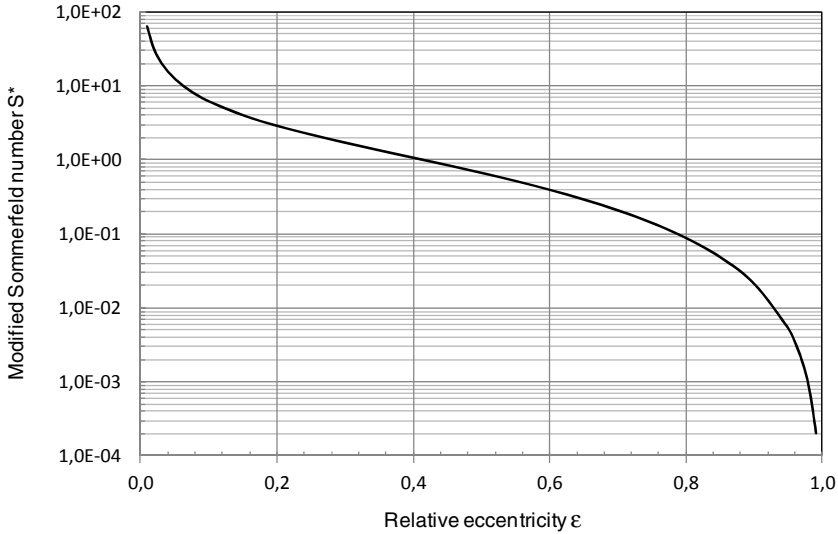$\beta \equiv \dfrac{L}{D}$ is the length to diameter ratio of the bearing.

Thus,

$$\frac{F_0}{F_\eta} \equiv A = \frac{1}{2\pi\beta^2 So} \equiv \frac{1}{S^*}$$

$$= \frac{\pi\varepsilon}{2(1-\varepsilon^2)^2}\sqrt{1-\varepsilon^2+\left(\frac{4\varepsilon}{\pi}\right)^2} \qquad (6.70)$$

where

S* is called the **modified Sommerfeld number**, which is resulted from So and β.

$$S^* \equiv 2\pi\beta^2 So = \frac{2(1-\varepsilon^2)^2}{\pi\varepsilon\sqrt{1-\varepsilon^2+\left(\dfrac{4\varepsilon}{\pi}\right)^2}} = f(\varepsilon) \qquad (6.71)$$

According to Eq. (6.71), the modified Sommerfeld number S* is a function of ε, as displayed in Fig. 6.24, in turn ε can be described in S* or So.



**Fig. 6.24** Modified Sommerfeld number S* versus ε for short bearings

The impedance method combined with using Eqs (6.59), (6.60), and (6.64) is applied to computing the transient nonlinear bearing forces at each iteration time step resulted from the bearing stiffness and damping coefficients.

The bearing stiffness coefficients $k_{ik}$ are defined

$$k_{ik} \equiv -\frac{\partial f_i}{\partial x_k} = \kappa_{ik} \frac{F_0}{c}; \ i;k = 1,2 \tag{6.72}$$

where
$\kappa_{ik}$ is the bearing dimensionless stiffness coefficients;
$F_0$ is the static load at equilibrium;
$c$ is the radial bearing clearance.

Similarly, the bearing damping coefficients $d_{ik}$ are defined

$$d_{ik} \equiv -\frac{\partial f_i}{\partial \dot{x}_k} = \beta_{ik} \frac{F_0}{c\Omega}; \ i;k = 1,2 \tag{6.73}$$

where
$\beta_{ik}$ is the bearing dimensionless damping coefficient;
$F_0$ is the static load at equilibrium;
$c$ is the radial bearing clearance;
$\Omega$ is the rotor speed.

Since $f_1$ and $f_2$ are the functions of $\varepsilon, \dot{\varepsilon}, \gamma, \dot{\gamma}$, as given in Eq. (6.59), one uses the chain rule of differentiation to compute the required partial derivatives of

$$\begin{cases} \dfrac{\partial f_i}{\partial x_k} = \dfrac{\partial f_i}{\partial \varepsilon}\dfrac{\partial \varepsilon}{\partial x_k} + \dfrac{\partial f_i}{\partial \gamma}\dfrac{\partial \gamma}{\partial x_k}; \ i;k = 1,2 \\[2mm] \dfrac{\partial f_i}{\partial \dot{x}_k} = \dfrac{\partial f_i}{\partial \dot{\varepsilon}}\dfrac{\partial \dot{\varepsilon}}{\partial \dot{x}_k} + \dfrac{\partial f_i}{\partial \dot{\gamma}}\dfrac{\partial \dot{\gamma}}{\partial \dot{x}_k}; \ i;k = 1,2 \end{cases} \tag{6.74}$$

Having used the coordinate transformation, as given in Fig. 6.25, The relations between the coordinates result by using the chain rule of differentiation in.

$$\begin{pmatrix} dx_1 \\ dx_2 \end{pmatrix} = \begin{bmatrix} \cos\delta & -\sin\delta \\ \sin\delta & \cos\delta \end{bmatrix} \begin{pmatrix} de \\ ed\gamma \end{pmatrix} \tag{6.75}$$

where

$$\delta = \gamma - \frac{\pi}{2}.$$
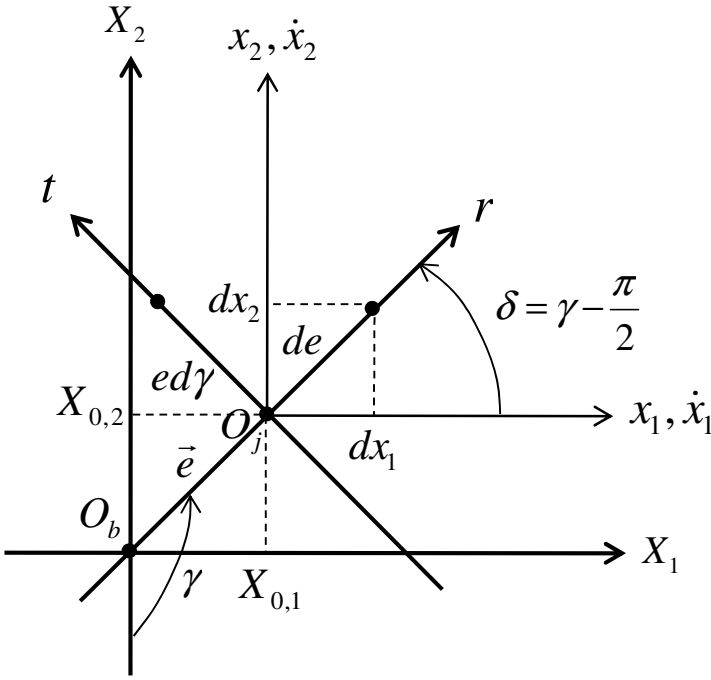
**Fig. 6.25** Coordinate transformation of the differentiation chain rule

Thus, Eq. (6.75) becomes

$$\begin{pmatrix} dx_1 \\ dx_2 \end{pmatrix} = \begin{bmatrix} \sin\gamma & \cos\gamma \\ -\cos\gamma & \sin\gamma \end{bmatrix} \begin{pmatrix} de \\ ed\gamma \end{pmatrix} \tag{6.76}$$

By inversely transforming Eq. (6.76), one gets the relation

$$\begin{pmatrix} de \\ ed\gamma \end{pmatrix} = \begin{bmatrix} \sin\gamma & -\cos\gamma \\ \cos\gamma & \sin\gamma \end{bmatrix} \begin{pmatrix} dx_1 \\ dx_2 \end{pmatrix} \tag{6.77}$$

Differentiating both sides of Eq. (6.77) with $e = c\,\varepsilon$, one obtains

$$\begin{pmatrix} c\dot{\varepsilon} \\ e\dot{\gamma} \end{pmatrix} = \begin{bmatrix} \sin\gamma & -\cos\gamma \\ \cos\gamma & \sin\gamma \end{bmatrix} \begin{pmatrix} \dot{x}_1 \\ \dot{x}_2 \end{pmatrix} \tag{6.78}$$

By partially differentiation of Eqs (6.77) and (6.78), one achieves the relations.

$$\frac{\partial\varepsilon}{\partial x_1} = \frac{\partial\dot{\varepsilon}}{\partial\dot{x}_1} = \frac{1}{c}\sin\gamma; \quad \frac{\partial\varepsilon}{\partial x_2} = \frac{\partial\dot{\varepsilon}}{\partial\dot{x}_2} = -\frac{1}{c}\cos\gamma; \tag{6.79}$$

$$\frac{\partial \gamma}{\partial x_1} = \frac{\partial \dot{\gamma}}{\partial \dot{x}_1} = \frac{1}{e}\cos\gamma; \quad \frac{\partial \gamma}{\partial x_2} = \frac{\partial \dot{\gamma}}{\partial \dot{x}_2} = \frac{1}{e}\sin\gamma \tag{6.80}$$

Having substituted Eqs (6.79) and (6.80) into Eq. (6.74), one computes the bearing dimensionless stiffness and damping coefficients $\kappa_{ik}$ and $\beta_{ik}$ for short bearings [8].

$$\begin{cases} \kappa_{11} = \left[2\pi^2 + \left(16 - \pi^2\right)\varepsilon^2\right]F(\varepsilon) \\[2mm] \kappa_{12} = \frac{\pi}{4}\left[\frac{-\pi^2 + 2\pi^2\varepsilon^2 + \left(16 - \pi^2\right)\varepsilon^4}{\varepsilon\left(1 - \varepsilon^2\right)^{1/2}}\right]F(\varepsilon) \\[3mm] \kappa_{21} = \frac{\pi}{4}\left[\frac{\pi^2 + \left(32 + \pi^2\right)\varepsilon^2 + 2\left(16 - \pi^2\right)\varepsilon^4}{\varepsilon\left(1 - \varepsilon^2\right)^{1/2}}\right]F(\varepsilon) \\[3mm] \kappa_{22} = \left[\frac{\pi^2 + \left(32 + \pi^2\right)\varepsilon^2 + 2\left(16 - \pi^2\right)\varepsilon^4}{\left(1 - \varepsilon^2\right)}\right]F(\varepsilon) \end{cases} \tag{6.81}$$

and

$$\begin{cases} \beta_{11} = \frac{\pi\left(1 - \varepsilon^2\right)^{1/2}}{2\varepsilon}\left[\pi^2 + 2\left(\pi^2 - 8\right)\varepsilon^2\right]F(\varepsilon) \\[2mm] \beta_{12} = \beta_{21} = 2\left[\pi^2 + 2\left(\pi^2 - 8\right)\varepsilon^2\right]F(\varepsilon) \\[2mm] \beta_{22} = \frac{\pi}{2}\left[\frac{\pi^2 + 2\left(24 - \pi^2\right)\varepsilon^2 + \pi^2\varepsilon^4}{\varepsilon\left(1 - \varepsilon^2\right)^{1/2}}\right]F(\varepsilon) \\[3mm] F(\varepsilon) \equiv \frac{4}{\left[\pi^2 + \left(16 - \pi^2\right)\varepsilon^2\right]^{3/2}} \end{cases} \tag{6.82}$$

In case of linear or quasi-linear rotordynamics, the bearing forces $F_1$ and $F_2$ in the coordinate system $(X_1, X_2)$ are linearized from the equilibrium at each iteration time step according to Eq. (6.83) for the small rotor amplitudes.

$$\begin{cases} F_1^i = F_{0,1} + \Delta F_1^i \\[2mm] F_2^i = F_{0,2} + \Delta F_2^i \end{cases} \tag{6.83}$$

where $\Delta F_1^i$, $\Delta F_2^i$ are the changes of force relating to small displacements and velocities of the rotor.

The changes of force at the equilibrium position are resulted from Eqs (6.60), (6.72), and (6.73).

$$\begin{bmatrix} \Delta F_1 \\ \Delta F_2 \end{bmatrix}^i = - \begin{bmatrix} k_{11} & k_{12} \\ k_{21} & k_{22} \end{bmatrix}^i \begin{bmatrix} x_1 \\ x_2 \end{bmatrix}^i - \begin{bmatrix} d_{11} & d_{12} \\ d_{21} & d_{22} \end{bmatrix}^i \begin{bmatrix} \dot{x}_1 \\ \dot{x}_2 \end{bmatrix}^i \qquad (6.84)$$

where

$k_{ik}$ and $d_{ik}$ are the bearing stiffness and damping coefficients, respectively. In case of short bearings, they only depend on the angular position $\gamma$ and journal relative eccentricity $\varepsilon$, in turn on the Sommerfeld number So and $\gamma$.

By solving the Reynolds lubrication equation of the bearings, one creates the impedance table. In case of nonlinear rotordynamics, the nonlinear bearing forces in the entire bearing clearance are resulted from the corresponding bearing stiffness and damping coefficients by linearly interpolating the computed values of the bearing characteristics at $\varepsilon$, $\gamma$, and So in the impedance table. They contain two force components: firstly, the bearing rotation force induced by the rotation with $\Omega$, and it depends on $\eta$, $\varepsilon$, and $\gamma$; secondly, the bearing damping force caused by the journal velocities $\dot{\varepsilon}, \dot{\gamma}$, and it depends on $\eta, \varepsilon, \gamma, \dot{\varepsilon}, \dot{\gamma}$.

### 6.5.3  Floating Ring Bearings

Floating ring bearings are usually applied to the automotive turbochargers to reduce airborne noises and rotor amplitudes at resonances. There are two common types of the floating ring bearings: semi-floating (SFRB) and rotating-floating ring bearings (RFRB). The common character of both floating ring bearings is having two oil films, the inner and outer oil films. However, they are different because the bearing ring does not rotate at the semi-floating bearing, and rotates at the rotating-floating ring bearing.

In order to reduce the bearing friction, the rotating-floating ring bearings (RFRB) are usually used in the turbochargers (s. Fig. 6.2). Due to reduction of the bearing friction at the low rotor speeds, the transient response of turbochargers is improved in low-end torque. Figure 6.26 shows the set-up of the rotating-floating ring bearing in the rotor shaft. Lubricating oil at the pressure $p_i$ from the inlet flows through the outer bearing clearance in the circumferential and axial directions; leaves the bearing ends at the ambient pressure $p_0$. By means of the oil holes in the bearing ring, lubricating oil enters the inner bearing clearance and flows in the circumferential and axial directions; leaves the bearing ends at the ambient pressure $p_0$. The oil volumetric flow rate depends on the oil inlet temperature, pressure drop of $p_i$ and $p_o$, rotor speed, and as well as the rotating speed of the bearing ring.

The inner oil film has a key function to carry the rotor against to the external forces acting upon the rotor. Therefore, its inner bearing radial clearance $c_1$ is relatively small to increase the bearing stiffness. On the contrary, the outer oil film provides the rotor with large damping coefficient to reduce the rotor deflection at resonances and suppress the airborne noises, like unbalance whistle and constant tone induced by the rotor unbalance and inner oil whirl in the bearing, respectively.
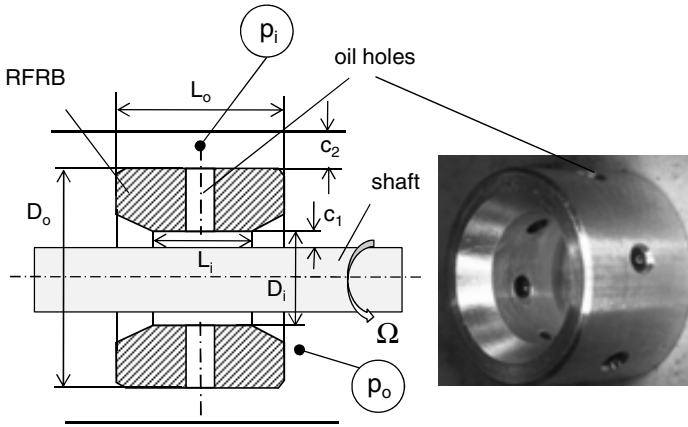
**Fig. 6.26** Sketch of a rotating floating ring bearing

Flow characteristics of the oil films are taken into account in computing the friction power in the bearing (s. Fig. 6.27).

The bearing friction power on the rotor shaft is written in

$$P_f = F_f U_j = U_j \int_A \tau dA = \eta_i \frac{\partial U}{\partial h} A_j U_j \approx \left( \eta_i \frac{U_j}{h} A_j \right) U_j \qquad (6.85)$$

where
$\eta_i$ is the dynamic viscosity of the inner oil film;
$\partial U / \partial h$ is the velocity gradient in the oil film;
h is the oil-film thickness;
$A_j$ is the journal frictional area;
$U_j$ is the journal circumferential velocity.

In order to reduce the friction power, the velocity gradient is decreased by letting the bearing ring rotate with a circumferential velocity $U_R$ at the bearing inner surface in case of the rotating floating ring bearings. Hence, the reduced bearing friction power becomes

$$P_f^* \approx \eta_i \frac{(U_j - U_R)}{h} A_j U_j \qquad (6.86)$$

The relative reduction of the friction power results from Eqs (6.85) and (6.86) in

$$\frac{\Delta P_f}{P_f} = \frac{P_f - P_f^*}{P_f} = 1 - \frac{P_f^*}{P_f} = \frac{U_R}{U_j} \approx \frac{\Omega_R}{\Omega} \equiv RSR \qquad (6.87)$$

where
$\Omega_R$ is the ring angular velocity $(\Omega_R < \Omega)$;
$\Omega$ is the rotor angular velocity.

Equation (6.87) indicates that the friction power reduction is proportional to the ring speed ratio RSR, the ratio of the bearing ring speed to the rotor speed.

Torque acting upon the bearing ring is calculated by the Petroff's law resulting from the Reynolds lubrication equation.

$$M = R\int_A \tau dA = R\int_A \eta \frac{\partial U}{\partial h}dA = \frac{2\pi\eta R^3 L\Omega}{c} \tag{6.88}$$

Having applied Eq. (6.88) to the bearing ring, one obtains the driving torque acting on the inner side of the bearing

$$M_i = \frac{2\pi\eta_i R_i^3 L_i(\Omega-\Omega_R)}{c_1} \tag{6.89}$$

and the friction torque on the outer side of the bearing

$$M_o = -\frac{2\pi\eta_o R_o^3 L_o\Omega_R}{c_2} \tag{6.90}$$

By using the angular momentum law, the ring speed ratio RSR is resulted at the steady state condition $(\ddot{\theta} = 0)$ .

$$\sum M = M_i + M_o = I_p\ddot{\theta}=0$$

Thus,

$$RSR_{steady} \equiv \frac{\Omega_R}{\Omega} \approx \frac{1}{1 + \dfrac{\eta_o(T_o)}{\eta_i(T_i)}\left(\dfrac{L_o}{L_i}\right)\left(\dfrac{c_1}{c_2}\right)\left(\dfrac{D_o}{D_i}\right)^3} \tag{6.91a}$$

where
$\eta_i$, $\eta_o$ are the dynamic viscosity of the inner and outer oil films;
$L_i$, $L_o$ are the inner and outer bearing width (s. Fig. 6.26);
$c_1$, $c_2$ are the inner and outer radial bearing clearance;
$D_i$, $D_o$ are the inner and outer bearing diameter;
$I_p$ is the polar mass inertia moment of the rotor.
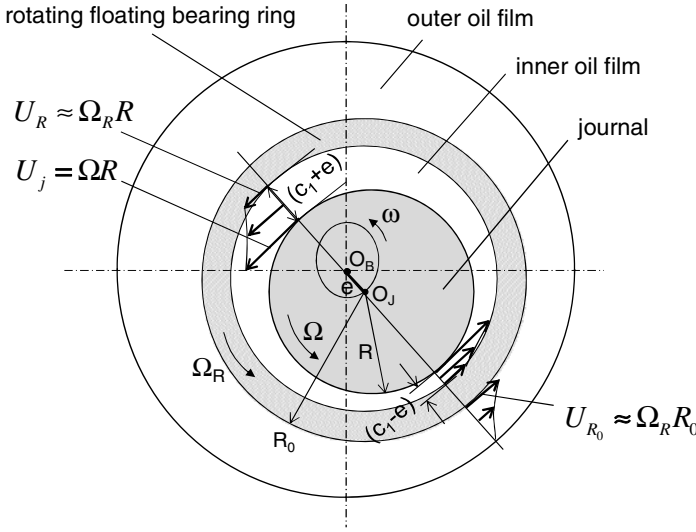
**Fig. 6.27** Flow velocities in the oil films

The modified steady state RSR* becomes when the inner and outer relative eccentricities $\varepsilon_1$ and $\varepsilon_2$ are taken into account, according to [5]:

$$RSR^*_{steady} \equiv \frac{\Omega^*_R}{\Omega} \approx \frac{1}{1 + \frac{\eta_o(T_o)}{\eta_i(T_i)}\left(\frac{L_o}{L_i}\right)\left(\frac{c_1\sqrt{1-\varepsilon_1^2}}{c_2\sqrt{1-\varepsilon_2^2}}\right)\left(\frac{D_o}{D_i}\right)^3} \qquad (6.91b)$$

In case of the unsteady state condition with $\ddot{\theta} \neq 0$, the ring speed ratio, as given in Eqs (6.91a) and (6.91b) becomes

$$RSR_{unsteady} = RSR_{steady} - \frac{I_p\ddot{\theta}}{M_t\Omega} \qquad (6.92)$$

where the factor

$$M_t = 2\pi\left(\frac{\eta_i R_i^3 L_i}{c_1} + \frac{\eta_o R_o^3 L_o}{c_2}\right)$$

Because the inner clearance is much smaller than the outer clearance, the inner oil-film temperature is higher than the outer oil-film temperature due to the induced bearing friction, especially at increasing the rotor speeds. Hence, the oil viscosity ratio that is larger than 1 (i.e., $\eta_o > \eta_i$) leads to decreasing the ring speed ratio RSR. The computed behavior of the ring speed ratio versus the rotor speed at various oil inlet temperatures of the rotating floating ring bearing is displayed in Fig. 6.28 [12].

The effective temperatures $T_i$ and $T_o$ of the inner and outer oil films are only induced by the bearing friction where the heat conduction of the bearing housing to the oil films is not taken into account. In fact, the heat conduction from the bearing housing increases the temperature of the outer oil film; therefore, the ring speed ratio increases. The ring speed ratio RSR varies between 15% and 30% at low rotor speeds to about 90,000 rpm (1,500 rps) at the oil inlet temperature of 90°C. Hence, the friction power of the rotating floating ring bearing (RFRB) on the rotor shaft could be reduced averagely by 20% compared to the semi-floating ring bearing in low-end torque (LET), leading to improving the response behavior of the turbocharger.

The higher the rotor speed, the higher the inner temperatures of the oil films become due to bearing friction, leading to reducing the ring speed. At high oil temperatures, the dynamic viscosity ratio of both outer and inner oil films does not change so much; therefore, the ring speed ratio reduces slowly, and tends to remain constant at the very high rotor speeds, as shown in Fig. 6.28. At decreasing the oil inlet temperature, large bearing friction is generated in the inner oil film, leading to higher oil temperature in the inner bearing clearance; as a reason, reducing the ring speed of the bearing. Generally, the ring speed ratio RSR decreases with the rotor speed at a constant oil inlet temperature and increases with the oil inlet temperature at a constant rotor speed.
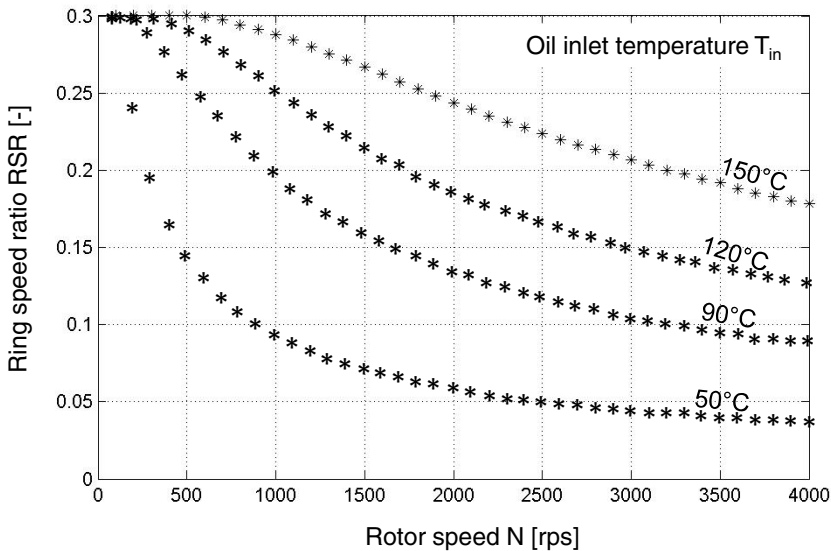


**Fig. 6.28** Computed ring speed ratio RSR$_{steady}$ vs. rotor speed and $T_{in}$

The rotating floating ring bearings take advantages of more damping due to the outer oil film and reducing the bearing friction power, especially in low-end torque. However, they need more oil volumetric flow rate, and the rotor deflection could be larger than the one of the semi-floating ring bearings.

If we consider the unsteady state, the ring speed ratio is very low at small rotor speeds and high oil inlet temperatures because the inertia term of the ring speed ratio

in eq. (6.92) is significantly large, especially at high angular accelerations. At increasing the rotor speeds, this term becomes smaller; hence, the ring speed ratio increases; then, it reduces again at further increasing the rotor speeds like in the steady state.

### 6.5.4 Influential Parameters of Rotating Floating Ring Bearings

To optimize the bearing design in terms of bearing friction, effective temperature in the bearing, and rotor stability, some influential parameters are discussed. They are the geometric ratios of $D_o/D_i$, $L_o/L_i$, and $c_2/c_1$, as displayed in Fig. 6.26. They have mutual effects on the characteristics of turbochargers, as shown in Fig. 6.18. As a reason, they must be carefully chosen after the given priorities. In the following section, some rotordynamic characteristics of the geometric ratios of the radial bearings are given.

- **Ratio Do/Di**

The larger the diameter ratio $D_o/D_i$ at the given inner bearing diameter $D_i$, the more the damping coefficient of the bearing acts upon the rotor due to the large outer surface of the bearing. It improves the rotor stability against oil whirl; reduces the rotor amplitude at resonance and induced airborne noises. However, it needs more oil volumetric flow rate in the bearings, and more blowby is resulted by the corresponding large seal rings. Blowby is the volumetric flow rate of the charge air and exhaust gas leaking in the seal rings to oil in the bearing housing. Additionally, the large diameter ratio strongly reduces the ring speed ratio according to eq. (6.91a); hence, it can lessen the main advantage of low bearing friction of the rotating floating ring bearings. At excessively large $D_o$, the bearing stiffness coefficient of the outer oil film increases, therefore, the outward move of the bearing ring in the outer bearing clearance is more difficult. Hence, bearing wear could occur between the shaft and the inner bearing.

- **Ratio Lo/Li**

The larger the length ratio $L_o/L_i$ at the given inner bearing width $L_i$, the more the damping coefficient of the bearing acts upon the rotor due to the large outer surface of the bearing. It improves the rotor stability; reduces the rotor amplitude at resonance and induced airborne noises. Moreover, it needs less oil volumetric flow rate through the bearings due to increased flow resistance in the outer oil film. However, the large length ratio reduces the ring speed ratio according to eq. (6.91a); hence, it could lessen the main advantage of the low bearing friction of the rotating floating ring bearings. The wider the outer width of the bearing $L_o$, the shorter the bearing span is. That reduces the rotor stability of the rotor. Similarly, at excessively wide $L_o$, the bearing stiffness coefficient of the outer oil film increases, therefore, the outward move of the bearing ring in the outer bearing clearance is more difficult. Hence, bearing wear could occur between the shaft and bearing.

- **Ratio c2/c1**

The larger the clearance ratio $c_2/c_1$ at the given inner bearing clearance $c_1$, the more the damping coefficient of the bearing is due to the large outer bearing clearance. It improves the rotor stability; reduces the rotor amplitude at resonance and induced airborne noises. Moreover, the large clearance ratio at the given inner bearing clearance increases the ring speed ratio because the bearing friction in the outer ring

surface reduces according to eq. (6.91a). However, it needs more oil flow rate due to the larger outer bearing clearance. At excessively large outer bearing clearance $c_2$, the bearing stiffness coefficient of the outer oil film decreases. It could cause high rotor deflection of the conical vibration mode in the outer oil film.

These important parameters of the oil-film bearings should be considered under various operating conditions, such as the oil types, oil inlet temperatures, pressures, rotor speed range, kinds of balancing, etc.

## 6.6  Rolling-Element Bearings

There are some common types of the rolling-element bearings [7]:

-   Angular contact ball bearings;
-   Ball thrust bearings;
-   Straight roller bearings;
-   Tapered roller bearings;
-   Needle roller bearings.

This section focuses on two normal types of the rolling-element bearings that are applied to the automotive turbochargers: angular contact ball and straight roller bearings, as shown in Fig. 6.29. The other types of rolling-element bearings are either similar to the ball and roller bearings or have already been existing in [4], [7], and [14].
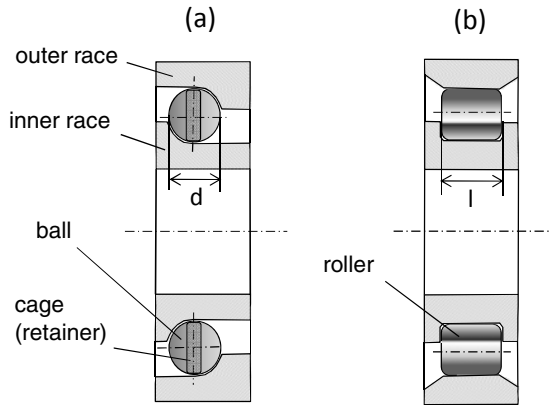


**Fig. 6.29** (a) Angular contact ball bearing; (b) Straight roller bearing

### 6.6.1  Characteristics of the Rolling-Element Bearings

At first, some advantages and disadvantages of the angular contact ball bearings applied to the automotive turbochargers are reviewed in [2]. Ball bearings have no intrinsic damping due to very small clearances between the balls and races. As a reason, they need an additional external damping coefficient to suppress the rotor

amplitude at resonance and to reduce the airborne noises, like unbalance whistle and constant tone (howling). In this case, a squeeze-film damper is unconditionally necessary for the ball bearings of the turbochargers. Contrary to the oil-film bearings, they do not have the inner oil whirl; therefore, no constant tone occurs. However, they usually have the multiple harmonic vibrations of 2X, 3X, 4X, or higher frequency orders, and modulation sidebands frequencies due to unsuitable clearance of the oil damper between the outer race and bearing housing. Moreover, some asynchronous vibrations could occur in the ball bearings if defects of balls, cage, inner, and outer races take place. Such high-frequency vibration components induce high-frequency noises in the ball bearings that are uncomfortable and unwanted audible noises in the passenger vehicles. Unbalance of the rolling elements, cage, and outer race cannot be directly balanced; however, it is very small. Sometimes unusual asynchronous responses could happen if the balls have slightly different diameters due to production or bearing wear.

The bearing stiffness coefficient of the ball and roller bearings depends on the acting forces whose amplitudes change with the rotor speed. Therefore, the bearing stiffness coefficient varies with the bearing forces and rotor speed as well.

**a) Rolling-element deflection**
According to the Hertzian theory, the deflection of the balls at the contact area is derived

$$\delta = \sqrt[3]{\frac{2.25(1-v^2)^2 F^2}{E^2 R}} \equiv c_K(E, v, r_1, r_2, ...) F^{2/3} \qquad (6.93)$$

where
$v$ is the Poisson's ratio;
$E$ is the elasticity module;
$F$ is the acting force on the balls;
$r_i$ is the radii of the ball bearing geometry;
$R$ is the equivalent radius;
$c_K$ is the deflection factor.

Having used the elasticity module E = 20.6x10⁴ N/mm² and Poisson's ratio $v$ = 0.3, one obtains the deflection of the rolling elements empirically [8].

- Ball bearings:

$$\delta = 4.37 \times 10^{-4} \frac{F^{2/3}}{d^{1/3}} \qquad (6.94)$$

where
$\delta$ is the ball deflection (mm);
$d$ is the ball diameter (mm);
$F$ is the acting force on the ball bearing (N).

- Roller bearings:

$$\delta = 0.77 \times 10^{-4} \frac{F^{0.9}}{l^{0.8}} \qquad (6.95)$$

where
δ is the roller deflection (mm);
l is the roller effective length (mm);
F is the acting force on the roller bearing (N).

The equivalent radius R between the balls and inner race are given for various geometries of convex, plane, and concave contact areas in the ball bearings, as shown in Fig. 6.30 [8].
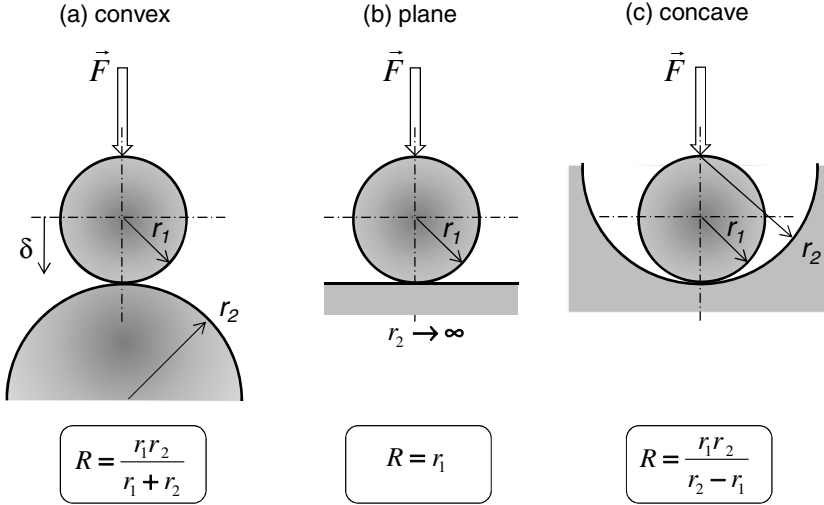


Fig. 6.30 Equivalent radius R of various contact surfaces

### b) Bearing force and its stiffness
The bearing force is empirically determined by the rolling-element deflection, number of rolling-elements, and some bearing parameters depending on the bearing types [8].

$$F = Sz \left( \frac{\delta}{C} \right)^n \tag{6.96}$$

where
z is the number of rolling elements (balls or rollers);
δ is the rolling-element deflection (mm) in direction of the acting force F (N);
S = 0.23 (all ball bearings); 0.24 (all roller bearings);
n = 3/2 (all ball bearings); 10/9 (all roller bearings);
C = $4.37 \times 10^{-4} d^{-1/3}$ in mm.$N^{-2/3}$ (all ball bearings) with d (ball diameter) in mm;
  = $0.77 \times 10^{-4} l^{-0.8}$ in mm.$N^{-0.9}$ (all roller bearings) with l (roller effective length) in mm.

Having combined the bearing force in Eq. (6.96) with the bearing parameter C, one obtains the bearing force in a function of rolling-element deflection for the ball and roller bearings, as illustrated in Fig. 6.31.

- Ball bearings:

$$F = 2.5 \times 10^4 \, z d^{0.5} \delta^{1.5} \text{ in N with d (mm), and } \delta \text{(mm)};$$

- Roller bearings:

$$F = 0.89 \times 10^4 \, z l^{0.9} \delta^{1.12} \text{ in N with d (mm), and } \delta \text{(mm)}.$$

The rolling-element deflection is derived from Eq. (6.96).

$$\delta = C \left( \frac{F}{Sz} \right)^{\frac{1}{n}} \tag{6.97}$$

Having inserted the bearing parameters C and S in Eq. (6.97), the rolling-element deflection results in a function of the acting force for

- Ball bearings:

$$\delta = 1.2 \times 10^{-3} d^{-1/3} \left( \frac{F}{z} \right)^{2/3} \text{ in mm with d (mm), and F (N)};$$

- Roller bearings:

$$\delta = 0.28 \times 10^{-3} l^{-0.8} \left( \frac{F}{z} \right)^{0.9} \text{ in mm with l (mm), and F (N)}.$$
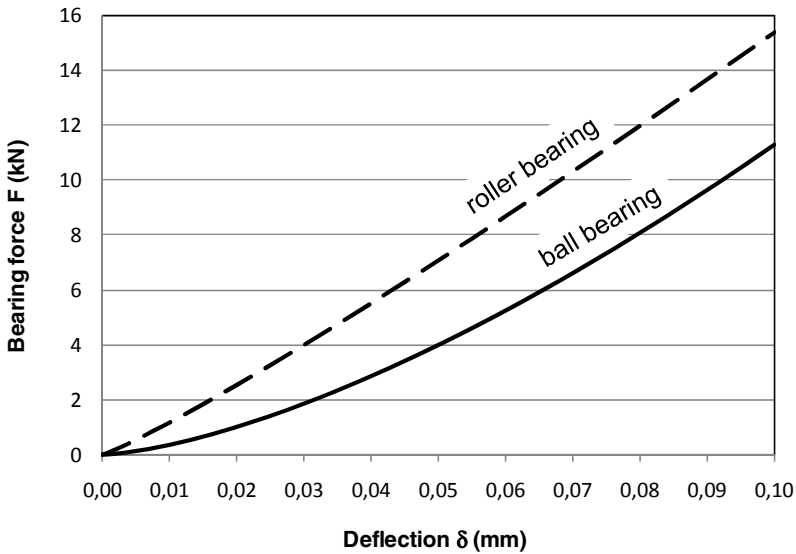


**Fig. 6.31** Bearing force vs. deflection (z = 8; d = l = 3.2 mm)

The bearing stiffness coefficient is resulted from the partial derivative of force to deflection by using Eqs (6.96) and (6.97).

$$k \equiv \left(\frac{\partial F}{\partial \delta}\right) = \frac{n}{C^n} Sz\delta^{n-1} = \frac{n}{C}(Sz)^{1/n} F^{\frac{n-1}{n}} \tag{6.98}$$

By inserting the parameters C and S for each bearing type in Eq. (6.98), one obtains the bearing stiffness for

- Ball bearings:

$$k = 1.3 \times 10^3 z^{2/3} d^{1/3} F^{1/3} \text{ in N/mm; d (mm); F (N);}$$

- Roller bearings:

$$k = 4 \times 10^3 z^{0.9} l^{0.8} F^{0.1} \text{ in N/mm; l (mm); F (N).}$$

Figure 6.32 displays the bearing stiffness coefficient of the ball and roller bearings in a function of acting force in case of z = 8 rolling elements, the ball diameter d, and roller length l of 3.2 mm.
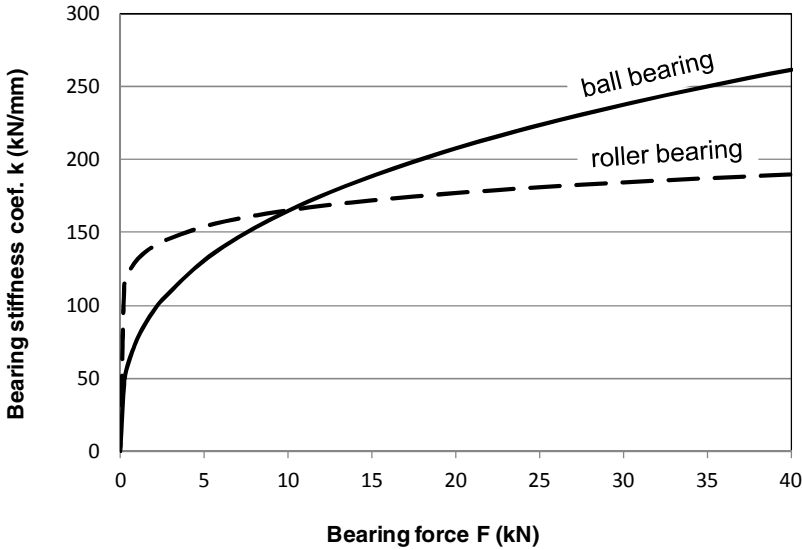


**Fig. 6.32** Bearing stiffness coefficient vs. acting force (z = 8; d = l = 3.2 mm)

## c)  Kinematics of the rolling-element bearing

To calculate the angular velocities of the cage $\omega_c$ and rolling element $\omega_b$ (ball or roller), a simple bearing model is used in Fig. 6.33. The inner race is fixed to the shaft, and it rotates with the rotor velocity $\omega_i$; the outer race rotates with an angular velocity $\omega_o$. The rolling element contacts the inner and outer races at the radius

$r_i$ and $r_o$, respectively. The pitch diameter $D_p$ is defined as the maximum diametral distance of the centers between two rolling elements.

The angular velocity of the bearing cage $\omega_c$ about the bearing axis $O_{ba}$ is written in

$$\omega_c = \frac{\frac{1}{2}(v_i + v_o)}{r_p} = \frac{v_i + v_o}{D_p} \qquad (6.99)$$

where

$-$ $v_i$ is the circumferential velocity at the contact area between the inner race and the rolling element, and resulted from

$$v_i = \omega_i r_i = \frac{\omega_i}{2}(D_p - d\cos\theta) = \frac{D_p}{2}\omega_i\left(1 - \frac{d}{D_p}\cos\theta\right) \qquad (6.100)$$

$-$ $v_o$ is the circumferential velocity at the contact area between the outer race and the rolling element, and resulted from

$$v_o = \omega_o r_o = \frac{\omega_o}{2}(D_p + d\cos\theta) = \frac{D_p}{2}\omega_o\left(1 + \frac{d}{D_p}\cos\theta\right) \qquad (6.101)$$
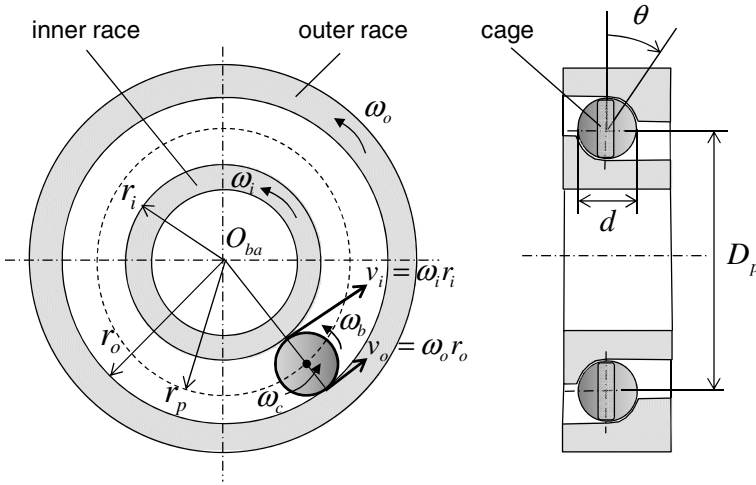


**Fig. 6.33** Model of a ball bearing with the angular velocities

By substitution of Eqs (6.100), (6.101), and (6.99), one obtains the angular velocity of the cage.

$$\omega_c = \frac{1}{2}\left[\omega_i\left(1 - \frac{d}{D_p}\cos\theta\right) + \omega_o\left(1 + \frac{d}{D_p}\cos\theta\right)\right] \qquad (6.102)$$

Similarly, one computes the angular velocity $\omega_b$ of the rolling element about its own axis without spin and slip at the races.

$$\omega_b = \frac{v_i - v_o}{d} \tag{6.103}$$

where
the velocity direction of $\omega_b$ is the same direction of $(v_i - v_o)$.

By substitution of Eqs (6.100) and (6.101) into Eq. (6.103), one obtains the angular velocity of the rolling element.

$$\omega_b = \frac{1}{2}\frac{D_p}{d}\left[\omega_i\left(1 - \frac{d}{D_p}\cos\theta\right) - \omega_o\left(1 + \frac{d}{D_p}\cos\theta\right)\right] \tag{6.104}$$

In a cylinder roller bearing with $\theta = 0$, the angular velocities of the cage and rolling element become obviously at $\cos\theta = 1$ in Eqs (6.102) and (6.104).

$$\omega_c = \frac{1}{2}\left[\omega_i\left(1 - \frac{d}{D_p}\right) + \omega_o\left(1 + \frac{d}{D_p}\right)\right] \tag{6.105}$$

and

$$\omega_b = \frac{1}{2}\frac{D_p}{d}\left[\omega_i\left(1 - \frac{d}{D_p}\right) - \omega_o\left(1 + \frac{d}{D_p}\right)\right] \tag{6.106}$$

Additionally, at non-rotating outer race of the bearing ($\omega_o = 0$), the angular velocities of the cage is resulted from Eqs (6.105).

$$\omega_c = \frac{\omega_i}{2}\left(1 - \frac{d}{D_p}\right) < \frac{\omega_i}{2} \text{ since } \frac{d}{D_p} > 0. \tag{6.107}$$

It indicates that the angular velocity of the cage of the bearing is always less than a half of the rotor velocity.

The angular velocity of the rolling element becomes at $\omega_o = 0$ (non-rotating outer race).

$$\omega_b = \frac{\omega_i}{2}\left(\frac{D_p}{d} - 1\right) \tag{6.108}$$

In case of $D_p/d \geq 2$, the angular velocity of the rolling element about its own axis is larger than or equal to a half of the rotor velocity.

$$\omega_b = \frac{\omega_i}{2}\left(\frac{D_p}{d} - 1\right) \geq \frac{\omega_i}{2} \tag{6.109}$$

## 6.6.2  Squeeze-Film Damper

As discussed earlier, the rolling-element bearings have no intrinsic damping; therefore, they need an additionally external damping measure in applications of turbochargers. In fact, they are usually integrated in the squeeze-film damper (diameter D, and length L) where the rotor shaft is built into the bearings at the inner races. The squeeze-film damper is floating, but normally non-rotating in the bearing housing with the squeeze oil film of a radial clearance c, as shown in Fig. 6.34, In case of a non-rotating damper, its whirl velocity ω equals zero. In case of *no-end oil damper* where the damping oil continually flows outside through the squeeze film, the theory of *short bearings* is generally used to calculate the damping forces. There are four cases: non-cavitating and cavitating squeeze oil films, each with *no-end* and *end oil damper*. The 2π-theory is applied to the first (non-cavitating); the π-theory, to the second (cavitating).
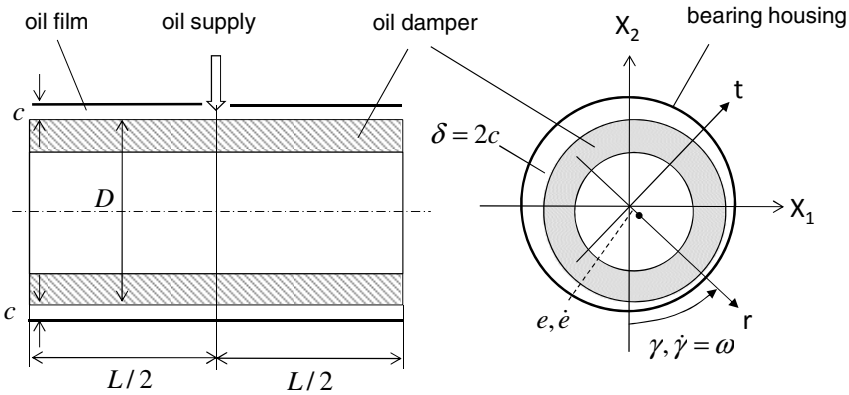


**Fig. 6.34** Squeeze-film damper in the bearing housing

**Case 1**
**No-end oil damper with a non-cavitating squeeze oil film (2π–theory)**

In this case, the cross-coupled damping coefficients $d_{rt}$ and $d_{tr}$ equal zero. The damping force is resulted from the short bearing theory [3].

$$F_d = \begin{pmatrix} F_r \\ F_t \end{pmatrix} = -\begin{bmatrix} d_{rr} & 0 \\ 0 & d_{tt} \end{bmatrix} \begin{pmatrix} \dot{e} \\ e\dot{\gamma} \end{pmatrix} \qquad (6.110)$$

where
$d_{rr}$ is the damping coefficient in the normal direction r;
$d_{tt}$ is the damping coefficient in the tangential direction t;
$d_{rt} = d_{tr} = 0$, the cross-coupled damping coefficients;
$\dot{e}$ is the eccentricity velocity of the damper;
$\dot{\gamma}$ is the whirl velocity ω of the damper (= 0 for non-rotating).

The damping coefficients result in

$$d_{rr} = 4\pi\eta D\left(\frac{L}{\delta}\right)^3\left[\frac{1+2\varepsilon^2}{(1-\varepsilon^2)^{5/2}}\right] \tag{6.111}$$

$$d_{tt} = 4\pi\eta D\left(\frac{L}{\delta}\right)^3\left[\frac{1}{(1-\varepsilon^2)^{3/2}}\right] \tag{6.112}$$

within
$\eta$ is the oil dynamic viscosity;
$\delta$ is the diametral damper clearance;
L is the damper length;
D is the damper diameter;
$\varepsilon$ is the relative eccentricity of the damper ($\varepsilon = e/c$).

Thus,

$$F_r = -d_{rr}\dot{e} = -4\pi\eta D\left(\frac{L}{\delta}\right)^3\left[\frac{1+2\varepsilon^2}{(1-\varepsilon^2)^{5/2}}\right]c\dot{\varepsilon} \tag{6.113}$$

$$F_t = -d_{tt}e\dot{\gamma} = -4\pi\eta D\left(\frac{L}{\delta}\right)^3\left[\frac{1}{(1-\varepsilon^2)^{3/2}}\right]c\varepsilon\dot{\gamma} \tag{6.114}$$

## Case 2
### No-end oil damper with a cavitating squeeze oil film ($\pi$-theory)

In this case, the cross-coupled damping coefficients $d_{rt}$ and $d_{tr}$ are not equal to zero. The damping force is resulted from the short bearing theory [3].

$$F_d = \begin{pmatrix} F_r \\ F_t \end{pmatrix} = -\begin{bmatrix} d_{rr} & d_{rt} \\ d_{tr} & d_{tt} \end{bmatrix}\begin{pmatrix} \dot{e} \\ e\dot{\gamma} \end{pmatrix} \tag{6.115}$$

where
$d_{rr}$ is the damping coefficient in the normal direction r;
$d_{tt}$ is the damping coefficient in the tangential direction t;
$d_{rt}$, $d_{tr} \neq 0$, the cross-coupled damping coefficients;
$\dot{e}$ is the eccentricity velocity of the damper;
$\dot{\gamma}$ is the whirl velocity $\omega$ of the damper (= 0 for non-rotating).

The damping coefficients result in case of a very small eccentricity velocity.

$$d_{rr} = 2\pi\eta D\left(\frac{L}{\delta}\right)^3\left[\frac{1+2\varepsilon^2}{(1-\varepsilon^2)^{5/2}}\right] \tag{6.116}$$

$$d_{tt} = 2\pi\eta D\left(\frac{L}{\delta}\right)^3\left[\frac{1}{(1-\varepsilon^2)^{3/2}}\right] \tag{6.117}$$

$$d_{rt} = d_{tr} = 4\eta D\left(\frac{L}{\delta}\right)^3\left[\frac{2\varepsilon}{(1-\varepsilon^2)^2}\right] \tag{6.118}$$

within
$\eta$ is the oil dynamic viscosity;
$\delta$ is the diametral damper clearance;
L is the damper length;
D is the damper diameter;
$\varepsilon$ is the relative eccentricity of the damper ($\varepsilon = e/c$).

Thus,

$$F_r = -d_{rr}\dot{e} - d_{rt}e\dot{\gamma} = -2\pi\eta D\left(\frac{L}{\delta}\right)^3\left[\frac{1+2\varepsilon^2}{(1-\varepsilon^2)^{5/2}}\right]c\dot{\varepsilon}$$
$$-4\eta D\left(\frac{L}{\delta}\right)^3\left[\frac{2\varepsilon}{(1-\varepsilon^2)^2}\right]c\varepsilon\dot{\gamma} \tag{6.119}$$

$$F_t = -d_{tr}\dot{e} - d_{tt}e\dot{\gamma} = -4\eta D\left(\frac{L}{\delta}\right)^3\left[\frac{2\varepsilon}{(1-\varepsilon^2)^2}\right]c\dot{\varepsilon}$$
$$-2\pi\eta D\left(\frac{L}{\delta}\right)^3\left[\frac{1}{(1-\varepsilon^2)^{3/2}}\right]c\varepsilon\dot{\gamma} \tag{6.120}$$

In case of end oil damper where the damping oil remains in the squeeze oil film closed by an O-seal ring, the theory of long bearings is generally used to calculate the damping forces. There are two cases: non-cavitating and cavitating squeeze oil films. The $2\pi$-theory is applied to the first; the $\pi$-theory, to the second.

### Case 3
### End oil damper with a non-cavitating squeeze oil film ($2\pi$-theory)

In this case, the cross-coupled damping coefficients $d_{rt}$ and $d_{tr}$ equal zero. The damping force is resulted from the long bearing theory [3].

$$F_d = \begin{pmatrix} F_r \\ F_t \end{pmatrix} = -\begin{bmatrix} d_{rr} & 0 \\ 0 & d_{tt} \end{bmatrix}\begin{pmatrix} \dot{e} \\ e\dot{\gamma} \end{pmatrix} \tag{6.121}$$

where
$d_{rr}$ is the damping coefficient in the normal direction r;
$d_{tt}$ is the damping coefficient in the tangential direction t;
$d_{rt} = d_{tr} = 0$, the cross-coupled damping coefficients;

$\dot{e}$ is the eccentricity velocity of the damper;
$\dot{\gamma}$ is the whirl velocity $\omega$ of the damper (= 0 for non-rotating).

The damping coefficients result in

$$d_{rr} = 12\pi\eta L\left(\frac{D}{\delta}\right)^3\left[\frac{1}{(1-\varepsilon^2)^{3/2}}\right] \tag{6.122}$$

$$d_{tt} = 24\pi\eta L\left(\frac{D}{\delta}\right)^3\left[\frac{1}{(2+\varepsilon^2)(1-\varepsilon^2)^{1/2}}\right] \tag{6.123}$$

within
$\eta$ is the oil dynamic viscosity;
$\delta$ is the diametral damper clearance;
L is the damper length;
D is the damper diameter;
$\varepsilon$ is the relative eccentricity of the damper ($\varepsilon = e/c$).

Thus,

$$F_r = -d_{rr}\dot{e} = -\pi\eta L\left(\frac{D}{\delta}\right)^3\left[\frac{12}{(1-\varepsilon^2)^{3/2}}\right]c\dot{\varepsilon} \tag{6.124}$$

$$F_t = -d_{tt}e\dot{\gamma} = -\pi\eta L\left(\frac{D}{\delta}\right)^3\left[\frac{24}{(2+\varepsilon^2)(1-\varepsilon^2)^{1/2}}\right]c\varepsilon\dot{\gamma} \tag{6.125}$$

## Case 4
### End oil damper with a cavitating squeeze oil film ($\pi$-theory)

In this case, the cross-coupled damping coefficients $d_{rt}$ and $d_{tr}$ are not equal to zero. The damping force is resulted from the short bearing theory [3].

$$F_d = \begin{pmatrix} F_r \\ F_t \end{pmatrix} = -\begin{bmatrix} d_{rr} & d_{rt} \\ d_{tr} & d_{tt} \end{bmatrix}\begin{pmatrix} \dot{e} \\ e\dot{\gamma} \end{pmatrix} \tag{6.126}$$

where
$d_{rr}$ is the damping coefficient in the normal direction r;
$d_{tt}$ is the damping coefficient in the tangential direction t;
$d_{rt}, d_{tr} \neq 0$ are the cross-coupled damping coefficients ($\neq 0$);
$\dot{e}$ is the eccentricity velocity of the damper;
$\dot{\gamma}$ is the whirl velocity $\omega$ of the damper (= 0 for non-rotating).

The damping coefficients result in case of a zero eccentricity velocity.

$$d_{tt} = 12\pi\eta L\left(\frac{D}{\delta}\right)^3\left[\frac{1}{(2+\varepsilon^2)(1-\varepsilon^2)^{1/2}}\right] \tag{6.127}$$

$$d_{rt} = d_{tr} = 24\eta L \left(\frac{D}{\delta}\right)^3 \left[\frac{\varepsilon}{(2+\varepsilon^2)(1-\varepsilon^2)}\right] \tag{6.128}$$

within

$\eta$ is the oil dynamic viscosity;

$\delta$ is the diametral damper clearance;

L is the damper length;

D is the damper diameter;

$\varepsilon$ is the relative eccentricity of the damper ($\varepsilon = e/c$).

Thus,

$$F_r = -d_{rt} e \dot{\gamma} = -24\eta L \left(\frac{D}{\delta}\right)^3 \left[\frac{\varepsilon}{(2+\varepsilon^2)(1-\varepsilon^2)}\right] c\varepsilon\dot{\gamma} \tag{6.129}$$

$$F_t = -d_{tt} e \dot{\gamma} = -12\pi\eta L \left(\frac{D}{\delta}\right)^3 \left[\frac{1}{(2+\varepsilon^2)(1-\varepsilon^2)^{1/2}}\right] c\varepsilon\dot{\gamma} \tag{6.130}$$

The damping forces $F_r$ and $F_t$ in the rotating coordinate system (r,t) are transformed to $F_1$ and $F_2$ in the inertial coordinate system ($X_1, X_2$) by using Eqs (6.60) and (6.74). The transformed damping forces $F_1$ and $F_2$ are used in the computation of nonlinear rotordynamics.

### 6.6.3  Bearing Defect-Related Frequencies

Defects in the rolling-element bearings, such as bearing defects in the inner and outer races, cage (retainer), and rolling-elements (balls or rollers) generate some asynchronous vibration components with high frequency orders and sidebands frequencies due to frequency modulations. They are called the bearing defect-related frequencies.

Figure 6.35 shows the key elements and their geometries of a ball bearing. The balls with diameter d are held in the cage (retainer); the pitch diameter $D_p$ is defined as the maximum diametral distance between the centers of two balls. Contact angle $\theta$ is the angle between the line perpendicular to the shaft and the radius of the ball at the contact point at the outer race. The inner race is fixed to the shaft; it rotates with the rotor speed N (rps); the outer race is mounted in the cartridge (damper) supported by the damper oil-film, as shown in Fig. 6.34.

The bearing defect-related frequencies are computed from the bearing geometries, number of balls, and rotor speed [2], [15].

- **Fundamental train frequency (*ftf*)**
  is caused by the defects of cage depending on the rotor speed N in rps.

$$ftf = \frac{N}{2}\left(1 - \frac{d}{D_p}\cos\theta\right) \tag{6.131}$$

**Fig. 6.35** Key elements of an angular contact ball bearing

- **Ball passing frequency over defective inner race (*bpfi*)**
  is generated when the $Z$ balls or rollers pass over the defective inner race.

$$bpfi = Z\frac{N}{2}\left(1 + \frac{d}{D_p}\cos\theta\right) \tag{6.132}$$

- **Ball passing frequency over defective outer race (*bpfo*)**
  is generated when the $Z$ balls or rollers pass over the defective outer race.

$$bpfo = Z\frac{N}{2}\left(1 - \frac{d}{D_p}\cos\theta\right) \tag{6.133}$$

- **Two-times ball spin frequency (*2bsf*)**
  is induced by the defective balls or rollers spinning over the inner and outer races.

$$2bsf = N\frac{D_p}{d}\left[1 - \left(\frac{d}{D_p}\right)^2\cos^2\theta\right] \tag{6.134}$$

where
d is the diameter of balls or rollers;
$D_p$ is the pitch diameter of the bearing;
$\theta$ is the contact angle of the rolling elements;
Z is the number of rolling elements;
N is the rotor speed in rps.

The bearing-defect-related frequencies are displayed in Fig. 6.36 for a ball bearing containing 8 balls with d = 3.2 mm, $D_p$ =12.2 mm, and $\theta$ = 45°. The frequencies-induced bearing defects bpfi, 2bsf, and bpfo are supersynchronous  (f > 1X); the ftf frequency is subsynchronous (f < 1X).
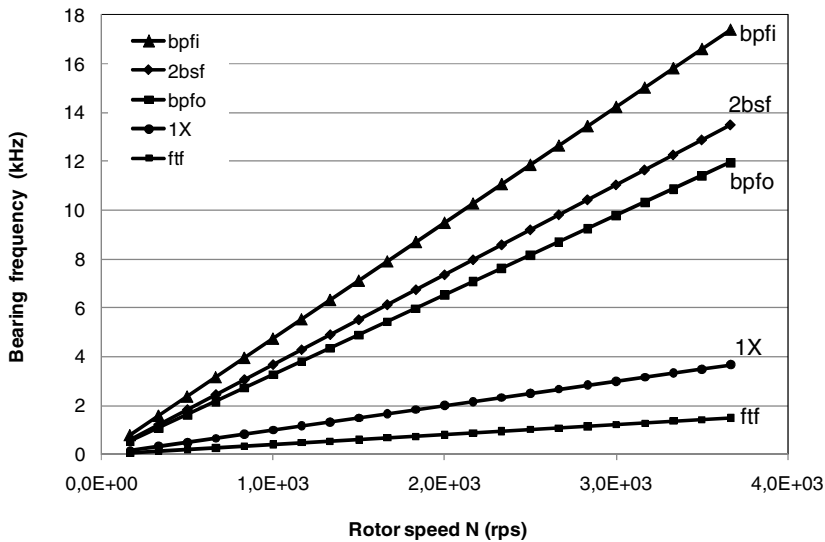
**Fig. 6.36** Bearing defect related frequencies

# References

1. DIN 31653 - Parts 1, 2, and 3: German Industry Norm - Hydraulic plan thrust bearings under steady-state conditions (1991)
2. Ehrich, F.: Handbook of Rotordynamics. Krieger Publishing Company (2004)
3. Gasch, R., Nordmann, R., Pfuetzner, H.: Rotordynamik, vol. 2. Auflage, Springer (2006)
4. Hamrock, B., Schmid, S.R., Jacobson, B.O.: Fundamentals of Fluid Film Lubrication, 2nd edn. Marcel Dekker Inc. (2004)
5. Hori, Y.: Hydrodynamic lubrication. Springer, Heidelberg (2006)
6. Kennedy, et al.: Tribology, Lubrication, and Bearing Design - The CRC Hand-book of Mechanical Engineers. CRC Press (1988)
7. Khonsari, M., Booser, E.: Applied Tribology and Bearing Design and Lubrication, 2nd edn. J. Wiley and Sons Ltd. (2008)
8. Kraemer, E.: Rotordynamics of Rotors and Foundations. Springer, Heidelberg (1993)
9. Mate, C.M.: Tribology on the Small Scale. Oxford University Press (2008)
10. Nguyen-Schaefer, H.: Internal Program CAF (Computing Axial Forces). BMTS (2008)
11. Nguyen-Schaefer, H., Di Giandomenico, G.: Internal Program TBD (Thrust Bearing Design). BMTS (2009)
12. Nguyen-Schaefer, H., Di Giandomenico, G.: Internal Program RFRB (Ro-tating Floating Ring Bearings). BMTS (2009)
13. Nguyen-Schaefer, H., Sprafke, P.: Numerical Study on Interaction Effects of the Bubbles induced by Air-Release and Cavitation in Hydraulic Systems. In: 10th Bath International Fluid Power Workshop, Bath, UK. Research Studies Press (1997)

14. Szeri, A.Z.: Fluid Film Lubrication. Cambridge University Press (1998)
15. Taylor, J., Kirkland, D.W.: The Bearing Analysis Handbook. Vibration Consultants Inc. (2004)
16. Vance, J.: Rotordynamics of Turbomachinery. J. Wiley and Sons Inc. (1988)

# Chapter 7
# Nonlinear Rotordynamics of Turbochargers

## 7.1 Boundary Conditions of the Rotordynamics

Some uncertain boundary conditions play a key role for the stability and functionality of the rotor, as shown in Fig. 7.1. Unfortunately, it is very difficult or impossible to take all of them into account in the rotordynamic computation where only the rotor containing the compressor, turbine wheels, rotor shaft, radial bearings, and seal rings is considered. Normally, the boundary conditions are generally assumed ideal in the computation, such as sufficient supply oil, good parallelism of the thrust bearing, all wedges of the thrust bearing having the same slope, good quality of the radial bearing in terms of the bearing non-coaxiality, non-roundness, and characteristics of surface roughness. Therefore, the rotordynamic computation cannot cure the instability and malfunctions of the rotor, or prevent it from damages at inappropriate boundary conditions, like oil insufficiency, oil contaminated with hard particles, foamy oil, or oil coking in the bearing in the operation. However, the computational results help us better to understand the rotor response. Therefore, further improvements could be done for the rotor stability and reduction of the bearing friction. Additionally, experimental measurements also provide us with the real rotor response at such unknown boundary conditions that one could not consider in the computation.

Some particularly unknown boundary conditions are discussed in the following section. If the compressor wheel speed takes turns changing from the high circumferential speeds (U > 560 m/s) to low speeds and vice versa during the operation with a driving cycle for a long time interval. The ultimate tensile stress of the compressor reduces with the operating cycles (about $10^5$ cycles); it is called low-cycle fatigue (LCF); leading to damages of the compressor wheel. The partly broken compressor wheel induces an extremely large unbalance to damage the entire turbocharger.

In case of oil insufficiency, the bearings operate in a poorly lubricated oil condition; hence, it causes the rotor instability and damages the bearings due to wear and seizure. Moreover, contaminated oil with hard particles or diluted oil with fuel and water causes wear in the bearing and reduces the rotor stability of the turbocharger.

Improperly balancing turbochargers induces excessively large unbalances that exceed the load capability of the bearings. Hence, the rotor instability at excessively high unbalance, bearing wear, and seizure of the shaft in the bearing follow. Without high-speed balancing (called trim balancing), the unbalance whistle is audible.
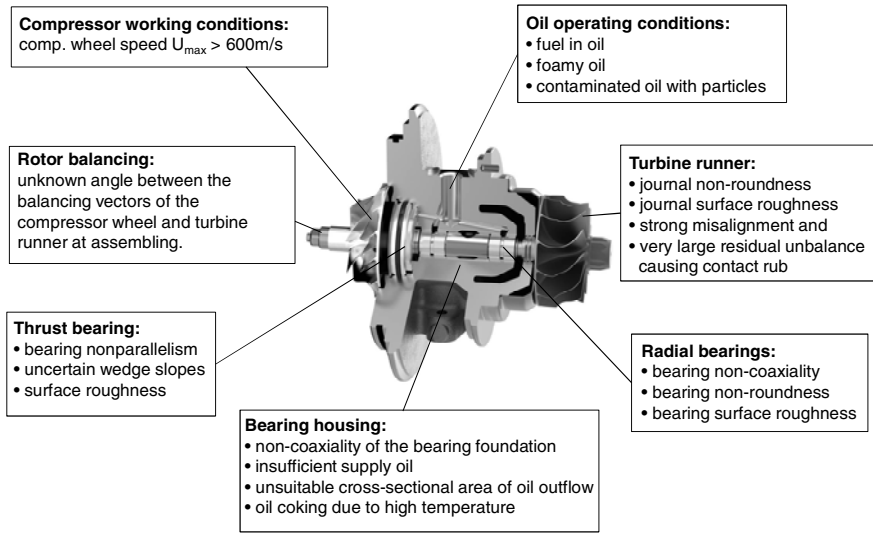
**Fig. 7.1** Unknown boundary conditions in the rotordynamic computation

Misaligned turbine shaft due to production mistake induces the dynamic unbalance of the rotor. It causes high rotor amplitude because of the conical mode of the vibration response. At last, the non-coaxiality of the bearing foundation is to blame for the rotor misalignment, leading to the rotor instability and inducing high-order frequencies. Moreover, the oil outflow in the bearing housing is very important for the bearing functionality and stability. If the foaming oil blocks the bearing outlet or does not leave the bearing outlet so quickly, the effective oil temperature increases inside the bearing. Hence, the bearing stiffness and damping coefficients drop, leading to the rotor instability and oil coking in the bearings as well.

## 7.2 Vibration Equations of the Rotor with RFRBs

Figure 7.2 displays the rotor of an automotive turbocharger including the rotor shaft, compressor wheel, turbine wheel, rotating floating ring bearings (RFRBs), seal rings, thrust rings. All components must be taken into account in the rotordynamic computation to study the vibration response of the rotor, such as the frequency components in Waterfall diagram, shaft orbit in the phase plane, and rotor amplitude of the response vibrations in the time diagram.

The continuum vibration equations of the rotor are discretized by two methods, the finite element and transfer matrix methods. By discretization of the vibration equations, one divides the rotor into a finite number of elements in the computational model including concentrated masses, cylindrical elements, disks, and interfaces between the rotor, bearings, and seal rings.

The finite element method, a discretization method of the continuum structure of the rotor, is based on the principle of D'Alembert where the sum of virtual work of

all rotor elements equals zero, as shown in Section 8.4.1. Therefore, the vibration equations of the rotor are derived and written in a discrete matrix equation. Another alternative method is the transfer matrix method developed by Myklestad and Prohl where the first element of the rotor is connected with the last one by the overall-transfer matrix that consists of the transfer matrices of all rotor elements. The main advantage of this method is to spare the computational working memory compared to the finite element method. They are not discussed further in details here because one can find them in other literatures, e.g. [10] and [19].
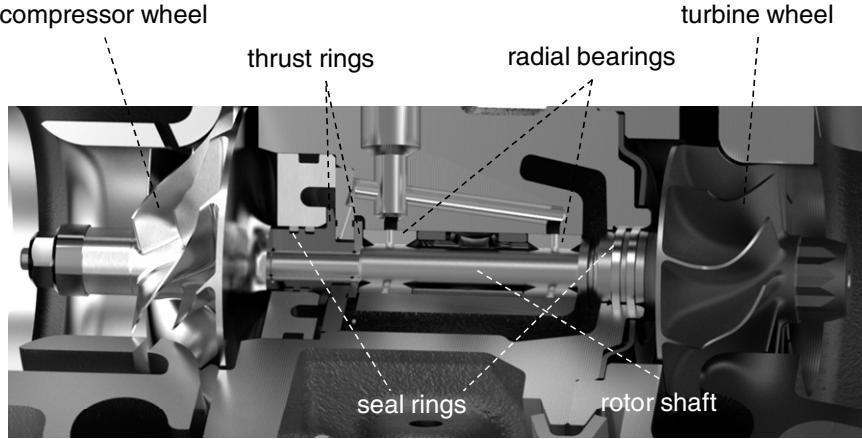


**Fig. 7.2** Layout of the rotor of an automotive turbocharger (Courtesy BMTS)

The vibration equations of the rotor with N degrees of freedom, as shown in Fig. 7.2 are written in the discrete matrix equation.

$$\mathbf{M}\ddot{\mathbf{x}} + \mathbf{C}_S\dot{\mathbf{x}} + \mathbf{K}_S\mathbf{x} = f(\mathbf{t}) \tag{7.1}$$

where

$\mathbf{M}$ = (N x N) mass matrix containing the masses and inertia moments of the rotor, similar to $\mathbf{M}$ given in Eq. (5.53) but for N = DOF;

$\mathbf{C}_S$ = (N x N) damping coefficient matrix of the shaft; it is negligibly small;

$\mathbf{K}_S$ = (N x N) stiffness coefficient matrix containing the diagonal and cross-coupled stiffness coefficients of the shaft;

$\mathbf{x}$ = (N x 1) vibration response vector includes all degrees of freedom of the rotor with two translational and two rotational displacements at each station of the element;

$f(t)$ = (N x 1) vector of the unbalance and nonlinear bearing forces.

To reduce the second-order to first-order equation system, the (2N x 1) vector $\mathbf{z}$ of the vibration response is defined as

$$\mathbf{z} \equiv \begin{bmatrix} \mathbf{x} \\ \mathbf{y} \end{bmatrix} = \begin{bmatrix} \mathbf{x} \\ \dot{\mathbf{x}} \end{bmatrix} \Rightarrow \dot{\mathbf{z}} = \begin{bmatrix} \mathbf{y} \\ \dot{\mathbf{y}} \end{bmatrix} = \begin{bmatrix} \dot{\mathbf{x}} \\ \ddot{\mathbf{x}} \end{bmatrix} \tag{7.2}$$

where
$$\mathbf{y} = \dot{\mathbf{x}}; \quad \dot{\mathbf{y}} = \ddot{\mathbf{x}}.$$

By substituting the vector $\mathbf{z}$ (t) into Eq. (7.1), 2N first-order vibration equations of $\mathbf{z}$ result in

$$\begin{bmatrix} \dot{\mathbf{x}} \\ \ddot{\mathbf{x}} \end{bmatrix} = \begin{bmatrix} \mathbf{0} & \mathbf{I} \\ -\mathbf{M}^{-1}\mathbf{K}_S & -\mathbf{M}^{-1}\mathbf{C}_S \end{bmatrix} \cdot \begin{bmatrix} \mathbf{x} \\ \dot{\mathbf{x}} \end{bmatrix} + \begin{bmatrix} \mathbf{0} \\ \mathbf{M}^{-1}\left[\mathbf{U}(\Omega) + \mathbf{F_B}(\mathbf{x},\dot{\mathbf{x}},t)\right] \end{bmatrix}$$

$$\Leftrightarrow \dot{\mathbf{z}} = \begin{bmatrix} \mathbf{0} & \mathbf{I} \\ -\mathbf{M}^{-1}\mathbf{K}_S & -\mathbf{M}^{-1}\mathbf{C}_S \end{bmatrix} \mathbf{z} + \begin{bmatrix} \mathbf{0} \\ \mathbf{M}^{-1}\left[\mathbf{U}(\Omega) + \mathbf{F_B}(\mathbf{x},\dot{\mathbf{x}},t)\right] \end{bmatrix}$$

(7.3)

where
$\mathbf{U}$ is the unbalance force and moment;
$\mathbf{F_B}$ is the nonlinear bearing force, as computed in eqs (6.83) and (6.84) or by the impedance table.

The coupled nonlinear vibration equation system (7.3) is written in the simple equation matrix of $\mathbf{z}$.

$$\dot{\mathbf{z}} = \mathbf{A}\mathbf{z} + \mathbf{b}(\mathbf{z},\Omega,t) \tag{7.4}$$

where
$\mathbf{A} = $ (2N x 2N) stiffness matrix of the shaft;
$\mathbf{b} = $ (2N x 1) vector of the external forces including unbalance and nonlinear bearing forces within

$$\mathbf{A} = \begin{bmatrix} \mathbf{0} & \mathbf{I} \\ -\mathbf{M}^{-1}\mathbf{K}_S & -\mathbf{M}^{-1}\mathbf{C_S} \end{bmatrix};$$

$$\mathbf{b}(\mathbf{z},\Omega,t) = \begin{bmatrix} \mathbf{0} \\ \mathbf{M}^{-1}\left[\mathbf{U}(\Omega) + \mathbf{F_B}(\mathbf{z},t)\right] \end{bmatrix}$$

The matrix $\mathbf{A}$ containing the matrices $\mathbf{M}$, $\mathbf{K_S}$, and $\mathbf{C_S}$ is obviously non-symmetric; i.e., $\mathbf{A} \neq \mathbf{A}^T$ where $\mathbf{A}^T$ is the transposed matrix of $\mathbf{A}$. As a reason, the bimodal method [14] is applied to solve the first-order nonlinear equation matrix of $\mathbf{z}$ with a (2N x 2N) large matrix $\mathbf{A}$ of N degrees of freedom.

The eigenvalue $\lambda$ of the vibration system is found by solving the characteristic equation of the homogeneous vibration equation (7.4).

$$(\mathbf{A} - \lambda\mathbf{I})\mathbf{r} = \mathbf{0} \tag{7.5}$$

where $\mathbf{r}$ is defined as the right eigenvector.

Having changed the matrix $\mathbf{A}$ by $\mathbf{A}^T$ in the homogeneous equation (7.4), one obtains

$$\dot{\mathbf{z}} - \mathbf{A}^T\mathbf{z} = \mathbf{0} \tag{7.6}$$

With $\mathbf{z} = \mathbf{l}e^{\lambda t}$ one gets the characteristic equation of Eq. (7.6).

$$\left(\mathbf{A}^T - \lambda\,\mathbf{I}\right)\mathbf{l} = \mathbf{0} \tag{7.7}$$

where $\mathbf{l}$ is defined as the left eigenvector.

In following section, it proves that the right and left eigenvectors of Eqs (7.5) and (7.7) are orthogonal; i.e., $\mathbf{r}.\mathbf{l}^T = \mathbf{l}.\mathbf{r}^T = \mathbf{I}$.

The left eigenvector $\mathbf{l_i}$ corresponding to the eigenvalue $\lambda_i$ is resulted from Eq. (7.7).

$$\mathbf{A}^T\,\mathbf{l}_i = \lambda_i\mathbf{l_i} \tag{7.8}$$

Multiplying both sides of Eq. (7.8) by $\mathbf{r}_j^T$, it results in

$$\mathbf{r}_j^T\mathbf{A}^T\,\mathbf{l}_i = \lambda_i\mathbf{r}_j^T\mathbf{l_i} \tag{7.9}$$

Having transposed Eq. (7.9), it gives

$$\mathbf{l}_i^T\mathbf{A}\,\mathbf{r}_j = \lambda_i\mathbf{l}_i^T\mathbf{r}_j \tag{7.10}$$

Similar to the left eigenvector, one obtains the corresponding relation for the right eigenvector.

$$\mathbf{l}_i^T\mathbf{A}\,\mathbf{r}_j = \lambda_j\mathbf{l}_i^T\mathbf{r}_j \tag{7.11}$$

The orthogonality of the eigenvectors is given by substituting of Eqs (7.10) and (7.11)

$$(\lambda_i - \lambda_j)\mathbf{l}_i^T\mathbf{r}_j = 0 \tag{7.12}$$

because of

$$i \neq j \text{ thus, } \mathbf{l}_i^T\mathbf{r}_j = 0\;;$$

$$i = j \text{ thus, } \mathbf{l}_i^T\mathbf{r}_i = a_i^2 \neq 0$$

Having normalized the eigenvectors by $a_i$ given in (7.12), the orthonormality of the normalized right and left eigenvectors is written in

$$\mathbf{l}_i^{*T}\mathbf{r}_j^* = \delta_{i,j} = \begin{cases} 0, & i \neq j \\ 1, & i = j \end{cases} \tag{7.13}$$

where

$$\mathbf{l}_i^{*T} = \mathbf{l}_i^T / a_i\;;$$

$$\mathbf{r}_j^* = \mathbf{r}_j / a_i\;;$$

$$\delta_{i,j} \text{ is the Kronecker symbol.}$$

The modal right and left matrices $\mathbf{R}$ and $\mathbf{L}$ are resulted from the corresponding normalized eigenvectors $\mathbf{l}^*$ and $\mathbf{r}^*$.

$$\mathbf{R} = \left( \mathbf{r}_j^* \right), \quad \mathbf{L} = \left( \mathbf{1}_i^* \right); \quad i, j = 1,\ldots, 2N \tag{7.14}$$

The new response vector $\mathbf{w}(t)$ is defined, so that

$$\mathbf{z}(t) = \mathbf{R}\mathbf{w}(t) \tag{7.15}$$

By inserting Eq. (7.15) in Eq. (7.4) and multiplying both sides by the transposed left modal matrix $\mathbf{L}^T$, it gives the vibration equation of $\mathbf{w}(t)$.

$$(\mathbf{L}^T \mathbf{R})\dot{\mathbf{w}}(t) = (\mathbf{L}^T \mathbf{A} \mathbf{R})\mathbf{w}(t) + \mathbf{L}^T \mathbf{b}(\mathbf{w}, t) \tag{7.16}$$

Due to the orthonormality of the right and left normalized eigenvectors, as proved in Eq. (7.13), one obtains two relations:

$\mathbf{L}^T \mathbf{R} = \mathbf{I}$ is the unit matrix; $\hspace{5cm}$ (7.17)

$$\mathbf{L}^T \mathbf{A} \mathbf{R} = (\mathbf{l}_i^{*T} \mathbf{A} \mathbf{r}_j^*) = \lambda_j \mathbf{l}_i^{*T} \mathbf{r}_j^* = \begin{cases} 0, & i \neq j \\ \lambda_j, & i = j \end{cases}$$

Therefore,

$$\mathbf{L}^T \mathbf{A} \mathbf{R} \equiv \mathbf{\Lambda} = diag \; [\lambda_1,\ldots, \lambda_k,\ldots, \lambda_{2N}] \tag{7.18}$$

Eq. (7.18) is the diagonal matrix of the eigenvalues $\lambda$.

Substituting Eqs (7.17) and (7.18) into Eq. (7.16) gives

$$\dot{\mathbf{w}}(t) = \mathbf{\Lambda}\mathbf{w}(t) + \mathbf{c}(\mathbf{w}, t) \tag{7.19}$$

where

$$\mathbf{c}(\mathbf{w}, t) \equiv \mathbf{L}^T \mathbf{b}(\mathbf{w}, t) .$$

Equation (7.19) can be written in 2N first-order decoupled nonlinear equations as follows

$$\dot{w}_k(t) = \lambda_k w_k(t) + c_k(w_k, t); \quad k = 1,\ldots, 2N \tag{7.20}$$

within

$$c_k(w_k, t) = l_k^{*T} b(w_k, t) = \sum_{i=1}^{2N} l_{i,k}^* b_i(w_k, t) \tag{7.21}$$

By using the Runge-Kutta scheme with the higher order to solve Eq. (7.20), one obtains the solution $w_k(t)$ for the $k^{th}$ degree of freedom, and the response vector $\mathbf{w}(t)$.

Then, inserting $\mathbf{w}(t)$ in Eq. (7.15), one computes backwards the vector $\mathbf{z}(t)$.

$$z_i(t) = \sum_{k=1}^{2N} r_{i,k}^* w_k(t); \quad i = 1,\ldots, 2N \tag{7.22}$$

The unknown vibration response vector $\mathbf{x}(t)$ is given by the substitution of Eqs (7.22) and (7.2).

$$x_i(t) = z_i(t); \quad i = 1,\ldots, N \tag{7.23}$$

where
N is the degree of freedom of the rotor.

## 7.3   Synchronous and Asynchronous Vibrations

The nonlinear bearing forces, as discussed in Chapter 6, are mainly to blame for the rotor responses in nonlinear rotordynamics. The vibration responses are resulted from superimposing the asynchronous frequencies of such malfunctions, like unbalance, oil whirls, rotor misalignment, excessively large unbalance, contact rub, wear, and sidebands of the frequency modulations, on the unbalance harmonics in the nonlinear system, as shown in Fig. 7.3. Additionally, the working conditions of the turbochargers at oil shortage, contaminated oil, or high oil temperatures affect the rotor responses. Depending on the malfunctions, the rotor responses consist of at least two or many frequency components of the unbalance excitation, oil whirls, and sidebands. Therefore, they are periodic or quasi-periodic vibrations that are superimposed by the synchronous and asynchronous frequency components, as discussed in Chapter 3.

**Working conditions**

- oil shortage
- contaminated oil
- high oil temperature

**Malfunctions**

- Unbalance
- Oil whirls
- Misalignment
- Excessive unbalance
- Contact rub, wear
- Modulations

**Nonlinear Rotordynamics due to nonlinear bearing forces**

**Responses**

- 1X (unbalance)
- 0.5 … 0.1X (oil whirls)
- 2X (misalignment, excessive unbalance)
- 1/2X, 1/3X (contact rub)
- $m\omega_i \pm n\omega_j$ (sidebands)
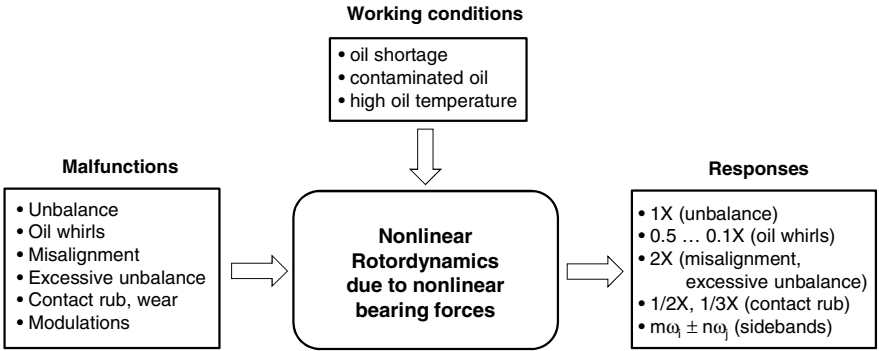
**Fig. 7.3** Rotor responses of nonlinear rotordynamics

The unbalance force excites the rotor with a harmonic vibration that is synchronous with the rotor speed at the frequency order of 1X. The rotor amplitude reaches a resonance when the eigenfrequency of the rotor equals the rotor frequency. The resonances occur at the intersections of the rotor eigenfrequencies and the synchronous excitation line 1X in the Campbell diagram.

Oil whirl is a kind of a self-excited vibration with the frequency order less than 1 (i.e. $\omega/\Omega < 1X$). Oil whirling in the bearing clearance induces the oil whirl. The rotational kinetic energy of the oil whirling excites the rotor and induces the subsynchronous self-excited vibration. When the whirl frequency $\omega$ equals the first critical bending frequency of the rotor, oil whip takes place in which the rotor amplitude continuously increases with time. The oil whip is very dangerous and destructive because the rotor deflection rises without limit in the bearing clearance and touches the bearing. It leads to bearing damage due to wear or seizure of the

journal in the bearing. The rotor speed where the oil whip begins occurring is called the threshold speed $\Omega_{th}$. In nonlinear rotordynamics, the rotor amplitude is mostly limited in the limit cycle, as discussed in Chapter 4. As long as the limit cycle is smaller the bearing clearance, the bearing contact does not happen.
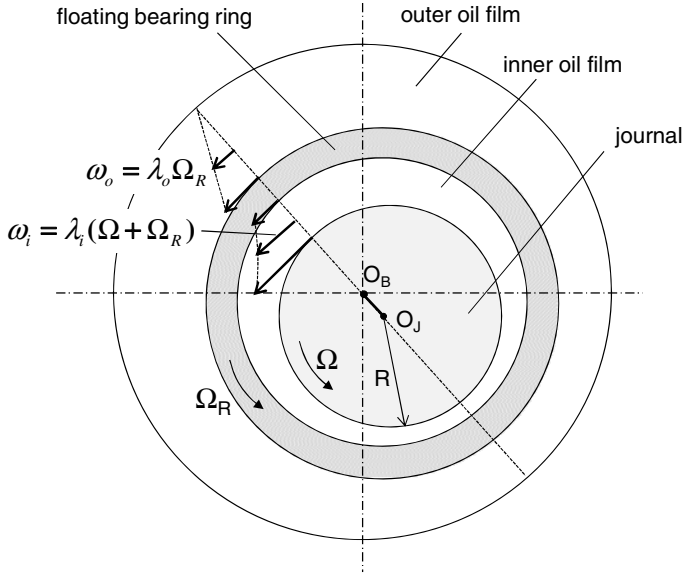


**Fig. 7.4** Oil whirl frequencies in the rotating floating radial bearing

The oil whirling frequency of the inner oil film (called inner-oil-whirl frequency) is resulted from the rotor speed $\Omega$ and bearing ring speed $\Omega_R$ (s. Section 7.5).

$$\omega_i = \lambda_i(\Omega + \Omega_R) = \lambda_i \Omega (1 + RSR) \qquad (7.24)$$

where

$\lambda_i$ is the fluid circumferential average velocity ratio of the inner oil film [11];

$RSR \equiv \dfrac{\Omega_R}{\Omega}$ is the ring speed ratio given in eq. (6.91a).

The ring speed ratio of the bearing was derived in Eq. (6.91a).

$$RSR \approx \cfrac{1}{1 + \cfrac{\eta_o(T_o)}{\eta_i(T_i)} \left(\cfrac{L_o}{L_i}\right)\left(\cfrac{c_1}{c_2}\right)\left(\cfrac{D_o}{D_i}\right)^3} \qquad (7.25)$$

The frequency order of the inner oil whirl results from Eq. (7.24) in

$$\frac{\omega_i}{\Omega} = \lambda_i(1 + RSR) \qquad (7.26)$$

The threshold speed $\Omega_{th}$ of the rotor is found by setting the inner oil-whirl frequency $\omega_i$ equals the critical frequency $\Omega_{cr,1}$.

$$\omega_i = \lambda_i (1 + RSR)\, \Omega_{th} \equiv \Omega_{cr,1} = \sqrt{\frac{K_{sys}}{m}} \tag{7.27}$$

Thus,

$$\Omega_{th} = \frac{1}{\lambda_i (1 + RSR)} \sqrt{\frac{K_{sys}}{m}} \tag{7.28}$$

where

$K_{sys}$ is the rotor stiffness coefficient including the shaft and bearing stiffness coefficients.

According to the computation of the ring speed ratio $RSR$ in Fig. 6.28, it varies with the oil inlet temperature from 0.30 to 0.05. Therefore, at low rotor speeds with $\lambda_i \approx 0.5$ and $RSR \approx 0.30$, the frequency order of the inner oil whirl results in

$$\frac{\omega_i}{\Omega} \approx 0.7 \text{ at low rotor speeds } \Omega. \tag{7.29a}$$

However, the oil average velocity ratio $\lambda_i$ reduces at increasing the journal eccentricities due to the oil friction in the narrow oil film (s. Fig. 7.11). Hence, it can be reduced from 0.5 to 0 at high rotor speeds. In this case, the frequency order of the inner oil whirl is calculated with $\lambda_i \approx 0.3$ and $RSR \approx 0.1$.

$$\frac{\omega_i}{\Omega} \approx 0.25...0.30 \text{ at high rotor speeds } \Omega. \tag{7.29b}$$

The oil whirl frequency of the outer oil film (called outer-oil-whirl frequency) is resulted only from the ring speed $\Omega_R$.

$$\omega_o = \lambda_o \Omega_R \tag{7.30}$$

where

$\lambda_0$ is the oil average velocity ratio of the outer oil film;

$\Omega_R \sim (0.30...0.15)\,\Omega$ at 120° C oil inlet temperature, as displayed in Fig. 6.28.

The oil velocity ratio $\lambda_o$ decreases from with the bearing ring eccentricity; therefore, the outer oil-whirl frequency order results in

$$\frac{\omega_o}{\Omega} \approx 0.10..0.15 \tag{7.31}$$

The response frequency orders of a typical turbocharger are found in Waterfall diagram (s. Fig. 7.5). The response orbit is a forward whirl, as displayed in Case History #3 (Section 3.6). In nonlinear rotordynamics, there is no apparent resonance but only quasi-resonance, unlike the typical resonance in linear rotordynamics. The reason for the quasi-resonance is explained that the bearing stiffness and damping coefficients increase with the rotor deflection; therefore, the eigenfrequency of the rotor continuously increases with the rotor deflection at raising the

rotor speed, so that the typical resonance does not happen obviously, instead a slight increase of the rotor amplitude. However, the resonance amplitude is relatively small compared to the oil whirl amplitudes. The orbit of the rotor response is limited in the limit cycle in nonlinear rotordynamics, as discussed in Chapter 4.
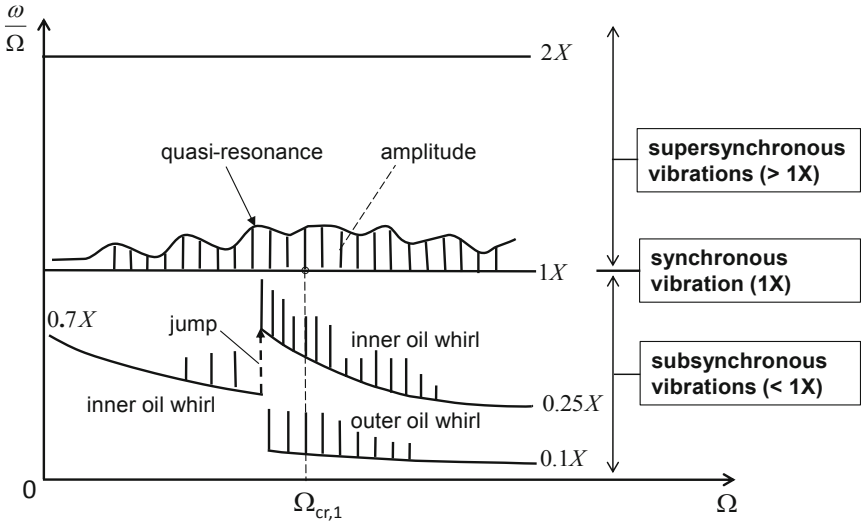


**Fig. 7.5** Modified Waterfall diagram of a typical turbocharger

In case of a contact rub at the normal tight condition in the bearings, the rotor response is resulted from the superimposition of the subsynchronous frequency components due to contact-rub-related nonlinearity on the unbalance vibration. In fact, the unbalance forces excite the subsynchronous frequency components of the nonlinear rotor to induce the rotor response. At the heavy rub in the bearings, the rub subsynchronous frequency components have fractional frequency orders of (1/2)X, (1/3)X, or higher orders. The fractional frequency orders (1/N)X indicates that one convolution of the whirl cycle is done in every N revolutions of the rotor; i.e., one rub contact takes place in the bearing in every N cycles of the rotor. In fact, the rotor bounces after it touched the bearing. Until the next contact rub occurs between the rotor and bearing, the rotor has made N revolutions during this time. Hence, the contact rub has a subsynchronous frequency order of (1/N)X. The rotor orbit corresponding to the unbalance and contact rub is a forward whirl, as shown in Case History #4 (Section 3.6).

In case of the misaligned or excessively large unbalanced rotor, such supersynchronous vibrations with multiple harmonic frequency orders of 2X, 3X occur in the nonlinear rotor. An excessively large unbalance of the rotor generally causes a large rotor deflection, leading to the contact rub at normally tight condition. Therefore, the subsynchronous frequency components with fractional frequency orders (1/2)X or (1/3)X occur as the consequence of the excessively large unbalance. The response orbit of the misaligned rotor is a forward whirl with a

"banana" shape. At increasing the radial bearing load, the response orbit changes from the "banana" to "lying eight" shape. The banana shape orbit bounces as it comes close to the bearing wall. In case of the very high radial loads in the bearing, the response orbit turns into the "lying eight" shape. On the contrary, the "lying eight" shape has the forward and backward loops. At the very high radial load at the bearing wall, the rotor bounces in the backward loop; as far away from the bearing wall, the radial load is decreased, the rotor moves in the forward loop, as displayed in Case History #5 (Section 3.6).

In the strongly nonlinear rotor, the sideband frequencies occur due to frequency modulations between the harmonic and asynchronous frequencies. The sideband frequencies consist of the sum of the multiple integers of all frequencies acting on the rotor. The frequency modulation shall be discussed later in Section 7.6.

In fact, it is very difficult to compute exactly such nonlinear effects, like the contact rub and wear due to the misalignment and excessively large unbalance of the rotor in the computation of nonlinear rotordynamics. The rotor response induced by the unbalance, inner, and outer oil whirls can be simulated in the nonlinear rotordynamics. However, the rotor responses caused by misalignment, contact rub, and wear could be recognized by the sideband frequencies in the measured Waterfall diagram.

## 7.4  Frequency Analysis in Waterfall Diagram

In nonlinear rotordynamics, Waterfall diagram (or frequency spectrum diagram) is used to analyze the frequency components over the rotor speed and whirl frequency. In fact, Waterfall diagram is the FFT (Fast Fourier Transform) of the rotor response; it is a three-dimensional diagram of spectra of the rotor deflection $\delta$ varying with the whirl frequency $\omega$ and rotor speed $\Omega$. The rotor deflection is displayed with the color scale in the vertical direction (s. Fig. 7.6).

To simplify the spectrum analysis, one plots the 3-D Waterfall diagram in a frequency spectrum diagram $\Omega$-$(\omega/\Omega)$, as shown in Figures 7.5 and 7.8. The color displayed in the frequency lines indicates the rotor amplitude; e.g., red for the maximum amplitude; blue for the minimum amplitude, and other colors for the amplitudes between the maximum and minimum values. This Waterfall diagram is called the modified Waterfall diagram, which is applicable to the turbocharger industry, instead of 3-D Waterfall diagrams.

The quasi-resonance of the rotor occurs at the first critical speed $\Omega_{cr,1}$ at which the rotor speed $\Omega$ equals the eigenfrequency $\omega$ in the excitation line 1X, as shown in Fig. 7.7. At further increasing the rotor speed, the inner oil-film temperature is higher than the outer oil film temperature due to larger bearing friction in the inner oil film; so, the damping coefficient of the inner oil film decreases. As soon as the destabilizing force induced by the cross-couple stiffness coefficient exceeds the damping force of the bearing, the inner oil whirl occurs with a frequency order of nearly 0.7X at low rotor speeds. The frequency order of the inner oil whirl is continuously reducing because the inner oil-film temperature further increases with the rotor speed, as discussed in Section 7.3.
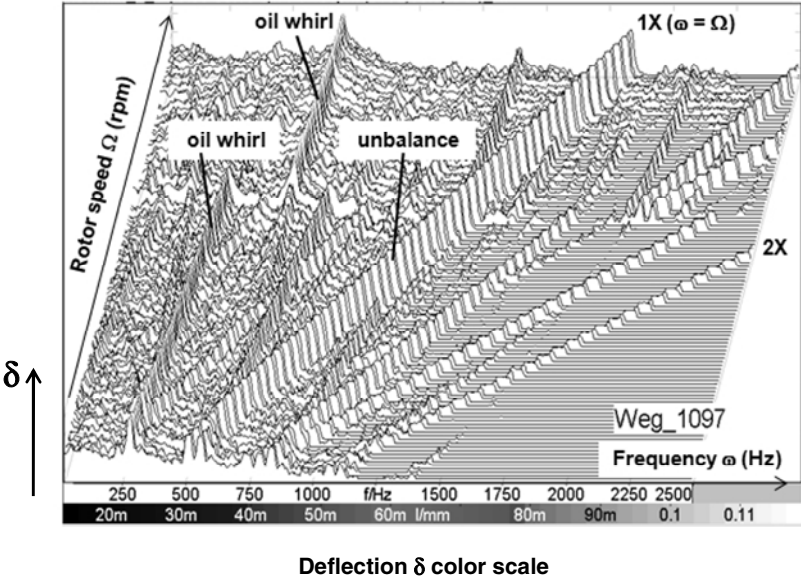
**Fig. 7.6** Typical three-dimensional Waterfall diagram
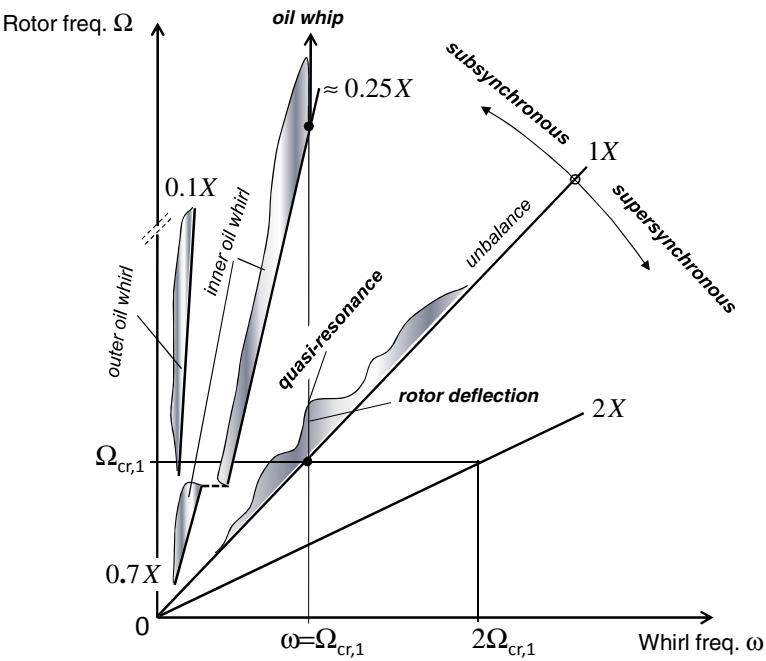


**Fig. 7.7** Modified two-dimensional Waterfall diagram

At increasing the rotor speed, the rotor unbalance becomes larger; hence, the vibration mode of the inner oil whirl changes from the conical into cylindrical mode in the inner bearing clearance. It leads to the jump of the inner oil whirl frequency, as shown in Fig. 7.8. The higher the rotor unbalance, the earlier the jump occurs; and vice versa. Therefore, the ring speed ratio RSR suddenly rises; the frequency order of the inner oil whirl jumps to the higher frequency order before the quasi-resonance occurs (s. Figs 7.5 and 7.7). After that, the inner oil whirl frequency order decreases with the rotor speed due to the increase of the inner oil-film temperature, and finally arrives at a frequency order of 0.20X to 0.25X.

Oil whip occurs at the threshold rotor speed at which the whirl frequency at 0.25X equals the first bending critical speed, as shown in Fig. 7.7. In this case, the oil whip takes place at the rotor speed of about four times of the first critical speed $\Omega_{cr,1}$. Therefore, the first critical frequency of the rotor should be designed as high as possible, so that the oil whip does not happen in the working speed range of the turbocharger. The outer oil whirl has the conical or cylindrical vibration mode; the frequency order is relatively small, reducing from 0.15X to 0.10X with the rotor speed according to Eq. (7.31). In case of the conical mode, the rotor amplitude induced by the outer oil whirl is much larger than the inner oil whirl amplitude because the outer bearing clearance is larger. Note that the outer oil whirl is less noisy because its whirl frequency is very small. The intensity of airborne noises is proportional to the whirl frequency squared ($I_{noise} \sim \omega^2$). On the contrary, the amplitude of the inner oil whirl is much lower but much noisy because the inner oil whirl frequency is higher; hence, it induces the constant tone.
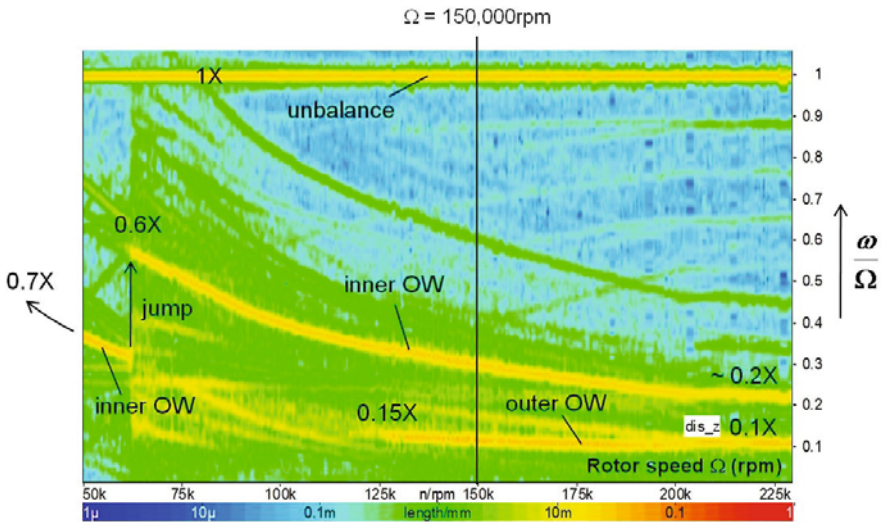


**Fig. 7.8** Measured Waterfall diagram of a turbocharger at 120°C oil [9]

At the given rotor speed of 150,000 rpm in Waterfall diagram (s. Fig. 7.8), the rotor consists of three frequency components of the unbalance (1X), inner oil whirl (ca. 0.30X), and outer oil whirl (nearly 0.12X). The amplitudes of each frequency

component are given in the curve of the frequency order $\omega/\Omega$ by the deflection color. The jump occurs at the rotor speed of about 65,000 rpm where the conical vibration mode changes into the cylindrical mode. The computed orbits of the journal locus in the rotating floating ring bearings are displayed in Figures 3.9c and 7.31.

## 7.5   Oil Whirl and Oil Whip in the Turbochargers

Oil whirl is a kind of the self-excited instability with a subsynchronous frequency that usually occurs in the automotive turbochargers. The occurrence of the oil whirl is caused by the oil whirling in the bearing clearance; therefore, it has nothing to do with the rotor unbalance. That means, it happens in the bearing without condition whether the rotor is well balanced or unbalanced. However, the strongly unbalanced rotor could reduce the oil whirl amplitude when the rotor is close to the bearing wall. Instability of the oil whirl at the threshold rotor speed leads to oil whip, which damages the bearing due to wear and seizure of the rotor in the bearing. Moreover, the inner oil whirl causes the airborne noise, called constant tone that is audible in the middle working range of the rotor speeds, particularly at the low oil temperature of 50°C. Therefore, the inner oil whirl is unwanted in the automotive turbochargers. In the following section, the root cause of the oil whirl is investigated, and discussed how to come up with the measure in order to reduce or eliminate the self-excitation instability of the oil whirl and its induced airborne noise in the turbochargers.

The computing model of the oil whirling in the inner bearing clearance shown in Figs 7.9 and 7.10 is used to investigate the cause of the oil whirl. At first, the journal moves outwards from the bearing center due to the rotor unbalance while the high oil pressure is generated in the convergent wedge of the bearing clearance. On the contrary, the low oil pressure occurs in the divergent wedge of the inner bearing clearance. As a result, the resulting oil pressure acting on the journal creates the bearing force.

### 7.5.1   Root Cause of the Oil Whirl

Having considered the convergent bearing clearance, the volumetric flow rate of oil at the inlet of the wedge is calculated.

$$\dot{Q}_{in} = v_{in} A_{in} = \lambda_i \left[ \Omega R + \Omega_R (R + c) \right] (c + e) L_i \qquad (7.32)$$

where
$\lambda_i$ is the fluid circumferential average velocity ratio [11];
c is the radial inner bearing clearance;
e is the journal eccentricity;
$L_i$ is the inner bearing width;
R is the journal radius.

$$v_{in} = \lambda_i [\Omega R + \Omega_R (R + c)]$$
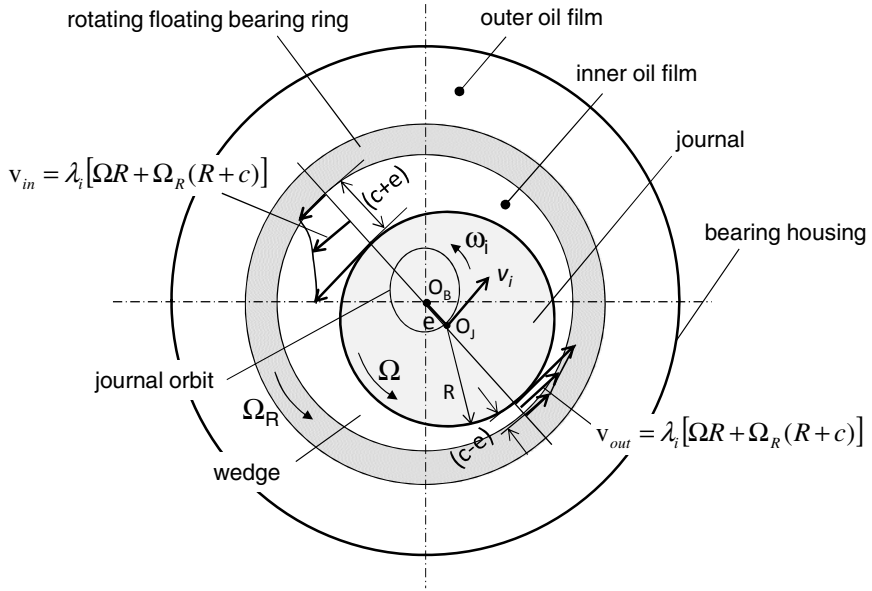
$$v_{out} = \lambda_i [\Omega R + \Omega_R (R + c)]$$

**Fig. 7.9** Oil whirling model in the inner bearing clearance

Analogous to Eq. (7.32), the volumetric flow rate of oil at the outlet of the wedge results in

$$\dot{Q}_{out} = v_{out} A_{out} = \lambda_i [\Omega R + \Omega_R (R + c)](c - e)L_i \qquad (7.33)$$

Obviously, the oil volumetric inflow in the convergent wedge is larger than the oil outflow from the wedge. As a reason, the journal has to move away from the wedge to satisfy the mass balance of the incompressible oil, with a whirling velocity $v_i$ perpendicular to the journal eccentricity e. However, oil can only flow in the axial direction to the ends of the bearing, but the axial outflow $\dot{Q}_{ax}$ is very small in a short time interval. During this time interval, the journal has whirled with a forward whirl speed $\omega_i$ corresponding to $v_i$, as shown in Fig. 7.9.

The surplus of oil flow rate in the wedge is resulted from Eqs (7.32) and (7.33).

$$\begin{aligned}
\Delta \dot{Q} = \dot{Q}_{in} - \dot{Q}_{out} &\approx 2RL_i e \lambda_i (\Omega + \Omega_R) \\
&= 2RL_i e \lambda_i \Omega (1 + RSR)
\end{aligned} \qquad (7.34)$$

where RSR = $\Omega/\Omega_R$ is the ring speed ratio of the bearing.

By the journal whirling, the oil removes the volumetric flow rate with the whirl speed $\omega_i$.

$$\dot{Q}_w = v_i A_i = (e\omega_i).(2RL_i) = 2RL_i e\omega_i \qquad (7.35)$$

where
$A_i$ is the whirling area of the journal ($A_i = 2RL_i$);
$\omega_i$ is the whirl speed of the journal.

Having used the continuity equation for the oil flow in the converged wedge, one obtains the relation between the volumetric flow rates.

$$\sum_i \dot{Q}_i = \Delta\dot{Q} - \dot{Q}_w - \dot{Q}_{ax} = 0 \qquad (7.36)$$

Thus,

$$2RL_i e\lambda_i(\Omega + \Omega_R) = 2RL_i e\omega_i + \dot{Q}_{ax} \qquad (7.37)$$

The forward whirl speed of the journal results in

$$\omega_i = \lambda_i(\Omega + \Omega_R) - \frac{\dot{Q}_{ax}}{2RL_i e} \qquad (7.38)$$

where
$\lambda_i \approx 0.5$ near the bearing center (s. Fig. 7.11).

Since the axial flow rate is negligibly small, Eq. (7.38) becomes with $\lambda_i \approx 0.5$.

$$\omega_i = \lambda_i(\Omega + \Omega_R) \approx \frac{1}{2}(\Omega + \Omega_R) \qquad (7.39a)$$
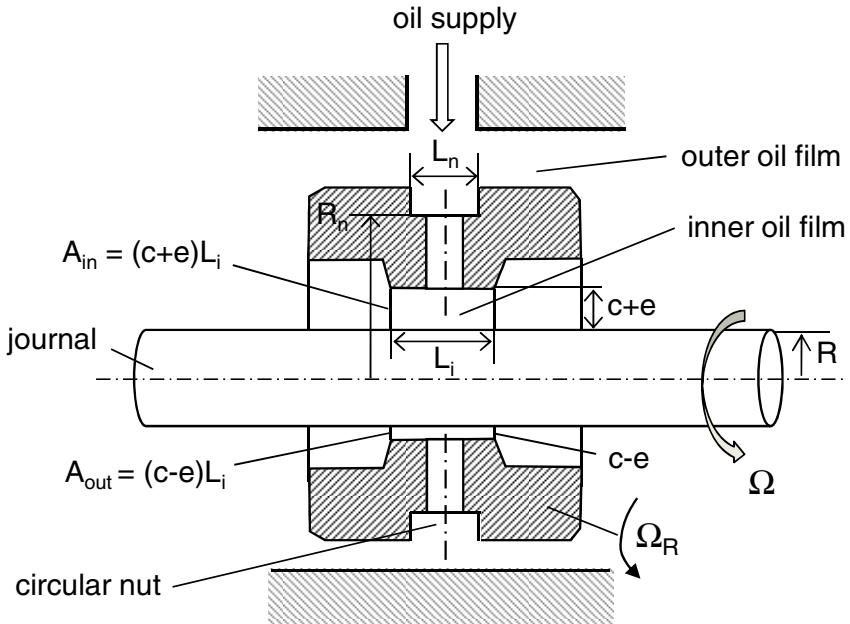


**Fig. 7.10** Flow cross-sectional areas in the radial bearing with a circular nut

Eq. (7.39a) proves that the assumption of the whirling speed of the inner oil whirl used in Eq. (7.24) is correct. In case of the semi-floating ring or fixed bearings at the bearing ring speed $\Omega_R$ equals zero, the oil whirl is usually called the half-frequency whirl ($\omega_i = \Omega/2$). This forward whirl speed $\omega_i$ of the journal induces an airborne noise called constant tone, which shall be discussed later in Section 7.7. The inner oil whirl is caused by the journal whirling with the whirl speed $\omega_i$ that depends on the velocity ratio $\lambda_i$. In fact, this velocity ratio varies with the journal relative eccentricity $\varepsilon$. Near the bearing center ($\varepsilon \approx 0$), the velocity ratio $\lambda$ is approximately 0.475 ($\approx 0.5$) by measurements in [11]. At increasing the journal eccentricity $\varepsilon$, the flow resistance in the bearing clearance rises due to the viscous friction in the oil boundary layer. Hence, the velocity profile becomes much concave, leading to decrease of the velocity ratio. Due to bearing contact with the journal, the velocity ratio $\lambda$ goes to zero as the journal moves close to the bearing wall ($\varepsilon \rightarrow 1$). Figure 7.11 displays the qualitative behavior of the average velocity ratio versus the journal relative eccentricity.
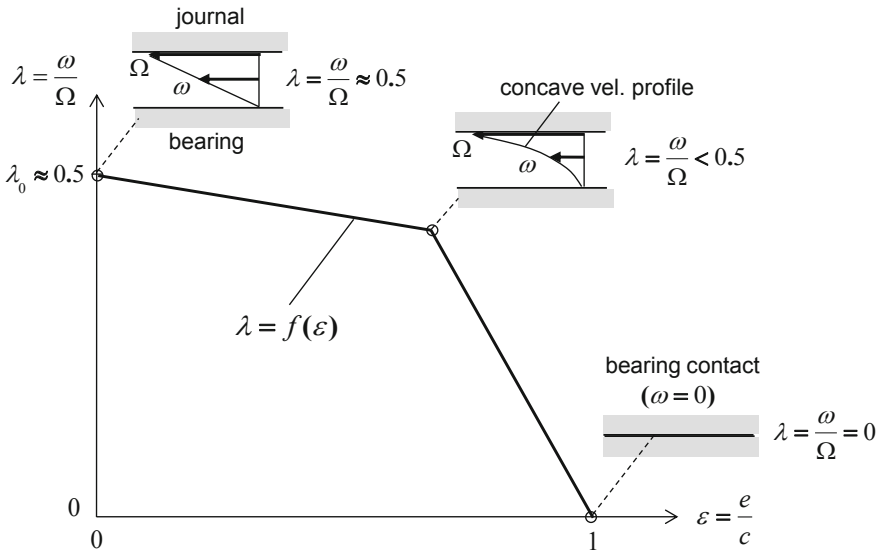


**Fig. 7.11** Velocity ratio $\lambda$ versus journal relative eccentricity $\varepsilon$

In case of the radial bearing with a circular nut in the outer bearing surface (s. Fig. 7.10), two outer oil whirls (called twofold outer oil whirl) mostly occur in the Waterfall diagram. According to eq. (7.30), the first outer oil whirl speed is calculated at a negligibly small axial flow rate due to the small outer bearing clearance.

$$\omega_{o,1} \approx \lambda_o \Omega_R \qquad (7.39b)$$

where $\Omega_R$ is the bearing ring speed.

The second outer oil whirl speed due to the circular nut is given according to eq. (7.38) as follows:

$$\omega_{o,2} = \lambda_o \Omega_R - \frac{\dot{Q}_{ax}}{2 R_n L_n e_n} < \omega_{o,1} \tag{7.39c}$$

The axial flow rate in eq. (7.39c) is no longer negligible because it flows in the inner oil film through the oil holes. The difference between both whirl frequencies is proportional to the second term in the right-hand side of eq. (7.39c). Similarly, the twofold inner oil whirl is induced in the inner oil film.

## 7.5.2  Threshold of Instability

To investigate the threshold of instability of the oil whirl, the force balance of the journal in the bearing is applied to the computed journal model, as displayed in Fig. 7.12. In the radial direction r, the journal stiffness force Ke, bearing cross-couple damping force $- jc_c\dot{e}$, inertial force $m\ddot{e}$, and centripetal force $mr_\varepsilon\omega^2 e^{j\alpha t}$ act on the journal. In the tangential direction t, the destabilizing force $jk_c e$ caused by the cross-couple stiffness coefficient $k_c$ of the oil-film and the damping force of the bearing $- jc\omega e$ act on the journal.

Have applied the impulse momentum theorem to the journal, its vibration equation is written in the rotating coordinate system (r,t).

$$m\ddot{e} + (c - jc_c)\dot{e} + (K - jk_c)e = mr_\varepsilon\omega^2 e^{j\alpha t} \tag{7.40}$$

where
m is the rotor mass;
j is the imaginary unit ($j^2$ = -1);
e is the eccentricity of the journal;
c is the diagonal damping coefficient of the oil-film bearing;
$c_c$ is the cross-couple damping coefficient of the oil-film bearing;
K is the stiffness coefficient of the shaft;
$k_c$ is the cross-couple stiffness coefficient of the oil-film bearing;
ω is the whirl speed of the journal in the bearing;
$r_\varepsilon$ is the unbalance radius of the rotor.

Having assumed that the journal response is an exponential function of the eigenvalue s and time t.

$$e(t) = Ae^{st} \tag{7.41}$$

where
s is the complex eigenvalue including the real part α and imaginary part $\omega_n$.

$$s = \alpha \pm j\omega_n \tag{7.42}$$
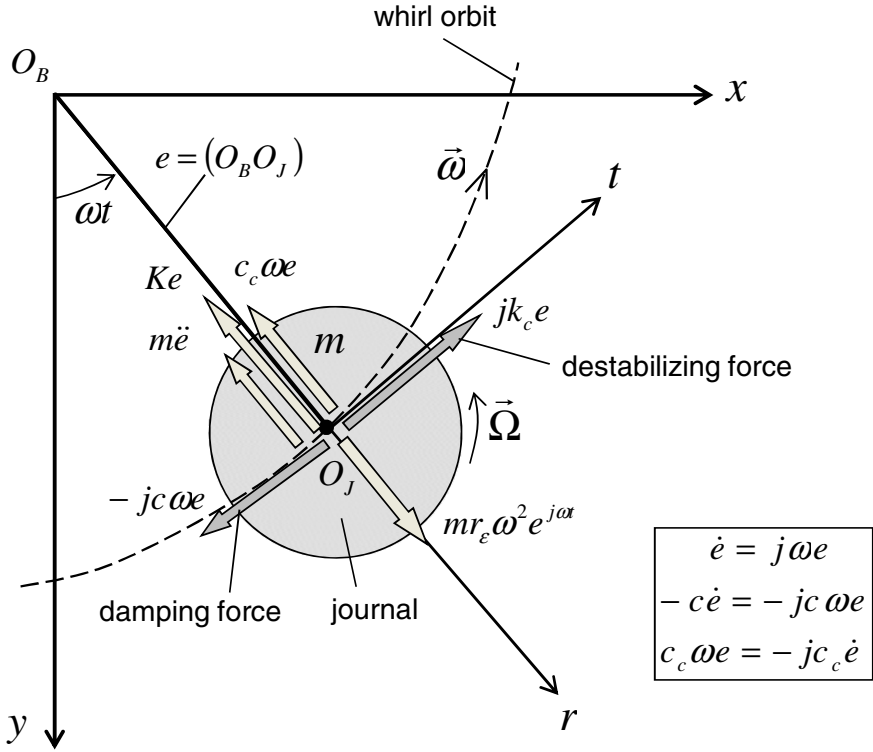
**Fig 7.12** Forces acting upon the journal in an oil-film radial bearing

By twice differentiating Eq. (7.41), one gets

$$\dot{e} = sAe^{st}; \quad \ddot{e} = s^2 Ae^{st} \tag{7.43}$$

Substituting eqs (7.41) and (7.43) into the homogeneous equation of Eq. (7.40), the characteristic equation results in

$$D(s) \equiv ms^2 + (c - jc_c)s + (K - jk_c) = 0 \tag{7.44}$$

The cross-couple stiffness coefficient $k_c$ of the bearing is generated by the whirl speed $\omega$; therefore, it is proportional to $\lambda\Omega$ and written in, s. [11]

$$k_c \equiv c\lambda\Omega \tag{7.45}$$

Thus, the characteristic equation (7.44) becomes

$$D(s) \equiv ms^2 + (c - jc_c)s + (K - jc\lambda\Omega) = 0 \tag{7.46}$$

The rotor stability condition is satisfied if the real part of the complex eigenvalue s is negative. The real part $\alpha$ is calculated as (s. Appendix C).

$$\alpha = -\frac{c}{2m} \pm \frac{1}{\sqrt{2}} \left[ -E + \sqrt{E^2 + F^2} \right]^{\frac{1}{2}} < 0 \qquad (7.47)$$

where

$$E \equiv \frac{K}{m} - \left( \frac{c^2 - c_c^2}{4m^2} \right); \quad F \equiv \frac{c}{m} \left( \lambda\Omega - \frac{c_c}{2m} \right)$$

By solving Eq. (7.47), one obtains the rotor stability condition of the oil whirl.

$$0 < \lambda\Omega < \frac{c_c}{2m} + \sqrt{\frac{K}{m} + \left( \frac{c_c}{2m} \right)^2} \qquad (7.48)$$

The frequency of the threshold of instability results in at $\alpha = 0$, where the oil whip takes place.

$$\Omega_{th} = \frac{1}{\lambda} \left( \frac{c_c}{2m} + \sqrt{\frac{K}{m} + \left( \frac{c_c}{2m} \right)^2} \right) \qquad (7.49)$$

where
$\lambda$ is the fluid average velocity ratio, as shown in Fig. 7.11.

The rotor response of Eq. (7.40) can be written in with a vibration phase $\beta$.

$$e(t) = A e^{j(\omega t + \beta)} \qquad (7.50)$$

Substituting Eqs (7.43) and (7.50) and into Eq. (7.40) with $k_c = c\lambda\Omega$, one obtains

$$\left( (K - m\omega^2 + c_c\omega) + jc(\omega - \lambda\Omega) \right) A e^{j(\alpha t + \beta)} = m r_\varepsilon \omega^2 e^{j\alpha t} \qquad (7.51)$$

The response amplitude of the journal is resulted in

$$A = \frac{\left| m r_\varepsilon \omega^2 e^{-j\beta} \right|}{\left| (K - m\omega^2 + c_c\omega) + jc(\omega - \lambda\Omega) \right|} \qquad (7.52)$$

Thus,

$$A = \frac{m r_\varepsilon \omega^2}{\sqrt{(K - m\omega^2 + c_c\omega)^2 + c^2(\omega - \lambda\Omega)^2}} \qquad (7.53)$$

The frequency of the threshold of instability is arrived when the amplitude A goes to infinity. Therefore, two working conditions are necessary at the same time:

$$K - m\omega^2 + c_c\omega = 0 \qquad (7.54a)$$

and

$$c(\omega - \lambda\Omega) = 0 \qquad (7.54b)$$

The first and second conditions in Eqs (7.54a) and (7.54b) give

$$\omega_{1,2} = \frac{c_c}{2m} \pm \sqrt{\frac{K}{m} + \left(\frac{c_c}{2m}\right)^2}$$ (7.55a)

and

$$\omega = \lambda\Omega$$ (7.55b)

Thus, the frequency of the threshold of instability is resulted by fulfilling both necessary conditions given in Eqs (7.55a) and (7.55b).

$$\Omega_{th} = \frac{1}{\lambda}\left(\frac{c_c}{2m} + \sqrt{\frac{K}{m} + \left(\frac{c_c}{2m}\right)^2}\right)$$ (7.56)

The threshold frequency $\Omega_{th}$ derived in Eq. (7.56) is the same threshold frequency in Eq. (7.49) that is resulted by solving the characteristic equation (7.46).

In case of the term $c_c/(2m)$ is negligibly small, the threshold frequency of the oil whirl becomes

$$\Omega_{th} = \frac{1}{\lambda}\sqrt{\frac{K}{m}} = \frac{\Omega_{cr,1}}{\lambda}$$ (7.57)

Equation (7.57) gives the stability condition for the oil whirl at $\alpha < 0$:

$$0 < \lambda\Omega < \sqrt{\frac{K}{m}}$$ (7.58)

where

$K$ is the rotor stiffness coefficient containing the shaft and bearing stiffness coefficients.

Oil whip occurs at the threshold speed $\Omega_{th}$ of the rotor at which the oil whirl frequency equals the first bending critical frequency. The oil whip, a kind of self-excited instability occurs when the rotor speed equals or exceeds the threshold speed. It is very dangerous and destructive because the rotor defection continuously increases with time in the bearing clearance, leading to bearing damage due to wear or seizure of the journal in the bearing.

## 7.6 Modulations of Vibrations

In the nonlinear rotordynamic system, some malfunctions, such as, rotor unbalance, oil whirl, misalignment, heavy rub, and excessively large unbalance cause truncations of the vibrations; therefore, the sidebands are additionally generated. The sideband frequencies are resulted by adding and subtracting multiple integers of the frequency components of the malfunctions. This is called frequency modulation (FM) of the frequency components in the nonlinear system.

Most of the sidebands take place at the high rotor speeds and amplify the amplitude of the rotor response. The sidebands occur at the sub- and supersynchronous

frequencies, which are generated by frequency components of the malfunctions. Note that the more visibly the sidebands appear in Waterfall diagram, the more nonlinearly the rotor system responds. The response amplitude of the strongly non-linear system is resulted from all component amplitudes of the malfunctions and as well as sidebands. As a reason, the rotor response amplitude is intensified; the rotor behavior becomes much more nonlinear at the large amplitudes.

## 7.6.1 Responses of Nonlinear Vibration Systems

Having considered a nonlinear rotordynamic system, the system response y(x) is resulted from the input signal x(t) with large amplitudes and the system transfer impedance $Z(\varepsilon)$, as shown in Fig. 7.13.
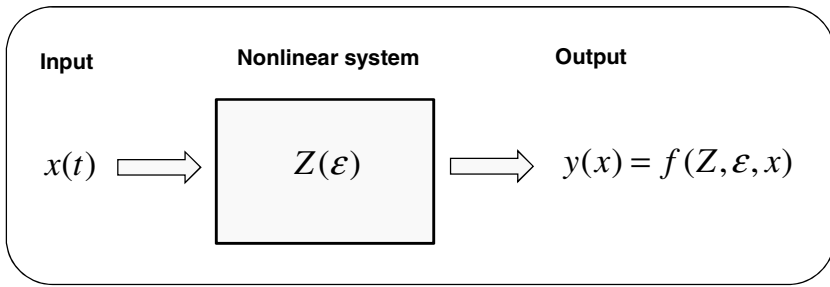


**Fig. 7.13** Response of a nonlinear vibration system

The nonlinear response y(x) of the system is written in the second order of the input function x(t).

$$y(x) = f(x,\varepsilon) = Z\left(x + \varepsilon.\mathrm{sgn}(x)x^2 + ...\right)$$
$$= Z(x + \varepsilon^* x^2 + ...)$$

(7.59)

where
x is the input signal with large amplitudes;
Z is the complex transfer impedance of the system;
Zx is the linear term of the response;
$\varepsilon$ is the nonlinear system factor ($\varepsilon \ll 1$);
$Z\varepsilon^* x^2$ is the nonlinear term of the response;
$\varepsilon^* = \varepsilon.\mathrm{sgn}(x)$ within sgn(x) is the signum function of x, which is defined as

$$\mathrm{sgn}(x) = \begin{cases} -1 & if \ x < 0 \\ 0 & if \ x = 0 \\ +1 & if \ x > 0 \end{cases}$$

Therefore,

$$\varepsilon^* \equiv \varepsilon \, \text{sgn}(\,x\,) = \begin{cases} -\varepsilon & \text{if } x < 0 \\ \phantom{-}0 & \text{if } x = 0 \\ +\varepsilon & \text{if } x > 0 \end{cases}$$

The nonlinear vibration response becomes

$$y(x) = Zx + Z\varepsilon \, \text{sgn}(\,x\,)x^2 + O(x^3) \tag{7.60}$$

The nonlinear vibration response $y(x)$ is displayed in Fig. 7.14, and compared to the linear response. In the linear system, the response of $Zx$ is proportional to the input function x. On the contrary, the nonlinear response is different to the linear term of $Zx$; it increases or decreases more quickly with the input amplitude $x(t)$ because the nonlinear term is proportional to $x^2$. As a reason, the nonlinear system can only be linearized at the small amplitudes because the nonlinear term is quite small.

   In case of the excessively large unbalance, the system behavior is strongly nonlinear. Thus, the response amplitude $y(x)$ increases faster than the amplitude of the linear system since the nonlinear term increases with the input amplitude squared that is no longer negligible, as shown in Fig. 7.14.
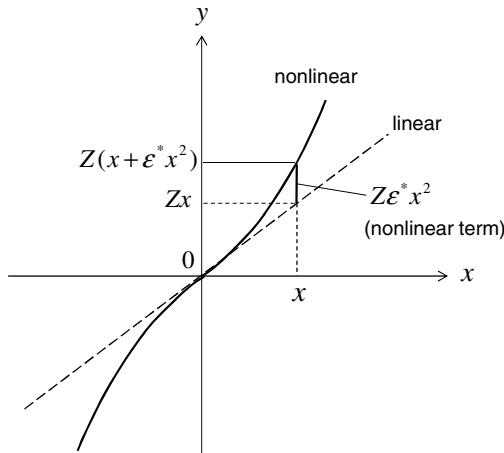


**Fig. 7.14** Comparison of the linear and nonlinear responses

## 7.6.2   Modulated Sideband Frequencies

Having supposed that the input $x(t)$ is a harmonic vibration with the amplitude X and single frequency $\omega_1$.

$$x = X \cos \omega_1 t \tag{7.61}$$

Its response is resulted from Eq. (7.59) with a second order of $x(t)$.

$$y = ZX \cos \omega_1 t + Z\varepsilon^* X^2 \cos^2 \omega_1 t$$

$$\equiv y_{L-term} + y_{NL-term}$$

(7.62)

The rotor response consists of two terms, the first term $y_{L-term}$ is linear with x(t) and the latter $y_{NL-term}$ is the nonlinear term of $x^2$. The nonlinear term can be written in other trigonometric formulation.

$$y_{L-term} \equiv ZX \cos \omega_1 t;$$

(7.63a)

$$y_{NL-term} \equiv Z\varepsilon^* x^2 = Z\varepsilon^* X^2 \cos^2 \omega_1 t$$

$$= \frac{1}{2} Z\varepsilon^* X^2 (1 + \cos 2\omega_1 t)$$

(7.63b)

By substituting of Eqs (7.62), (7.63a), and (7.63b), one gets the overall rotor response.

$$y = ZX \cos \omega_1 t + \frac{1}{2} Z\varepsilon^* X^2 + \frac{1}{2} Z\varepsilon^* X^2 \cos 2\omega_1 t$$

(7.64)

Compared to the linear system, the nonlinear response has two new additional terms: the rectification term of $X^2$ and the second-order harmonic term of $2\omega_1$.

Now, we consider the input function x(t) of a periodic vibration containing two frequency components of $\omega_1$ and $\omega_2$ and corresponding amplitudes $X_1$ and $X_2$.

$$x = X_1 \cos \omega_1 t + X_2 \cos \omega_2 t; \quad \omega_1 > \omega_2$$

(7.65)

To simplify, we consider only the nonlinear term of the rotor response in the following calculation.

$$y_{NL-term} \equiv Z\varepsilon^* x^2 = Z\varepsilon^* (X_1 \cos \omega_1 t + X_2 \cos \omega_2 t)^2$$

$$= Z\varepsilon^* (X_1^2 \cos^2 \omega_1 t + X_2^2 \cos^2 \omega_2 t + 2X_1 X_2 \cos \omega_1 t.\cos \omega_2 t)$$

$$\equiv y_1 + y_2 + y_3$$

(7.66)

Similarly, the first two terms $y_1$ and $y_2$ provide two additional second-order harmonics of the frequencies $2\omega_1$ and $2\omega_2$, respectively. Furthermore, one obtains the third term $y_3$ that generates sidebands of $\omega_1$ and $\omega_2$ after a few trigonometric calculating steps.

$$y_3 = Z\varepsilon^* X_1 X_2 (2 \cos \omega_1 t.\cos \omega_2 t)$$

$$= Z\varepsilon^* X_1 X_2 [\cos(\omega_1 t - \omega_2 t) + \cos(\omega_1 t + \omega_2 t)]$$

$$= Z\varepsilon^* X_1 X_2 [\cos(\omega_1 - \omega_2)t + \cos(\omega_1 + \omega_2)t]$$

$$\equiv Z\varepsilon^* X_1 X_2 (\cos \omega_{LSB} t + \cos \omega_{USB} t)$$

(7.67)

with

$$\omega_{USB} = \omega_1 + \omega_2; \quad \omega_{LSB} = \omega_1 - \omega_2 \qquad (7.68)$$

where

$\omega_{USB}$ is the upper sideband frequency (rad/s);
$\omega_{LSB}$ is the lower sideband frequency (rad/s).

Thus,

$$\omega_1 = \tfrac{1}{2}(\omega_{USB} + \omega_{LSB}) \equiv \omega_c = 2\pi f_c; \qquad (7.69)$$

with $f_c$ is defined as the carrier frequency (1/s);

$$\omega_2 = \tfrac{1}{2}(\omega_{USB} - \omega_{LSB}) \equiv \omega_m = 2\pi f_m; \qquad (7.70)$$

with $f_m$ is defined as the modulation frequency (1/s).

Figure 7.15 shows the sideband frequencies of the modulation. Due to nonlinearity of the system, the lower and upper sidebands are induced by the amplitude and frequency modulations of $f_c$ and $f_m$. In fact, the sideband frequency varies in a bandwidth of frequency $\Delta f_m$, e.g. in case of oil whirl. Therefore, the sideband frequencies $f_{LSB}$ and $f_{USB}$ scatter in the corresponding frequency bandwidth $\Delta f_m$.
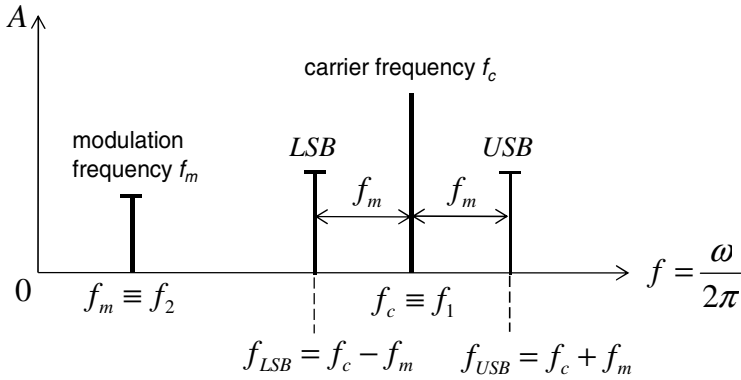


**Fig. 7.15** Frequency modulation of double sidebands

In the radio engineering, the carrier frequency $f_c$ is much higher than the modulation frequency $f_m$ ($f_c \gg f_m$). To broadcast the modulation signal in a long distance, the carrier signal modulates it in the double sideband (DSB) containing the lower (LSB) and upper sidebands (USB) with the ultra-high frequencies $f_{LSB}$ and $f_{USB}$ (s. Figs 7.15 and 7.16). The sideband frequencies are modulated by the carrier and modulation frequencies in the wide band of frequency.
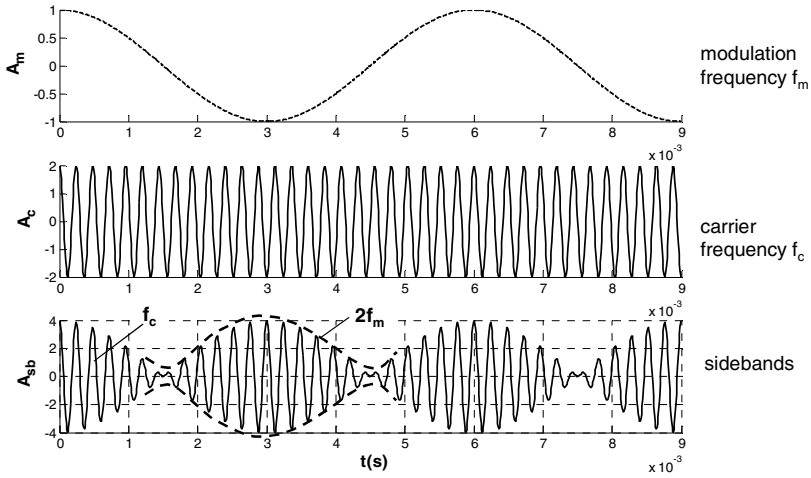
**Fig. 7.16** Double sideband (DSB) of the frequency modulation

The modulation frequency $f_m$ is normally the human voice frequency spreading from 300 Hz to 3 kHz; therefore, the sidebands are generated with the maximum frequency width of the DSB of $2f_m$ about 6 kHz. The modulation signal is recovered at receiving by using demodulation or detection of the received sideband signals where the signal detector and low-pass filter are used. The entire process of sending and receiving signal is carried out by the MODEM method that consists of MOdulation and DEModulation of the signals, generally applied in the wide band technique.

The sideband signal generated by the carrier and modulating signals is displayed in Fig. 7.16, in which one finds the carrier and modulation frequencies again in the sideband signal. The envelop signal of the sideband has a frequency of $2f_m$ since its period equals one-half of the period of the modulation signal, as shown in Fig. 7.17.

The lower and upper sideband frequencies of $f_{LSB}$ and $f_{USB}$ are calculated from the carrier $f_c$ and modulation frequencies $f_m$ with $f_m \ll f_c$; hence, $f_1 \gg f_2$:

- Lower sideband frequency (LSB):

$$f_{LSB} = f_c - f_m \equiv f_1 - f_2 \tag{7.71}$$

- Upper sideband frequency (USB):

$$f_{USB} = f_c + f_m \equiv f_1 + f_2 \tag{7.72}$$

$$T_c = \frac{1}{f_c} \qquad T_{sb} = \frac{1}{2} T_m = \frac{1}{2 f_m}$$
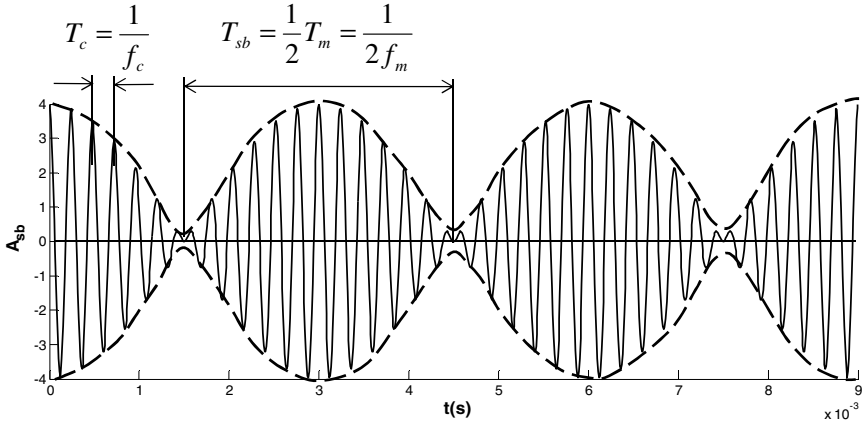
**Fig. 7.17** Frequencies and periods of the sideband signal

To sum up, the nonlinear rotordynamic system induces some new additional terms due to the amplitude and frequency modulations as follows:

- The rectification term $\frac{1}{2} Z \varepsilon^* X^2$ in Eq. (7.64);

- Second-order harmonic frequencies of $2\omega_1$ and $2\omega_2$ with the amplitudes $X_1^2$ and $X_2^2$ in Eqs (7.64) and (7.66);

- Sideband frequencies modulated by the excitation frequencies of $\omega_1$ and $\omega_2$ have the amplitudes that are proportional to the term of $Z\varepsilon^* X_1 X_2$. According to Eqs (7.67) and (7.68), the sideband frequencies are the sum or difference of the frequency components; hence, the first-order sideband frequencies result in $3\omega_2$-$2\omega_1$, $2\omega_2$-$\omega_1$, $2\omega_1$-$\omega_2$, $3\omega_1$-$2\omega_2$, $4\omega_1$-$3\omega_2$, etc., s. Eqs (7.74a), (7.74b), and Fig. 7.21.

In case of the unbalanced and misaligned rotor, the sidebands induced by the frequency modulations of misalignment, unbalance, and inner oil whirl are found in Waterfall diagram of noise spectra in Fig. 7.18.

Beat phenomenon, a special case of the modulation, is caused by the modulation of two harmonic vibrations with the frequency components of $\omega_1$ and $\omega_2$ that are close to each other. If their amplitudes are equal, only the amplitude modulation occurs. Otherwise, both amplitude and frequency modulations take place at the same time. The input signal is the sum of two sinus functions with the amplitudes $a_1 = a_2 \equiv a$.

$$
\begin{aligned}
x &= a_1 \sin \omega_1 t + a_2 \sin \omega_2 t \\
&= a(\sin \omega_1 t + \sin \omega_2 t) \\
&= 2a \sin\left[\tfrac{1}{2}(\omega_1 + \omega_2)\right] t . \cos\left[\tfrac{1}{2}(\omega_1 - \omega_2)\right] t \\
&\equiv 2a \sin \omega_c t . \cos \omega_m t
\end{aligned}
\qquad (7.73)
$$

where

$$\omega_c = \tfrac{1}{2}(\omega_1 + \omega_2) = 2\pi f_c \, ;$$

with $f_c$ is the carrier frequency.

$$\omega_m = \tfrac{1}{2}(\omega_1 - \omega_2) = 2\pi f_m \, ;$$

with $f_m$ is the modulation frequency.
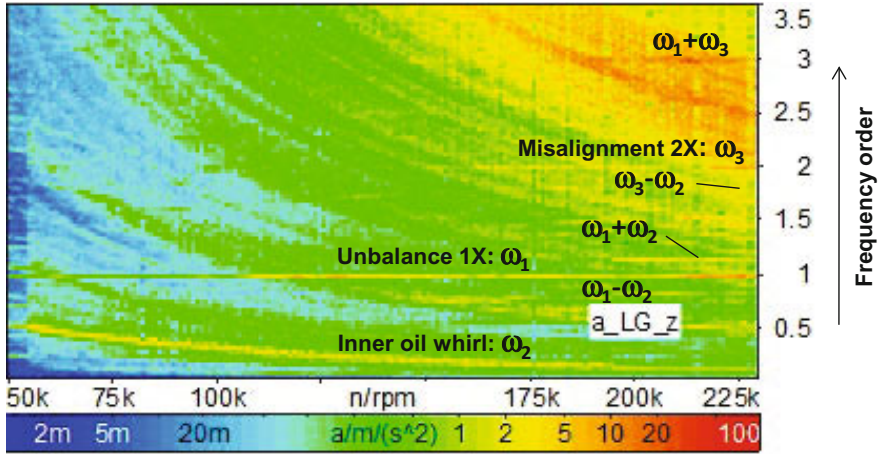


**Fig. 7.18** Sideband frequencies in Waterfall diagram [9]
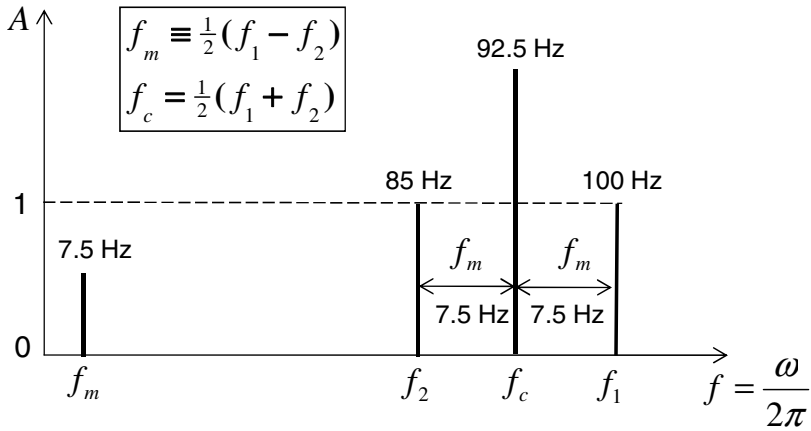


**Fig. 7.19** Beat frequency $2f_m$ of the frequencies $f_1$ and $f_2$

We choose two frequency components of $f_1 = 100$ Hz and $f_2 = 85$ Hz for the beat modulation that is shown in the frequency domain (s. Fig. 7.19). The carrier frequency $f_c$ is the average frequencies of $f_1$ and $f_2$ and equals 92.5 Hz, and the modulation frequency $f_m$ equals 7.5 Hz. The beat frequency of $2f_m$(15 Hz) is defined as the frequency difference of $f_1$ and $f_2$.

Figure 7.20 shows that the closer the frequency components, the smaller the beat frequency; obviously, the larger the period of the beat signal. The beat period is inversely related to the beat frequency $2f_m$; hence, the beat period is about 0.067 s at the beat frequency of 15 Hz. The carrier frequency has a period of 0.011 s at 92.5 Hz in the time domain.

$$T_c = \frac{1}{f_c} = \frac{1}{\frac{1}{2}(f_2 + f_1)} = 0.011\,s \qquad T_b = \frac{1}{2f_m} = \frac{1}{(f_1 - f_2)} = 0.067\,s$$
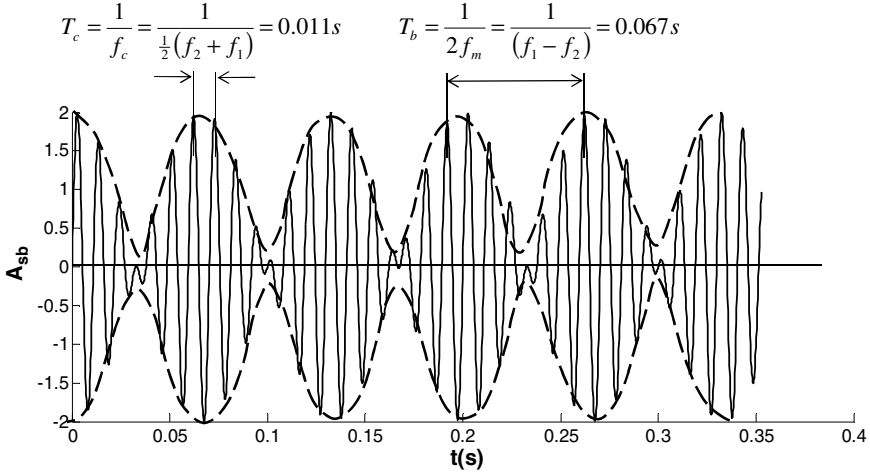


**Fig. 7.20** Beat response in the time domain

The generated first-order frequencies of the LSB and USB sidebands are resulted from the sum or difference of the frequency components of $f_1$ and $f_2$, which are located in the left and right hand-sides of the carrier frequency $f_c$, as plotted in Fig. 7.21.

$$f_{LSB} = \begin{cases} f_1 - 2f_m = f_c - f_m = f_2 \\ f_1 - 4f_m = f_c - 3f_m = 2f_2 - f_1 \\ f_1 - 6f_m = f_c - 5f_m = 3f_2 - 2f_1 \\ \dots \end{cases} \tag{7.74a}$$

and

$$f_{USB} = \begin{cases} f_1 + 0f_m = f_c + f_m = f_1 \\ f_1 + 2f_m = f_c + 3f_m = 2f_1 - f_2 \\ f_1 + 4f_m = f_c + 5f_m = 3f_1 - 2f_2 \\ f_1 + 6f_m = f_c + 7f_m = 4f_1 - 3f_2 \\ \dots \end{cases} \tag{7.74b}$$
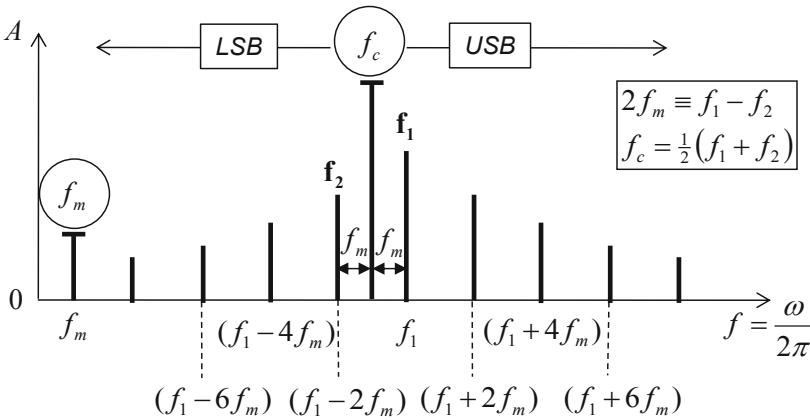
**Fig. 7.21** LSB and USB sideband frequencies

However, the nonlinear terms of the rotor response are not only proportional to the input amplitude squared $x^2$ but also the high-order input amplitude, such as $x^3$ or higher orders compared to eq. (7.59). According to Ehrich [4], the truncation of the modulation frequencies of $f_1$ and $f_2$ could induce two new second harmonic frequencies of $(f_1 - f_2)$ and $(f_1 + f_2)$ that in turn generate the third harmonics of $(2f_2 + f_1)$ and $(2f_1 + f_2)$ in a strongly nonlinear rotor system, as demonstrated in Table 7.1.

**Table 7.1** Sideband frequencies generated by the frequency modulations

| Lower sideband (LSB) | | | $f_c$ | Upper sideband (USB) | | | f Order |
|---|---|---|---|---|---|---|---|
| | $2f_2 - f_1$ | $f_2$ | $(f_1 + f_2)/2$ | $f_1$ | $2f_1 - f_2$ | | 1X |
| $3f_2 - f_1$ | | $2f_2$ | $(f_1 + f_2)$ | | $2f_1$ | $3f_1 - f_2$ | 2X |
| $4f_2 - f_1$ | $3f_2$ | $2f_2 + f_1$ | $3(f_1 + f_2)/2$ | $2f_1 + f_2$ | $3f_1$ | $4f_1 - f_2$ | 3X |

To generate the LSB frequencies, one substitutes the excitation frequency $f_2$ to $(2f_2 - f_1)$ to get the second-order frequency $(3f_2 - f_1)$ following the thin arrow, and substituting $f_2$ again into the second-order frequency to generate the third-order frequency $(4f_2 - f_1)$. Another way, following the dark arrow, one obtains the new high-order harmonic frequencies of $2f_2$ and $3f_2$ by adding $f_2$ to itself and $2f_2$, respectively. In order to receive the third-order frequency $(2f_2 + f_1)$, one does the same way by adding $f_2$ to $(f_1 + f_2)$ in the direction of the dash arrow. Similarly, the USB frequencies are generated as the same way.

## 7.7 Induced Airborne Noises in the Turbochargers

Noises induced in the turbocharger transmit through the bearing oil films, bearing housing, exhaust-gas manifold, engine block, and exhaust-gas pipe to car inside. The induced noises excite vibrations of the exhaust-gas pipe and chassis and generate the airborne noises that are uncomfortable for drivers and passengers. They are undesirable and therefore should be reduced in the passenger vehicles.

### 7.7.1 Classification of Noises

The induced noises in the turbocharger are caused by the airflow in the compressor wheel, rotation of the compressor and turbine wheels, rotor unbalance, and oil whirling in the radial bearings. They excite the vibrations of the intake air filter, charge air intercooler, and exhaust gas system and therefore cause the airborne noises to the environment.

- *Pulsation noise* is caused by the different volume chambers of the compressor wheel. Its frequency spreads from 1,200 Hz to 4,500 Hz that occurs at the engine speed range from 1,500 rpm to 3,500 rpm in the second gear with the high loads, and depends on the number of unequal chambers of the compressor wheel.

- *Rotation noise (rotating-blades-related noise)* is generated by the rotating blades of the compressor or turbine wheels at the engine speed range from 1,400 rpm to 2,500 rpm at the second and third gear. These noises have very high frequencies between about 3,000 Hz and 18,000 Hz or higher that are resulted from the number of blades and rotor speed. Although human ears cannot recognize noises higher than 16 kHz, animals inside the car could hear such high-frequency noises.

- *Growling noise (compressor-stall-related noise)* is induced by the partial recirculation of the intake air in the compressor wheel due to flow separation at the blades. Its frequency spreads in a wide band between 1,200 Hz and 3,500 Hz containing partly metallic noise. It occurs at the engine speed range between 1,400 rpm and 2,500 rpm in the second and third gear.

- *Whining noise (compressor-surge-related noise)* induced by the surge condition in the compressor wheel where the intake air entirely recirculates to the compressor inlet. The whining noise occurs when the gas pedal is suddenly released. Therefore, the mass flow rate of the charge air is strongly reduced at a still high speed of the turbocharger, leading to the surge working condition in the compressor (s. Fig. 2.7). Its frequency spreads in a wide band from nearly 800 Hz to 2,700 Hz containing partly metallic noise that occurs at the engine speed range from 1,400 rpm to 2,500 rpm in the second and third gear.

- *Unbalance whistle* is caused by the unbalanced rotor and unbalance change of the rotor after the long operating time interval. Its harmonic frequency (1X) is between 1,200 Hz and 4,500 Hz. It happens at the engine speed range between 1,500 rpm and 3,500 rpm in the second gear with the relatively low loads.

- *Constant tone* is induced by the inner oil whirl due to oil whirling in the radial bearing; its frequency lies between 600 Hz and 900 Hz in the human audible

range. The frequency order of the inner oil whirl in the rotating floating ring bearings reduces from about 0.35 to 0.25 as the rotor speed increases according to Eq. (7.29b). Therefore, the induced frequency of the inner oil whirl varies in the small range between 600 Hz and 900 Hz; its frequency can be considered nearly constant in the operating speed range of the automotive turbochargers. The constant tone often occurs at the speed ranges between 1,500 rpm and 3,500 rpm in the second to fifth gear with the middle to the high loads.

The automotive turbocharger designers are really concerned about both last airborne noises (unbalance whistle and constant tone) and try to minimize them to bring comfort to drivers and passengers. Besides, designers make efforts to study the noise behaviors with the goal of reducing their undesirable effects as well.

## 7.7.2 Unbalance Whistle and Constant Tone

The malfunctions of the unbalance whistles and constant tone are found in Waterfall diagram of noise spectra, as shown in Fig. 7.22.
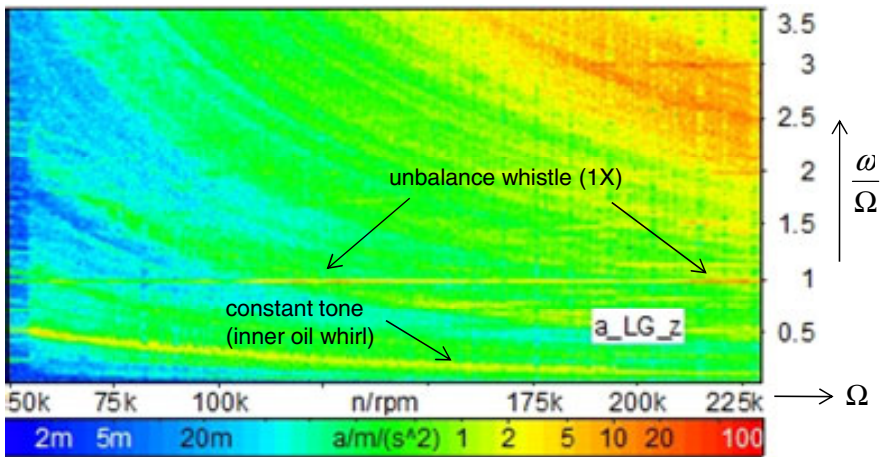


**Fig. 7.22** Unbalance whistle and constant tone in Waterfall diagram [9]

**a) Unbalance whistles (1X)**
It is caused by the residual unbalance of the rotor after balancing. The possible reasons for the unbalance whistle are either the rotor is not well balanced or the unbalance change takes place after a long operating time.

In order to reduce the unbalance whistle at the harmonic frequency 1X, the rotor is balanced by the low-speed (shop balancing) and high-speed balancing (trim balancing) at the two balancing planes. They will be discussed more details in the next chapter. Moreover, one should check whether the compressor wheel is loose

in the shaft because the rotor is over-speeding, or the screw-nut is not enough tightened or loose at the compressor wheel. Additionally, the rotor unbalance significantly increases when the compressor or turbine wheels were damaged or partly broken by any reason during the operation, such as impact of hard particles on them, blade rubbing on the housing, or low-cycle fatigue.

**b) Constant tone (subsynchronous noise)**
To study the root cause of the constant tone, we turn back to Fig. 7.9 and find that the oil inflow rate at the convergent wedge is larger than the outflow rate at any time t. As a reason, the journal has to move away from the bearing with a velocity $v_i$ perpendicular to the journal eccentricity e in order to fulfill the mass balance of the incompressible oil. Furthermore, oil could only flow in the axial direction along the inner bearing width to outside; however, the axial flow rate $\dot{Q}_{ax}$ is very small. Therefore, the journal whirling with the whirl velocity $\omega_i$ induces the constant tone. As long as the damping force in the bearing is larger than the destabilizing force caused by the cross-couple stiffness coefficient of the inner oil film, the journal whirling amplitude is relatively small in a quasi-stable working condition; hence, the constant tone is inaudible inside the car (s. Section 7.5.2). In this case, the whirling kinetic energy of the rotor, which is proportional to the rotor speed squared, is dissipated by the damping energy of oil in the bearing. In fact, the damping force of the bearing decreases with the rotor speed because the oil temperature in the inner bearing rises; therefore, its viscosity strongly reduces at high oil temperatures. The journal begins whirling in the bearing when the damping force is smaller than the destabilizing force in the inner bearing, in which the non-dissipated whirling kinetic energy increasing with the rotor speed excites itself to the oil whirl instability. On the contrary, the outer oil whirl does not induce any subsynchronous noise because its frequency is extremely low so that the intensity of noise that is proportional to frequency squared is negligible. As a reason, the outer oil whirl is inaudible although its deflection amplitude is larger due to the conical vibration mode.

There are some possible measures to reduce or avoid the constant tone by minimizing the inner oil whirl amplitude.

**- Passive measures**
The outer bearing clearance is designed large enough to suppress the constant tone amplitude as it transmits through the outer oil film of the bearing. However, an excessively large bearing clearance could induce the rotor instability because its bearing stiffness coefficient reduces. Another possible measure is the large outer diameter of the bearing; hence, the damping effect of the outer oil film increases in order to dampen the constant tone. However, the ring speed ratio RSR of the bearing reduces, leading to increasing the bearing friction on the rotor, as discussed in Chapter 6.

**- Active measures**
The main reason of the oil whirl is the surplus of oil flow rate in the converged wedge of the inner bearing clearance. In order to minimize the constant tone, the

surplus of oil flow rate must be relieved to keep the amplitude of the inner oil whirl as small as possible; therefore, the rotor remains in the stable condition.

According to Eq. (7.34), the surplus of oil flow rate in the inner bearing is

$$\Delta \dot{Q} = \dot{Q}_{in} - \dot{Q}_{out} \approx 2RL_i e \lambda_i \Omega (1 + RSR) \tag{7.75}$$

By applying the mass balance of oil to the convergent wedge, one obtains the continuity equation of the oil flow rates.

$$\sum_i \dot{Q}_i = \Delta \dot{Q} - \dot{Q}_w - \dot{Q}_{ax} = 0 \tag{7.76}$$

within

$$\dot{Q}_w = 2RL_i e \omega_i \text{ is the journal-whirling-related oil flow rate.} \tag{7.77}$$

By substituting Eqs (7.75), (7.76), and (7.77), one obtains the journal-whirling-related oil flow rate in the converged wedge.

$$\dot{Q}_w = 2RL_i e \omega_i = 2RL_i e \lambda_i \Omega (1 + RSR) - \dot{Q}_{ax} \tag{7.78a}$$

The constant tone is avoided if the whirl velocity $\omega_i$ or whirl eccentricity e in eq. (7.78a) equals zero. That gives

$$\dot{Q}_w = 2RL_i e \lambda_i \Omega (1 + RSR) - \dot{Q}_{ax} = 0 \tag{7.78b}$$

Equation (7.78b) shows that the journal-whirling related oil flow rate can be minimized by either reducing the surplus of oil flow rate (the first term) or increasing the axial oil flow rate (the second term) to compensate the surplus of oil flow rate. As a reason, the journal-whirling related oil flow rate is smaller, leading to reducing the constant tone.

For the first one, some measures are possible to reduce the surplus of oil flow rate according to eq. (7.75). They are namely, reducing the inner bearing clearance c to increase the bearing stiffness so that the journal eccentricity $e = c.\varepsilon$ becomes much smaller; shortening the inner bearing width $L_i$; reducing the journal radius R; decreasing the ring speed ratio RSR. However, all these measures have to be thoroughly investigated since they could cause the rotor instability, bearing wear due to reducing the bearing load capacity, increase of the bearing friction due to reducing the bearing ring speed, and oil coking in the inner bearing clearance.

The second one is increasing the axial oil flow rate by installing a few axial oil grooves in the inner bearing wall to compensate the surplus of oil flow rate (s. Fig. 7.23). Therefore, the journal whirling amplitude is reduced; in turn, the constant tone is minimized or avoided. However, wear could occur in the bearing because lubricating oil does not maintain sufficiently enough in the bearing clearance, especially at the start-stop driving condition or highly unbalanced rotor.
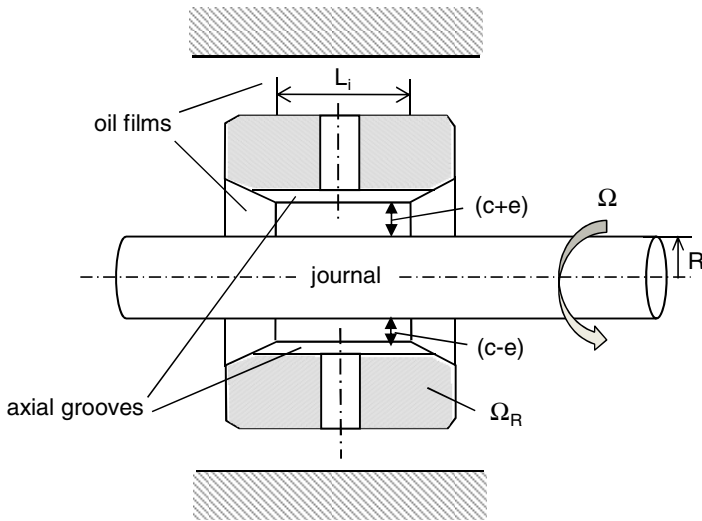
**Fig. 7.23** Rotating-floating ring bearing with axial grooves

## 7.8  Aliasing in DFT and Nyquist Frequency

Fast Fourier transform (FFT) developed by Cooley and Tukey in 1965 is the computing algorithm for discrete Fourier transforms (DFT) that have been used to analyze digitalized time signals of the rotor responses in Waterfall diagram. The DFT is used not only in the rotordynamic computation but also in the measurement.

The fast Fourier transform (FFT) has an advantage of reducing the computing operations of the DFT based on the Fourier transform from $N^2$ to $N\log_2 N$ where N is the discrete values of the continuous time signal. Therefore, the DFT based on the FFT computes much faster and increases the computing accuracy due to round-off errors compared to the Fourier transform. At a given number of sampling points $N = 2^{10}$ (1,024 timely discrete values), the required computing operations in the FFT is nearly $1.024 \times 10^4$ compared to $1.048 \times 10^6$ in the Fourier transform. It results to reducing the number of computing operations in the FFT by the factor of $N/\log_2 N$, approximately 100 times; nearly 2,200 times for $N = 2^{15}$ timely discrete values. One can find the DFT based on the FFT in [12], which calculates the timely discrete values by partitioning the original full sequence into a number of shorter sequences. Hence, it is not dealt with in this book.

## 7.8.1  Discrete Fourier Transform (DFT)

The periodic time signal x(t) is discretized by the Fourier transform (i.e. DFT based on the Fourier transform) and resulted in the discrete time series (s. Fig. 7.24).

$$x(t) = a_0 + 2\sum_{k=1}^{\infty}\left(a_k \cos\frac{2\pi kt}{T} + b_k \sin\frac{2\pi kt}{T}\right) \tag{7.79}$$

where the Fourier coefficients $a_k$ and $b_k$ are defined

$$a_k = \frac{1}{T}\int_0^T x(t)\cos\frac{2\pi kt}{T}dt; \ k \geq 0;$$

$$b_k = \frac{1}{T}\int_0^T x(t)\sin\frac{2\pi kt}{T}dt; \ k \geq 1. \tag{7.80}$$

Instead of two Fourier coefficients, one complex Fourier coefficient $X_k$ combined $a_k$ with $b_k$ is used in the DFT [12].

$$X_k \equiv a_k - jb_k \tag{7.81}$$

By using Euler's theorem, the new Fourier coefficient $X_k$ becomes

$$X_k = \frac{1}{T}\int_0^T x(t)e^{-j\left(\frac{2\pi kt}{T}\right)}dt; \ k \geq 0 \tag{7.82}$$

One writes the Fourier coefficient $X_k$ in the discrete time series of $\{x_n\}$ for n = 0, 1,..., (N-1).

$$X_k \approx \frac{1}{T}\sum_{n=0}^{N-1} x_n e^{-j\left(\frac{2\pi n\Delta t k}{T}\right)}\Delta t \tag{7.83}$$

within
$\Delta t$ is the discrete time interval;
N is the number of discrete sampling points in N discrete intervals.
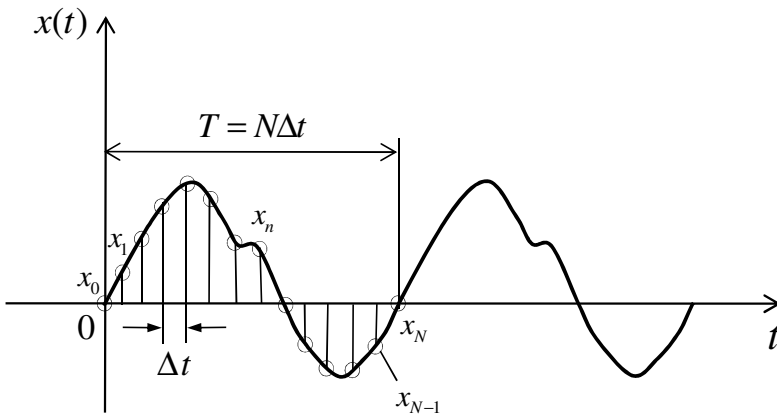


**Fig. 7.24** Discrete periodic time signal x(t)

By substituting T = N.Δt into Eq. (7.83), the Fourier coefficients in the discrete Fourier transform (DFT) are formulated in the discrete time series $\{x_n\}$ for n = 0, 1, ..., (N−1), as displayed in Fig. 7.24.

$$X_k = \frac{1}{N} \sum_{n=0}^{N-1} x_n e^{-j\left(\frac{2\pi n\, k}{N}\right)}; \quad k = 0, 1, ..., N-1 \tag{7.84}$$

By inversing the discrete Fourier transform (IDFT: inverse discrete Fourier transform), one obtains the values of $x_n$.

$$x_n = \sum_{k=0}^{N-1} X_k e^{j\left(\frac{2\pi k\, n}{N}\right)}; \quad n = 0, 1, ..., N-1 \tag{7.85}$$

With the periodic frequency

$$\omega_k = \frac{2\pi k}{T} = \frac{2\pi k}{N\Delta t}, \tag{7.86}$$

the Fourier coefficients $X_k$ result in the discrete Fourier transform (DFT)

$$X_k = \frac{1}{N} \sum_{n=0}^{N-1} x_n e^{-jn\omega_k \Delta t}; \quad k = 0, 1, ..., N-1 \tag{7.87}$$

According to Eq. (7.84), the amplitude $|X_k|$ of the Fourier coefficient $X_k$ is an even function; hence, it is symmetric about $\omega_k = 0$, as shown in Fig. 7.25. It is written in.

$$|X_k| = |X_{-k}| \tag{7.88}$$

The amplitudes $|X_k|$ of the timely discrete components $x_n$ at the frequencies $\omega_k$ for k = 0, 1, ..., N are plotted in Fig. 7.25. At the higher frequencies $\omega_k > \omega_{lim}$ (i.e., k > N/2), the amplitudes $|X_k|$ of the Fourier coefficients $X_k$ are periodically repeated from the values corresponding to the frequencies $\omega_k$ that are symmetrical at the limit frequency $\omega_{lim}$. Therefore, the Fourier coefficients $X_k$ computed by the DFT are only correct for angular frequencies up to $\omega_{lim}$ [12].

$$\omega_k \leq \omega_{lim} \equiv \frac{\pi}{\Delta t} \tag{7.89}$$

### 7.8.2 Aliasing in DFT

If any frequency of the real signal exceeds the limit frequency $\omega_{lim}$ given in Eq. (7.89), the Fourier coefficients computed by the DFT have no longer been correct, leading to aliasing (distortion) of the amplitudes between the DFT computed and real spectra in the frequencies above $\omega_{lim}$, as shown in Fig. 7.25.
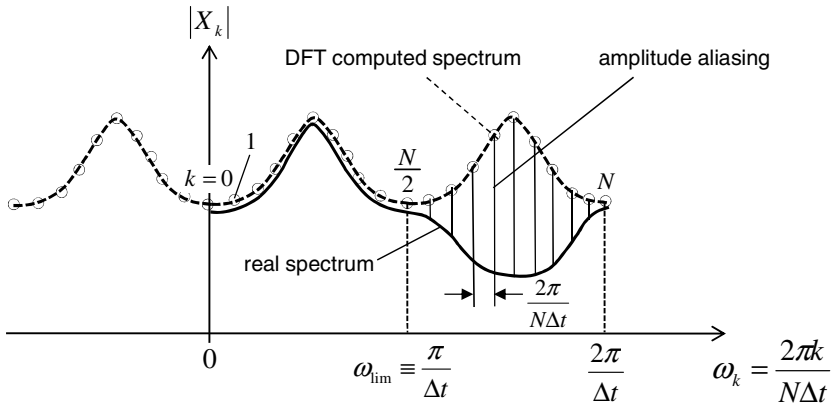
**Fig. 7.25** Aliased amplitudes between the DFT computed and real spectra

## 7.8.3 Nyquist Frequency

For anti-aliasing of the DFT computed amplitudes, the maximum angular frequency $\omega_{max}$ (rad/s) of the real time signal must be below the limit frequency.

$$\omega_{max} < \omega_{lim} \equiv \frac{\pi}{\Delta t} \tag{7.90}$$

Thus, the maximum frequency $f_{max}$ ($s^{-1}$) of the vibration response should be limited by

$$f_{max} = \frac{\omega_{max}}{2\pi} < \frac{\omega_{lim}}{2\pi} = \frac{1}{2\Delta t} \tag{7.91}$$

The frequency $1/(2\Delta t)$ in the rhs term of Eq. (7.91) is called the Nyquist frequency where $\Delta t$ is the time interval between two discrete time values of the vibration response, as shown in Fig. 7.24.

Hence, the Nyquist criterion is satisfied for anti-aliasing when the maximum sampling frequency is below the Nyquist frequency.

$$f_{Nyq} \equiv \frac{1}{2\Delta t} > f_{max} \tag{7.92}$$

To satisfy the Nyquist criterion in Eq. (7.92), the discrete time interval $\Delta t$ at sampling must be as small as

$$\Delta t \equiv \frac{1}{2f_{Nyq}} < \frac{1}{2f_{max}} = \Delta t_{max} \tag{7.93}$$

The sampling time interval $\Delta t$ is selected for the integrating time step in computation of nonlinear rotordynamics. In other words, the time interval must be small

enough to cover the entire frequency range of the vibration response. Hence, the aliasing of the DFT computed amplitudes is prevented in the computation. Moreover, at measurements of the vibration responses, the sampling time interval is chosen according to the Nyquist criterion, as given in Eqs (7.92) and (7.93) for anti-aliasing of the measured amplitudes (s. Fig. 7.26).
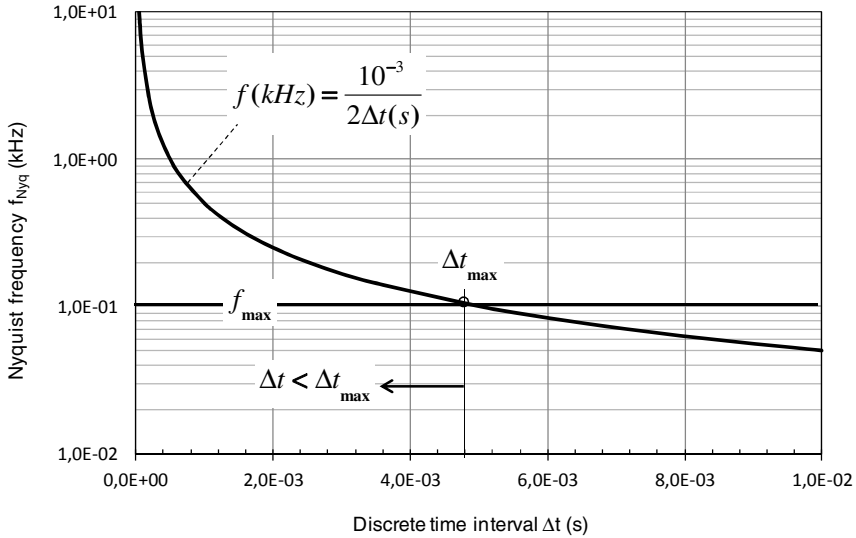


**Fig. 7.26** Nyquist frequency versus discrete time interval

The diagram of Fig. 7.62 shows how to select the discrete time interval. At the maximum frequency $f_{max}$ of the sampling time signal, the intersection between the frequency line $f_{max}$ and frequency curve f gives the maximum time interval $\Delta t_{max}$. To fulfill the Nyquist criterion, the discrete time interval $\Delta t$ must be smaller than $\Delta t_{max}$, so that $f_{Nyq} > f_{max}$, as shown in Fig. 7.26.

If the real time signal contains a very high frequency, an extremely short integrating or sampling time step is required for anti-aliasing, leading to an extreme computing time (CPU). Therefore, these high frequencies are filtered from the real signal by using the under-sampling or band-pass sampling technique at an appropriate time interval. Hence, the maximum frequency of the real time signal after under-sampling is lower than the Nyquist frequency in order to satisfy the Nyquist criterion.

## 7.9   Computations of Nonlinear Rotordynamics

A computation of nonlinear rotordynamics for a typical automotive turbocharger using rotating floating ring bearings has been carried out in the case history. Following characteristics are taken into account in the rotordynamic computation with the program MADYN 2000 [10] based on the extensionally extra-developed module for nonlinear rotordynamics of high-speed turbochargers:

- run-up simulation to very high rotor speeds;
- transient behavior of the rotor responses;
- gyroscopic effect of the flexible rotor;
- cavitating two-phase flows of the oil films in the bearing clearances;
- unbalance forces and moments acting upon the rotor;
- damping effects of the seal rings;
- nonlinear bearing forces of the rotating-floating ring bearings;
- synchronous (unbalance) and asynchronous vibrations (oil whirls);
- rotating-floating ring bearings with changing ring speed ratios;
- computing the ring speed ratios of the bearings;
- heat convection in the oil films in the axial direction;
- heat conduction between the oil films in the radial direction;
- various types of lubricating oil (e.g. SAE 0W30, 5W30, 10W40, 15W40);
- various pressures and temperatures of lubricating oil.

Figure 7.27 shows the computed rotor of an automotive turbocharger including the compressor and turbine wheels, rotor shaft, thrust rings, seal rings, and rotating-floating ring bearings. One transforms the computed rotor to the discretized finite-element model where the components of the rotor, such as the compressor and turbine wheels, rotor shaft, and radial bearings are discretized in a finite number of concentrated mass points, disks, cylinder elements, and interfaces of the bearings and seals to the rotor, as shown in Fig. 7.28. The finite-element model of the rotor contains of many sections that are connected by the stations at both ends of each section.

By applying the principle of D'Alembert to the finite-element rotor, the vibration equations of the rotor with N degrees of freedom are written in the discrete matrix equation, as given in Section 7.2.

$$\mathbf{M}\ddot{\mathbf{x}} + \mathbf{C}_S\dot{\mathbf{x}} + \mathbf{K}_S\mathbf{x} = f(\mathbf{t})$$

where
$\mathbf{M}$ = (N x N) mass matrix containing the masses and inertia moments of the rotor;
$\mathbf{C_S}$ = (N x N) damping coefficient matrix of the shaft;
$\mathbf{K_S}$ = (N x N) stiffness coefficient matrix containing the diagonal and cross-coupled stiffness coefficients of the shaft;
$\mathbf{x}$ = (N x 1) vibration response vector including all degrees of freedom of the rotor with two translational and two rotational displacements at each station of the finite element;
$\mathbf{f}(t)$ = (N x 1) vector of the unbalance and nonlinear bearing forces.

By solving the Reynolds lubrication equation of the bearings, one creates the impedance table. The nonlinear bearing forces in the entire bearing clearance are resulted from the corresponding bearing stiffness and damping coefficients by linearly interpolating the computed values of the bearing characteristics at ε, γ, and Sommerfeld number (So) in the impedance table. The nonlinear bearing forces contain two force components: the rotation force induced by the rotation with Ω depends on Ω, η, ε, and γ, and the damping force caused by the journal velocities $\dot{\varepsilon}, \dot{\gamma}$ depends on $\eta, \varepsilon, \gamma, \dot{\varepsilon}, \dot{\gamma}$.
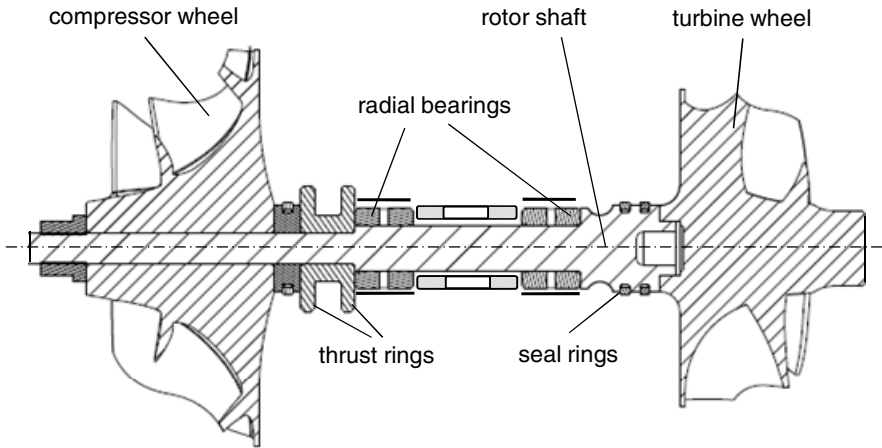
**Fig. 7.27** Computed rotor of an automotive turbocharger
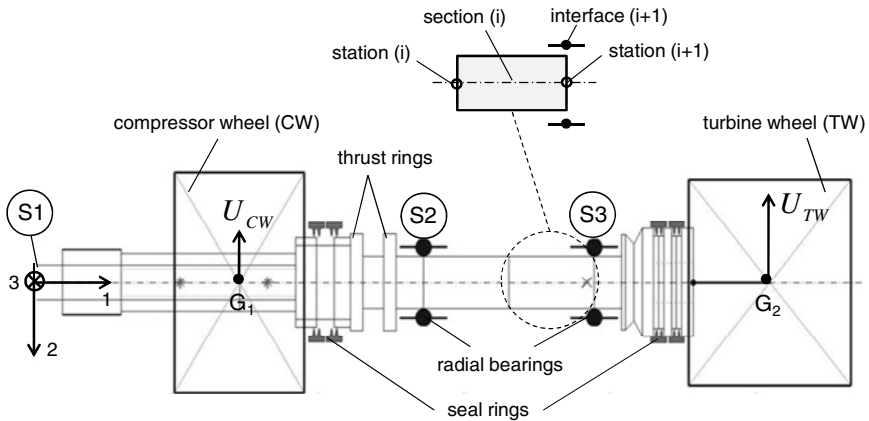


**Fig. 7.28** Computed finite-element model of the rotor

The nonlinear bearing forces acting upon the rotor are computed at each iterating step based on the Sommerfeld number So of the impedance method (s. Sections 6.5.2 and 6.5.3). The coupled nonlinear vibration equations of the rotor are given in eq. (7.4), in which we set the nonlinear bearing forces in the right hand side of the equation. By using the bimodal method, we decouple the coupled nonlinear equations (7.4) in the decoupled nonlinear equations (7.20); then, the vibration responses are solved by the high-order Runge-Kutta scheme at each iterating step with the time interval given in eq. (7.92). By using the Discrete Fourier Transform (DFT), the frequency spectrum of the rotor responses is displayed and analyzed in the spectrogram (Waterfall diagram). The orbits of the rotor at the station S1 of the compressor inlet, and at the stations S2 and S3 of the journal loci in the radial bearings are computed in the run-up simulation, as shown in Fig.7.28.

Two rotating floating ring bearings and two sealing rings at each side support the computed rotor with a mass of about 150 g including the shaft with a diameter of 7 mm, compressor wheel, turbine shaft, and thrust rings. The relative inner diametral clearance of the bearing is initially about $3 \times 10^{-3}$ due to the temperature difference between the inner and outer oil films, and the centrifugal force of the bearing ring, the bearing ring expands in the radial direction. Hence, the relative inner diametral clearance increases to a maximum about $4 \times 10^{-3}$ during the operation. The ratio of the outer and inner bearing clearances is varied by a factor between 3 and 4. The maximum rotor speed is limited to nearly 225,000 rpm ($\Omega = 3750$ Hz). The compressor wheel and turbine shaft have residual unbalances of approximately 0.1 g.mm and 0.2 g.mm, respectively. The lubricating oil SAE 5W30 is used in the run-up computation; the oil dynamic viscosity changes with the effective oil temperatures in the oil films at every iterating step according to the Cameron and Vogel equation (6.44). The oil condition at the inlet is given at the relative pressure of 0.3 MPa (3 bar) and oil temperature of 90°C at S2; 100°C at S3.
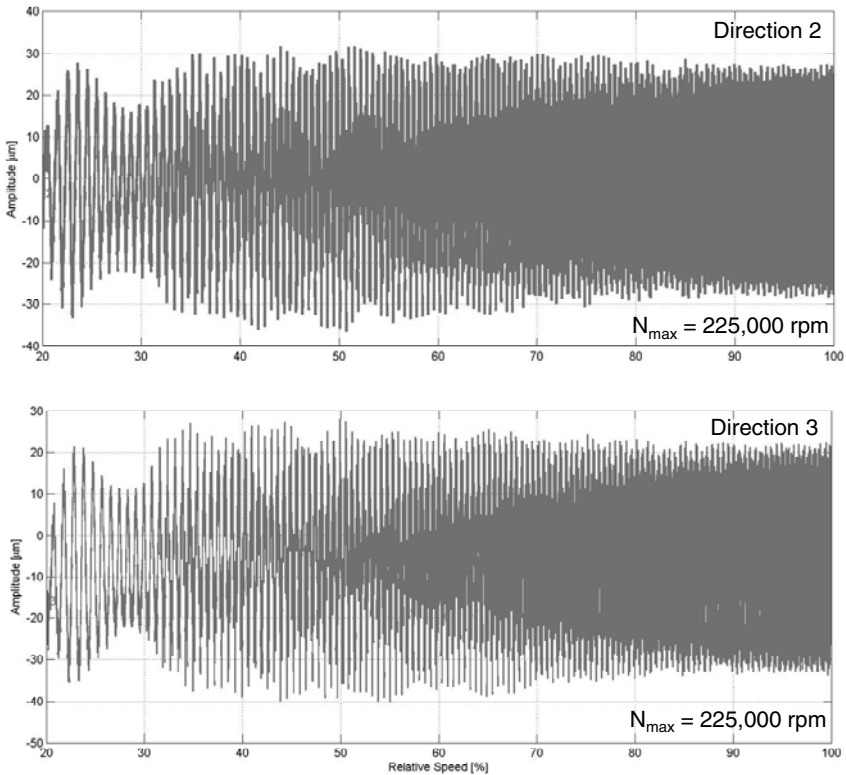


**Fig. 7.29** Computed vibration response of the rotor at the station S1
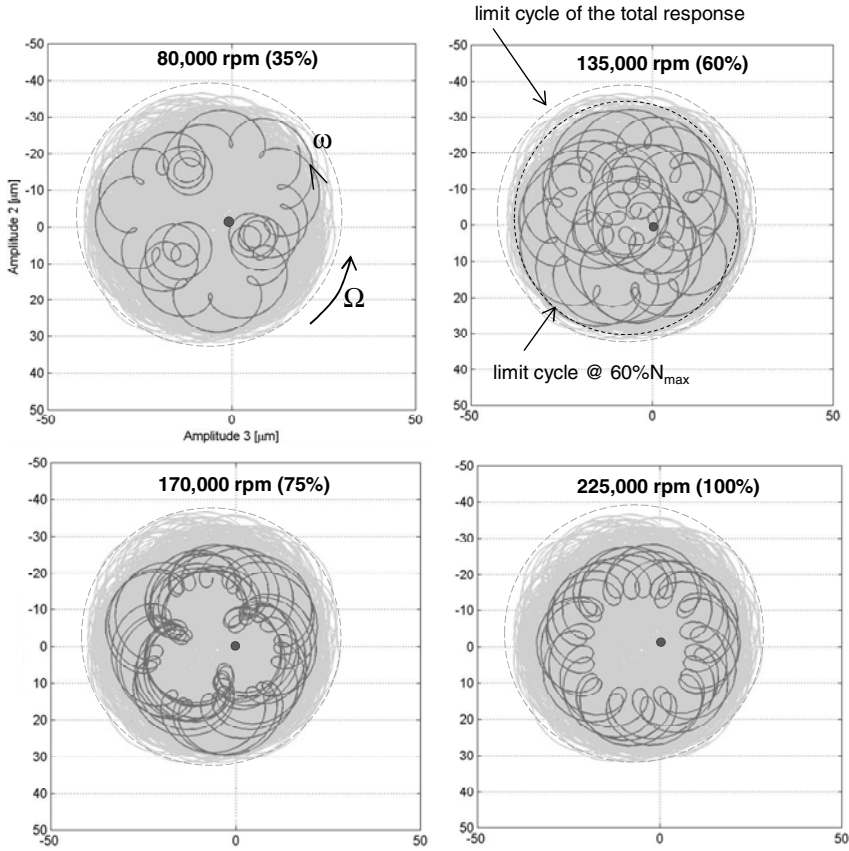
**Fig. 7.30** Computed response orbits of the rotor at the station S1

The computing time for the run-up simulation of about 20-hour-CPU is necessary on a PC with a dual-core AMD Opteron of 3 GHz and 8 GB RAM. This computing time is quite acceptable in the industry instead of a-few-week-CPU in case of instantaneously solving the Reynolds equation at each iteration step.

Fig. 7.29 shows the rotor response in the directions 2 and 3 at the station S1 (s. Fig. 7.28) versus rotor speeds in the run-up simulation up to the rotor speed of 225,000 rpm. The amplitude of the rotor response is resulted by superimposing the harmonic unbalance excitation on the subsynchronous frequency components of the inner and outer oil whirls. At the beginning, the rotor amplitude is mainly induced by the outer oil whirl up to the relative rotor speed of nearly 30%; its vibration mode is conical and whirls in the outer bearing clearance, as shown in Figs 7.31 and 7.32. From the relative rotor speed of 30% up to 60%, the rotor response is superimposed by the unbalance, inner, and outer oil whirls; the conical mode of

the rotor response tends toward the cylindrical mode. From the relative rotor speed of 60% to the maximum rotor speed of 225,000 rpm, the rotor response is excited by the inner oil whirl and unbalance; its response has the cylindrical mode, as shown in Figures 7.32a and 7.32b.

Due to the irrational frequency ratio of the inner and outer oil whirls, the rotor response is quasi-periodic vibrations, as discussed in Chapter 3. However, the rotor amplitude is stabilized in the limit cycle at any rotor speed ; e.g., at the relative rotor speed of 60% (135,000 rpm), the limit cycle at the station S1 has a peak-to-peak amplitude of nearly 65 µm, as shown in Figure 7.30.
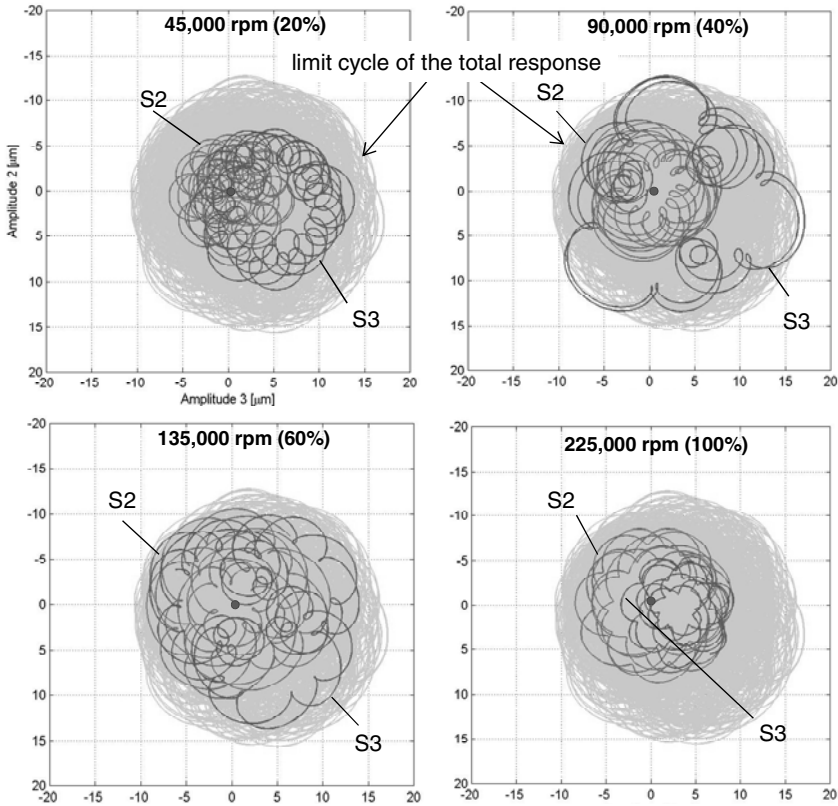


**Fig. 7.31** Computed response orbits of the rotor at the stations S2 and S3

Figure 7.30 indicates that the rotor response is a forward whirl because its orbit contains only the inner loops (s. Chapter 3); i.e., their whirl speeds $\omega$ have the same direction of the rotor speed $\Omega$. Within the limit cycle, the rotor orbit is unstable due to the self-excited vibrations with subsynchronous frequencies ($\omega < \Omega$) of the oil whirls. Therefore, the rotor orbit at S1 moves towards the stable limit cycle; during this time, the eccentricity of the journal locus increases in the bearing clearances, leading to reducing the oil-film thickness, in turn increasing the stiffness and

damping coefficients of the bearing. As a reason, the rotor orbit stabilizes in the limit cycle of the Hopf bifurcation (s. Chapter 4). From the rotor speed of 170,000 rpm (75% relative rotor speed), the limit cycle of the rotor response is reduced from the maximum cycle limit of 70 μm to about 55 μm due to the increase of the bearing stiffness and damping coefficients, as shown in Fig. 7.30. As long as the limit cycle of the rotor response is smaller than both bearing clearances in the entire operating speed range, and each minimum oil-film thickness is larger than the limit oil-film thickness, as given in Fig. 6.11, no wear occurs in the bearing.
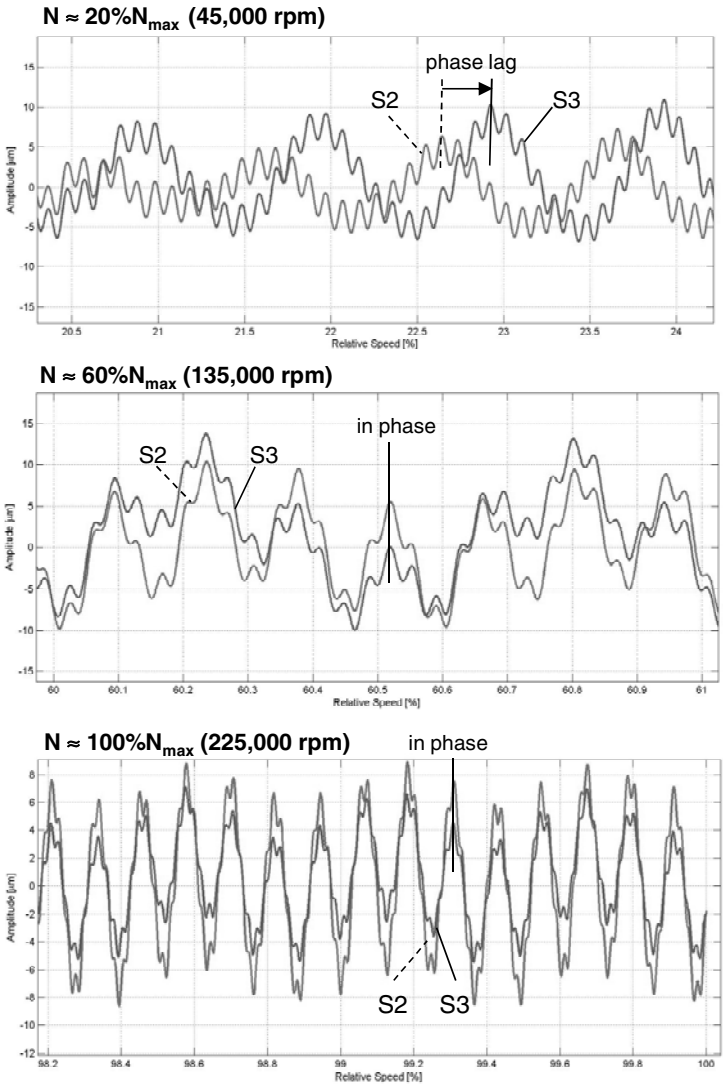


**Fig. 7.32a** Computed rotor responses at the stations S2 and S3 at various rotor speeds

The vibration mode of the flexible rotor in the run-up simulation is analyzed by using the vibration phases at the stations S2 and S3. At low rotor speeds up to nearly 40% $N_{max}$, the rotor orbits at S2 and S3 are mostly eccentric to each other (s. Fig. 7.31), i.e. the mode shape of the rotor response is conical since the rotor is still rigid at low rotor speeds. As high rotor speeds, the bearing stiffness and damping coefficients increase, the conical mode of the rotor vibration tends toward cylindrical mode. Figure 7.31 shows that the orbits at S2 and S3 are nearly concentric from the relative speed of 60% up to the maximum rotor speed. The limit cycles of the rotor response at S2 and S3 have a peak-to-peak amplitude of about 25 µm at 60% and reduce to 15 µm at 100% relative rotor speed ($N_{max}$ = 225,000 rpm).

Figure 7.32a displays the time responses of the rotor at the stations S2 and S3 at the relative rotor speeds of 20%, 60%, and 100%. At small rotor speeds up to 60% rel. speed, the time vibration responses at S2 and S3 are out of phase (with a phase lag), leading to the eccentric orbits (conical vibration mode), as shown in Fig. 7.31. At increasing rotor speeds from 60% up to 100% rel. speed, the time responses at S2 and S3 are in phase (without phase lag), causing the concentric orbits at S2 and S3 (cylindrical vibration mode). In this case, the vibration mode of the rotor response is cylindrical. At each rotor speed, the rotor orbit stabilizes in the limit cycle, as displayed in Fig. 7.31.
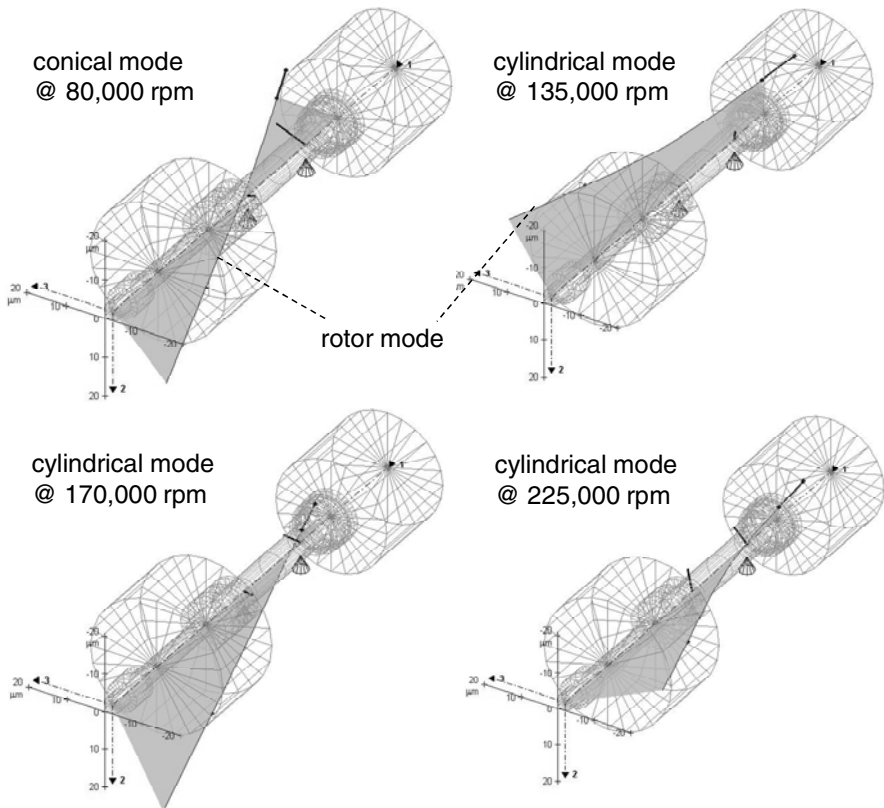


**Fig. 7.32b** Computed vibration modes of the rotor at various speeds

Figure 7.32b displays the vibration modes of the rotor at various rotor speeds. At the low speeds, the rotor vibration has a conical mode. From the rotor speed of about 81,000 rpm (36% relative rotor speed) to 225,000 rpm (100% relative rotor speed), the rotor vibration changes from the conical to cylindrical mode.

We apply the discrete Fourier transform (DFT) to compute the frequency spectra of the rotor vibration response in the run-up simulation up to 225,000 rpm. Figure 7.33 shows the Waterfall diagram of the computed rotor response. Oil whirling in the outer bearing clearance causes the outer oil whirl. It affects the conical vibration of the rotor response at the relative rotor speed of 20% with a frequency order of nearly 0.15X (s. Fig. 7.34). At increasing the rotor speeds, the oil temperature of the inner oil film is higher than the temperature of the outer oil film due to the bearing friction. Therefore, the ring speed ratio of the bearing reduces, leading to decreasing the frequency order of the outer oil whirl to approximately 0.1X at the maximum rotor speed of 225,000 rpm. Similarly, the inner oil whirl takes place a little bit later with the whirl frequency order of about 0.4X at the relative rotor speed of 30%. Because of the reduced bearing ring speed during the operation at high rotor speeds, the frequency order of the inner oil whirl drops from 0.4X to nearly 0.2X at the maximum rotor speed. Its vibration response is a cylindrical mode; the journal amplitude moves the bearing ring towards, and is limited in the limit cycle inside both bearing clearances. The rotor response at each rotor speed is resulted from superimposing the harmonic unbalance excitation on the subsynchronous vibration components induced by the inner and outer oil whirls. The rotor orbits at the stations S1, S2, and S3 are plotted in the phase plane 2-3 at various rotor speeds, as shown in Figures 7.30 and 7.31, respectively.
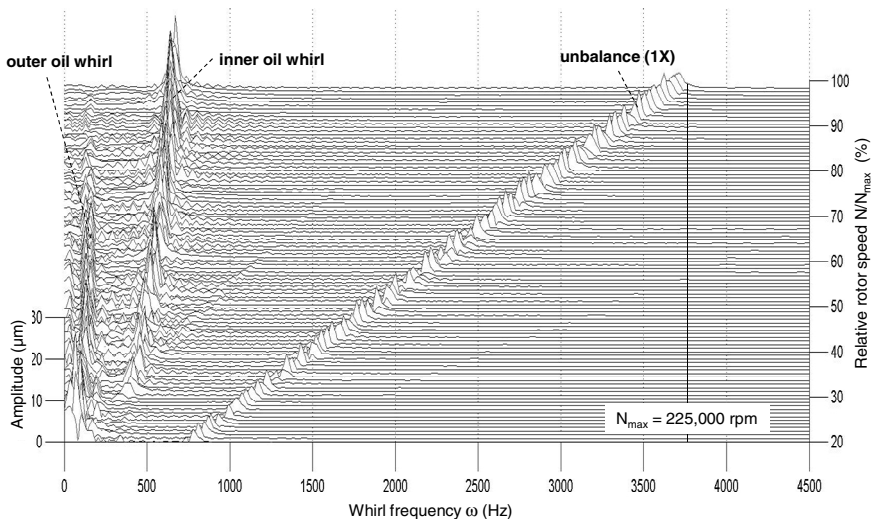


**Fig. 7.33** Computed Waterfall diagram at the station S1

The unbalance amplitude (1X) is relatively small compared to the asynchronous amplitudes in the entire rotor speed range. In fact, the typical resonance due to unbalance does not exist in nonlinear rotordynamics (s. Fig. 7.33), but only the limit cycle of the rotor response occurs at each rotor speed. The reason is that the effective stiffness coefficient of the rotor depends not only on the stiffness coefficient of the rotor shaft itself but also on the bearing stiffness coefficient; the equivalent stiffness coefficient of the rotor is called the complex rotor dynamic stiffness coefficient. In turn, the bearing stiffness is dependent of the effective oil pressure, temperature, rotor speed, bearing ring speed, and journal eccentricity as well. At large rotor deflections, the journal eccentricity increases in the bearing clearance; the oil-film thickness reduces in the clearance. Therefore, the stiffness and damping coefficients of the bearing increase with the rotor deflection until the journal orbit stabilizes in the limit cycle at each rotor speed in the supercritical Hopf bifurcation. In this case, no typical resonance occurs in the entire rotor speed range, as shown in the Waterfall diagram (s. Fig. 7.33).

In practice, one plots Waterfall diagram in a two-dimensional diagram (called modified Waterfall diagram), in which the amplitudes of the vibrations are displayed in the color (gray) scale in the frequency-order spectra, as shown in Fig. 7.34. Instead of the whirl frequency $\omega$, its frequency order $\omega/\Omega$ is used in the modified Waterfall diagram, of which advantage is easier to analyze the frequency-order spectra of the synchronous and asynchronous vibrations versus the rotor speed in the abscissa. The frequency jump of the inner oil whirl takes place where the conical vibration mode changes into the cylindrical mode.
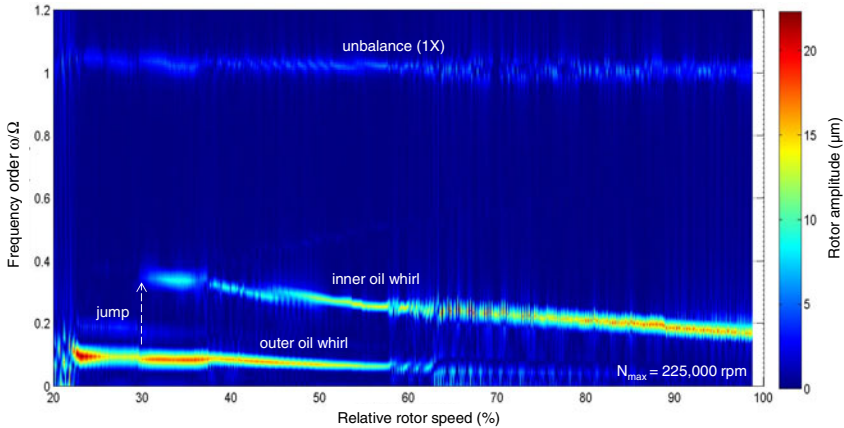


**Fig. 7.34** Computed modified Waterfall diagram at the station S1

Figure 7.35 shows the comparison of Waterfall diagram between the computation and measurement. Compared to the measurement, the computed inner oil whirl takes place a little bit later at the relative rotor speed of about 30% (67,500 rpm) instead of at nearly 27% (62,000 rpm) at measurement. The frequency order of the computed inner oil whirl (called inner OW) begins at a lower frequency order of 0.4X compared to about 0.55X in the measurement and ends at the frequency order of 0.2X, nearly the same measurement results.

  The reason for the low frequency order of the inner oil whirl is that the bearing ring speed in the measurement is higher than the ring speed in the computation. The unknown heat flow transferred from the bearing housing to the outer oil film of the bearing has not been taken into account in the computation. As a reason, compared to the computation, the outer oil film temperature increases in the measurement; therefore, the ring speed ratio of the bearing is higher, leading to the higher frequency order of the inner oil whirl according to eq. (7.26). The frequency jump of the inner oil whirl occurs at a relative rotor speed of 30% (about 65,000 rpm). Similarly, the computed frequency order of the outer oil whirl (called outer OW) is a little bit lower than the frequency order in the measurement due to the reduced bearing ring speed, especially at low rotor speeds. However, it is nearly the same frequency order of the measurement at high rotor speeds since
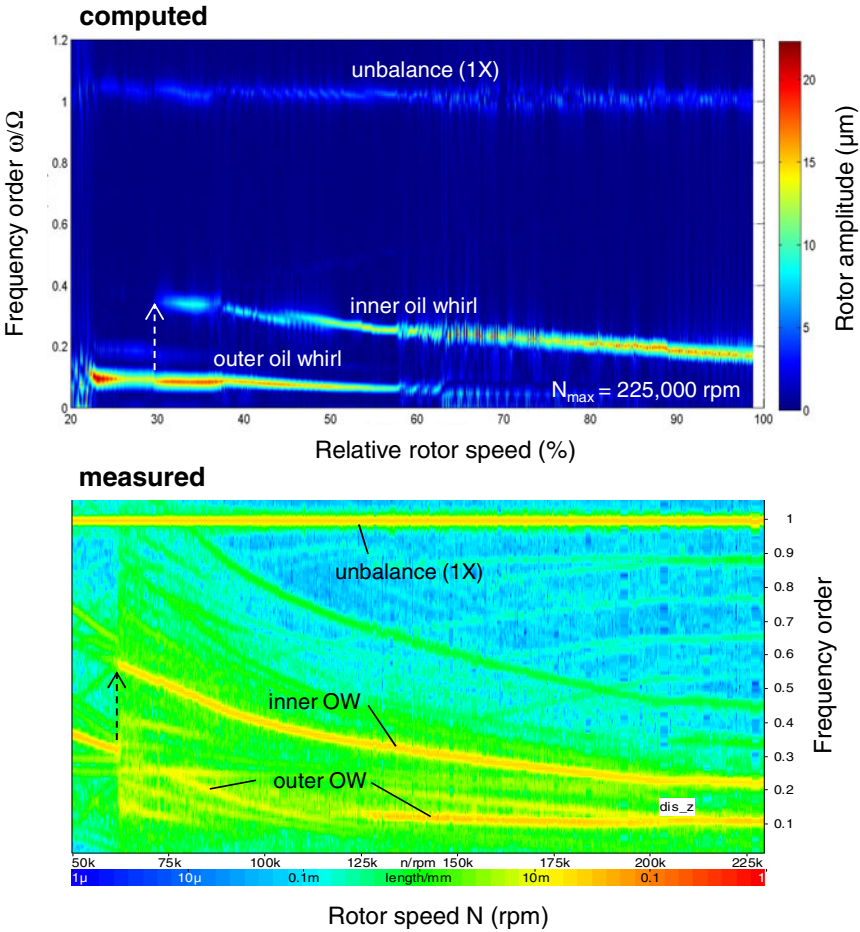


**Fig. 7.35** Comparison of Waterfall diagrams at the station S1

the ring speed ratio of the bearing does not change much at the high-speed range, as shown in Fig. 6.28.

Some unknown boundary conditions that could not be taken into account in the rotordynamic computation are:

- Producing form tolerances;
- Exact inner and outer bearing clearances due to surface non-roundness of the journal, bearing, bearing foundations;
- Non-roundness of the journal and bearing surfaces;
- Non-coaxiality of the bearing and bearing foundations;
- Change of the bearing clearances during the operation;
- Tribological surface roughness ($R_z$, $R_a$, $R_{pk}$, $R_k$, $R_{vk}$) of the bearing and journal;
- Real oil temperatures at the bearing inlet at the compressor and turbine sides;
- Fully or poorly lubricating oil conditions;
- Bearing inlet and outlet geometries in the bearing housing;
- Contaminated oil with particles;
- Foamy oil due to air releasing and cavitation;
- Angular position between the unbalance vectors of the compressor and turbine wheels.

However, the rotordynamic computation gives us more deeply understanding how the rotor reacts at the given boundary conditions, so that the rotor response of the turbocharger can be improved; the development time is shortened. In practice, one uses both computations and measurements to predict, analyze, and validate the amplitudes and frequency spectra of the rotor response. In fact, they help to each other in development of turbochargers. Furthermore, one validates the lifetime of turbochargers (LCF $< 10^5$ cycles, HCF $> 10^5$ cycles) and wears in the bearings by the measurements because such effects have been not yet calculated by the rotor-dynamic computation under the real operating conditions.

Although Campbell diagram is not valid in nonlinear rotordynamics, as discussed in Chapter 5, it is however useful to find the bending critical frequency of the rotor that is used in the trim balancing (Chapter 8). The Campbell diagram in Fig. 7.36 shows the eigenfrequencies (natural frequencies) of the forward and backward whirls of the free rotor vibration. In case of linear rotordynamics, the first bending mode of the forward whirl #10 happens at the critical speed $\Omega_{cr1}$ of approximately 147,000 rpm. The second bending resonance of the forward whirl #12 occurs outside the rotor speed range of 225,000 rpm. The first critical speed must be high enough to avoid the rotor instability during the operation. Note that the rotor should be designed, so that the first bending critical frequency is as high as possible in order to keep the rotor from oil whip induced by the self-excited vibration in the bearing. The backward whirls #9 and #11 generally do not excite the rotor into resonance in case of a symmetric rotor. At unsymmetrical rotors and excitation forces with alternately changing directions, the backward whirls could cause resonances at the intersections between the synchronous excitation line (1X) and the backward eigenfrequencies.

In case of the rotating floating ring bearing, the journal moves relatively to the bearing ring at any rotor speed; i.e., the journal motion moves the bearing ring in
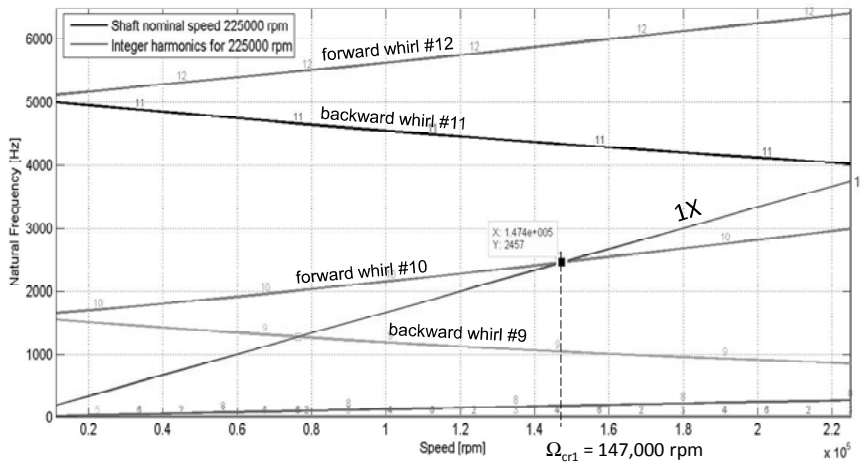
**Fig. 7.36** Campbell diagram of the free rotor vibration

the radial direction. In practice, it is very difficult to measure the relative displacements between the journal and bearing ring during the rotation. Hence, the rotordynamic computation is a useful tool to compute the relative displacements and the current oil-film thickness in the rotating floating ring bearings at any rotor speed.

Figure 7.37 displays the relative displacements between the journal and bearing ring at various rotor speeds. At the beginning, the journal and bearing ring are nearly concentric to each other since the rotor mass is very small of nearly 150 g. If the relative displacement is positive, the journal moves closer to the bearing ring because the journal displacement is larger than the ring displacement. In other case, the journal moves away from the bearing ring. The current oil-film thickness is resulted from the bearing clearance and relative displacement. When the oil-film thickness is larger than the limit oil-film thickness, as given in Fig. 6.11, the lubrication regime is fully hydrodynamic and outside the mixed and boundary lubrications; no or less wear occurs in the bearing.

The computed results show the maximum relative displacement of is about 9 µm in the limit cycle for the entire rotor speed range. It indicates that the minimum oil-film thickness in the inner bearing clearance is nearly 5 µm with the inner radial clearance of 14 µm. The minimum oil-film thickness of 5 µm in the bearing clearance is larger than the limit oil-film thickness; hence, no wear occurs in the bearing.

Therefore, the lubrication regime in the bearing is fully hydrodynamic for all working conditions. Due to the difference of temperature between two oil films at high rotor speeds, the bearing ring expands in the radial direction, leading to extending the inner bearing clearance and reducing the outer bearing clearance. As a reason, the minimum inner oil film thickness is larger than 5 µm in practice, leading to the larger contact circle.

Figure 7.38 displays the bearing forces acting on the bearings at the stations S2 and S3 of the rotor running with various rotor speeds. The bearing forces acting
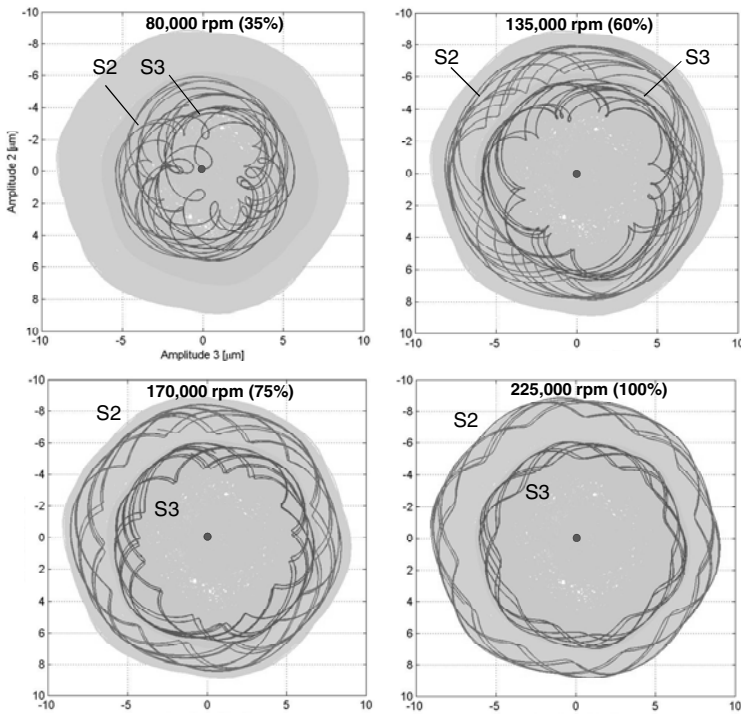
**Fig. 7.37** Computed relative displacements of the rotor and bearing ring at the stations S2 and S3

upon the rotor at the stations S2 and S3 keep the rotor in balance between the gyroscopic moments of the wheels, and the unbalance forces and moments of the displaced shaft, compressor and turbine wheels. The bearing force is mainly resulted from the unbalance of the compressor and turbine wheels and the shaft unbalance induced by its displacement due to oil whirls.

The induced nonlinear bearing forces are resulted from two force components of the rotation and damping forces, as discussed in Section 6.5.2. The rotation force is generated by the rotor speed $\Omega$; it also depends on the oil viscosity $\eta$, journal relative eccentricity $\varepsilon$, and the angular position $\gamma$. The journal velocities $\dot{\varepsilon}, \dot{\gamma}$ cause the damping force that also depends on $\eta, \varepsilon, \gamma, \dot{\varepsilon}, \dot{\gamma}$. At the low rotor speeds up to about 30% relative speed, the bearing force at the turbine side (S3) is quite larger than the bearing force at the compressor side (S2). At increasing the rotor speed, the bearing force at the turbine side S3 is however smaller than the bearing force at the compressor side S2. The journal amplitude at the turbine side S3 is higher than the journal amplitude at S2, as shown in Fig. 7.31, leading to the higher oil temperature induced in the inner oil film due to bearing friction, in turn the significant reduction of oil viscosity. It results to the lower bearing force at the turbine side S3 compared to the bearing force at the compressor side S2. In this

case, the influence of the oil viscosity on the bearing force is stronger than the other effects. At the small bearing force capability at the turbine side S3, its bearing could be damaged by the large excitation force acting on it, in which the oil film thickness is in the mixed or boundary lubrication layer.
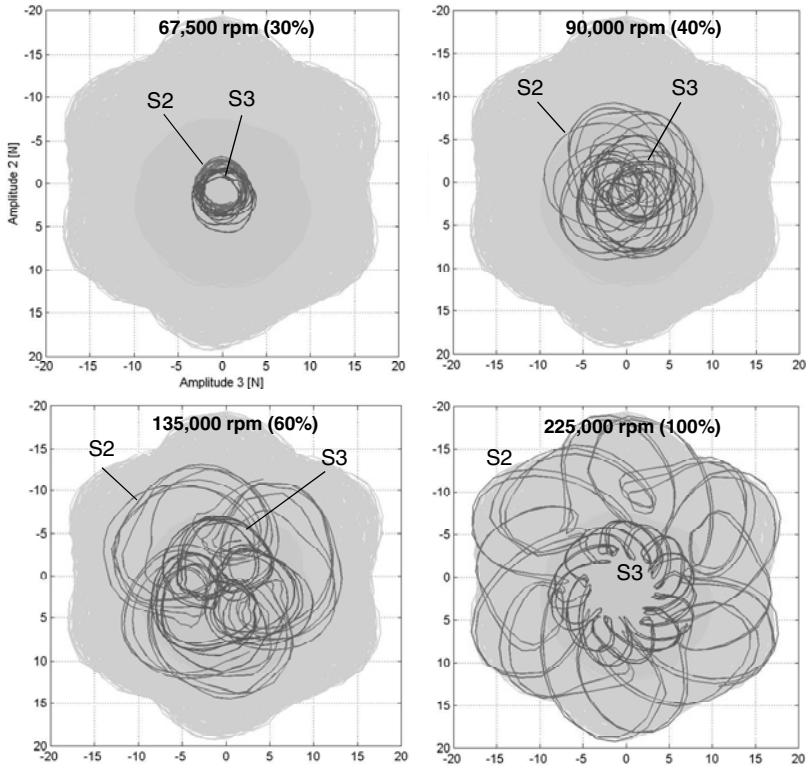


**Fig. 7.38** Computed bearing forces at the stations S2 (compressor) and S3 (turbine)

The maximum bearing forces at each rotor speed are shown in Fig. 7.38. At the maximum rotor speed of 225,000 rpm, the peak amplitude of the bearing force at the station S2 (compressor) is about 20 N and approximately 10 N at the station S3 (turbine). To investigate further the induced bearing forces, their time signals at the stations S2 and S3 are analyzed in Waterfall diagrams by using DFT (Discrete Fourier Transform), as shown in Fig. 7.39. The bearing force consists of two force components with the different frequencies: the rotation force has the harmonic frequency ($\omega = 1X$); the damping force, the subsynchronous frequency ($\omega < 1X$). Obviously, the frequency order of the rotation force is synchronous with the rotor speed (1X) because it is proportional to the rotor speed. Similarly, the frequency order of the damping force is subsynchronous with the frequency of the inner oil whirl. The frequency order of the damping force begins with 0.4X at the relative rotor speed of 30% and continuously decreases to the frequency order of nearly

0.2X at the maximum rotor speed. Its frequency order is the same of the frequency order of the inner oil whirl, as displayed in Fig. 7.34. The color (gray) scale denotes their force amplitudes in the frequency curves. The resulting bearing force is superimposed by the rotation and damping forces with an irrational frequency ratio; therefore, the force vibration is quasi-periodic.
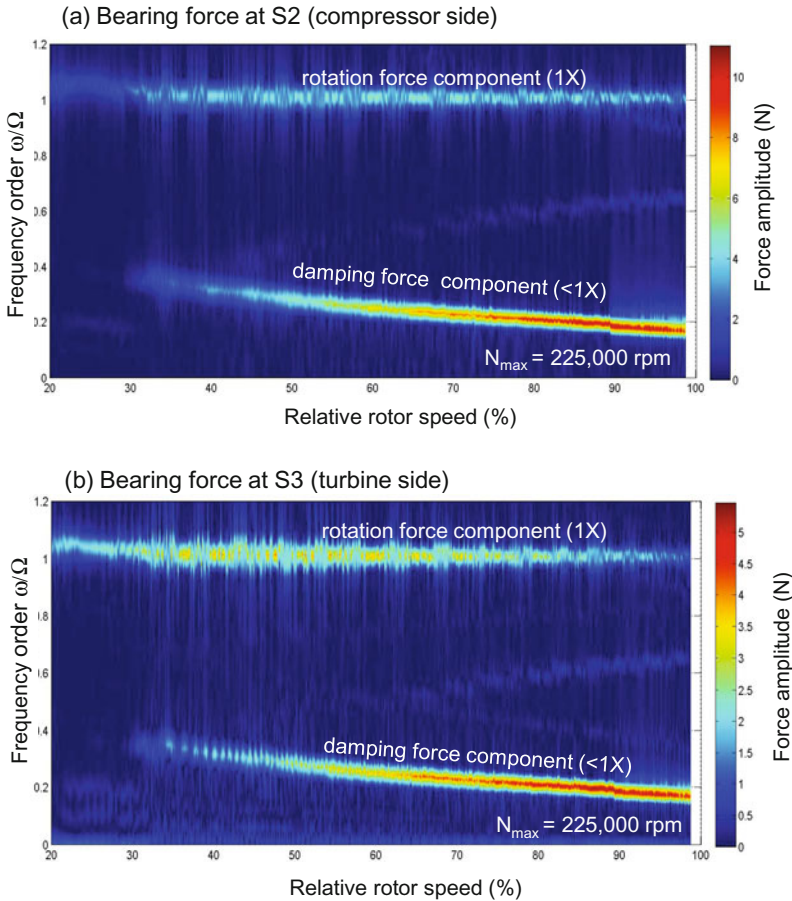


Fig. 7.39 Computed Waterfall diagrams of the bearing forces at the stations S2 and S3

   To reduce the unwanted constant tone (subsynchronous noise) induced by the inner oil whirl, one possible measure can reduce the inner bearing clearance, as discussed in Section 7.7.2. In case of the large diametral bearing clearance of about 27 µm, the inner oil whirl takes place with a high amplitude, leading to the obvious constant tone besides the unbalance whistle, as displayed in Fig. 7.40a. As having already known, by reducing the inner bearing clearance, the oil whirl amplitude decreases; hence, the constant tone is weakened. The computed result with the diametral bearing clearance reduced by 25% to about 20 µm shows that the inner oil

whirl disappears nearly in the entire speed range. However, it only occurs with a very small amplitude from the relative rotor speed of 90% (s. Fig. 7.40b). On the contrary, the outer oil whirl does not induce any subsynchronous noise because its frequency is extremely low, so that the intensity of noise that is proportional to frequency squared is negligible. As a reason, the outer oil whirl is inaudible although its deflection amplitude is larger due to the conical vibration mode.

**(a) Large inner bearing clearance**



**(b) Small inner bearing clearance**
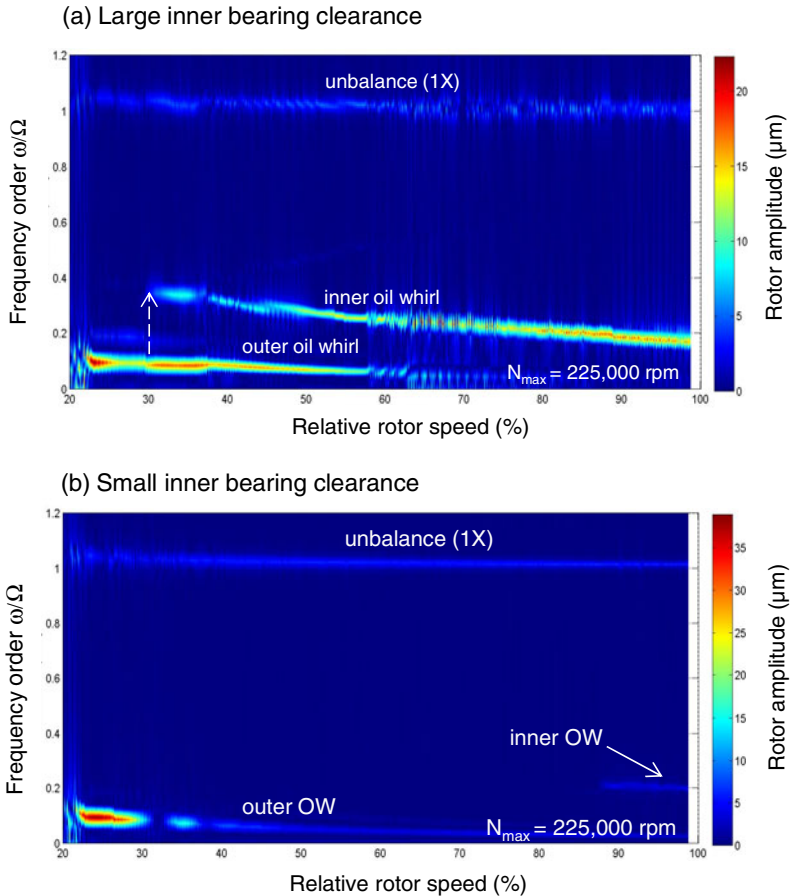


**Fig. 7.40** Computed Waterfall diagrams of the rotor responses at different bearing clearances

# References

1. Adams Jr., M.L.: Rotating Machinery Vibration. CRC, Taylor and Francis (2001)
2. Bently, D.E., Hatch, C.: Fundamentals of Rotating Machinery Diagnostics. Bently Pressurized Bearing Press (2002)
3. Childs, D.: Turbomachinery Rotordynamics. J. Wiley and Sons Inc. (1993)

4. Ehrich, F.: Handbook of Rotordynamics. Krieger Publishing Company (2004)
5. Gasch, R., Nordmann, R., Pfuetzner, H.: Rotordynamik, vol. 2. Auflage, Springer (2006)
6. Genta, G.: Dynamics of Rotating Systems. Springer, Heidelberg (2005)
7. Hori, Y.: Hydrodynamic lubrication. Springer, Heidelberg (2006)
8. Kraemer, E.: Rotordynamics of Rotors and Foundations. Springer, Heidelberg (1993)
9. Kothe, P., Ahrens, T., Kleinschmidt, R.: Measurements of Rotordynamics of Turbochargers. Internal Report BMTS (2010)
10. MADYN 2000: Program of Computational Rotordynamics. Delta JS (2011)
11. Muszýnska, A.: Rotordynamics. CRC, Taylor and Francis (2005)
12. Newland, D.E.: An Introduction to Random Vibrations, Spectral & Wavelet Analysis, 3rd edn. Dover Publications Inc. (2005)
13. Nguyen-Schaefer, H., Sprafke, P.: Numerical Study on Interaction Effects of the Bubbles induced by Air-Release and Cavitation in Hydraulic Systems. In: Tenth Bath International Fluid Power Workshop. Research Studies Press, Bath (1997)
14. Nordmann, R.: Schwingungsberechnung von nichtkonservativen Rotoren mit Hilfe von Links- und Rechts-Eigenvektoren. VDI Bericht 269 (1976)
15. Rao, J.S.: Rotor Dynamics, 3rd edn. New Age Intl. Publishers (2007)
16. Rieger, N.F.: Rotordynamics 2 - Problems in Turbomachinery. CISM Courses and Lectures No. 297 (1988)
17. Rieger, N.F.: Balancing of Rigid and Flexible Rotors. U.S. DoD (1986)
18. Vance, J.: Rotordynamics of Turbomachinery. J. Wiley and Sons Inc. (1988)
19. Yamamoto, T., Ishida, Y.: Linear and Nonlinear Rotordynamics. J. Wiley and Sons Inc. (2001)

# Chapter 8
# Rotor Balancing in Turbochargers

## 8.1  Reasons for the Rotor Balancing

In the following section, we focus only on the rotor balancing in turbochargers and not in the industrial turbomachines because we can find them in [1], [4], [6], and [10].

Production process of the compressor wheel and turbine shaft causes an initial unbalance where the mass center does not lie in the geometrical axis of the compressor wheel or turbine shaft. Excessively large unbalance force and moment induce large amplitudes of the rotor response, leading to the bearing wear, rub contact, and seizure of the journal and bearings and as well as the compressor, turbine wheels and their housings. Additionally, the rotor unbalance generates unbalance whistle that has the synchronous frequency order (1X) of the rotor frequency. The unbalance whistle is one of the undesirable airborne noises in the automotive turbochargers.

There are two possibilities of producing the turbocharger rotor: either production of the rotor *without* or *with* the rotor balancing. If we choose the first one *without* the rotor balancing, the production of the compressor wheel and turbine shaft must be highly precise, so that the mass-center eccentricity of the rotor is in the order of a few microns ($\sim 10^{-6}$ m) from its geometric axis. It leads to large deficient producing rates and therefore very high producing cost. Notice that *producing cost* is one of the most important competition key of products in the industry, and "*cost, cost cut, and cost breakdown*" always accompanies the products on their lifetimes. Therefore, the economical way is producing turbochargers *with* the rotor balancing, at which the production process is less precise. Despite the less precise production process, the rotor arrives at an acceptable residual unbalance after the balancing procedure that brings the mass center of the rotor possibly close to the rotational geometric axis.

## 8.2  Kinds of Rotor Balancing

There are two kinds of the rotor balancing in the automotive turbochargers:

- *Low-speed balancing (called shop balancing)* is used in the rigid rotors at a low balancing speed up to 3,400 rpm, depending on the balancing machine types, to reduce the initial unbalance caused by the production process. Generally, the

whole rotor is not balanced at the shop balancing, but only the compressor wheel and turbine shaft are separately balanced at the rigid state with the low-speed balancing. Hence, it is also named *single part balancing*. The low-speed balancing is generally carried out with two balancing planes at the nose and back face of the wheel. The goal of this balancing is to reduce the unbalanced force and moment to minimize the induced unbalanced excitations and therefore to prevent the radial bearings from damages due to contact rub and seizure between the journal and bearings caused by the excessive rotor unbalances.

- *High-speed balancing (called trim balancing)* is applied to the flexible rotors at a high balancing speed (generally above the first critical speed) at which the rotor deflects in the lateral direction due to large unbalance forces and moments. Besides the initial unbalance due to production, an additional unbalance is resulted from mounting the compressor wheel on turbine shaft and as well as the deformed rotor at high rotor speeds during the operation. Hence, it leads to the unbalanced whistle; therefore, the additional unbalance must be removed by the trim balancing. The high-speed balancing is carried out with two balancing planes at the screw-nut of the compressor wheel and the hub surface between the blades at the compressor wheel outlet. The purpose of the trim balancing is only to reduce the unbalance whistle during the operation at high rotor speeds, especially in passenger vehicles. Generally, one omits the trim balancing in the turbochargers of commercial vehicles and industrial applications unless the customers explicitly require.

## 8.3 Two-Plane Low-Speed Balancing of a Rigid Rotor

The production of the compressor wheel and turbine shaft induces the static, couple, and dynamic unbalances. The static unbalance occurs when the polar mass-inertia axis differs from the rotational axis by an eccentricity $\varepsilon$. On the contrary, the couple unbalance occurs when the polar mass-inertia axis differs from the rotational axis by an angle $\alpha$; however, they intersect each other at the mass center G.
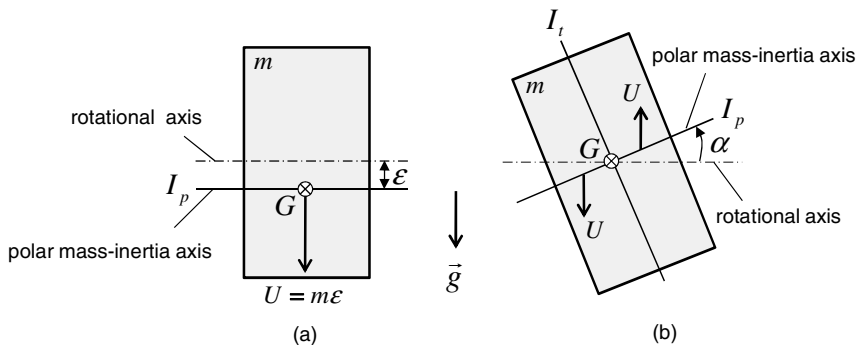


**Fig. 8.1** (a) Static unbalance; (b) Couple unbalance

In the static unbalance, the mass center G always lies below the rotational axis due to the gravity at the equilibrium position (s. Fig. 8.1). That means the rotor component moves from any beginning position to the equilibrium because of its weight. Hence, it has the name *static unbalance*; obviously, one recognizes that the rotor moves itself to the equilibrium position in the static unbalance. On the contrary, the rotor in the couple unbalance does not move itself to the equilibrium position because the mass center G is always in the rotational axis. It is only recognized in the rotating condition, in which the unbalanced moment acts upon the rotor although the static unbalance equals zero, as shown in Fig. 8.1b.
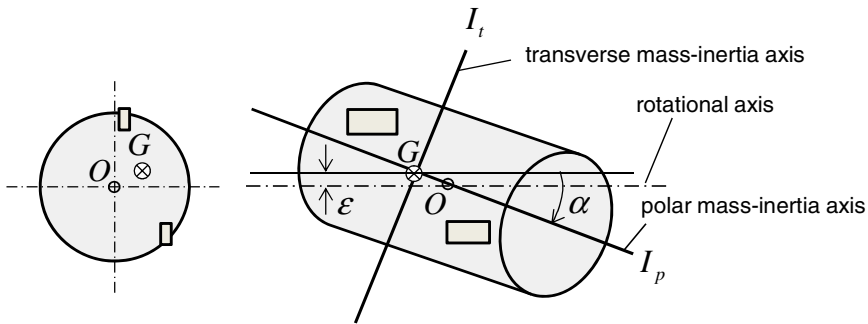


**Fig. 8.2** Dynamic unbalance of the rotor

The static unbalance is caused by the production mistakes, large eccentricity at welding the turbine wheel on the rotor shaft, non-homogeneous material, and residual unbalance after the shop balancing. Moreover, it is also induced by thermal deformations, wears, and plastic deformations that are generated by over-speeding the rotor, over-heating the turbine wheel, and the impact of hard particles in the mixed intake air in case of the low-pressure EGR on the compressor wheel after a long operating period. On the contrary, the couple unbalance is created by a large non-coaxiality at welding the turbine wheel on the rotor shaft, thermal, and plastic deformations of the rotor due to over-speeding or loose screw-nut of the compressor wheel during the operation of turbochargers. In practice, we have both static and couple unbalances at producing the turbine shaft including the turbine wheel and rotor shaft, leading to the dynamic unbalance of the rotor.

The dynamic unbalance is similar to the couple unbalance, but the mass center of the rotor does not lie in the rotation axis (s. Fig. 8.2). Therefore, the dynamic unbalance can be decomposed in the static and couple unbalances. In fact, the dynamic unbalance often occurs at manufacturing the turbine shaft by welding the turbine wheel on the rotor shaft. The eccentricity $\varepsilon$ of the static unbalance and the non-coaxiality with an angle $\alpha$ of the couple unbalance are combined together, leading to the dynamic unbalance, as displayed in Fig. 8.2. The unbalance of the turbine shaft is the largest part of the entire rotor unbalance at the production; it contains the initial unbalance of the turbine wheel itself and the eccentricity and non-coaxiality between the shaft and turbine wheel.

Having considered the rotor with an unbalanced mass $m_u$ at a radius $r_u$, as shown in Fig. 8.3, the static unbalance of the rotor results in

$$U = m_u r_u \tag{8.1}$$

Due to the unbalanced mass $m_u$, the new mass center G of the rotor is located at the unbalance radius $\varepsilon$. The rotor unbalance is written in

$$U = (m + m_u)\varepsilon \tag{8.2}$$

By substituting of Eqs (8.1) and (8.2), one calculates the unbalance radius at $m_u \ll m$.

$$\varepsilon = \frac{m_u r_u}{(m + m_u)} \approx \frac{U}{m} \Rightarrow U \approx m\varepsilon \tag{8.3}$$
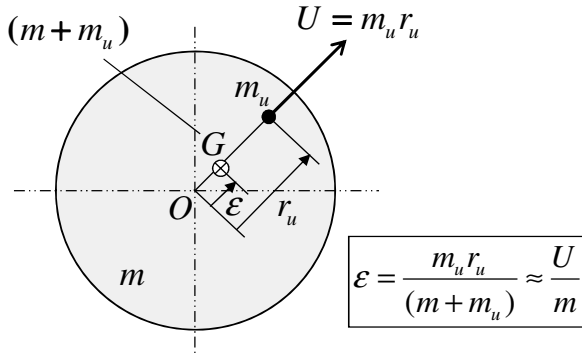


**Fig. 8.3** Unbalanced radius $\varepsilon$ of the unbalanced rotor component

Figure 8.4 shows an unbalanced compressor wheel with the unbalanced vector $U_\varepsilon$ that is balanced at the nose face (plane 1) and back face (plane 2) of the wheel. Hence, the unbalanced vector $U_\varepsilon$ is balanced by two balanced vectors $U_1$ and $U_2$ at the balancing planes 1 and 2, respectively. Generally, the balance vectors are induced by removing masses of material $m_1$ and $m_2$ at the given radii of $r_1$ and $r_2$ in the opposite direction of the balance vectors $U_1$ and $U_2$, respectively. The unbalanced vector $U_\varepsilon$ is called the initial unbalance of the compressor wheel.

The balance masses of $m_1$ and $m_2$ are computed from the equations of the unbalanced vectors and moments.

$$\begin{cases} \sum U_i = U_\varepsilon - U_1 - U_2 = m\varepsilon - m_1 r_1 - m_2 r_2 = 0; \\ \sum M_i = U_1 a - U_2 b = m_1 r_1 a - m_2 r_2 b = 0 \end{cases} \tag{8.4}$$

Thus,

$$\begin{cases} m_1 = \dfrac{m\varepsilon b}{r_1(a+b)} = \dfrac{U_\varepsilon b}{r_1(a+b)}; \\[3mm] m_2 = \dfrac{m\varepsilon a}{r_2(a+b)} = \dfrac{U_\varepsilon a}{r_2(a+b)} \end{cases} \tag{8.5}$$

By giving the balancing radii of $r_1$ and $r_2$ at the balancing planes, the removed masses $m_1$ and $m_2$ in the opposite directions of the balanced vectors $U_1$ and $U_2$ of the compressor wheel are computed according to Eq. (8.5). The balancing procedure is carried out at the low balancing speed up to 3,400 rpm, depending on the balancing machine types.

To balance the compressor wheel, a well-balanced master shaft is needed to mount the compressor wheel on it. The compressor wheel unit including the master shaft and compressor wheel is rotated on the air bearings in the balancing machine. Despite using the master shaft, it has however a small static unbalance that can be eliminated by calibrating. To calibrate the master shaft at the first time of balancing a compressor wheel, we mount it on the shaft and move the compressor wheel at three marked angular positions $\theta$ of 0°, 120°, and 240°, as shown in Fig. 8.5. The unbalanced vector $T_i$ of the compressor wheel unit has been successively measured by three times; each time at the given angular position $\theta_i$.
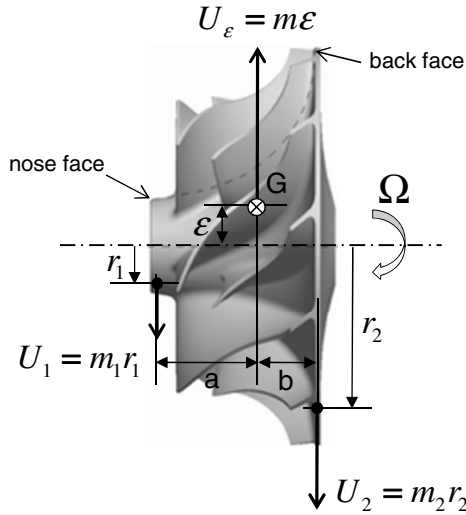


**Fig. 8.4** Two-plane low-speed balancing of the compressor wheel

At $\theta_1 = 0°$ the measured unbalance vector can be written in

$$\vec{T}_1 = \vec{S} + \vec{U}_\varepsilon \qquad (8.6)$$

where

$\vec{S}$ is the unbalance vector of the master shaft;

$\vec{U}_\varepsilon$ is the initial unbalance vector of the compressor wheel.

By the two other angular positions, the initial unbalanced amplitudes are unchanged, but their vector directions changes at the positions 120° and 240°. Therefore, the vector $\vec{S}$ determines the unbalance vector of the master shaft where S is

the center of the equilateral triangular. The initial unbalance of the master shaft is stored in the balancing machine for further balancing the compressor wheels.

Thus, the initial unbalance vector of the compressor wheel results in

$$\vec{U}_\varepsilon = \vec{T}_1 - \vec{S} \tag{8.7}$$
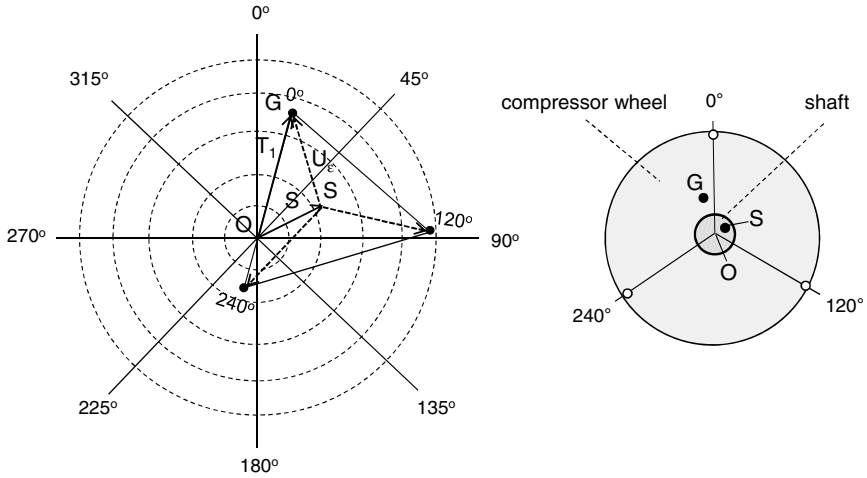


**Fig. 8.5** Calibrating the master shaft for the compressor wheel

The static unbalance $U_\varepsilon$ causes the unbalance force $F_u$ acting on the compressor wheel.

$$F_u = m\,\varepsilon\Omega^2 = U_\varepsilon\Omega^2 \tag{8.8}$$

where $\Omega$ is the rotor speed.

The initial unbalance of the turbine shaft normally contains two main parts: the dynamic unbalance due to welding the turbine wheel to the shaft; and the unbalance of the turbine wheel itself due to casting. Figure 8.6 displays the turbine shaft with the dynamic unbalance caused by the eccentricity $\varepsilon$ and misalignment angle $\alpha$ between the shaft and turbine wheel. The dynamic unbalance induces the moment *unbalance* $U_m$ and unbalance *moment* $M_u$ acting on the turbine shaft, as derived in Eqs (5.49) and (5.50).

The moment unbalance vector is perpendicular to the drawing plane.

$$\vec{U}_m = (I_t - I_p)\alpha\vec{k} \tag{8.9}$$

where
$U_m$ is the moment unbalance (g.mm²), different to the static unbalance $U_\varepsilon$ (g.mm);
$I_t$, $I_p$ are the transverse and polar mass-inertia moments (kg.mm²), respectively.

Similar to the static unbalance, the moment unbalance $U_m$ generates the unbalance moment $M_u$ acting on the rotor in the dynamic unbalance. The unbalance moment is written according to Eq. (5.49).

$$\vec{M}_u = \vec{U}_m \Omega^2 = (I_t - I_p)\alpha \Omega^2 \vec{k} \tag{8.10}$$

where $M_u$ is the unbalance moment (Nm).

The unbalance force $\vec{F}_u$ and unbalance moment $\vec{M}_u$ are the external excitation sources acting on the rotor in the vibration equations of the rotor, as given in Eqs (5.52) and (5.53).
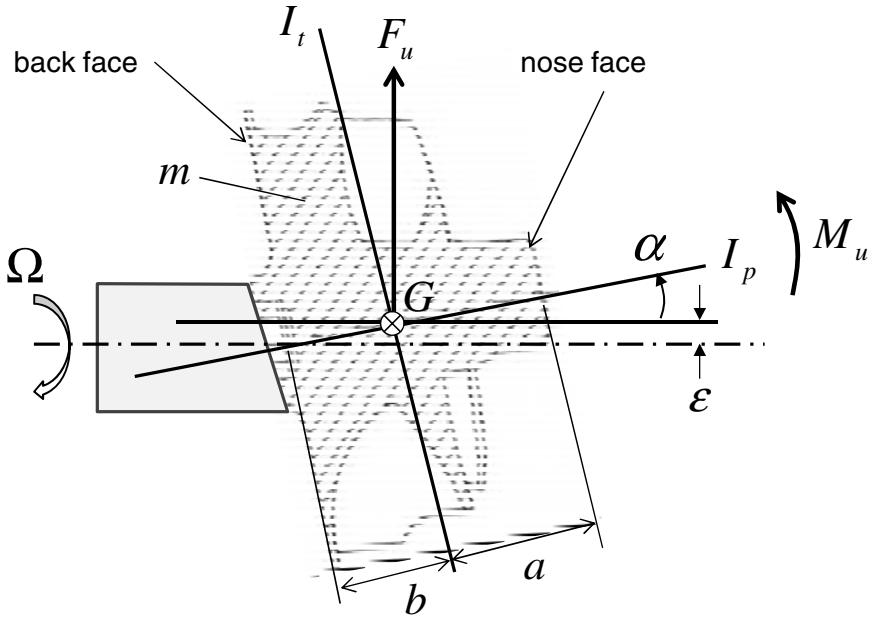


**Fig. 8.6** Dynamic unbalance of the turbine runner

The turbine shaft is balanced with the low balancing speed up to about 3,400 rpm at the nose and back faces. At first, its unbalance is determined by the measuring Schenck machine supported on the air bearings (s. Fig. 8.7). Then, the turbine shaft is balanced in the balancing machine by removing material at the nose and back faces in the opposite directions of the balance vectors.

The balance vectors are resulted from the equations of the unbalance vectors and unbalance moments at the initial condition, as shown in Fig. 8.8.

$$\begin{cases} \sum U_i = -U_1 - U_2 + U_\varepsilon = -U_1 - U_2 + m\varepsilon = 0; \\ \sum M_i = -U_1 a + U_2 b + U_m = -U_1 a + U_2 b + (I_t - I_p)\alpha = 0 \end{cases} \tag{8.11}$$

The balance vectors at the nose and back faces are calculated from Eq. (8.11).

$$\begin{cases} U_1 = \dfrac{m\varepsilon b + (I_t - I_p)\alpha}{(a+b)} = m_1 r_1 \\[4mm] U_2 = \dfrac{m\varepsilon a - (I_t - I_p)\alpha}{(a+b)} = m_2 r_2 \end{cases} \qquad (8.12)$$
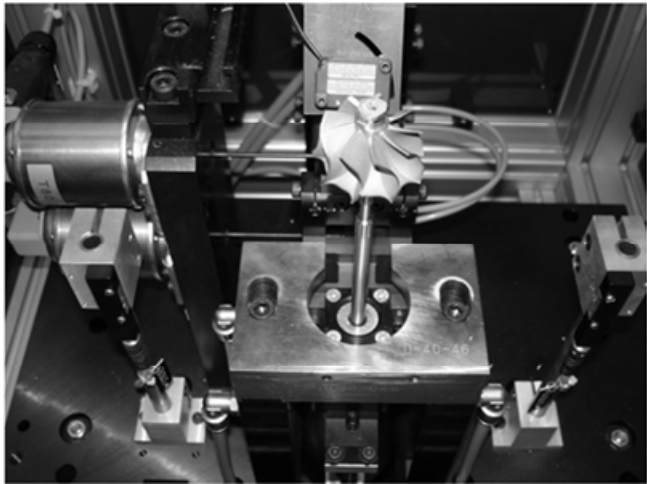


**Fig. 8.7** Unbalance measurement in a Schenck machine (Courtesy BMTS)
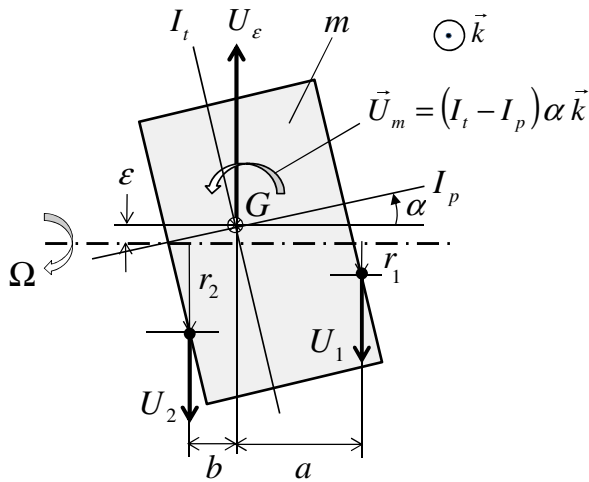


**Fig. 8.8** Low-speed balancing at two planes in the dynamic unbalance

Similar to the compressor wheel, by the giving balancing radii $r_1$ and $r_2$ in the balancing planes, the removed masses $m_1$ and $m_2$ in the opposite directions of $U_1$ and $U_2$ of the turbine wheel are determined by Eq. (8.12). Notice that the misalignment angle $\alpha$ remains after the low-speed balancing in the dynamic unbalance. A large misalignment angle induces the rotor response with a superharmonic frequency order of 2X in the Waterfall diagram, as shown in Fig. 7.18.

Theoretically, the unbalances would be fully eliminated if the removed masses were exactly removed at the given balancing radii. In practice, the removed masse has a mass tolerance of $\pm\Delta m$ and the removed masse scatters around the given balancing position in the circumferential and radial directions. Therefore, it always remains the small residual unbalances $U_{1,r}$ and $U_{2,r}$ at the balancing planes, as shown in Fig. 8.9. However, the residual unbalance at the balancing planes must be less than the permissible unbalance $U_{lim}$ according to the ANSI Standard for Balance Quality of Rotating Rigid Body, ANSI S2.19-1975 or DIN-ISO 1940-1. The balancing quality grade of the automotive turbochargers of passenger and commercial vehicles is chosen between G40 and G100 of the DIN-ISO 1940-1, which gives the permissible residual unbalance.

The reason for the high G level is on the one hand the very high rotor speed of the automotive turbochargers; on the other hand, the possible balance radius $e_{lim}$. Having chosen the balancing quality grade of G100 for a small turbocharger of passenger vehicles, one obtains

$$e_{lim}\Omega = 100\, mm/s$$

where
$e_{lim}$ is the acceptable balance radius (mm);
$\Omega$ is the maximum rotor speed (rad/s).

At the maximum rotor speed of $N_{max}$ = 280,000 rpm ($\Omega \approx$ 29,320 rad/s), the acceptable balance radius is calculated at G100.

$$e_{lim} = \frac{100\, mm/s}{29,320\, rad/s} \approx 3.4x10^{-3}\, mm$$

If we use a lower G level for high rotor speeds, the balancing radius becomes much smaller and is impossible for the rotor balancing. Therefore, the balancing quality grade G40 is used in the turbochargers of commercial vehicles in which their rotor speeds are not too high due to the large wheels.

With the rotor mass $m \approx$ 120 g, the permissible residual unbalance at G100 for small turbochargers results in

$$U_{lim} = me_{lim} = (120\, g).(3.4x10^{-3}\, mm) \approx 0.4\, g.mm$$

Thus, the residual unbalance for the compressor wheel and shaft runner should be smaller than one-half of the permissible residual unbalance of the rotor.

$$U_{CW}, U_{TR} \leq \frac{U_{\lim}}{2} \tag{8.13}$$

The results of Fig. 8.9 show that the directions of the residual unbalanced vectors after the low-speed balancing differ from the balance vectors $\vec{U}_1$ and $\vec{U}_2$ because the removed masses scatter around the given balancing points in the circumferential and radial directions. Hence, the residual unbalanced vectors at the mass centers of the compressor wheel (CW) and turbine shaft (TS) are resulted in

$$\begin{cases} \vec{U}_{CW} = \vec{U}_{1,rC} + \vec{U}_{2,rC} \\ \vec{U}_{TR} = \vec{U}_{1,rT} + \vec{U}_{2,rT} \end{cases} \tag{8.14}$$
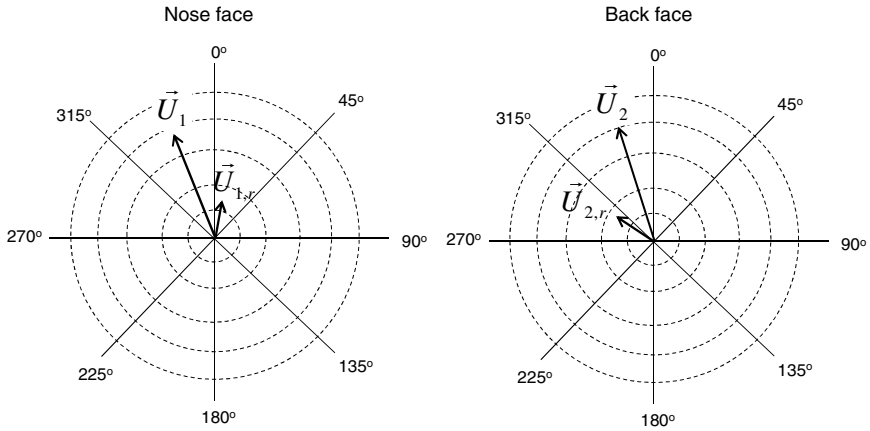


**Fig. 8.9** Residual unbalance vectors $\mathbf{U}_{1,r}$ and $\mathbf{U}_{2,r}$ at the balancing planes

By assembling the compressor wheel in the turbine shaft, the residual unbalanced vectors $\mathbf{U}_{CW}$ and $\mathbf{U}_{TR}$ are set in fact by an arbitrary angle $\theta$ between $0°$ and $180°$ (s. Fig. 8.10a). If the residual unbalance vectors have the same direction ($\theta = 0°$), the rotor is called the in-phase couple unbalance. At $\theta = 180°$, the residual unbalance vectors are opposite to each other, the rotor unbalance is called the out-of-phase couple unbalance, as shown in Fig. 8.10b.
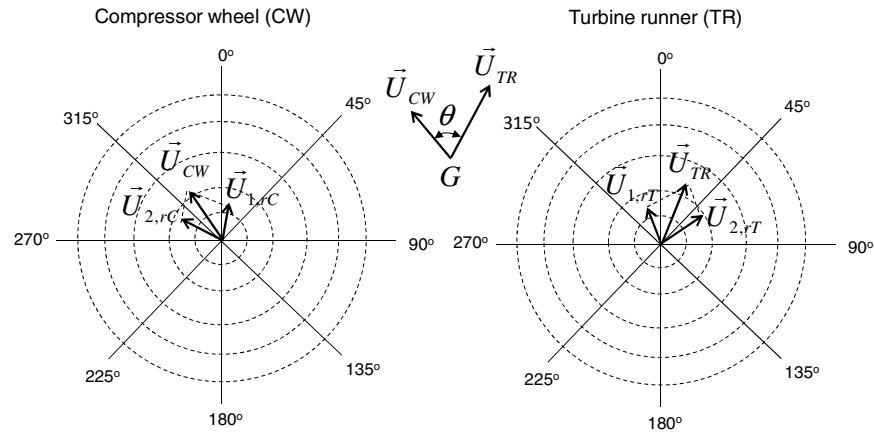
**Fig. 8.10a** Residual unbalance vectors in the compressor wheel and turbine shaft
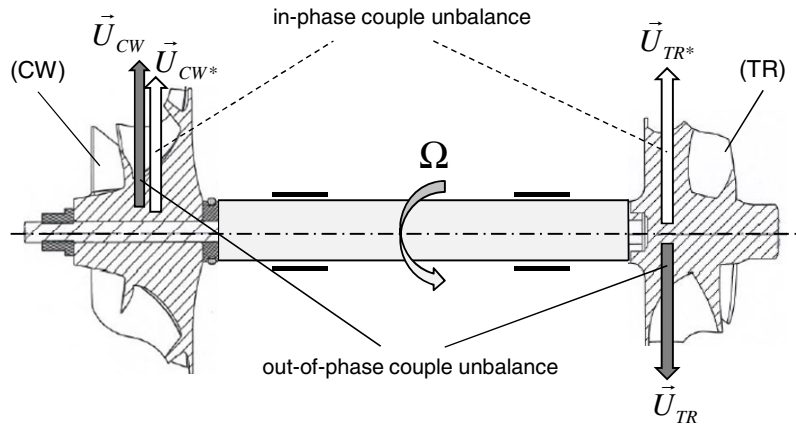


**Fig. 8.10b** In-phase and out-of-phase couple unbalances

## 8.4 Two-Plane High-Speed Balancing of a Flexible Rotor

Assembling the compressor wheel in the turbine shaft causes the additional static and dynamic unbalances. Due to acoustics (unbalance whistle) induced by the additional unbalance, the rotor must be balanced at the high balancing speeds (trim balancing). Moreover, the rotor is flexible at the high-speed working conditions that induce unbalance and therefore unbalance whistle. For this reason, the rotor should be balanced at the high speeds with two balancing planes in the screw-nut of the compressor wheel (balancing plane 1*) and the hub surface between the blades at the compressor wheel outlet (balancing plane 2*), as displayed in Fig. 8.11.

To accelerate the rotor up to 200,000 rpm, we use a nozzle ring supplied by a high air pressure of about 3 bar absolute; the nozzle ring is set at the inlet of the turbine wheel. The pressure energy of the pressurized air is transformed in the kinetic energy with the sonic speed of air (Mach number M = 1) at the nozzle ring that speeds up the turbine wheel.

There are two common methods of the two-plane high-speed balancing (called trim balancing): Modal Balancing theory (MB) and Influence Coefficient Method Balancing (ICM).

### 8.4.1  Modal Balancing Theory

The modal balancing based on the bending modes of the flexible rotor at high speeds was developed between 1959 and 1967 by many pioneers, such as Bishop, Parkinson, Gladwell, Kennedy-Pancu, Lindley, and Rieger in [7] and [8]. Due to unbalance, the flexible rotor deflects at the amplitude y(z) at the axial position z, as shown in Fig. 8.11.

The rotor deflection shape is described by the series of the modal deflection $Y_i(z)$ according to Rieger [8].

$$y(z) = \sum_{i=1}^{n=\infty} \phi_i Y_i(z) = \phi_1 Y_1(z) + ... + \phi_n Y_n(z) \qquad (8.15)$$

where
$\phi_i$ is the deflection coefficient of the vibration mode i;
$Y_i$ is the modal deflection of the rotor of the vibration mode i.
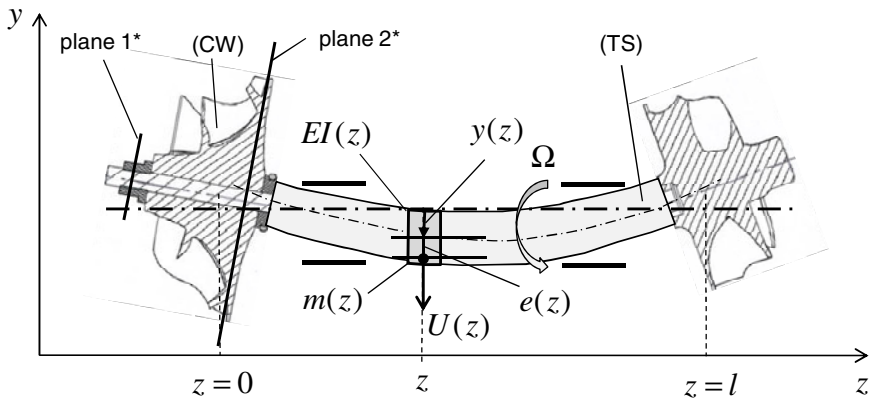


**Fig. 8.11** Two-plane modal balancing of a flexible rotor

Similarly, the mass eccentricity of the rotor is written in the series of $Y_i(z)$.

$$e(z) = \sum_{i=1}^{n=\infty} e_i Y_i(z) = e_1 Y_1(z) + ... + e_n Y_n(z) \qquad (8.16)$$

The induced rotor unbalance at the axial position z is written in the series of $Y_i(z)$.

$$U(z) = \sum_{i=1}^{n=\infty} \lambda_i Y_i(z) = \lambda_1 Y_1(z) + ... + \lambda_n Y_n(z) \tag{8.17}$$

where $\lambda_i$ is the unbalance coefficient of the vibration mode i at the position z.

The virtual kinetic work done by the rotor deflection is calculated

$$\delta W_{kinetic} = \int_0^l m(z)\left[y(z) + e(z)\right]\Omega^2 \delta y.dz \tag{8.18}$$

where
$\delta y = Y_i(z)\delta\phi_i$ is the virtual displacement of the rotor;
m(z) is the mass distribution of the rotor at the axial position z;
$\Omega$ is the balancing speed of the rotor.

By using the orthogonality of the vibration modes, one obtains the relation of

$$\int_0^l m(z)Y_i(z)Y_j(z)dz = \begin{cases} 0; & i \neq j \\ M_i; & i = j \end{cases} \tag{8.19a}$$

within

$$M_i \equiv \int_0^l m(z)Y_i^2(z)dz \tag{8.19b}$$

and

$$\int_0^l EI(z)Y_i''(z)Y_j''(z)dz = \begin{cases} 0; & i \neq j \\ K_i; & i = j \end{cases} \tag{8.20a}$$

within

$$K_i \equiv \int_0^l EI(z)Y_i''^2(z)dz \tag{8.20b}$$

By substituting Eqs (8.15), (8.16), (8.18), (8.19a), and (8.19b), the virtual kinetic work of the vibration mode i becomes

$$\delta W_{kinetic} = M_i\left(\phi_i + e_i\right)\Omega^2 \delta\phi_i \tag{8.21}$$

The virtual potential work of the vibration mode i of the rotor is computed.

$$\delta W_{pot} = -\frac{\partial V}{\partial \phi_i}\delta\phi_i \tag{8.22}$$

where the potential energy $V$ is calculated by using Eqs (8.20a) and (8.20b)

$$
\begin{aligned}
V &= \int_0^l \tfrac{1}{2} EI(z) y''^2(z) dz \\
&= \int_0^l \tfrac{1}{2} EI(z) \left( \sum_i^\infty \phi_i Y_i''(z) \right)^2 dz = \frac{1}{2} \sum_i^\infty K_i \phi_i^2
\end{aligned}
\tag{8.23}
$$

Thus,

$$
\delta W_{pot} = -\frac{\partial V}{\partial \phi_i} \delta \phi_i = -K_i \phi_i \delta \phi_i
\tag{8.24}
$$

According to the principle of virtual work at the equilibrium ($\delta W = 0$), one obtains the total virtual work of the rotor from Eqs (8.21) and (8.24).

$$
\begin{aligned}
\delta W &= \delta W_{kinetic} + \delta W_{pot} \\
&= M_i(\phi_i + e_i)\Omega^2 \delta \phi_i - K_i \phi_i \delta \phi_i = 0
\end{aligned}
\tag{8.25}
$$

Thus,

The coefficients of the deflection and mass eccentricity of the rotor are given in

$$
\phi_i = \frac{\eta_i^2 e_i}{1 - \eta_i^2}; \quad e_i = \frac{(1 - \eta_i^2)\phi_i}{\eta_i^2}
\tag{8.26}
$$

within

$$
\eta_i \equiv \frac{\Omega}{\Omega_{cr,i}} = \Omega \sqrt{\frac{M_i}{K_i}}
\tag{8.27}
$$

where

$\eta_i$ is the speed ratio of the vibration mode i;
$\Omega$ is the balancing speed.

The unbalance coefficient $\lambda_i$ is resulted by using the orthogonality of $Y(z)$, as given in Eq. (8.19a).

$$
\begin{aligned}
\int_0^l U(z)m(z)Y_j(z)dz &= \int_0^l \left( \sum_i^\infty \lambda_i Y_i(z) \right) m(z)Y_j(z)dz \\
&= \int_0^l \lambda_i m(z)Y_i^2(z)dz = \lambda_i M_i
\end{aligned}
$$

Thus,

$$
\lambda_i = \frac{1}{M_i} \int_0^l m(z)U(z)Y_i(z)dz
\tag{8.28}
$$

By rotor balancing, one creates the balance vector $\vec{p}$ at z = c by the load $q$ in the small length $\xi$ in the opposite direction of the unbalance vector $\vec{U}(z)$.

$$p = q.\xi = \sum_{i=1}^{\infty} \alpha_i Y_i(z)$$

$$= -U(z) = -\sum_{i=1}^{\infty} \lambda_i Y_i(z)$$

(8.29)

Therefore,

$$\alpha_i = -\lambda_i$$

(8.30)

The balance correction vector p(z) at the position z results in

$$p(z) = q.\xi = -U(z) = -m(z).e(z)$$

(8.31)

At the modal balance in the vibration mode i, the following characteristics that are necessary to be known in advance are the mass distribution of the rotor m(z), modal deflection amplitude $Y_i(z)$, measured mode shape of the rotor y(z), rotor eigenfrequency $\omega_i$ of the vibration mode i, and critical frequencies of the rotor as well. Therefore, the coefficient $\phi_i$ of the rotor deflection is calculated from y(z) and $Y_i(z)$ in Eq. (8.15) and the mass eccentricity coefficient $e_i$ is resulted from $\phi_i$ in Eq. (8.26). Then, the mass eccentricity of the rotor e(z) is computed from $e_i$ and $Y_i(z)$ in Eq. (8.16).

By using Eq. (8.31), the balancing length $\xi$ at the position z is determined at a given removed load $q < 0$ in the same direction of the unbalance vector $\vec{U}(z)$, so that the balance vector is opposite to the unbalance vector.

$$\xi = \frac{-U(z)}{q} = \frac{-m(z).e(z)}{q}$$

(8.32)

The main disadvantage of the modal balancing is the necessity of knowing many unknown or not-easily-known characteristics of the rotor, such as m(z), $Y_i(z)$, y(z), and $\omega_i$, as discussed earlier. Furthermore, the additional disadvantage is that the balancing correction vector depends on the balancing speed $\Omega$, as shown in Eqs (8.26) and (8.27). In fact, the automotive turbochargers operate in the wide rotor speed range, not just at the constant speed in the normally working condition, such as turbomachines using in the power plants and chemical industries. Hence, the modal balancing of the flexible rotors is not suitable for the applications to automotive turbochargers. On the contrary, the Influence Coefficient Method

balancing can provide an easy-to-use, efficient, and well-done balancing procedure of the turbochargers.

## 8.4.2  Influence Coefficient Method

The Influence Coefficient Method (ICM) has been developed by Goodman, Rieger, Lund and Tonnesen, Tessarzik, Badgley, and Anderson, etc. since 1961 [8]. The application of the ICM balancing in turbochargers is normally carried out at two balancing planes in the screw-nut of the compressor wheel (plane 1*) and the hub surface between the blades at the compressor wheel outlet (plane 2*), as indicated in Fig. 8.13.

Based on the complex transfer impedance $Z$ of the balancing system, i.e. the inversion of the complex dynamic stiffness coefficient $K_S$ of the system, including the turbocharger rotor and less influent balancing machine, the unbalance response at the trim balancing is resulted from the complex transfer impedance and unbalance excitation force, as displayed in Fig. 8.12.

The measured unbalance responses could be the acceleration or vibration velocity of the rotor in the measuring planes. Theoretically, the measuring planes should be the same places of the balancing planes in the compressor wheel, which rotates however with the high rotor speeds. As a reason, it is time and cost intensive at the trim balancing in the production to measure the rotor unbalance responses in the rotating balancing planes. Hence, in practice, they are computed from the measured rotor responses in the certain non-rotating position in the bearing housing or the compressor and turbine casings at the trim balancing in the production.

Unbalance excitation            Balancing system            Unbalance response

$$F_u = U\Omega^2 e^{j\Omega t} \implies \boxed{\begin{array}{c} \textbf{Transfer impedance} \\ Z \equiv \dfrac{1}{K_S} \end{array}} \implies a = ZF_u$$
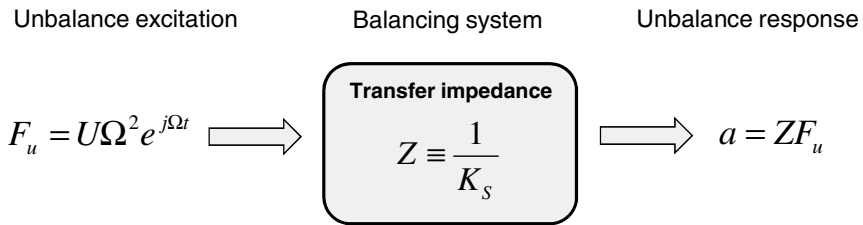
**Fig. 8.12** Unbalance response of the balancing system

Figure 8.13 shows two balancing planes 1* and 2* in the compressor wheel used in the ICM balancing. The reason of the rotor balancing in the compressor wheel (CW) rather than in the turbine wheel (TW) is the high temperature of exhaust gas in the turbine, nearly 820°C to 870°C in diesel engines and even 950°C to 1050°C in gasoline engines.
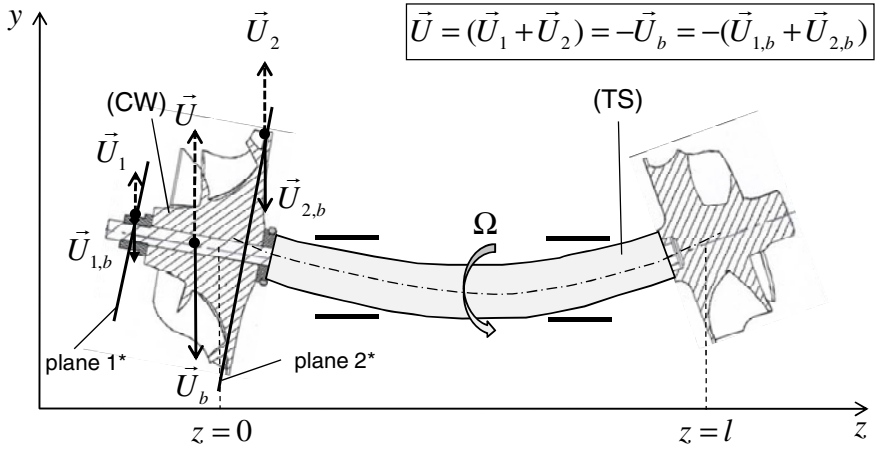
**Fig. 8.13** Two-plane ICM balancing of a flexible rotor

The measured response vectors of acceleration $\mathbf{a_1}$ and $\mathbf{a_2}$ at the planes 1* and 2*, respectively are resulted from the unbalance vector $\mathbf{F_u}$ and the complex transfer impedance $\mathbf{Z}$, which is inversely related to the complex dynamic stiffness $\mathbf{K_S}$, as shown in Fig. 8.12 [4].

$$\mathbf{a} = \mathbf{Z}\mathbf{F_u}$$
$$\begin{bmatrix} \mathbf{a_1} \\ \mathbf{a_2} \end{bmatrix} = \begin{bmatrix} \alpha_{11} & \alpha_{12} \\ \alpha_{21} & \alpha_{22} \end{bmatrix} \begin{bmatrix} \mathbf{F_1} \\ \mathbf{F_2} \end{bmatrix} \tag{8.33a}$$

where
$\alpha_{ij}$ are the influence coefficients with the index i for the balancing plane i, and j for the excitation force at the plane j.

Thus, the acceleration vectors $\mathbf{a_1}$ and $\mathbf{a_2}$ are resulted from the unbalance forces $\mathbf{F_1}$ and $\mathbf{F_2}$ in the balancing planes 1* and 2*.

$$\begin{cases} \mathbf{a_1} = \alpha_{11}\mathbf{F_1} + \alpha_{12}\mathbf{F_2} \\ \mathbf{a_2} = \alpha_{21}\mathbf{F_1} + \alpha_{22}\mathbf{F_2} \end{cases} \tag{8.33b}$$

The complex dynamic stiffness coefficient matrix of the balancing system containing the unbalanced rotor and balancing machine is nearly unchanged at the calibration with the masses $m_{1,c}$ and $m_{2,c}$.

$$\mathbf{K_S} \equiv \mathbf{Z^{-1}} = \begin{bmatrix} \alpha_{11} & \alpha_{12} \\ \alpha_{21} & \alpha_{22} \end{bmatrix}^{-1} \tag{8.34}$$

To calibrate the rotor, two given masses $m_{1,c}$ and $m_{2,c}$ are setup at the given positions $(r_1, \theta_1)$ and $(r_2, \theta_2)$ in the inlet and outlet of the compressor wheel (CW). They

correspond to the calibration unbalances $U_{1,c}$ and $U_{2,c}$, respectively. At first, the first given mass $m_{1,c}$ is added in the position $(r_1, \theta_1)$ at the CW inlet.

The response vectors with the first calibration mass results in

$$\begin{bmatrix} \mathbf{a_{11}} \\ \mathbf{a_{21}} \end{bmatrix} = \begin{bmatrix} \alpha_{11} & \alpha_{12} \\ \alpha_{21} & \alpha_{22} \end{bmatrix} \begin{bmatrix} \mathbf{F_1 + F_{1,c}} \\ \mathbf{F_2} \end{bmatrix} \tag{8.35a}$$

From Eq. (8.35a), one gets the relation between the unbalance vectors $\mathbf{F_1}$ and $\mathbf{F_{1,c}}$.

$$\begin{cases} \mathbf{a_{11}} = \alpha_{11}(\mathbf{F_1 + F_{1,c}}) + \alpha_{12}\mathbf{F_2} \\ \mathbf{a_{21}} = \alpha_{21}(\mathbf{F_1 + F_{1,c}}) + \alpha_{22}\mathbf{F_2} \end{cases} \tag{8.35b}$$

where $\mathbf{a_{ij}}$ is the response vector at the balancing plane $\mathbf{i}$ with the calibration unbalance force $\mathbf{F_{j,c}}$.

After removing the first calibration mass, the second calibration mass $m_{2,c}$ is added in the position $(r_2, \theta_2)$. Similarly, the rotor response with the second calibration mass corresponding to the unbalance force $\mathbf{F_{2,c}}$ becomes

$$\begin{bmatrix} \mathbf{a_{12}} \\ \mathbf{a_{22}} \end{bmatrix} = \begin{bmatrix} \alpha_{11} & \alpha_{12} \\ \alpha_{21} & \alpha_{22} \end{bmatrix} \begin{bmatrix} \mathbf{F_1} \\ \mathbf{F_2 + F_{2,c}} \end{bmatrix} \tag{8.36a}$$

Therefore,

$$\begin{cases} \mathbf{a_{12}} = \alpha_{11}\mathbf{F_1} + \alpha_{12}(\mathbf{F_2 + F_{2,c}}) \\ \mathbf{a_{22}} = \alpha_{21}\mathbf{F_1} + \alpha_{22}(\mathbf{F_2 + F_{2,c}}) \end{cases} \tag{8.36b}$$

By subtracting Eqs (8.35b) and (8.36b) from Eq. (8.33b), one obtains

$$\begin{bmatrix} (\mathbf{a_{11} - a_1}) & (\mathbf{a_{12} - a_1}) \\ (\mathbf{a_{21} - a_2}) & (\mathbf{a_{22} - a_2}) \end{bmatrix} = \begin{bmatrix} \alpha_{11} & \alpha_{12} \\ \alpha_{21} & \alpha_{22} \end{bmatrix} \begin{bmatrix} \mathbf{F_{1,c}} & 0 \\ 0 & \mathbf{F_{2,c}} \end{bmatrix} \tag{8.37}$$

The response vectors in the balancing planes 1* and 2* are demonstrated in the polar plots $(r, \theta)$ of Fig. 8.14. The balance vectors $U_{1,b}$ and $U_{2,b}$ in the balancing planes 1* and 2* are equal and opposite to the unbalance vectors $U_1$ and $U_2$, respectively (s. Fig. 8.13).

$$\mathbf{U_b} = \begin{bmatrix} \mathbf{U_{1,b}} \\ \mathbf{U_{2,b}} \end{bmatrix} = -\mathbf{U} = -\begin{bmatrix} \mathbf{U_1} \\ \mathbf{U_2} \end{bmatrix} = -\frac{1}{\Omega^2}\begin{bmatrix} \mathbf{F_1} \\ \mathbf{F_2} \end{bmatrix} \tag{8.38}$$

Equations (8.33a) and (8.34) give the relation between the excitation forces and rotor responses.

$$\begin{bmatrix} \mathbf{F_1} \\ \mathbf{F_2} \end{bmatrix} = \begin{bmatrix} \alpha_{11} & \alpha_{12} \\ \alpha_{21} & \alpha_{22} \end{bmatrix}^{-1} \begin{bmatrix} \mathbf{a_1} \\ \mathbf{a_2} \end{bmatrix} = \mathbf{K}_S \begin{bmatrix} \mathbf{a_1} \\ \mathbf{a_2} \end{bmatrix} \tag{8.39}$$

where $\mathbf{K_S}$ is calculated from Eq. (8.37)

$$\mathbf{K_S} = \begin{bmatrix} \alpha_{11} & \alpha_{12} \\ \alpha_{21} & \alpha_{22} \end{bmatrix}^{-1} = \begin{bmatrix} \mathbf{F_{1,c}} & 0 \\ 0 & \mathbf{F_{2,c}} \end{bmatrix} \begin{bmatrix} (\mathbf{a_{11}} - \mathbf{a_1}) & (\mathbf{a_{12}} - \mathbf{a_1}) \\ (\mathbf{a_{21}} - \mathbf{a_2}) & (\mathbf{a_{22}} - \mathbf{a_2}) \end{bmatrix}^{-1} \tag{8.40}$$

Substituting Eqs (8.38), (8.39), and (8.40), the balance vector $\mathbf{U_b}$ results in

$$\mathbf{U_b} = \begin{bmatrix} \mathbf{U_{1,b}} \\ \mathbf{U_{2,b}} \end{bmatrix} = -\frac{1}{\Omega^2} \begin{bmatrix} \mathbf{F_{1,c}} & 0 \\ 0 & \mathbf{F_{2,c}} \end{bmatrix} \begin{bmatrix} (\mathbf{a_{11}} - \mathbf{a_1}) & (\mathbf{a_{12}} - \mathbf{a_1}) \\ (\mathbf{a_{21}} - \mathbf{a_2}) & (\mathbf{a_{22}} - \mathbf{a_2}) \end{bmatrix}^{-1} \begin{bmatrix} \mathbf{a_1} \\ \mathbf{a_2} \end{bmatrix} \tag{8.41}$$

By using the calibrating unbalance vectors of $\mathbf{U_{1,c}}$ and $\mathbf{U_{2,c}}$, one obtains the balance vector resulted from the rotor responses and calibrating unbalances.

$$\mathbf{U_b} = \begin{bmatrix} \mathbf{U_{1,b}} \\ \mathbf{U_{2,b}} \end{bmatrix} = \begin{bmatrix} \mathbf{U_{1,c}} & 0 \\ 0 & \mathbf{U_{2,c}} \end{bmatrix} \begin{bmatrix} (\mathbf{a_1} - \mathbf{a_{11}}) & (\mathbf{a_1} - \mathbf{a_{12}}) \\ (\mathbf{a_2} - \mathbf{a_{21}}) & (\mathbf{a_2} - \mathbf{a_{22}}) \end{bmatrix}^{-1} \begin{bmatrix} \mathbf{a_1} \\ \mathbf{a_2} \end{bmatrix} \tag{8.42}$$

Note that the balance vector $\mathbf{U_b}$ given in Eq. (8.42) is independent of the balancing speed. Hence, the balance vectors in the balancing planes 1* and 2* given in Eq. (8.42) are determined in the wide range of the balancing speeds up to 200,000 rpm. The ICM balancing procedures are so long repeated that the delivery acceleration response is below the *delivery acceleration levels* of $a_{I*}$, $a_{II*}$, and $a_{III*}$ that are normally smaller than the *limit acceleration levels* of $a_I$, $a_{II}$, and $a_{III}$. The limit acceleration levels are directly determined in the car, so that the unbalance whistle and constant tone are inaudible in all operating speed ranges of the turbocharger. They are divided into many speed ranges of the balancing speeds N(rpm), as illustrated in Fig. 8.15.
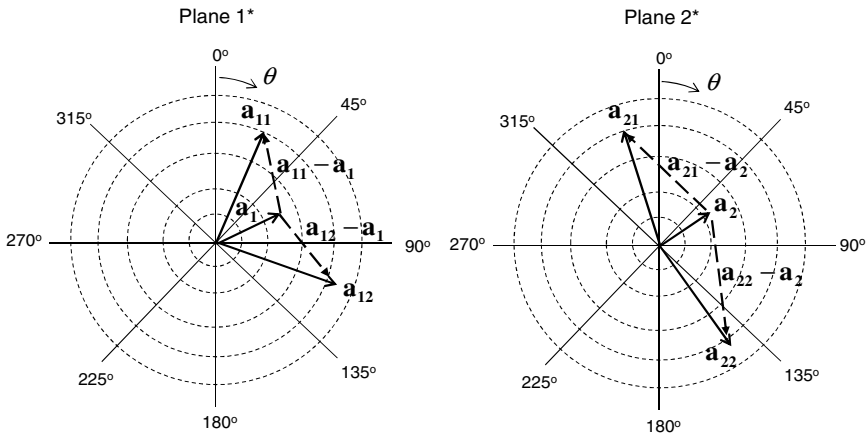


**Fig. 8.14** Calibration response vectors in the balancing planes 1* and 2*

After a long operating period, the unbalance change of the rotor takes place due to the thermal and plastic deformations of the wheels. It mostly increases to nearly twice the delivery acceleration responses at the trim balancing according to experience. The one-third goes to the turbine runner due to heat-related plastic deformation, and the left two-third goes to the compressor wheel. This unbalance change of the compressor wheel is generally created by the inappropriate new positions of eccentricity, misalignment, unbalance change caused by the plastic deformation, loose screw-nut, and therefore slipping of the compressor wheel on the rotor shaft in the radial direction. As a reason, the *delivery acceleration levels* at the trim balancing must be at least reduced by nearly one-half of the *limit acceleration levels* where the unbalance whistle is inaudible in the car.
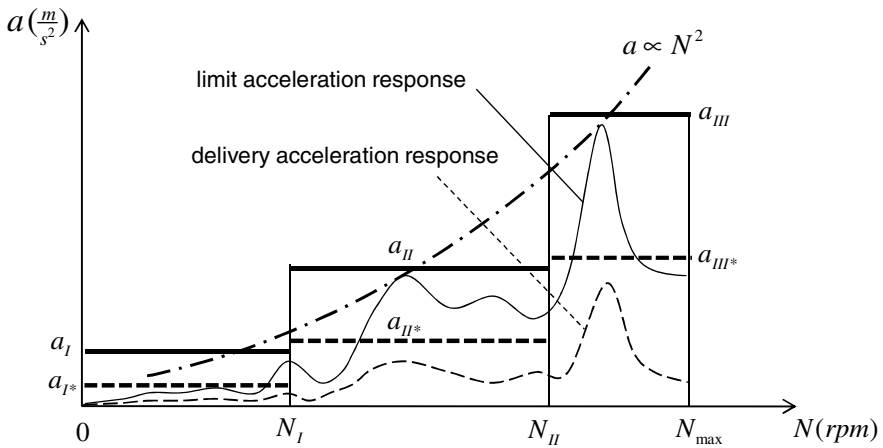


**Fig. 8.15** Limit and delivery acceleration levels in the ICM balancing

By twice timely differentiating the rotor amplitude, one obtains the acceleration amplitude measured at the trim balancing.

$$|a| = |\ddot{x}(t)| = \Omega^2 |x(t)| \propto N^2 |x(t)| \tag{8.43}$$

Note that the measured acceleration amplitude is proportional not only to the rotor amplitude but also to the rotor speed squared according to eq. (8.43). Therefore, it displays not exactly the resonance behavior of the rotor of the turbocharger; the acceleration behavior is strongly affected by the rotor speed squared $N^2$, as shown in Fig. 8.15. As discussed in the earlier chapter, the typical resonance due to unbalance does not exist in nonlinear rotordynamics, but only the limit cycle of the rotor response occurs at each rotor speed. The unbalance amplitude (1X) is relatively small compared to the asynchronous amplitudes in the entire rotor speed range (s. Fig. 7.33).

According to eq. (8.43), the acceleration amplitude at high rotor speeds (N between $N_{II}$ and $N_{max}$) could be higher than the acceleration amplitude at the quasi-

resonance ($N_{res}$ between $N_I$ and $N_{II}$) although its rotor amplitude is smaller than the other one. Therefore, the failure of the radial bearings at the trim balancing happens at the first quasi-resonance instead of at the maximum acceleration amplitude at the higher rotor speeds.

Figure 8.15 and Table 8.1 give the delivery and limit acceleration levels for the rotor acceleration responses at the trim balancing [5].

**Table 8.1** Delivery and limit acceleration levels in the balancing speed ranges

| Balancing speed range N (rpm) | Delivery acceleration levels $a_*$ (m/s²) | Limit acceleration levels a (m/s²) |
|---|---|---|
| $0 < N < N_I$ | $a_{I^*} < a_I$ | $a_I$ |
| $N_I \leq N < N_{II}$ | $a_{II^*} < a_{II}$ | $a_{II}$ |
| $N_{II} \leq N < N_{max}$ | $a_{III^*} < a_{III}$ | $a_{III}$ |

The unbalance-change ratio between the delivery and limit acceleration responses must be statistically determined by testing many turbochargers in a long operating period. If the ratio is chosen too large, many balancing steps are required at the trim balancing, leading to much time needed for the balancing process; therefore, more costs for wear of the cutting tools and low production performance. Otherwise, the unbalance whistle is audible after a long operating period due to the unbalance change if one selects the unbalance-change ratio too small.

### 8.4.3 Comparison between the Modal Balancing and ICM

The modal balancing is valid not only for rigid but also flexible rotors. However, the following characteristics that are necessary to be known in advance are, such as the mass distribution m(z), modal deflection amplitude $Y_i(z)$, vibration mode shape y(z), rotor eigenfrequency $\omega_i$, and critical frequencies $\Omega_{cr}$. Moreover, the modal balancing is dependent of the balancing speed. In practice, it is very difficult to determine or know them in advance. The necessary balancing planes are at least the number of rotor vibration modes plus 1; i.e., three necessary balancing planes for the rotor that has two vibration modes. However, the turbocharger has only two possible balancing planes in the compressor wheel. As a reason, the modal balancing method is not practical and useable for applications to the high-speed balancing of the automotive turbochargers.

By using the Influence Coefficient Method (ICM), the response accelerations are measured over the large range of high balancing speeds. The removed masses at the given radii in the balancing planes 1* and 2* are computed without condition of knowing many necessary parameters of the rotor characteristics in the modal balancing. Furthermore, the ICM balancing is independent of the balancing speed; therefore, it is suitable for balancing over the large balancing speed range. However, it is needed to find a suitable position in the balancing machine or in the

turbocharger to high-speed balance the flexible rotor by means of the measured response accelerations. Nevertheless, the ICM balancing is the state-of-the-art method of the trim balancing that is usually applied to the automotive turbochargers rather than the modal balancing.

## References

1. Ehrich, F.: Handbook of Rotordynamics. Krieger Publishing Company (2004)
2. Kraemer, E.: Rotordynamics of Rotors and Foundations. Springer, Heidelberg (1993)
3. Lingener, A.: Auswuchten - Theorie und Praxis. Verlag Technik, Berlin (1992)
4. Muszýnska, A.: Rotordynamics. CRC, Taylor and Francis (2005)
5. Nguyen-Schaefer, H.: Technical Instructions for Rotor Balancing of Automotive Turbochargers. Internal Documents, BMTS (2011)
6. Rao, J.S.: Rotordynamics, 3rd edn. New Age Intl. Publishers (2007)
7. Rieger, N.F.: Rotordynamics 2 - Problems in Turbomachinery. CISM Courses and Lectures No. 297 (1988)
8. Rieger, N.F.: Balancing of Rigid and Flexible Rotors. U.S. DoD (1986)
9. Schneider, H.: Auswuchttechnik, vol. 7. Auflage, Springer (2007)
10. Vance, J.: Rotordynamics of Turbomachinery. J. Wiley and Sons Inc. (1988)

# Chapter 9
# Applied Tribology in the Oil-Film Bearings

## 9.1 Introduction

Tribology is derived from the Greek word *tribos,* which means rubbing. It deals with the tribological phenomena, such as lubrication, friction, and wears in the moving parts. It becomes more and more important in the turbochargers in terms of synthetic lubricating oils, friction reduction, adhesion and abrasion friction, and wear protection of the oil-film bearings including radial and thrust bearings.

## 9.2 Characteristics of Lubricating Oils

Lubricating oils are based on mineral and synthetic oils. Mineral oils are produced by refining crude oil containing long hydrocarbon chains of paraffin, and aromatic hydrocarbon rings. On the contrary, synthetic oils are manufactured by polymerizing olefin ethylene gained from cracking of petroleum to produce poly-alpha-olefins (PAOs) that have similar chemical properties as paraffinic oils (mineral oils), but they could be used in the extreme conditions of high thermal and mechanical loads. There are two true synthetic oils, esters (chemical compounds like alcohols or phenols) and poly-alpha-olefins. Synthetic oils used in automotive engines have been resulted by combining PAOs with about 15% of a synthetic ester [7]. Some high-end synthetic engine oils are sold under commercial names, such as Castro Edge, Castro Magnatec (Castro), Mobil 1-5W30, SHC 824, and SHC 629 (ExxonMobil).

Lubricant oils are classified into SAE viscosity grades (Society of Automotive Engineers) for automotive applications and ISO grades (International Organization for Standardization) for industrial applications. The ISO viscosity grades (VG) are based on the average kinematic viscosity in Centistokes (cSt) at oil temperature of 40°C.

The kinematic oil viscosity is defined as the ratio of the dynamic viscosity to its density.

$$\nu = \frac{\eta}{\rho} \tag{9.1}$$

where

ν is the kinematic viscosity [units: m²/s; mm²/s; 1 cSt (Centistokes) = 1 mm²/s];

η is the dynamic viscosity [units: N.s/m²; Pa.s; 1 cP (Centipoise) = 1 mPa.s];

ρ is the oil density, nearly unchanged in the working range of temperatures.

The SAE grade has a general form SAE xWy (e.g. SAE 5W30) where xW stands for the oil viscosity grade of SAE xW (i.e. SAE 5W, W for Winter) at -18°C (0°F) for low temperature applications. The index y relates to the oil viscosity grade SAE y (i.e. SAE 30) at about 100°C (212°F) for high temperature applications.

Table 9.1 gives the equivalent lubricant oils between the ISO VG (Viscosity Grade) and SAE specifications, and their HTHS viscosities according to SAE J300. The lubricant oil of SAE 5W30 corresponds to ISO VG 22 for SAE 5W in low temperatures and ISO VG 100 for SAE 30 in high temperatures with an HTHS viscosity of 2.9 mPa.s at 150°C and oil share rate of $10^6$ s$^{-1}$.

**Table 9.1** Viscosity grades and HTHS viscosities of lubricating oils of the ISO and SAE specifications (SAE J300)

| ISO VG Grade | SAE Grade | HTHS Viscosity (mPa.s) |
|:---:|:---:|:---:|
| - | 0W | - |
| 22 | 5W | - |
| 32 | 10W | - |
| 46 | 15W | - |
| 68 | 20W/20 | 2.6 |
| 100 | 30 | 2.9 |
| 150 | 40 | 2.9*/3.7** |
| 220 | 50 | 3.7 |
| 320 | 60 | 3.7 |

\* 0W40; 5W40; 10W40: \*\* 15W40; 20W40; 25W40

In fact, the oil viscosity changes almost with temperature at small or moderate oil shear rate. Generally, the higher the oil temperature, the lower the oil viscosity. The oil dynamic viscosity versus temperature is calculated by the Cameron and Vogel equation, as given in Eq. (6.44). Figure 9.1 gives the dynamic viscosities depending on oil temperatures for some common automotive engine oils.
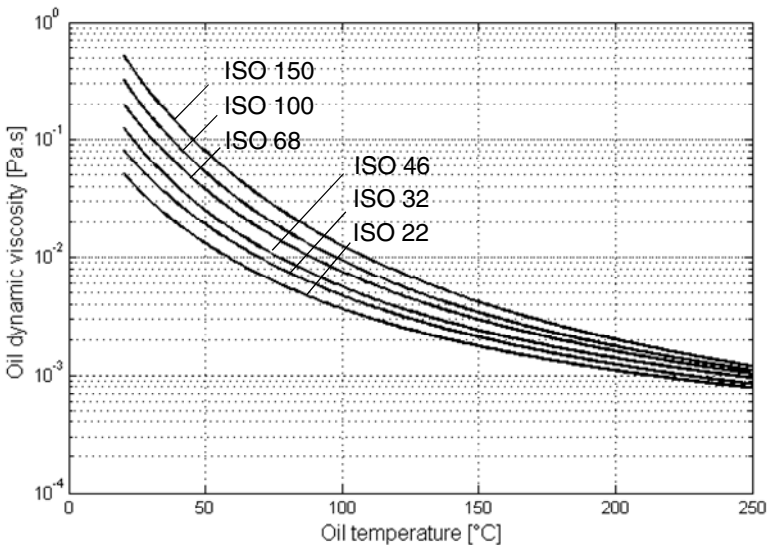
**Fig. 9.1** Computed dynamic viscosity of lubricating oils versus temperature

The related coefficients in the Cameron and Vogel equation of some common automotive engine oils are given in Table 9.2. According to this equation, they are computed from three points of the oil grade and used further to calculate the dynamic viscosities η (Pa.s) versus temperature T (K). These oil viscosities are often used at each iteration step in the bearing dynamics and rotordynamic computation.

**Table 9.2** Related coefficients in the Cameron and Vogel equation

| ISO VG Grade | Dyn. viscosity $\eta(T) = a\exp\left(\dfrac{b}{T(K)-c}\right)$ | | |
|:---:|:---:|:---:|:---:|
| | a (Pa.s) | b (K) | c (K) |
| 22 | 12.312e-5 | 6.181e+2 | 1.906e+2 |
| 32 | 9.618e-5 | 7.391e+2 | 1.883e+2 |
| 46 | 11.387e-5 | 7.014e+2 | 1.930e+2 |
| 68 | 8.396e-5 | 8.520e+2 | 1.835e+2 |
| 100 | 7.547e-5 | 9.081e+2 | 1.844e+2 |
| 150 | 5.399e-5 | 10.747e+2 | 1.758e+2 |

## 9.3   HTHS Viscosity of Lubricating Oils

HTHS viscosity (high temperature high shear) is defined as the effective oil dynamic viscosity (mostly in mPa.s) in the working condition at high temperature of 150°C and large shear rate of $10^6$ s$^{-1}$.

The shear rate $\dot{\gamma}$ is the velocity gradient of the oil film that is defined as the change rate of the oil velocity to oil-film thickness, as shown in Fig. 9.2.

$$\dot{\gamma} \equiv \frac{\partial U}{\partial h} \tag{9.2}$$

Figure 9.2 shows the velocity profile of the oil film in the bearing clearance of a fixed radial bearing with the journal velocity $U_0$. The shear stress of the oil film at the journal is defined as a function of the shear rate.

$$\tau_S = \frac{F_f}{A_S} = \eta \frac{\partial U}{\partial h} = \eta(\dot{\gamma})\dot{\gamma} \equiv f(\dot{\gamma}) \tag{9.3}$$

where
$\tau_S$ is the shear stress of the oil film acting on the journal;
$F_f$ is the friction force acting on the journal;
$A_S$ is the oil lubricated surface of the journal.
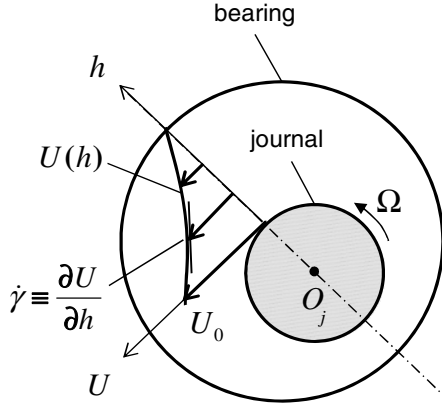


**Fig. 9.2** Oil velocity profile and shear rate of the oil film

In case of a Newtonian fluid, such as single-grade oils (base oils) the dynamic viscosity depends only on the fluid temperature and not on the shear rate, as shown in Fig. 9.3a. Hence, the shear stress is linear to the oil shear rate (s. Fig. 9.4).

$$\eta = \eta(T) \rightarrow \tau = \eta\dot{\gamma} \tag{9.4}$$

In fact, multi-grade lubricant oils are generally non-Newtonian fluids because of long hydrocarbon chains and aromatic rings. As a result, the oil dynamic viscosity depends on not only the oil temperature but also on the oil shear rate (s. Fig. 9.3b). Hence, the shear stress is nonlinear to the oil shear rate, as shown in Fig. 9.4.

$$\eta = \eta(T, \dot{\gamma}) \rightarrow \tau = \eta(\dot{\gamma})\dot{\gamma} \tag{9.5}$$



**(a) Newtonian fluids**

**(b) Non-Newtonian fluids (oils)**
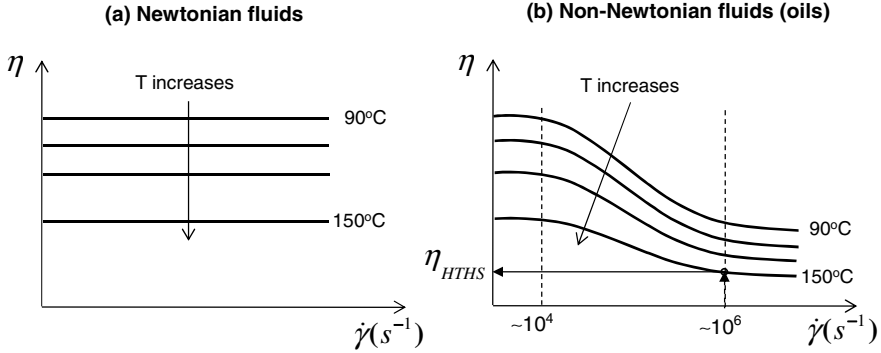
**Fig. 9.3** Viscosity behavior of lubricating oils versus shear rate

Figure 9.3 shows the dynamic viscosity of a Newtonian fluid is constant with the shear rate at a constant temperature; it reduces only with oil temperatures. On the contrary, the oil viscosity (mostly non-Newtonian fluids) is nearly constant as long as the shear rate is below the critical shear rate of $10^4$ s$^{-1}$ and strongly decreases with the oil shear rate up to $10^6$ s$^{-1}$. From this shear rate, the oil viscosity remains unchanged at the lowest viscosity that one defines as the HTHS viscosity at the oil temperature of 150°C. Generally, the oil shear rate in the bearing of automotive turbochargers is very large due to their high rotor speeds in the small bearing clearances.

In the following section, a calculating example of the oil shear rate in the radial bearing of a typical turbocharger with a shaft diameter D = 7 mm supported on two rotating floating ring bearings (RFRBs) with a radial bearing clearance h = 10 µm is demonstrated.

According to Eq. (9.2), the shear rate of the oil film results in

$$\dot{\gamma} \equiv \frac{\partial U}{\partial h} \approx \frac{U_{eff}}{h} = \frac{(1 - RSR)U_0}{h} = (1 - RSR)\frac{\pi ND}{60h} \tag{9.6}$$

where
$U_{eff}$ is the effective oil velocity in the RFRBs (m/s);
RSR is the ring speed ratio (-), as given in Eq. (6.91a);
D is the shaft diameter (m);
N is the rotor speed (rpm);
h is the bearing clearance (m).

According to Eq. (9.6), the oil shear rate is approximately $1.1 \times 10^6$ s$^{-1}$ at the rotor speed from 40,000 rpm with a ring speed ratio of 25%. Additionally, the effective oil temperature in the bearing clearance is mostly at 150°C or higher at high rotor speeds. Therefore, the oil viscosity almost in the working conditions of turbochargers is the HTHS viscosity, as displayed in Fig. 9.3b.
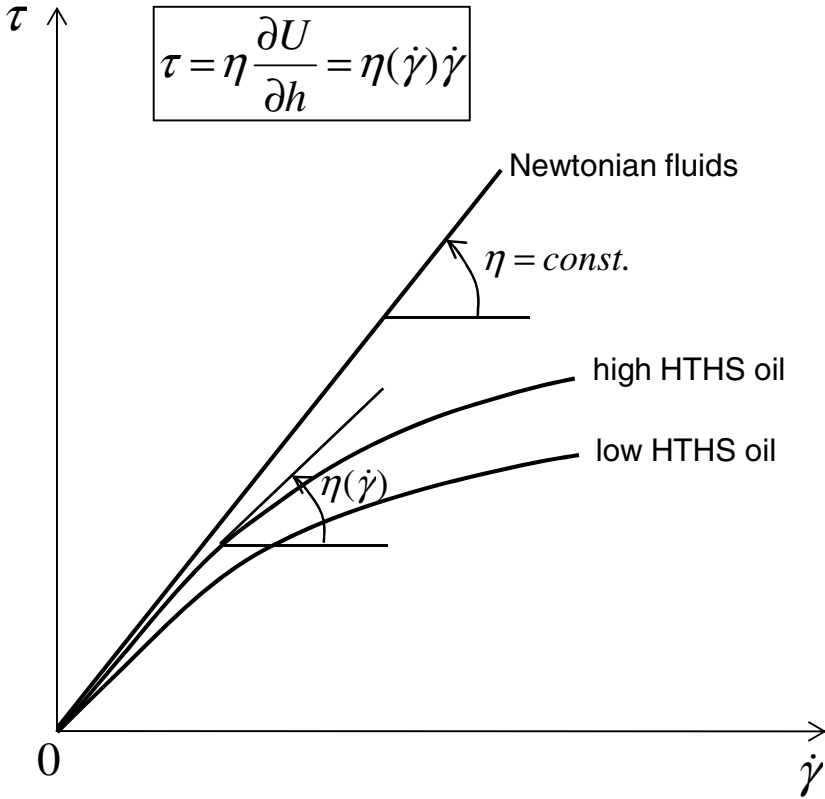


**Fig. 9.4** Shear stress vs. shear rate of lubricating oils

Obviously, Fig. 9.4 indicates that the shear stress gradient $\eta$ (i.e., oil dynamic viscosity) reduces with the shear rate in case of the non-Newtonian oils; it is constant in the Newtonian fluids. Hence, the lower the HTHS of the lubricating oil, the less the friction power generated in the engine and in the turbocharger as well, leading to the lesser fuel consumption and the higher fuel mileage MPG (miles per gallon).

Lubricating oils are generally divided into two HTHS levels: low HTHS viscosity with $\eta_{HTHS} < 3.5$ mPa.s and high HTHS viscosity with $\eta_{HTHS} \geq 3.5$ mPa.s, as given in Table 9.1. The low HTHS oils with the HTHS viscosity between 2.9 mPa.s and 3.5 mPa.s enable less friction in the engine (i.e., higher mileage MPG, lower $NO_x$, $CO_2$ emissions), but more wears could occur in the moving parts, such

as cylinders and pistons of the engine, bearings in the turbochargers, etc.. However, the lifetime of the engine becomes shorter due to wears. On the contrary, the high HTHS oils with the HTHS viscosity larger than 3.5 mPa.s cause more friction power in the engine (i.e., lower mileage MPG, higher $NO_x$, $CO_2$ emissions), but the moving parts are protected from wears. As a reason, the long lifetime is warranted for the engine even at high thermal and mechanical working conditions. Therefore, the automotive industry must take the compromise between the low HTHS for high mileage MPG and low $NO_x$, $CO_2$ emissions and the high HTHS for the wear protection and the long lifetime of the engines to find out which HTHS value is appropriate for the engines. Recently, in order to reduce $NO_x$, $CO_2$ emissions according to the new emission law, some car manufacturers have been thinking of using an ultra-low HTHS oil of 2.6 mPa.s, such as lubricating oil SAE 0W20. To overcome the problem of wears, the materials of moving parts must be improved, such as coatings or new endurable materials. As a reason, the car costs a little bit more; eventually, customers have to pay the price increase for the environment protection; in turn, they could spare the fuel consumption.

At high HTHS working conditions, the effective HTHS oil viscosity reduces; therefore, the bearing stiffness and damping coefficients decrease. To keep the rotor in balance of forces, the induced pressure in the bearing clearance has to increase by reducing the oil-film thickness itself. Hence, the journal eccentricity $\varepsilon$ increases in order to enlarge the bearing stiffness and damping coefficients. If the oil-film thickness is below the limit oil-film thickness, as given in Fig. 6.11, the mixed or boundary lubrication takes place in the bearing clearance. Note that the more the bearing friction, the smaller the oil film thickness becomes due to high oil temperature. Finally, the oil film ruptures in the radial direction because the boundary contact occurs between the journal and bearing (s. Fig. 9.5), leading to the seizure of the journal in the bearing. Hence, the HTHS viscosity has nothing to do with the shear instability of the oil film that causes the oil-film rupture in the tangential direction.
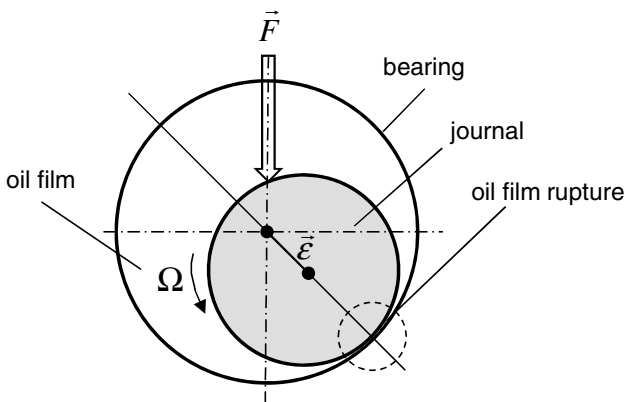


**Fig. 9.5** Oil-film rupture in the bearing clearance

## 9.4  Viscosity Index of Lubricating Oils

To prevent wears, VI improvers (polymeric additives) are added in lubricating oils in order to modify the viscosity change with oil temperature based on the VI index. The viscosity index (VI) relates to the change rate of the dynamic viscosity to temperature.

$$VI \propto \left| \frac{\partial T}{\partial \eta} \right| \tag{9.7}$$

According to Eq. (9.7), the smaller the viscosity changes with oil temperature, the higher the viscosity index VI, leading to the better oil quality. The viscosities of lubricating oils with the high and low VI versus oil temperatures are shown in Fig. 9.6. The viscosity of the high VI oil decreases with temperature more slowly than the viscosity of the low VI oil. That means the negative viscosity gradient of the high VI oil is larger than the low VI oil. According to Eq. (9.7), the higher the viscosity index VI, the less the viscosity changes with oil temperature; therefore, it is a superior oil for wear protection.
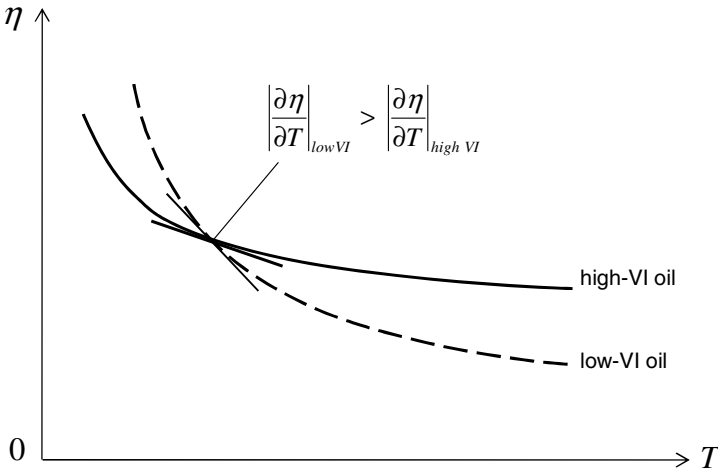


**Fig. 9.6** Dynamic viscosities with the low and high VI oils

Synthetic oils (PAOs, esters) have mostly higher VI than mineral oils because many chemical additives are added in the lubricants at the hydrocracking process. They have been produced and customer tailored to optimize and simplify the molecular structures of the hydrocarbon chains and aromatic rings with predictably designed oil properties, instead of complex unpredictable molecular structures of the mineral oils with lower VI. As a result, synthetic lubricating oils are suitable for the extreme working conditions with the high thermal and mechanical loads at high rotor speeds of the automotive turbochargers. By adding VI improvers (polymeric molecular additives) in the lubricating oils, the viscosity change with oil temperature reduces, so that the HTHS effective viscosity is improved to prevent wears. The VI improvers regulate the oil viscosity with temperature

as follows. First, at low oil temperatures, the molecule chain contracts itself to generate more empty rooms for the oil molecules, and therefore the oil viscosity slightly reduces or much more slowly increases. Second, at high oil temperatures, the molecule chain expands itself to occupy more rooms in the oil molecules; hence, the oil viscosity slightly increases or much more slowly reduces.

The viscosity index VI is a dimensionless number; it has been calculated by the method described in the ASTM D-2270 (American Society for Testing and Materials).

$$VI = 100 \left( \frac{L - U}{L - H} \right)$$ (9.8)

where
U is the viscosity of the test oil at 40°C (~100°F) in cSt;
L is the viscosity parameter at 40°C of the first reference oil,
defined as VI = 0  (L > H);
H is the viscosity parameter at 40°C of the second reference oil, defined as
VI=100;
L and H are corresponding to the dynamic viscosity (cSt) of the test oil at 100°C
(~210°F) and are given in the ASTM D-2270.

To calculate the VI index, the oil viscosities at 40 and 100°C are required; the viscosity-related parameters L and H are given in the ASTM D-2270. The VI indexes of some commonly used lubricating oils are given in Table 9.3.

**Table 9.3** VI indexes of some automotive lubricating oils

| Lubricating oils | Viscosity Index (VI) |
|---|---|
| Mineral oils | 80…120 |
| Hydrocraking oils | 125…150 |
| Synthetic oils (PAOs) | 140…160 |
| Silicone oils (hydraulic fluids) | > 200 |

## 9.5 Stribeck Curve

In this section, the lubrication regions in the bearing clearance over the oil-film thickness are studied in the Stribeck curve. The oil-film thickness is resulted from many rotordynamic and tribological influences, such as the acting force on the bearing, rotor speed, journal eccentricity, surface roughness, oil temperature, and oil viscosity. If the current oil-film thickness is larger than the limit oil-film thickness, the friction in the bearing remains small; the bearing surface is wear protected from wear. In this case, the lubrication is fully hydrodynamic.

In order to look into the lubricating behaviors in the bearing, the dimensionless oil-film thickness λ, the ratio of the minimum oil-film thickness to the root-mean-square (rms) combined surface roughness, is defined according to [4].

$$\lambda \equiv \frac{h_{\min}}{R_q} \tag{9.9}$$

where

$h_{\min}$ is the minimum oil-film thickness;

$R_q$ is the root-mean-square (rms) combined surface roughness of the surfaces #1 and #2.
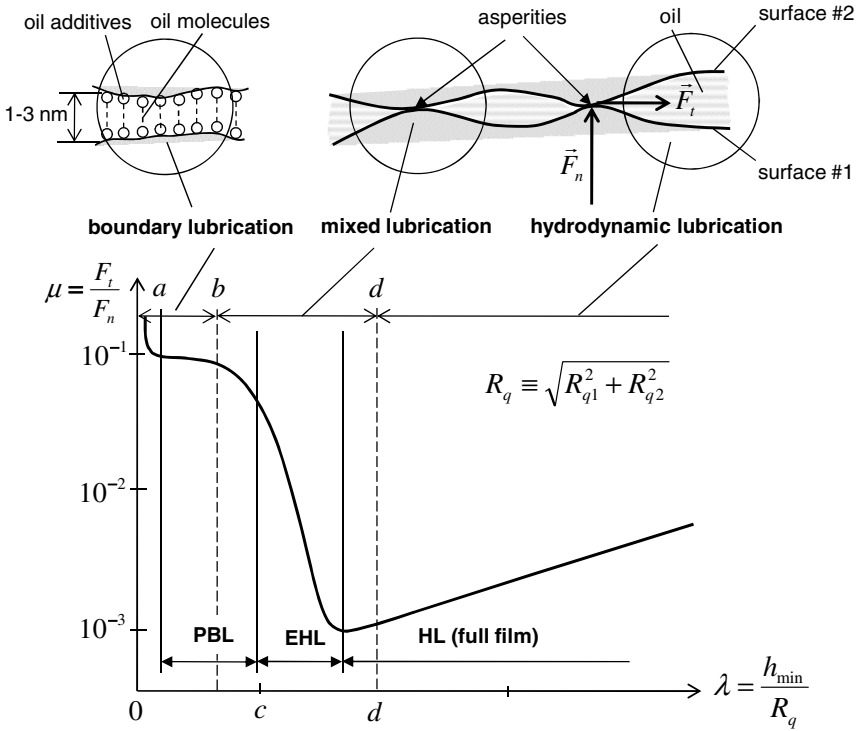


**Fig. 9.7** Lubrication regions in the Stribeck curve

The rms combined surface roughness is defined as

$$R_q \equiv \sqrt{R_{q1}^2 + R_{q2}^2} \tag{9.10}$$

where

$R_{q1}$ and $R_{q2}$ are the rms roughness of the surfaces #1 and #2, respectively.

We transform the rms roughness $R_q$ into the arithmetic average roughness $R_a$ by a factor of 1.25 of the Gaussian surface height distribution.

$$R_q = 1.25 R_a$$

Thus, one writes the rms roughness in the average roughness.

$$R_q = 1.25\sqrt{R_{a1}^2 + R_{a2}^2} \tag{9.11}$$

where

$R_{a1}$ and $R_{a2}$ are the arithmetic average roughness of the surfaces #1 and #2, respectively.

The lubrication regions in the Stribeck curve are classified into four lubrication regions at $\lambda = a \approx 1$, $b \approx 3$, $c \approx 5$, and $d \approx 10$ according to [4]:

- $\lambda \le a$: boundary lubrication (BL)
- $a < \lambda \le c$: partial boundary lubrication (PBL)
- $b < \lambda < d$: mixed lubrication (ML) containing elasto-hydrodynamic
    lubrication (EHL)
- $\lambda \ge d$: fully hydrodynamic lubrication (HL)

In case of $\lambda \le 1$, the boundary lubrication occurs between the surfaces in which the oil-film thickness is very small in the order of a few nanometers ($10^{-9}$ m). In this oil film thickness, the molecules of hydrocarbon chains of the lubricating oil or polymer additives keep the moving surfaces separate in the nanotribology consideration. Due to the very narrow oil film thickness, the friction coefficient strongly increases, leading to seizure of materials between the moving surfaces.

As the dimensionless film thickness $\lambda$ increases from 1 to 5, the partial boundary lubrication takes place in which the surfaces partially contact each other between the boundary lubrication (in the nanotribology ~$10^{-9}$ m) and mixed lubrication (in the microtribology ~$10^{-6}$ m). The nanotribology is generally used to explain the tribological effects occurring in the microtribology. At first, the friction coefficient remains nearly constant in the boundary lubrication and then slightly decreases with the oil-film thickness in the mixed lubrication. However, the friction coefficient is still high because the abrasive and adhesive frictions occur between the moving surfaces in the mixed boundary lubrication.

The elasto-hydrodynamic lubrication (EHL) occurs in the mixed lubrication at $3 < \lambda < 10$, in which the asperities between the surfaces have been plastically deformed or removed due to abrasive and adhesive wears. As soon as the asperities of the surfaces disappear or do not touch with each other at increasing the oil-film thickness, the friction coefficient drops significantly to the minimum where the fully hydrodynamic lubrication begins, as shown in Fig. 9.7.

In case of $\lambda \ge 10$, the moving surfaces are fully separated by the large oil-film thickness without contact of any asperity, abrasive, and adhesive frictions. This lubrication regime is called the fully hydrodynamic lubrication (HL). The friction induced in this region is only the viscous friction of the oil film.

The friction coefficient in the fully hydrodynamic lubrication is calculated by

$$\mu_{HL} \equiv \frac{F_t}{F_n} \propto \frac{(1/h)}{(1/h)^2} \propto h \propto \lambda \tag{9.12}$$

where

$F_t$ is the friction force proportional to $(1/h)$, inversely related to the film thickness;
$F_n$ is the normal force proportional to $(1/h)^2$;
$h$ is the current minimum oil-film thickness;
$\lambda$ is the dimensionless oil-film thickness.

According to Eq. (9.12), the friction coefficient is proportional to the dimensionless oil-film thickness in the fully hydrodynamic lubrication (HL).

In the partial boundary or mixed lubrication regions, the oil temperature in the bearing clearance is relatively high due to the large bearing friction. When the effective oil temperature in the bearing exceeds the flash points of the lubricating oil 210°C (SAE 5W30) and 250°C (SAE 20W30) [6], the oil film begins coking inside the bearing clearance and leaves the hard coked-oil layer on the rotor shaft.

The process of oil coking generates a hard black thin layer of the carbonaceous residue on the surface of the journal inside the bearing clearance. The hard coked-oil layer increases continually after a long operating time; hence, the radial bearing clearance reduces. As a result, the oil temperature has been further increases as the bearing clearance reduces, and the coking process takes place continuously. Finally, it leads to seizure of the shaft in the bearing and fatal damage of turbochargers.

## 9.6   Surface Texture Parameters

Surface tribological characteristics play a key role in the rotor stability and wears in the bearings as well. They strongly affect the oil-film thickness that depends on the lubrication regime in the bearings (s. Fig. 9.7). The oil film involves in the rotordynamic stability, induced airborne noises, and prevention of wears in the bearings. The oil-film bearings work on the hydrodynamic principle where the inner oil film bears the rotor against the unbalance excitation forces and keep it stable during the operation. Moreover, the outer oil film provides the rotor with large damping to keep it in the small amplitudes at resonances, preventing the rotor from the oil whirl instability. Therefore, it reduces the induced airborne noises, such as the unbalance whistle and constant tone. Without or poorly-lubricated oil supply, the bearings cannot fulfill their functions in the turbocharger. It could cause damages in the bearings and furthermore in the compressor and turbine wheels due to seizure of the wheels in their housings. Thus, we discuss the surface texture parameters in the following section.

### 9.6.1   Surface Height Profile

The surface roughness characteristics of the bearings, journal in the radial bearing, and thrust rings in the thrust bearing are tribologically analyzed. At first, the surface roughness height of the surface is measured by a stylus, as shown in Fig. 9.8.

By sampling the surface, the surface traced profile consisting of the waviness and roughness profile is measured and digitalized. The peak-to-peak amplitude of the waviness profile is defined as the waviness height $W_t$. The measured signal of the surface traced profile is amplified and analyzed by the band-filter technique, as displayed in Fig. 9.9a. By using the high-pass filter, one obtains the surface roughness profile; by using the low-pass filter, the surface waviness profile is resulted. The waviness profile shows the plateau shape of the surface; the roughness profile indicates the real surface roughness height that is measured from the reference line. The surface roughness profile is the arithmetic average value of the surface height in an evaluation length. The roughness profile contains many peaks (asperities) and valleys of the measured surface.
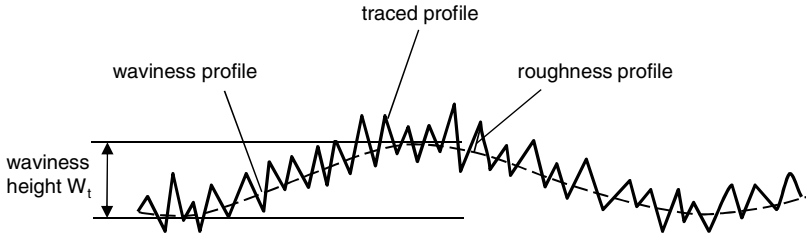
**Fig. 9.8** Measured surface roughness height

The mean line of the surface roughness is defined in the evaluation length $l_n$ as

$$\bar{z} \equiv \frac{1}{l_n} \int_0^{l_n} z\, dx \approx \frac{1}{N} \sum_{i=1}^{N} z_i \qquad (9.13)$$

where
N is the number of the sampling heights $z_i$ measured from the reference line $z_{ref}$ within the evaluation length.

The mean line is determined by the weighted average height of the surface profile within the sampling length $l_r$ with a phase corrector filter. The average roughness height is calculated from the measured weighting function $p(z)$ in the sampling length, as shown in Fig. 9.9b.

The variance s of the surface roughness height is calculated as follows:

$$s \equiv \frac{1}{(N-1)} \sum_{i=1}^{N} z_i^2 \qquad (9.14)$$

The standard deviation $\sigma$ is defined as the square root of the variance s. It shows the variation of the measured values from the mean value of the surface roughness height in the distribution density function (s. Appendix D). A low standard deviation indicates that the measured values tend to be close to the mean value, whereas high standard deviation shows that the measured values are spread out over a large range from the mean line.

Thus, the standard deviation is derived from Eq. (9.14).

$$\sigma \equiv \sqrt{s} = \sqrt{\frac{1}{(N-1)} \sum_{i=1}^{N} z_i^2} \qquad (9.15)$$

where $z_i$ is the roughness height measured from the mean line $\bar{z}$. According to Appendix D, the smaller the standard deviation $\sigma$, the better the production; e.g., production at $\pm 3\sigma$ gives 99.7% of products that are within the given tolerances.
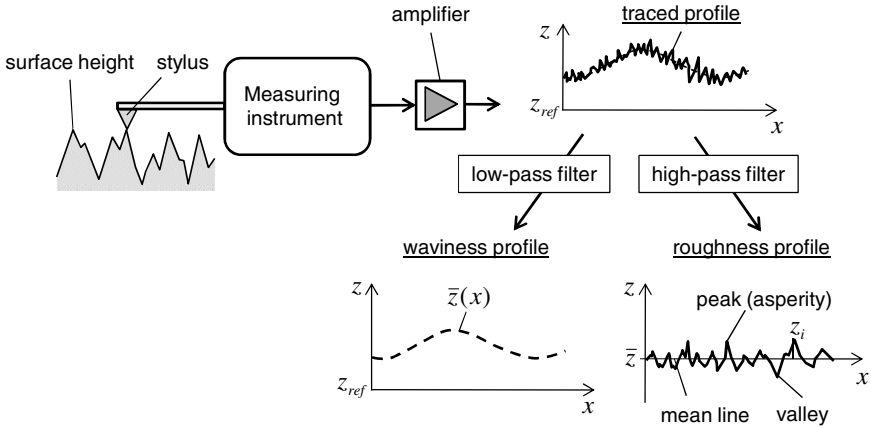
**Fig. 9.9a** Analyzing the measured surface traced profile
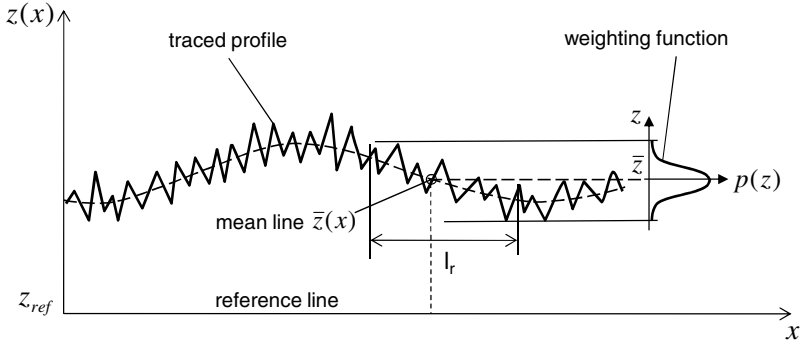


**Fig. 9.9b** Mean line of the measured surface traced profile

## 9.6.2  Surface Tribological Parameters

In this section, we deal with some tribological parameters that are usually applied to analyze the bearing surface roughness in the turbochargers [8].

- *Evaluation length $l_n$* is the length in which the values of the surface height are selected and evaluated. Its length is normally chosen by five times of the cutoff wavelength $\lambda_c$.

$$l_n \approx 5\lambda_c \tag{9.16}$$

- *Sampling length $l_r$* is the reference length for the roughness evaluation and nearly equals the cutoff wavelength $\lambda_c$.

$$l_r \approx \lambda_c \tag{9.17}$$

- *Cutoff wavelength* $\lambda_c$ is the profile filter that is used by analyzing the surface roughness heights. It is generally chosen, so that the surface roughness amplitude with a sine function is reduced to about 50% after filtering the measured signals. According to DIN EN ISO 4288:1998 and DIN EN ISO 3274:1998, some wavelengths are determined for profile filters as follows:

$$\lambda_c = 0.08; 0.25; 0.8; 2.5; 8.0 \, mm \tag{9.18}$$

At decreasing the cutoff wavelength, the amplitude of the filtered surface roughness profile is also reduced; the amplitude of the filtered waviness profile of the surface roughness increases. Therefore, the short cutoff wavelength is rather preferred at small surface roughness of $R_a$ and $R_z$.

- *Roughness $R_{sm}$* (DIN EN ISO 4287, ASME B46.1)
is called the *mean peak spacing* and defined as the arithmetic average value of five mean peak spacings of the roughness profile within the evaluation length $l_n$ (s. Fig. 9.10).

$$R_{sm} = \frac{1}{5} \sum_{i=1}^{5} s_{mi} \tag{9.19}$$

The mean peak spacing $s_{mi}$ is the wavelength of the roughness profile that must contain at least one peak and one valley of the surface roughness, as shown in Fig. 9.10.
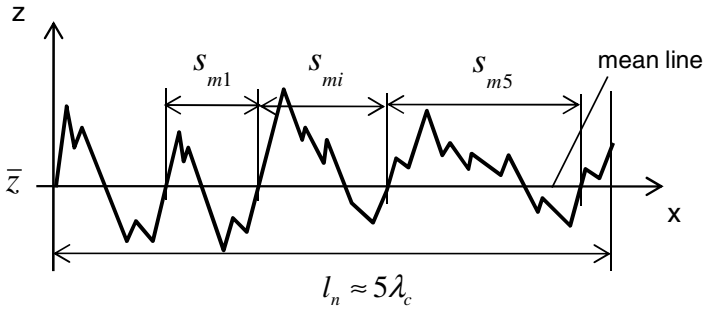


**Fig. 9.10** Mean peak spacing $R_{sm}$

- *Mean roughness $R_a$* (DIN EN ISO 4287, ASME B46.1)
is the arithmetic average roughness of N roughness heights $z_i$ that are measured from the mean line within the sampling length $l_r$.

$$R_a \equiv \frac{1}{l_r} \int_0^{l_r} |z(x)| dx = \frac{1}{N} \sum_{i=1}^{N} |z_i| \tag{9.20}$$
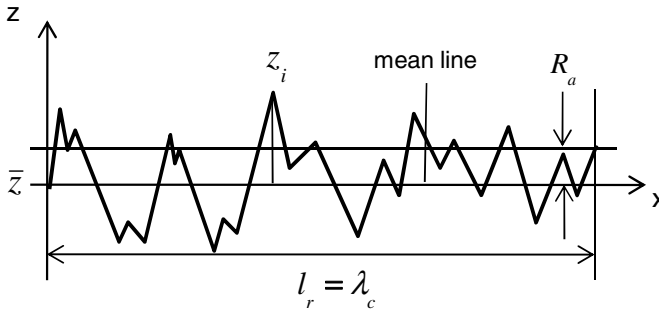
**Fig. 9.11** Arithmetic mean roughness $R_a$

 - *Root mean square (rms) roughness $R_q$* (DIN EN ISO 4287, ASME B46.1)
is the rms roughness of N points of the surface roughness heights within the sampling length $l_r$, in which the influences of the peak and valley values are additionally considered.

$$R_q \equiv \sqrt{\frac{1}{l_r}\int_0^{l_r} z^2(x)dx} = \sqrt{\frac{1}{N}\sum_{i=1}^{N} z_i^2} \qquad (9.21)$$
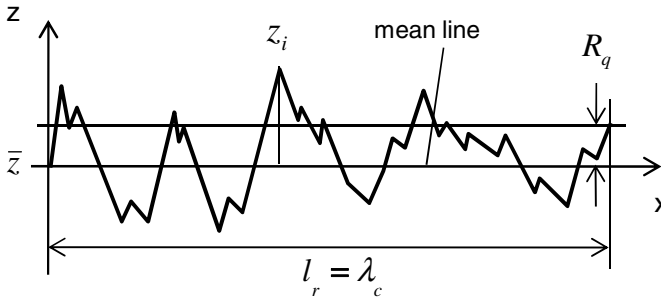


**Fig. 9.12** Root mean square roughness $R_q$

- *Mean roughness depth $R_z$ and maximum roughness depth $R_{max}$* (DIN EN ISO 4287, ASME B46.1).
    The mean roughness depth $R_z$ is the arithmetic average value of the five single roughness depths $R_{z,i}$ of five consecutive sampling lengths $l_r$ within the evaluation length $l_n$.

$$R_z \equiv \frac{1}{5}\sum_{i=1}^{5} R_{z,i} \qquad (9.22)$$

The maximum roughness depth $R_{max}$ is the largest single roughness depth of the five roughness depths within the evaluation length $l_n$.

$$R_{max} \equiv \max_{i=1,..,5} (R_{z,i}) \qquad (9.23)$$

where
$R_{z,i}$ and $R_{max}$ are as shown in Fig. 9.13.
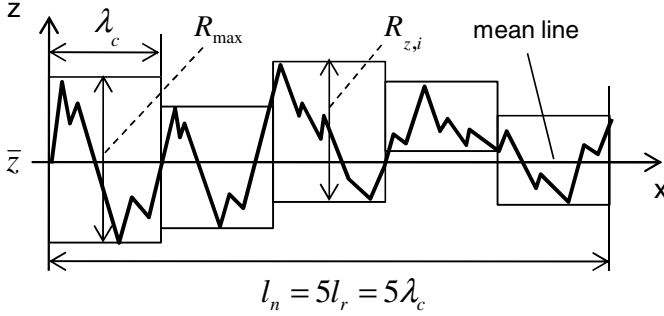


**Fig. 9.13** Mean roughness depth $R_z$ and maximum roughness depth $R_{max}$

*- Material ratio $R_{mr}$* (DIN EN ISO 4287, ASME B46.1)
is the ratio of the sum l(c) of all material lengths $l_i$ at the surface height z to the total material length $l_n$. It is called the *bearing length ratio* in the ASME B46.1.

$$R_{mr}(z) \equiv \frac{\sum l_i(z)}{l_n} 100[\%] \qquad (9.24)$$

*- Abbott-Firestone curve (also Abbott curve)*
is the most important surface roughness parameter that one additionally uses to evaluate the surface roughness quality. The Abbott curve evaluates the tribological surface roughness quality of the samples that have the same mean roughness $R_a$ and $R_z$. In this case, the shape of the Abbott curve decides which surface roughness is better.

According to the ASME B46.1, the Abbott curve is called the *bearing area curve* (BAC). In the statistical analysis, the Abbott curve is in fact the probability distribution function of the surface roughness heights that is resulted from its distribution density function, as discussed in Appendix D. At first, the construction of the Abbott curve is derived from the profile of the surface roughness heights z(x). At the cutting line with the surface height z, the material ratio $R_{mr}$ is computed from the sum of all cutting lengths $l_i$ to the total length $l_n$, as demonstrated in Fig. 9.14.

Having non-dimensioned surface height z, the new dimensionless surface height c is defined.

$$c \equiv \frac{z - \bar{z}}{\sigma} \qquad (9.25)$$

where
$\sigma$ is the standard deviation of the distribution density roughness height.
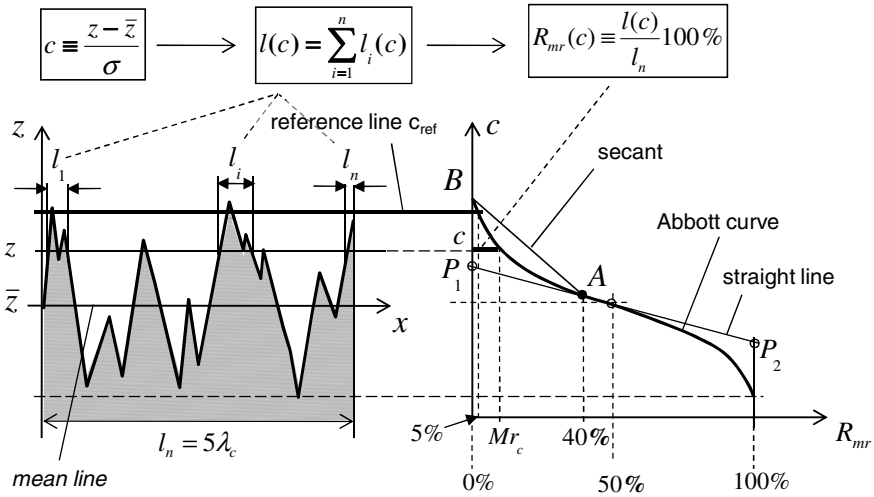
**Fig. 9.14** Abbott curve and the material ratio $R_{mr}$

The dimensionless surface height c versus the material ratio $R_{mr}$ is plotted on the right-hand side of Fig. 9.14. The bell-shaped curve is called the *Abbott-Firestone curve*. Obviously, the material ratio equals 0% at the maximum peak because no peak is cut; the material ratio arrives at 100% at the minimum valley since all cutting lengths equal the total length. However, in practice, one moves the ordinate surface height c from the initial position of $R_{mr} = 0\%$ to 5% (experience value) in the direction of the abscissa material ratio $R_{mr}$. Therefore, it makes sure that the reference line $c_{ref}$ lies at the highest peak of the surface height because of initial wears after a short operating period.

In other way, the Abbott curve can be derived by using the amplitude density function p(c) of the surface roughness profile, as shown in Fig. 9.15 [2].
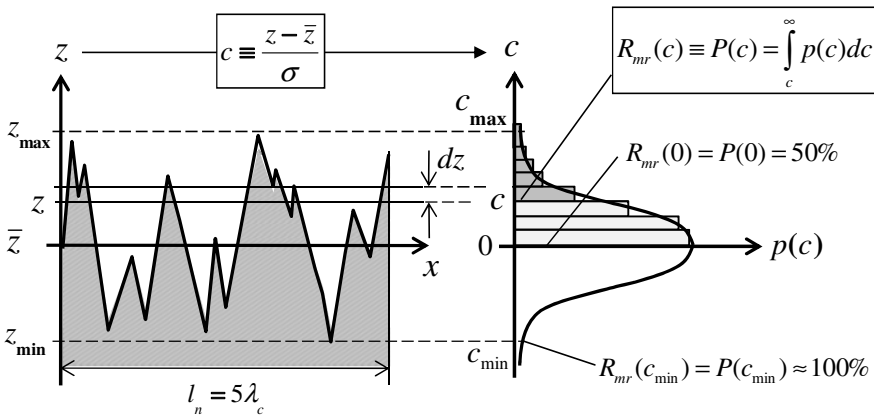


**Fig. 9.15** Amplitude density function (ADF) of the surface roughness profile

The amplitude density function p(c) is the number of surface heights between the two cutting heights z and z+dz. The cumulative distribution function P(c) of the amplitude density function p(c) of the surface roughness heights is in fact the material ratio at the dimensionless surface height c (s. Appendix D).

$$P(c) = \int_c^\infty p(c)dc \equiv R_{mr}(c) \qquad (9.26)$$

Thus,

$R_{mr}(c_{max}) = P(c_{max}) \approx 0\%$ at the highest peak of the surface height;

$R_{mr}(0) = P(0) \approx 50\%$ at the mean line (c = 0);

$R_{mr}(c_{min}) = P(c_{min}) \approx 100\%$ at the lowest valley of the surface height.

- *Roughness $R_{pk}$, $R_k$, $R_{vk}$* (DIN EN ISO 13565-1 and -2)

$R_{pk}$ is the reduced peak height in the Abbott curve in Fig. 9.16 that indicates the peak roughness of the surface; $R_k$ is the core roughness depth indicating the plateau shape of the roughness surface; $R_{vk}$ is the reduced valley height of the surface indicating the oil reservoir in the roughness surface.
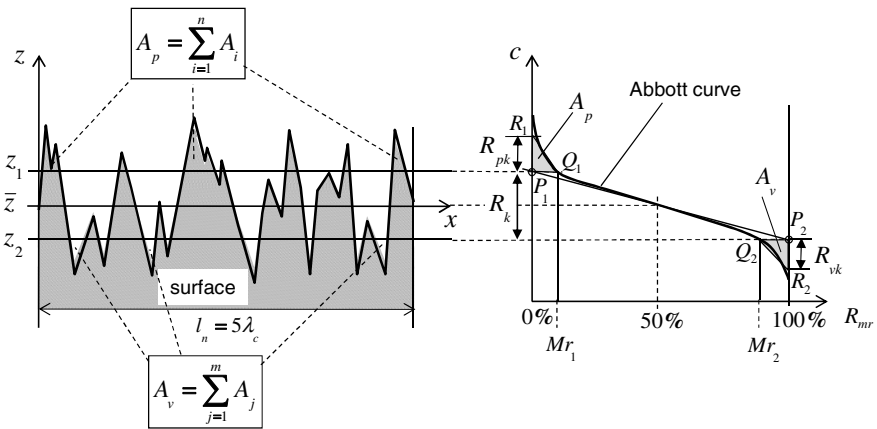


**Fig. 9.16** Roughness $R_{pk}$, $R_k$, $R_{vk}$; material ratios $Mr_1$ and $Mr_2$

The material ratios $Mr_1$ and $Mr_2$ are the smallest and largest material ratios at $R_{pk}$ and $R_{vk}$, respectively. Both material ratios determine the shape of the Abbott curve that indicates the important tribological parameter besides the mean roughness $R_a$ and mean roughness depth $R_z$.

In the following section, the roughness $R_{pk}$, $R_k$, $R_{vk}$, and the material ratios $Mr_1$ and $Mr_2$ are determined in the Abbott curve in Figures 9.14 and 9.16. At first, we create the secant AB with $R_{mr}(A)$ of 40% in Fig. 9.14; then, we rotate the secant AB about point A until it is tangential to the left half-branch of the Abbott curve at

the point A. The prolonged secant, called the straight line $P_1AP_2$, cuts the ordinates with $R_{mr} = 0\%$ and $100\%$ at $P_1$ and $P_2$, respectively, as plotted in Fig. 9.16. The corresponding surface heights $z_1$ and $z_2$ at $P_1$ and $P_2$ intersect the Abbott curve at $Q_1$ and $Q_2$, respectively. Therefore, the smallest and largest material ratios $Mr_1$ and $Mr_2$ are found at $Q_1$ and $Q_2$, as shown in Fig. 9.16.

The area $A_p$ is the sum of all peak surfaces $A_i$ above the cutting surface height $z_1$. In the Abbott curve, the triangle $P_1Q_1R_1$ is constructed, so that its area equals $A_p$. The altitude $P_1R_1$ is defined as the reduced peak height $R_{pk}$. Similarly, the reduced valley height $R_{vk}$ is equal to $P_2R_2$ that is derived from the triangle $P_2Q_2R_2$ whose area equals $A_v$ of the total groove area below the cutting surface height $z_2$. Finally, the core roughness depth $R_k$ is the surface roughness height of $P_1P_2$, as shown in Fig. 9.16.

Thus, the reduced peak and valley heights are calculated as follows:

$$R_{pk} = \frac{2A_p}{l_n Mr_1}.100\% \tag{9.27}$$

$$R_{vk} = \frac{2A_v}{l_n(100 - Mr_2)}.100\% \tag{9.28}$$

Generally, the core roughness depth $R_k$ ($< \sim 1\ \mu m$ to $2\ \mu m$) should be kept small in the bearings to increase the bearing load capability because the bearing surface has less plateau shape. Note that the smaller the reduced peak height $R_{pk}$ ($< \sim 0.5\ \mu m$ to $1\mu m$), the better the surface quality. On the contrary, the reduced valley height $R_{vk}$ ($< \sim 1\ \mu m$ to $2\ \mu m$) should be much larger than $R_{pk}$ to maintain the residual lubricating oil in the valley grooves; hence, the bearing is well lubricated at the start-stop driving cycle.
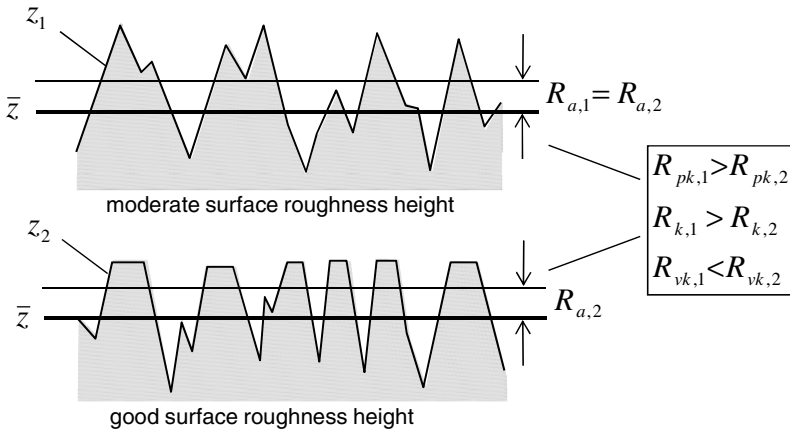


**Fig. 9.17** Comparison of two surface roughness heights

Figure 9.17 shows an example of two surface roughness heights that have the same $R_a$ but different roughness values of $R_{pk}$, $R_k$, and $R_{vk}$. Obviously, the first one has only a moderate tribological surface characteristic due to the higher value of $R_{pk,1}$ compared to $R_{pk,2}$ that could cause wear in the surface. On the contrary, the latter with smaller values of $R_{k,2}$ and $R_{pk,2}$ is tribologically better because the surface has less plateau and the peaks of the surface roughness are reduced; its $R_{vk,2}$ is higher than the first one; hence, the surface has more oil reservoir to lubricate the bearing surface.

Figure 9.18 shows three surface roughness heights that are finished by different methods of honing, eroding, and turning. Despite the nearly same roughness $R_a$ and $R_{max}$, they have different qualities of tribological surface characteristics. The honed surface is the best because all peak heights were removed and the groove depths are large enough to maintain sufficiently reserved oil for lubrication. The eroded surface has a moderate quality since many peaks remain and thus could cause wears at the asperities and reduces the bearing load capability. The turning surface with the largest $R_z$ is the worst since it has many peaks with the largest reduced peak height $R_{pk}$ due to the turning traces. It causes reduction of the bearing load capability and therefore induces the bearing friction due to abrasive wear at the peaks (asperities). In this case, we have to consider the other roughness parameters of $R_{pk}$, $R_k$, $R_{vk}$, and $R_{mr}$.



$$R_{a,1} \approx R_{a,2} \approx R_{a,3}$$
$$R_{max,1} \approx R_{max,2} \approx R_{max,3}$$
$$R_{z,1} < R_{z,2} < R_{z,3}$$

honed surface: best

eroded surface: moderate

turned surface: bad
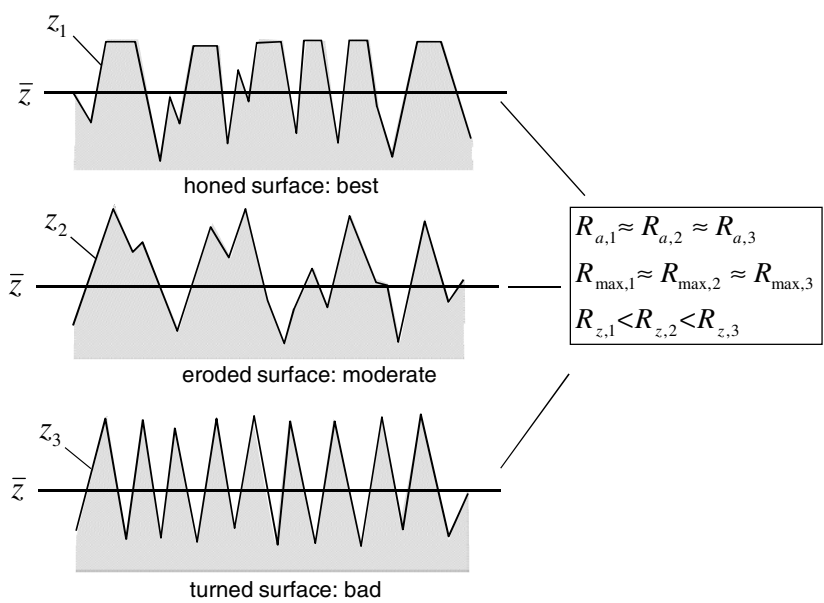
**Fig. 9.18** Roughness heights at different finishing methods

Besides the surface roughness depths $R_z$ and $R_a$, the Abbott curve is additionally used to analyze the surface roughness quality. Generally, good tribological surface roughness characteristics are possibly smallest reduced peak heights $R_{pk}$ and possibly largest reduced valley heights $R_{vk}$.
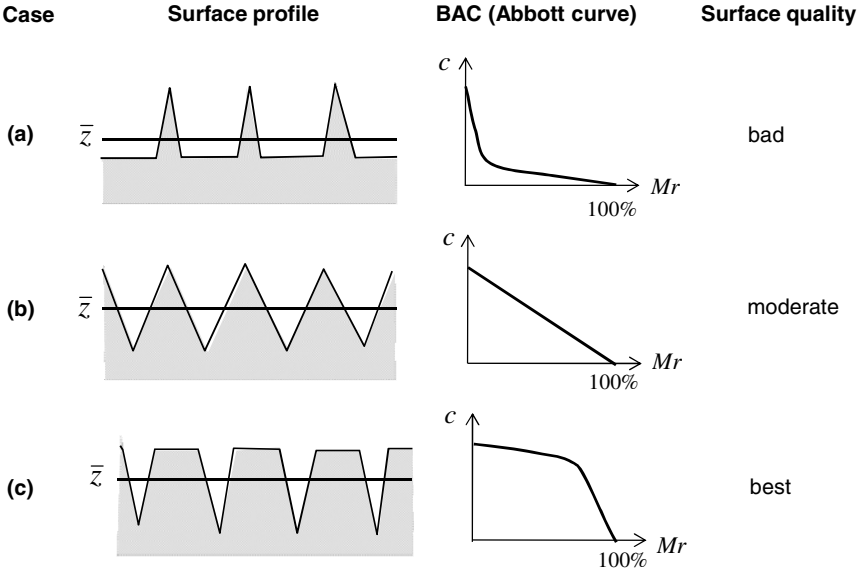


**Fig. 9.19** Analyzing surface quality by means of Abbott curves

The Abbott curve is derived from the measured values of the surface roughness height with the lowest and largest material ratios of $Mr_1$ and $Mr_2$ according to Eqs (9.27) and (9.28), as shown in Fig. 9.19. They determine the shape of the Abbott curve of the roughness surface height. By experience, at the same roughness $R_a$ or $R_z$, the Abbott curve with a *convex shape* indicates the best tribological quality of the surface roughness height (case c). Therefore, the best surface roughness characteristic in Fig. 9.19 is the third case with the small reduced peak heights $R_{pk}$ (low peak surface roughness), the high reduced valley heights $R_{vk}$ (more oil reservoir), and the small core roughness depth $R_k$ with less plateau of the surface roughness. On the contrary, the surface with a *concave shape* shows the bad tribological surface roughness quality (case a). They have many sharp asperities with the large reduced peak heights $R_{pk}$ (high peak surface roughness) and the low reduced valley heights $R_{vk}$ (less oil reservoir). The Abbott curve of the case b has a *linear shape*; one considers its tribological surface quality as moderate.

## 9.7   Elastic and Plastic Deformations in the Bearings

To study the wear mechanism in the bearings, some backgrounds of the elastic and plastic deformations of material are necessary. At a small load, the material begins deforming, as soon as one removes the load, its form returns to the initial condition. This deformation is called *elastic deformation*. On the contrary, in case of *plastic deformation*, in which the load-related stress exceeds the yield stress $\sigma_o$, the material remains the current form and does not return to the initial condition although one removed the load acting on it. At further increasing the load in the plastic deformation, the material suddenly fractures at the ultimate tensile stress $\sigma_u$. Then, the wear process begins with the loss of the surface asperities (roughness peaks), which abrade the moving surfaces and further cause wear traces in the surface.

### 9.7.1   Normal Stress

Having applied the tensile force F on a cylindrical specimen with the initial cross-sectional area $A_0$ and length $l_0$, the body begins deforming in the axial direction.
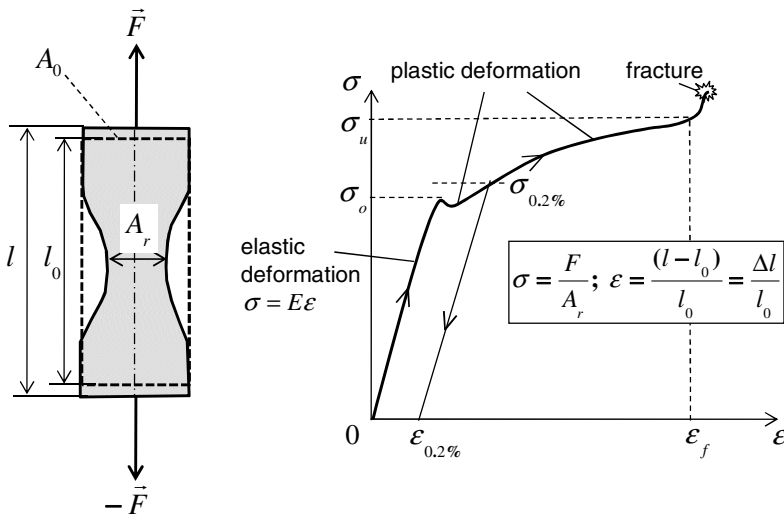


**Fig. 9.20** Stress-strain diagram of a ductile material

The normal stress $\sigma$ is defined as the ratio of the acting force to the real cross-sectional area.

$$\sigma = \frac{F}{A_r} \tag{9.29}$$

In the elastic deformation, the stress is proportional to the strain according to the Hooke's law.

$$\sigma = E\left(\frac{l - l_0}{l_0}\right) = E\,\frac{\Delta l}{l_0} \equiv E\varepsilon \tag{9.30}$$

where
E is the elasticity modulus (called the Young's modulus);
$\varepsilon$ is the normal strain defined as the relative change of the length from $l_0$ to l.

The Hooke's law is valid as long as the stress is less than the *yield stress* $\sigma_0$; i.e., the deformation is elastic and returns to zero when the acting load is removed. At further increasing the acting force, the normal stress increases higher than the yield stress; hence, the deformation of the body becomes plastic where the Hooke's law has been no longer valid. With a plastic stress of 0.2%, the strain remains at $\varepsilon = 0.2\%$ after removing the acting force. The deformation is plastic up to the *ultimate tensile stress* $\sigma_u$. After exceeding the ultimate tensile stress, the normal stress sharply increases in a very short time, and the material fractures. Shortly before the fracture occurs, the real cross-sectional area $A_r$ significantly reduces dramatically due to material contraction at a constant load F, as shown in Fig. 9.20. Therefore, the normal stress sharply increases before the material fracture happens according to Eq. (9.29).

### 9.7.2 Shear Stress

Having applied the force F acting on a specimen in the tangential direction, the body form deforms at a shear strain t. The ratio of the shear strain t to the specimen height h is called the *shear rate* $\gamma$, as shown in Fig. 9.21.

The *shear stress* is given at the contact surface A.

$$\tau = \frac{F}{A} = G\,\frac{\partial t}{\partial h} \equiv G\gamma \tag{9.31}$$

where G is the *shear modulus* of the material.
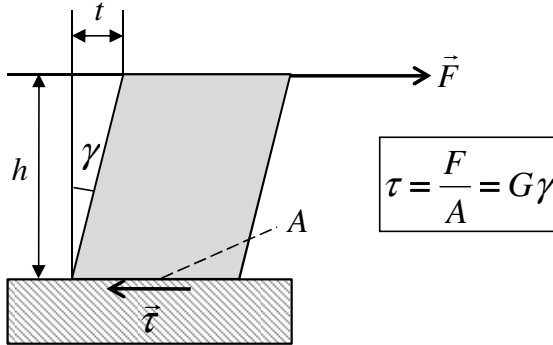


**Fig. 9.21** Shear stress and rate in a testing specimen

The shear modulus is calculated from the *elasticity modulus* E and the *Poisson ratio* $\nu$.

$$E = 2G(1+\nu)$$ (9.32)

where $\nu$ equals 0.25 to 0.30 for most metals.
Thus,

$$G = \frac{E}{2(1+\nu)} \approx (0.385...0.400)E$$ (9.33)

The elasticity modulus E can be used for
  - low-alloy steels: $E \approx 212$ GPa;
  - tool steels (highly-alloyed steels): $E \approx 230$ GPa;
  - brasses, copper alloys, and bronzes: $E \approx 96$ to $114$ GPa.

## 9.7.3  Friction Force in the Bearings

The rotor unbalance induces the normal load $F_n$ acting on the bearing surface. At the contact zone between the journal and bearing, the friction force $F_t$ occurs on the journal surface against the rotational direction of the rotor. The friction force is proportional to the normal load by a friction coefficient. Figure 9.22 shows the acting forces including the normal load and the friction force in the bearing. In fact, the adhesion and abrasion frictions between the bearing and journal induce the total friction force.

$$F_t = \mu_f F_n$$
$$= F_{adh} + F_{abr} = (\mu_{adh} + \mu_{abr})F_n$$ (9.34)

where the total friction coefficient is combined of the adhesive and abrasive friction coefficients.

$$\mu_f = \mu_{adh} + \mu_{abr}$$ (9.35)
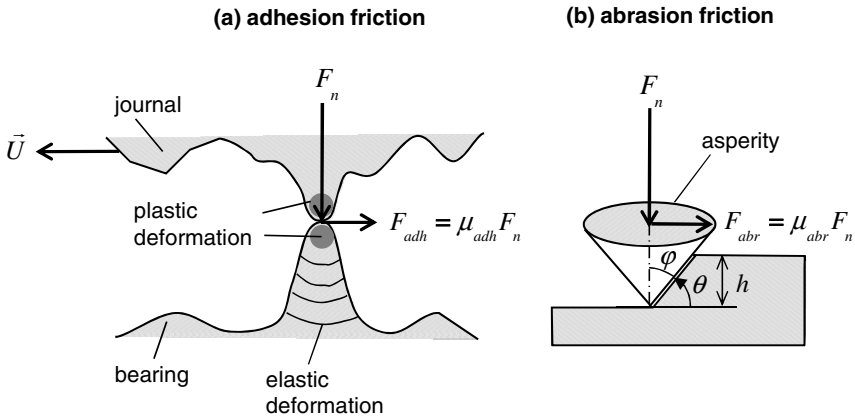


**Fig. 9.22** Adhesive and abrasive friction forces in the bearing

The adhesive friction force is resulted from the shear stress and real contact area.

$$F_{adh} = \tau \, A_r \tag{9.36}$$

within the real contact area $A_r$ is determined as the ratio of the normal load to the hardness H of the softer material in the plastic deformation.

$$A_r = \frac{F_n}{H} \tag{9.37}$$

where the hardness of material H is the mean contact pressure that is resulted from the normal load and permanent indentation in the plastic deformation.

$$H \equiv p_{mean} = \frac{F_n}{A_r} \tag{9.38}$$

The plastic deformation begins with $p_{mean} \approx 1.07\sigma_o$ to $1.1\sigma_o$ ($\sigma_o$= yield stress). At $p_{mean} \approx 3\sigma_o$, it fully develops in the permanent indentation. According to [5], the hardness $H$ is nearly 2.8 to 3 times of the yield stress for intenders with spherical, conical, pyramid, and flat-end shaped geometries.

$$H \approx (2.8...3)\,\sigma_o \tag{9.39}$$

Having combined Eqs (9.36) and (9.37), one obtains the adhesive friction coefficient.

$$\mu_{adh} \equiv \frac{F_{adh}}{F_n} = \frac{\tau}{H} \tag{9.40}$$

According to [9], the abrasive friction coefficient is calculated as follows:

$$\mu_{abr} = \frac{2}{\pi}\cot\varphi = \frac{2}{\pi}\tan\theta \tag{9.41}$$

where
$\varphi$ is the cone semi-angle of the asperity;
$\theta$ is the abrasive angle of material, as shown in Fig. 9.22.

Thus, the total friction coefficient is resulted from Eqs (9.35), (9.40), and (9.41).

$$\mu_f = \mu_{adh} + \mu_{abr} = \frac{\tau}{H} + \frac{2}{\pi}\tan\theta \tag{9.42}$$

Normally, the abrasive angle of most materials is less than 10°; hence, the abrasive friction coefficient is about 0.1. The adhesive friction coefficient is 0.17 to 0.2 for similar hardness of materials where the abrasive friction coefficient is negligible, and < 0.3 for hard to softer materials. In fact, the total friction coefficient is quite larger than these theoretical values between 0.3 and 0.4  due to the work

hardening and junction growth in the contact zone [9]. At the plastic deformation, the atomic dislocations are removed from the material grid structure; therefore, the material becomes harder; the shear and yield stress, and as well as hardness have been strengthened. This process is called the *work hardening* during the plastic deformation. Additionally, the real contact area increases due to plastic deformation, as given in Eq. (9.37). It is called the *junction growth* at the contact zone.

Straightforwardly, the plastic deformation takes place in the contact zone because the normal load and friction force concentrate on a very small contact area of the surface roughness asperities (high $R_{pk}$ and $R_z$). The normal stress that is far away from the asperity is smaller than in the contact zone; therefore, the elastic deformation occurs there instead of plastic deformation. During the plastic deformation in the contact zone, the shear stress increases faster than the hardness. As a reason, the friction coefficient increases in the contact zone between the journal and the bearing; therefore, the friction force increases in the plastic deformation due to the work hardening and junction growth according to eqs (9.34), (9.38), (9.40), and (9.42).

### 9.7.4  Friction Power in the Bearings

The following section deals with the friction power in the bearings that occurs in the boundary, mixed, and hydrodynamic lubrications in the Stribeck curve, as displayed in Fig. 9.7.

The friction power $P_f$ in the bearings is resulted from the friction force $F_f$ and relative velocity U. It consists of the friction powers in the mixed lubrication $P_m$ and the hydrodynamic lubrication $P_h$. At the large oil-film thickness, the friction power in the hydrodynamic lubrication $P_h$ ($\varepsilon = 1$) dominates the bearing friction power. In other case, the friction power in the mixed lubrication $P_m$ ($\varepsilon = 0$) is dominant in the bearing friction power at the small oil-film thickness.

$$
\begin{aligned}
P_f = F_f U &= \tau\, AU \\
&= (1 - \varepsilon)P_m + \varepsilon P_h \\
&= (1 - \varepsilon)\mu\sigma_N AU + \varepsilon\eta(T)\frac{\partial U}{\partial h} AU
\end{aligned}
\tag{9.43}
$$

where
$\varepsilon$ is the lubrication factor;
in the fully hydrodynamic ($\varepsilon = 1$), and mixed lubrication ($\varepsilon = 0$);
$\mu$ is the friction coefficient of the bearing surface;
$\sigma_N$ is the normal stress on the bearing;
$\eta$ is the oil viscosity;
h is the oil-film thickness;
A is the bearing surface;
U is the moving relative velocity;

In case of the small bearing surface, the oil-film thickness reduces itself to increase the oil pressure in the bearing clearance against the given bearing load. At further increasing the bearing load, the oil-film thickness becomes smaller than the limit oil-film thickness. Thus, the mixed lubrication regime occurs in the bearing in which the friction coefficient $\mu$ and normal stress $\sigma_N$ significantly increase due to the adhesive and abrasive frictions in the bearing surface. According to eq. (9.43), the friction power $P_m$ extremely increases, much higher than the friction power $P_h$ in the fully hydrodynamic lubrication. As a result, the effective friction power in the bearing increases much more although we reduce the bearing surface. On the contrary, we enlarge the bearing surface excessively; in turn, the oil-film thickness increases, leading to the fully hydrodynamic lubrication in the bearing. In this case, the hydrodynamic friction power $P_h$ significantly increases due to the large bearing surface and high oil viscosity. Therefore, the effective bearing friction power also increases by enlarging the bearing surface. The friction power reaches the minimum at the oil-film thickness $h_{min}$ at which the fully hydrodynamic lubrication begins, as illustrated in Fig. 9.23.

Figure 9.23 shows the behavior of the friction power of the bearing in the mixed and fully hydrodynamic lubrication regimes. The result indicates that decreasing the bearing surface to reduce the friction power in the bearing is not always correct; sometimes, we obtain the negative result of increasing instead of reducing the friction power of the bearing. The reduction of the bearing friction by decreasing the bearing surface is only correct when the working condition of the bearing is in the fully hydrodynamic lubrication ($h \geq h_{min}$). In the mixed lubrication ($h < h_{min}$), we must enlarge the bearing surface to reduce the bearing friction, as shown in Fig. 9.23.
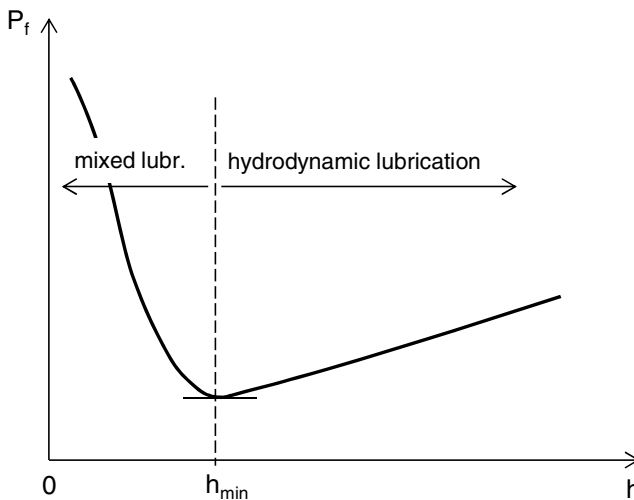


**Fig. 9.23** Effective friction power in the bearing versus oil-film thickness

### 9.7.5  Mohr's Circle Method

The normal force and bending moment caused by the friction force act upon the asperities of the bearing, as displayed in Fig. 9.24. The asperities begin deforming; at increasing the external forces and moments, the plastic deformation takes place at the asperities. When the normal and shear stresses exceed their ultimate stresses, the asperities rupture in the bearing clearance, leading to abrasive wears. In the following section, we compute the general stresses by using the Mohr's circle method.
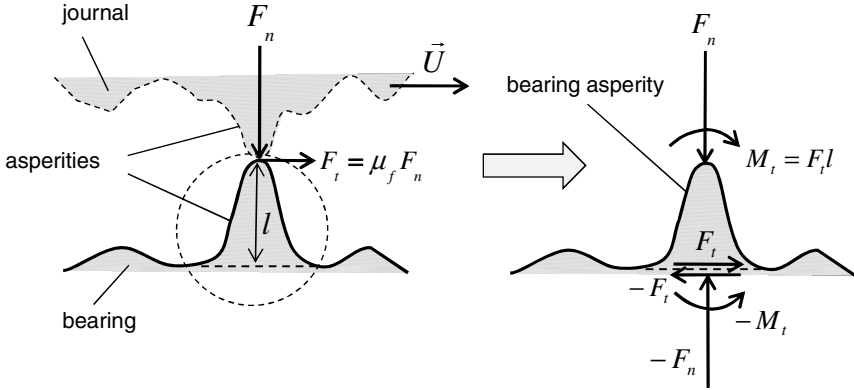


**Fig. 9.24** Acting loads on the bearing asperity

The principle normal stresses are computed by solving the cubic stress equation of $\sigma$ given in [3].

$$\begin{vmatrix} (\sigma_x - \sigma) & \tau_{xy} & \tau_{zx} \\ \tau_{xy} & (\sigma_y - \sigma) & \tau_{yz} \\ \tau_{zx} & \tau_{yz} & (\sigma_z - \sigma) \end{vmatrix} = 0 \qquad (9.44)$$

Thus,

$$\sigma_1, \sigma_2 = \left( \frac{\sigma_x + \sigma_y}{2} \right) \pm \sqrt{\left( \frac{\sigma_x - \sigma_y}{2} \right)^2 + \tau_{xy}^2} \qquad (9.45)$$

and

$$\sigma_3 = \sigma_z \qquad (9.46)$$

The material failure takes place if the maximum tensile stress $\sigma_1$ in Eq. (9.45) due to bending moment exceeds the ultimate tensile stress $\sigma_u$, or the maximum shear stress $\tau_{max}$ in Eq. (9.49) is larger than the critical shear stress $\tau_c$.

In a three-dimensional case, all six components of normal and shear stresses in the directions of x, y, and z exist in the asperities. By using the coordinate

transformation between the inertial coordinate system (x,y,z) and coordinate system (1,2,3) of the principle normal stress, we obtain only the normal stresses $\sigma_1$, $\sigma_2$, and $\sigma_3$ in the directions 1, 2, and 3 where the shear stresses $\tau_1$, $\tau_2$, and $\tau_3$ equal zero [3]. Having applied the Mohr's circle method, the related stresses in the coordinate system (1,2,3) are graphically calculated from the principle normal stresses $\sigma_1$, $\sigma_2$, and $\sigma_3$, as displayed in Fig. 9.25.
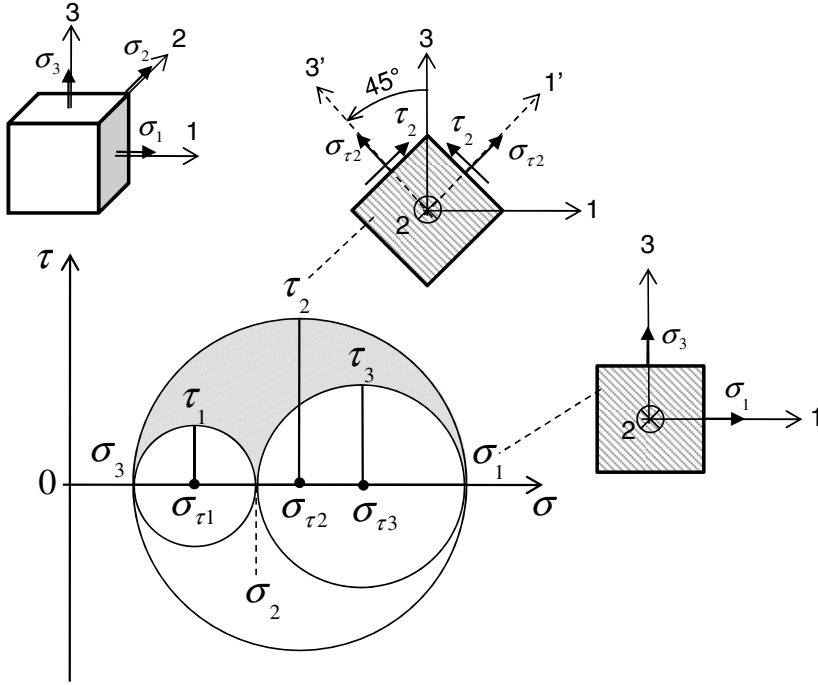


**Fig. 9.25** Mohr's circles for a three-dimensional state of stress

The maximum principle shear stresses occurring in the planes inclined 45° to the principle normal stress axes in the directions 1, 2, and 3 are calculated.

$$\tau_1 = \frac{|\sigma_2 - \sigma_3|}{2}; \ \tau_2 = \frac{|\sigma_1 - \sigma_3|}{2}; \ \tau_3 = \frac{|\sigma_1 - \sigma_2|}{2} \tag{9.47}$$

The normal stresses perpendicular to the principle shear stresses result in

$$\sigma_{\tau1} = \frac{\sigma_2 + \sigma_3}{2}; \sigma_{\tau2} = \frac{\sigma_1 + \sigma_3}{2}; \ \sigma_{\tau3} = \frac{\sigma_1 + \sigma_2}{2} \tag{9.48}$$

The maximal shear stress for any plane in the asperity is the largest shear stress of the principle shear stresses given in Eq. (9.47).

$$\tau_{max} = \max(\tau_1, \tau_2, \tau_3) \tag{9.49}$$

All states of stress ($\sigma$, $\tau$) in the asperities occur in the shaded area, which lies in the upper half plane outside the two small circles and inside the large one displayed in the Mohr's circle diagram, as shown in Figure 9.25.

## 9.8 Wear Mechanisms in the Oil-Film Bearings

Oil-film bearings work on the hydrodynamic principle in the various lubrication regimes, such as fully hydrodynamic, mixed, and boundary lubrications in the Stribeck curve, as displayed in Fig. 9.7.

Theoretically, wear in the bearing does not occur or is negligibly small in the fully hydrodynamic lubrication because the oil film is thick enough to prevent wear in the bearing. In case of clean oils, only the hydrodynamic friction occurs in the oil film, as discussed in Section 9.3. However, oil contaminated with hard particles causes wear in the bearing due to the adhesion and abrasion forces between the bearing and journal. As reducing the oil-film thickness below the limit oil-film thickness, the mixed and boundary lubrications take place in the bearing clearance. The asperities of the bearing and journal surfaces slide to each other, leading to the plastic deformation due to thermo-mechanical loads acting on the asperities. As a reason, it causes at first the *adhesive wear* at the asperities due to plastic shearing, then losses the material because of their asperities break. In the abrasive wear, the hard particles in the contaminated oil, broken bits of the asperities, and still remaining asperities of the surfaces abrade the surface of the softer material; therefore, the material is removed from the bearing surface with time, leading to wear. In the mixed and partial boundary lubrications, the wear process in the bearing begins with the adhesive friction at the asperities of the roughness surfaces. Wears continue further by loss of the asperities, and it is eventually intensified by the abrasive wear of the hard particles in the boundary lubrication, leading to seizure and damage of the bearing.

Figure 9.26 demonstrates the adhesive wear mechanism where the asperities in the softer material bearing (brass) contact the other asperities of the moving journal of hard materials (highly alloyed steels) under the unbalance force or bending moment acting upon the bearing asperities.
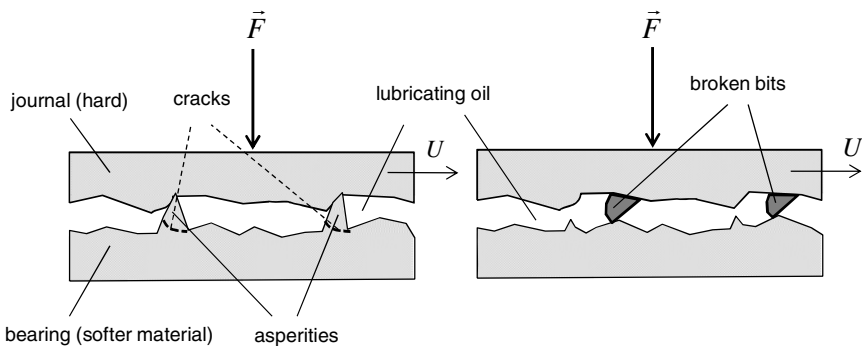


**Fig. 9.26** Adhesive and abrasive wear in the bearing clearance

According to the deformation mechanism, as shown in Fig. 9.4, the asperities of the bearing surface begin deforming plastically under the acting loads. When the tensile and shear stresses in the asperities exceed the ultimate tensile and critical shear stresses, some asperities of the bearing and journal break off. Then, the broken bits together with the hard particles in lubricating oil cause abrasive wear in the bearing.

The theoretical critical shear stress of a perfect material without any atomic dislocations in the material grid structure is given in [3] and [9].

$$\tau_{c,th} = \frac{Gb}{2\pi\, h} \approx \frac{G}{10} \approx 10^2 \sigma_o \tag{9.50}$$

where
G is the shear modulus;
b, h are the distance between the atoms in horizontal and vertical direction
(b/h ~ 0.5 to 1);
$\sigma_o$ is the yield stress of material.

However, the real critical shear stress in an imperfect pure metal can be reduced by a factor of 300 – 10,000 of its theoretical value.

The theoretical tensile stress to break chemical bonds between the atoms in a perfect metal grid is estimated at

$$\sigma_{u,th} \approx \frac{E}{10} \tag{9.51}$$

where E is the elasticity modulus of material.

In fact, the real ultimate tensile stress of the common metals could be lower than the theoretical value by a factor of 10 – 100.

The contact types of wears are normally classified into *sliding, rolling, erosive, fretting,* and *slurry wear* [1].

The *sliding wear* occurs when the hard and soft surfaces move to each other; the hard asperities slide over the soft ones; hence, the soft material has been removed due to plastic deformation and fracture of asperities.

The *rolling wear* happens when the hard particles floating in lubricating oil roll over two moving surfaces in the small gap, such as the convergent clearance of the radial bearing and axial clearance of the thrust bearing (s. Figs 9.27 and 9.28). The asperities of the surfaces are removed because of their fractures.

The *erosive wear* is induced by the impact of the particles in lubricating oil or hard asperities against the surface. The impacting kinetic energy of the hard particles and moving broken asperities deforms the asperities at the contact zones and causes material fracture when the tensile and shear stresses exceed the ultimate and critical values.

The *fretting wear* is caused by the repeated cyclical rub between two moving surfaces, especially in the bearing. Due to the continuously periodic rubbing, the

bonding force between the atoms is weakened after repeating cyclical rub over a long operating period. Hence, the asperities are broken and removed from the surface.

Finally, the *slurry wear* occurs when the abrasive particles in lubricating oil move in the bearing clearance and abrade the asperities and surface of the bearing.

In the radial bearings, lubricating oil contaminated with hard particles is supplied to the bearing. The hard particles enter the bearing convergent wedge by pumping effect of the rotating journal and cause abrasive wear in the bearing that is classified into three different types of wears A, B, and C (s. Figs 9.27 and 9.29).
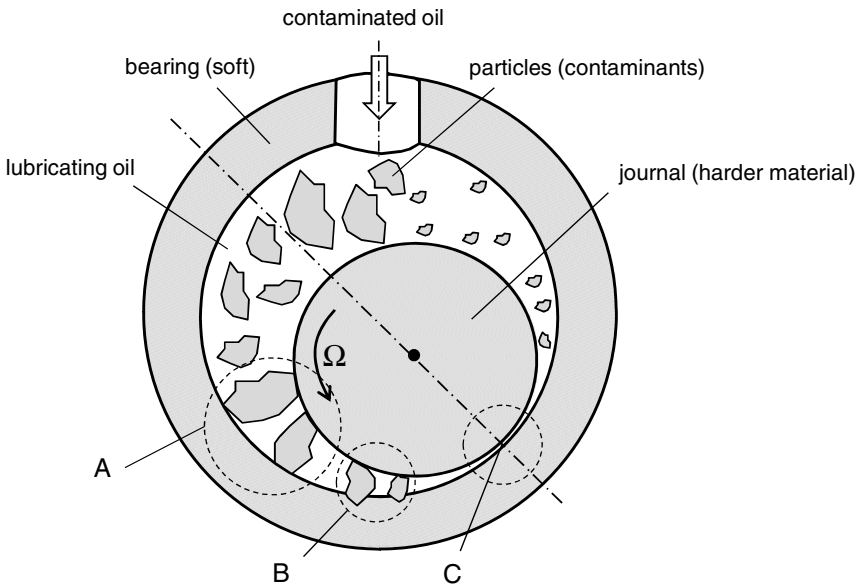
**Fig. 9.27** Abrasive wear in a radial bearing

In the thrust bearings, the oil-film thickness becomes large at a small thrust load; hence, the hard particles in lubricating oil enter the axial bearing clearance between the thrust bearing and thrust rings. At increasing the thrust load, the oil-film thickness decreases to the minimum of the axial clearance. The large thrust load induces the friction force between the particles and surfaces; the friction force causes abrasive wear in the surfaces of the thrust bearing and thrust rings, especially in the soft bearing surface. Figure 9.28 demonstrates the wear mechanism in the thrust bearing. Finally, the abrasive wear leaves deep wear traces in the bearing and disk surfaces (s. Fig. 9.29). These wear traces do not cause the failure of the bearing at once. However, the bearing failure could happen if the abrasive wear is continuously fortified until the mixed and boundary lubrications take place in the bearing clearance.
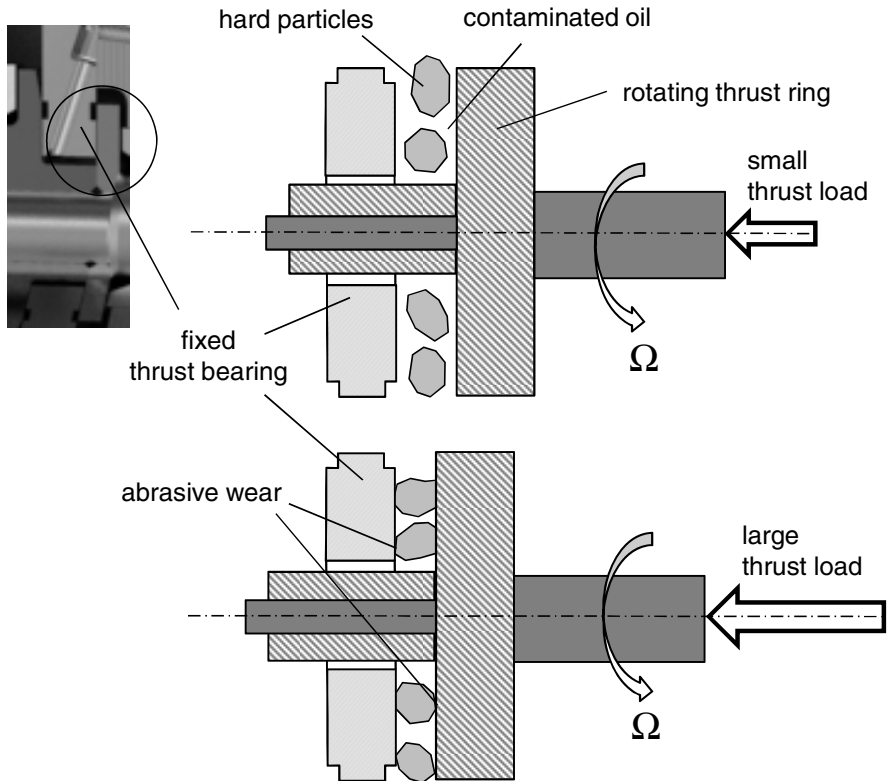
**Fig. 9.28** Abrasive wear in a thrust bearing

Figures 9.27 and 9.28 show the most typical types of the abrasive wear occurring in the radial and thrust hydrodynamic bearings of the automotive turbochargers. The abrasive wear is classified into three different types A, B, and C according to [9], as shown in Fig. 9.29 at which the journal material of highly alloyed steels is much harder than the bearing material of brass.

- Type A, called the *three-body abrasive wear* shows the hard particles slide and roll on the bearing and journal surfaces, touch the asperities, deform them plastically, and finally remove them from the bearing surface.
- Type B, called the *two-body abrasive wear* shows the hard particles and broken bits of the asperities are embedded in the softer bearing surface. Due to rotation, they abrade the journal surface as if a sand paper slides on it with the high speeds. To prevent the journal from the abrasive wear, its surface is treated by nitriding. Nitriding is a heat-treating process of diffusing nitrogen ($N_2$) into the surface to create a hard coating layer on the surface, such as boron nitride (BN), titanium nitride (TiN), and silicon nitride ($Si_3N_4$).
- Type C, called the *surface abrasive wear* shows the hard asperities of the journal surface abrade the softer bearing surface in case of poorly lubricated oil film in the partly and boundary lubrications. It mostly occurs at the minimum

oil-film thickness in the bearing clearance, as displayed in Figs 9.27, 9.28, and 9.29. The abrasive wear leaves wear traces in the bearing surface, as shown in Fig. 9.29.
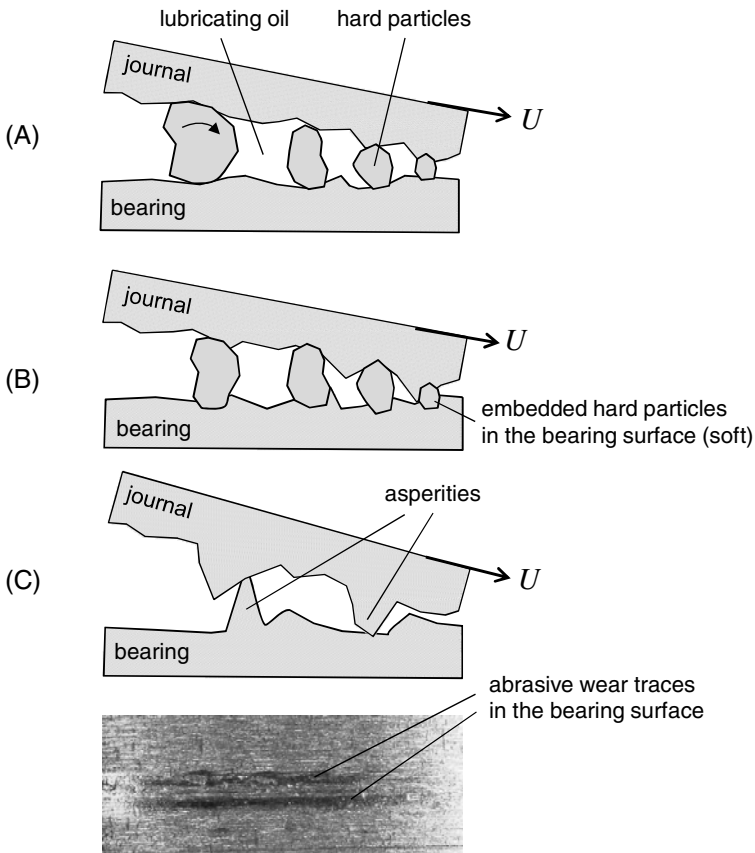


**Fig. 9.29** Types of abrasive wears in the bearing convergent wedge of a radial bearing

In the point of view of the tribological mechanism of wears, *fatigue, and corrosive wears* should be taken into account besides the adhesive and abrasive wears.

*Fatigue wear* is generated by the repeated cyclical friction between two moving surfaces after a certain number of rubbing cycles. It is caused by the fatigue fracture where the yield stress of material strongly reduces at increasing the numbers of rubbing cycles according to the Woehler curve. There are two kinds of fatigue wear, the high-cycle fatigue wear (HCFW) occurs at the high number of rubbing cycles; the low-cycle fatigue wear (LCFW), at the low number of rubbing cycles.

*Corrosive wear* takes place when materials of the surfaces contact a corrosive substance (liquid or gas), such as dissolved water, fuel, and diffused air in lubricating oil, that induces tribochemical reactions (chemical and electrochemical) in the surfaces of the journal and bearing; therefore, materials of the surfaces are removed by the tribochemical corrosion.
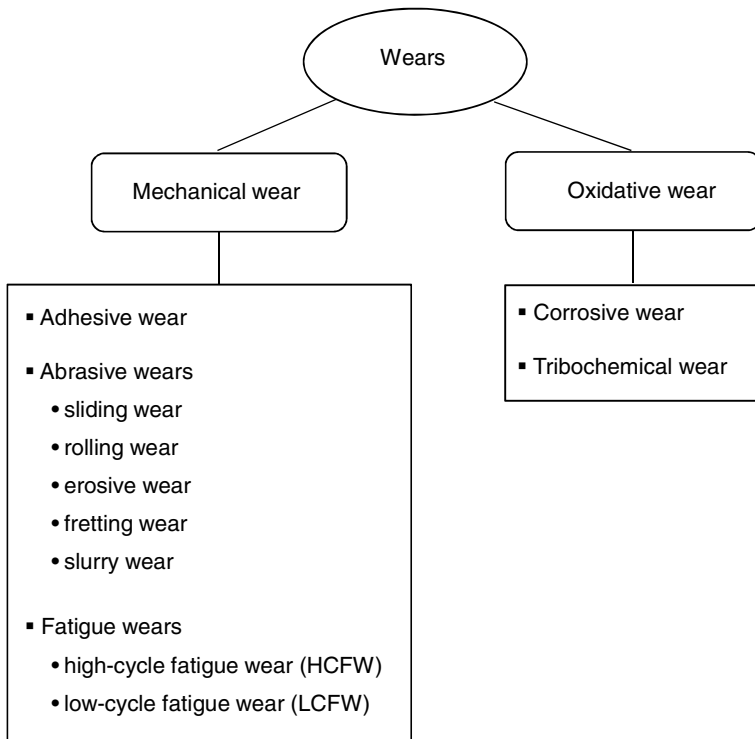
**Fig. 9.30** Classification of wear mechanisms

Adhesive, abrasive, and fatigue wears are followed by the plastic deformation and fracture of materials; hence, one calls them "*mechanical wear*". On the contrary, corrosive wear is caused by the tribochemical reactions contacting a corrosive medium; therefore, it is called "*oxidative wear*", as displayed in Fig. 9.30.

Used and old lubricating oil in the automotive turbochargers contains besides hard particles about 5% volumetric dissolved water, and approximately 10% volumetric dissolved fuel. Therefore, in order to prevent the bearings from wears, both lubricating oil and oil filter must be regularly replaced in every period of 12 months to 18 months at an average driving rate of 10,000 km/year according to ISO 4406-1999: 24/23/18.

# References

1. Bhushan, B.: Modern Tribology Handbook – Two-Volume Set. CRC Press Inc. (2000)
2. Bhushan, B.: Introduction to Tribology. J. Wiley and Sons Inc. (2002)
3. Dowling, N.E.: Mechanical Behavior of Materials, 3rd edn. Pearson-Prentice Hall (2007)

4. Hamrock, B., Schmid, S.R., Jacobson, B.O.: Fundamentals of Fluid Film Lubrication, 2nd edn. Marcel Dekker Inc. (2004)
5. Johnson, K.L.: Contact Mechanics. Cambridge University Press (1985)
6. Kennedy, et al.: Tribology, Lubrication, and Bearing Design. In: The CRC Hand-book of Mechanical Engineers. CRC Press (1988)
7. Khonsari, M., Booser, E.: Applied Tribology and Bearing Design and Lubrication, 2nd edn. J. Wiley and Sons Ltd. (2008)
8. Mahr: Surface texture parameters. Mahr GmbH, Germany (1999)
9. Mate, C.M.: Tribology on the Small Scale. Oxford University Press (2008)

# Appendix A

## Transformation of the Rotating to Inertial Coordinate Systems

To calculate the moment acting upon the rotor by using the angular momentum theorem, the product rule of differentiation is applied. The resulting moment in the rotating coordinate system (x',y',z') is transformed into the inertial coordinate system (x,y,z). Therefore, the relations between the unit vectors of two coordinate systems are needed.
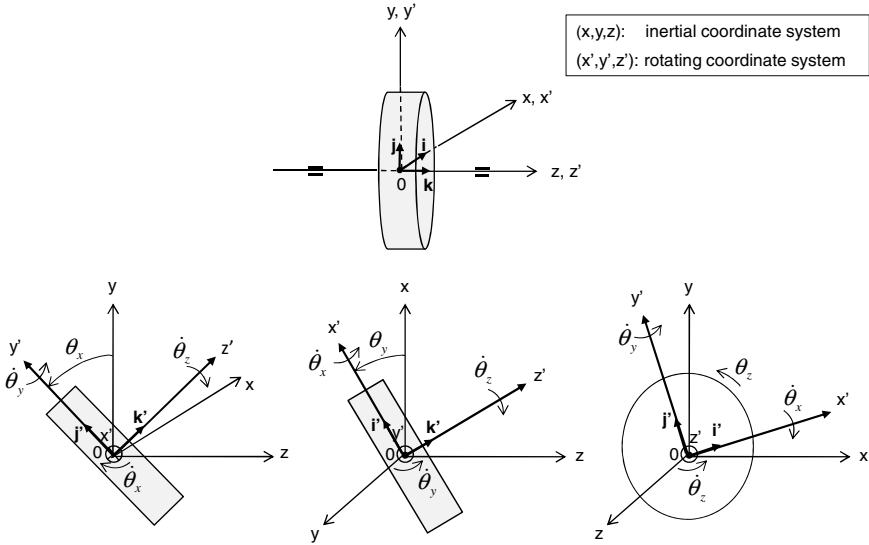


**Fig. 1** Transformation between the rotating and inertial coordinate systems

Two-dimensional angular position vector $\boldsymbol{\theta}$ is written in the rotating coordinate system (x',y',z') with $\theta_z = 0$.

$$\boldsymbol{\theta} = \theta_x \mathbf{i}' + \theta_y \mathbf{j}' \tag{1}$$

where

$\theta_x$, $\theta_y$, and $\theta_z$ are the proper Euler angles in the directions x', y', and z'.

The relation between the unit vectors (**i'**, **j'**, **k'**) and (**i**, **j**, **k**) of the rotating and inertial coordinate systems is derived [1].

$$\begin{pmatrix} \mathbf{i'} \\ \mathbf{j'} \\ \mathbf{k'} \end{pmatrix} = \mathbf{IR}_{\theta x} \mathbf{R}_{\theta y} \begin{pmatrix} \mathbf{i} \\ \mathbf{j} \\ \mathbf{k} \end{pmatrix} = \mathbf{R} \begin{pmatrix} \mathbf{i} \\ \mathbf{j} \\ \mathbf{k} \end{pmatrix} \tag{2}$$

where
**I** is the unit matrix;

$\mathbf{R}_{\theta x}$ and $\mathbf{R}_{\theta y}$ are the transform matrices in functions of $\theta_x$ and $\theta_y$, respectively.

$$\mathbf{R}_{\theta x} = \begin{pmatrix} 1 & 0 & 0 \\ 0 & \cos\theta_x & \sin\theta_x \\ 0 & -\sin\theta_x & \cos\theta_x \end{pmatrix} ; \; \mathbf{R}_{\theta y} = \begin{pmatrix} \cos\theta_y & 0 & -\sin\theta_y \\ 0 & 1 & 0 \\ \sin\theta_y & 0 & \cos\theta_y \end{pmatrix} \tag{3}$$

The transform matrix **R** is calculated from **I**, $\mathbf{R}_{\theta x}$ and $\mathbf{R}_{\theta y}$ as follows:

$$\mathbf{R} \equiv \mathbf{IR}_{\theta x}\mathbf{R}_{\theta y} = \begin{pmatrix} \cos\theta_y & 0 & -\sin\theta_y \\ \sin\theta_x \sin\theta_y & \cos\theta_x & \sin\theta_x \cos\theta_y \\ \cos\theta_x \sin\theta_y & -\sin\theta_x & \cos\theta_x \cos\theta_y \end{pmatrix} \tag{4}$$

Therefore,

$$\begin{cases} \mathbf{i'} = \cos\theta_y\, \mathbf{i} - \sin\theta_y\, \mathbf{k} \\ \mathbf{j'} = (\sin\theta_x \sin\theta_y)\mathbf{i} + \cos\theta_x\, \mathbf{j} + (\sin\theta_x \cos\theta_y)\mathbf{k} \\ \mathbf{k'} = (\cos\theta_x \sin\theta_y)\mathbf{i} - \sin\theta_x\, \mathbf{j} + (\cos\theta_x \cos\theta_y)\mathbf{k} \end{cases} \tag{5}$$

At small angles $\theta_x, \theta_y \ll 1$ with $\cos\theta \approx 1-\theta^2/2$ and $\sin\theta \approx \theta$, one obtains

$$\begin{cases} \mathbf{i'} \approx \mathbf{i} - \theta_y\mathbf{k} \approx \mathbf{i} \\ \mathbf{j'} \approx \mathbf{j} + \theta_x\mathbf{k} \approx \mathbf{j} \\ \mathbf{k'} \approx \theta_y\mathbf{i} - \theta_x\mathbf{j} + \mathbf{k} \approx \mathbf{k} \end{cases} \tag{6}$$

Generally, the three-dimensional angular position vector $\boldsymbol{\theta}$ is written in the rotating coordinate system (x',y',z').

$$\boldsymbol{\theta} = \theta_x\mathbf{i'} + \theta_y\mathbf{j'} + \theta_z\mathbf{k'} \tag{7}$$

The relations of the unit vectors are formulated by the transform matrices.

$$\begin{pmatrix} \mathbf{i}' \\ \mathbf{j}' \\ \mathbf{k}' \end{pmatrix} = \mathbf{R}_{\theta z}\,\mathbf{R}_{\theta x}\,\mathbf{R}_{\theta y} \begin{pmatrix} \mathbf{i} \\ \mathbf{j} \\ \mathbf{k} \end{pmatrix} \equiv \mathbf{R}^{*} \begin{pmatrix} \mathbf{i} \\ \mathbf{j} \\ \mathbf{k} \end{pmatrix} \tag{8}$$

with
the transform matrices $\mathbf{R_{\theta x}}$ and $\mathbf{R_{\theta y}}$ given in Eq. (3) and

$$\mathbf{R}_{\theta z} = \begin{pmatrix} \cos\theta_z & \sin\theta_z & 0 \\ -\sin\theta_z & \cos\theta_z & 0 \\ 0 & 0 & 1 \end{pmatrix} \tag{9}$$

The transformation matrix R* is calculated from $\mathbf{R_{\theta z}}$, $\mathbf{R_{\theta x}}$ and $\mathbf{R_{\theta y}}$.

$$\mathbf{R}^{*} = \begin{pmatrix} \cos\theta_z\cos\theta_y + \sin\theta_z\sin\theta_x\sin\theta_y & \sin\theta_z\cos\theta_x & -\cos\theta_z\sin\theta_y + \sin\theta_z\sin\theta_x\cos\theta_y \\ -\sin\theta_z\cos\theta_y + \cos\theta_z\sin\theta_x\sin\theta_y & \cos\theta_z\cos\theta_x & \sin\theta_z\sin\theta_y + \cos\theta_z\sin\theta_x\cos\theta_y \\ \cos\theta_x\sin\theta_y & -\sin\theta_x & \cos\theta_x\cos\theta_y \end{pmatrix} \tag{10}$$

At small angles $\theta_x$, $\theta_y$, $\theta_z \ll 1$ with $\cos\theta \approx 1-\theta^2/2$ and $\sin\theta \approx \theta$, one obtains

$$\begin{cases} \mathbf{i}' \approx \mathbf{i} + \theta_z\mathbf{j} - \theta_y\mathbf{k} \approx \mathbf{i} \\ \mathbf{j}' \approx -\theta_z\mathbf{i} + \mathbf{j} + \theta_x\mathbf{k} \approx \mathbf{j} \\ \mathbf{k}' \approx \theta_y\mathbf{i} - \theta_x\mathbf{j} + \mathbf{k} \approx \mathbf{k} \end{cases} \tag{11}$$

# Appendix B

## Calculating Value x from X in the Log₁₀ Scale

The value x at an arbitrary ratio ξ is interpolated from the measured values X at an arbitrary ratio ξ in the $\log_{10}$ scale, as shown Fig. 1.
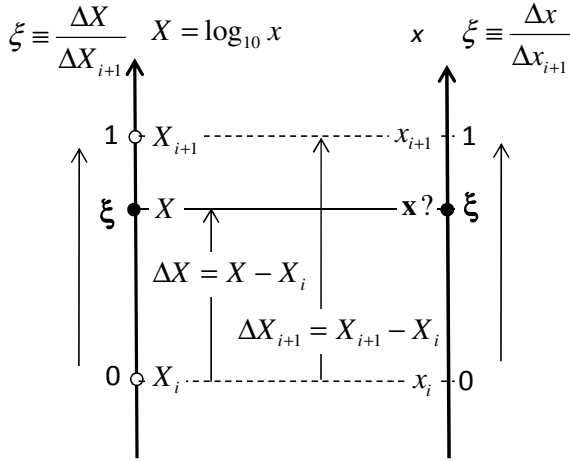


**Fig. 1** Calculating value x from X in the $\log_{10}$ scale

The intervals $\Delta X$ and $\Delta X_{i+1}$ in the $\log_{10}$ scale are calculated.

$$\Delta X = X - X_i = \log_{10}\left(\frac{x}{x_i}\right) \tag{1}$$

$$\Delta X_{i+1} = X_{i+1} - X_i = \log_{10}\left(\frac{x_{i+1}}{x_i}\right) \tag{2}$$

Having divided Eq. (1) to Eq. (2), one obtains

$$\log_{10}\left(\frac{x}{x_i}\right) = \left(\frac{\Delta X}{\Delta X_{i+1}}\right)\log_{10}\left(\frac{x_{i+1}}{x_i}\right) = \log_{10}\left(\frac{x_{i+1}}{x_i}\right)^{\left(\frac{\Delta X}{\Delta X_{i+1}}\right)} \tag{3}$$

Thus,

$$\left(\frac{x}{x_i}\right) = \left(\frac{x_{i+1}}{x_i}\right)^{\left(\frac{\Delta X}{\Delta X_{i+1}}\right)} = \left(\frac{x_{i+1}}{x_i}\right)^{\xi} = 10^{\xi} \tag{4}$$

where

$$\xi \equiv \frac{\Delta X}{\Delta X_{i+1}} = \frac{X - X_i}{X_{i+1} - X_i}; \ 0 < \xi < 1 \tag{5}$$

The corresponding value x of X in the $\log_{10}$ scale is computed from the ratio $\xi$ according to Eq. (4) where $\xi$ is the relative distance of X between $X_{i+1}$ and $X_i$. The values x are plotted for various values $\xi$ in case $x_i = 10^1$ in Figure 2. The results help us to calculate the value x at the ratio $\xi$ by interpolating the measured values at the ratio $\xi$ in the $\log_{10}$ scale.

**Table 1** Computed values x from $\xi$ of the $\log_{10}$ scale

| $\xi$ | $x/x_i$ | $x = x_i . 10^{\xi}$ for | | |
|---|---|---|---|---|
| | | $x_i = 10^0$ | $x_i = 10^1$ | $x_i = 10^2$ |
| 0,00 | 1 | 1,00 | 10,00 | 100,00 |
| 0,05 | 1,12 | 1,12 | 11,22 | 112,20 |
| 0,10 | 1,26 | 1,26 | 12,59 | 125,89 |
| 0,15 | 1,41 | 1,41 | 14,13 | 141,25 |
| 0,20 | 1,58 | 1,58 | 15,85 | 158,49 |
| 0,25 | 1,78 | 1,78 | 17,78 | 177,83 |
| 0,30 | 2,00 | 2,00 | 19,95 | 199,53 |
| 0,35 | 2,24 | 2,24 | 22,39 | 223,87 |
| 0,40 | 2,51 | 2,51 | 25,12 | 251,19 |
| 0,45 | 2,82 | 2,82 | 28,18 | 281,84 |
| 0,50 | 3,16 | 3,16 | 31,62 | 316,23 |
| 0,55 | 3,55 | 3,55 | 35,48 | 354,81 |
| 0,60 | 3,98 | 3,98 | 39,81 | 398,11 |
| 0,65 | 4,47 | 4,47 | 44,67 | 446,68 |
| 0,70 | 5,01 | 5,01 | 50,12 | 501,19 |
| 0,75 | 5,62 | 5,62 | 56,23 | 562,34 |
| 0,80 | 6,31 | 6,31 | 63,10 | 630,96 |
| 0,85 | 7,08 | 7,08 | 70,79 | 707,95 |
| 0,90 | 7,94 | 7,94 | 79,43 | 794,33 |
| 0,95 | 8,91 | 8,91 | 89,13 | 891,25 |
| 1,00 | 10 | 10,00 | 100,00 | 1000,00 |
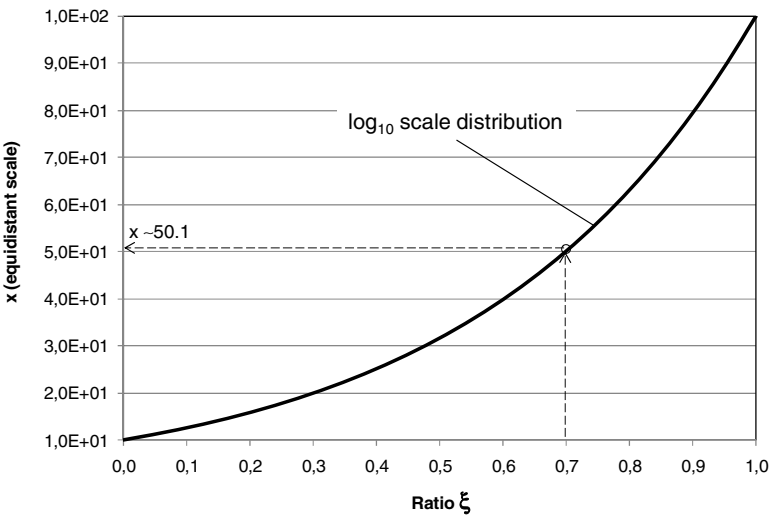
**Fig. 2** Calculating x from the $\log_{10}$ scale distribution X at $\xi = 0.7$

# Appendix C

## Solutions of the Characteristic Equation with Complex Coefficients

The characteristic quadratic equation with complex coefficients is derived from the vibration equation [2].

$$D(s) \equiv s^2 + (a + jb)s + (c + jd) = 0 \qquad (1)$$

where

$$s = (\alpha \pm j\omega_n) \in \mathbf{C} \text{ are the complex eigenvalues;}$$

$$a, b, c, d \in \mathbf{R} \text{ are the real numbers.}$$

By solving the characteristic equation $D(s) = 0$, the eigenvalue s results in

$$s_{1,2} = -\left(\frac{a + jb}{2}\right) \pm \sqrt{\left(\frac{a + jb}{2}\right)^2 - (c + jd)} \qquad (2)$$

$$= \alpha \pm j\omega_n$$

After calculating and rearranging the real and imaginary terms of the eigenvalue, one obtains

$$\alpha = -\frac{a}{2} \pm \frac{1}{\sqrt{2}}\left[\left(\frac{a^2 - b^2}{4} - c\right) + \sqrt{\left(\frac{a^2 - b^2}{4} - c\right)^2 + \left(\frac{ab}{2} - d\right)^2}\right]^{\frac{1}{2}}$$

$$(3)$$

and

$$\omega_n = \frac{b}{2} \pm \frac{1}{\sqrt{2}}\left[-\left(\frac{a^2 - b^2}{4} - c\right) + \sqrt{\left(\frac{a^2 - b^2}{4} - c\right)^2 + \left(\frac{ab}{2} - d\right)^2}\right]^{\frac{1}{2}}$$

$$(4)$$

Necessary condition for the rotordynamic stability is that the real term $\alpha$ of the eigenvalue must be negative (s. Section 4.2).

$$\alpha = -\frac{a}{2} \pm \frac{1}{\sqrt{2}} \left[ -E + \sqrt{E^2 + F^2} \right]^{\frac{1}{2}} < 0 \tag{5}$$

within

$$E \equiv -\left( \frac{a^2 - b^2}{4} - c \right) = -\left( \frac{a^2 - b^2}{4} \right) + c \tag{6a}$$

$$F \equiv \left( \frac{ab}{2} - d \right) \tag{6b}$$

Thus, the stability condition ($\alpha < 0$) for the rotor given in eq. (5) becomes after a few calculation steps.

$$a(ac + bd) - d^2 \geq 0 \tag{7}$$

# Appendix D

## Normal Distribution Density Function and Probability Function

The normal distribution density function is defined with parameters $\bar{z}$ and $\sigma$ as follows:

$$p(z) = \frac{1}{\sigma\sqrt{2\pi}} \exp\left[ -\frac{1}{2}\left( \frac{z - \bar{z}}{\sigma} \right)^2 \right] \tag{1}$$

where
$\bar{z}$ is the mean value of the sampling values;
$\sigma$ is the standard deviation resulted from the sampling values.

$$\sigma = \sqrt{\frac{1}{(N-1)} \sum_{i=1}^{N} (z_i - \bar{z})^2} \tag{2}$$

within

$$\bar{z} = \frac{1}{N} \sum_{i=1}^{N} z_i \tag{3}$$
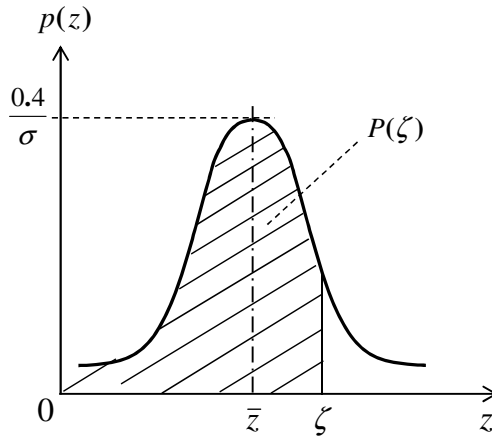


**Fig. 1** Distribution density function p(z) and its probability function

The normal distribution function is called the *Gaussian density function* with a bell shape; its probability distribution function is calculated by integrating p(z) from -∞ to ζ. This integrated value $P(\zeta)$ is the area under the bell curve, as shown in Fig. 1.

$$P(\zeta) = \frac{1}{\sigma\sqrt{2\pi}} \int_{-\infty}^{\zeta} \exp\left[-\frac{1}{2}\left(\frac{z - \bar{z}}{\sigma}\right)^2\right] dz \tag{4}$$

By substituting z by the new dimensionless variable,

$$c \equiv \frac{z - \bar{z}}{\sigma} \tag{5}$$

the normal distribution function p(z) is written in

$$p(c) = \frac{1}{\sqrt{2\pi}} \exp\left[-\frac{c^2}{2}\right] \tag{6}$$

The new probability function is written in the new variable c.

$$P(c) = \frac{1}{\sqrt{2\pi}} \int_{-\infty}^{c} \exp\left[-\frac{1}{2}c^2\right] dc \tag{7}$$
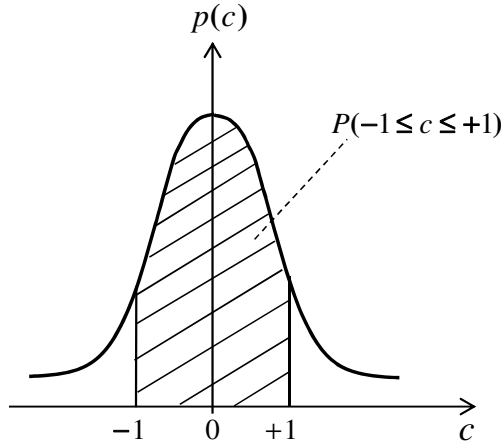


**Fig. 2** Distribution density function p(c) and its probability function P(c)

Thus,

$$P(-1 \le c \le +1) = \frac{1}{\sqrt{2\pi}} \int_{-1}^{1} \exp\left[-\frac{1}{2}c^2\right] dc \tag{8}$$

The probability distribution values for various parameters are calculated from Eq. (8).

$$\begin{cases} P(-1 \leq c \leq +1) = 68.3\% \\ P(-2 \leq c \leq +2) = 95.4\% \\ P(-3 \leq c \leq +3) = 99.7\% \\ P(-4 \leq c \leq +4) = 99.99\% \end{cases} \tag{9}$$

This result indicates that a production with $\pm 3\sigma$ would deliver 99.7% of the products that fulfill the given lowest and highest tolerances.

# References

1. Adams Jr., M.L.: Rotating Machinery Vibration. CRC, Taylor and Francis (2001)
2. Muszýnska, A.: Rotordynamics. CRC, Taylor and Francis (2005)
3. Taylor, J.R.: An Introduction to Error Analysis. University Science Books (2005)

# Further Readings

1. Adams Jr., M.L.: Rotating Machinery Vibration. CRC, Taylor and Francis (2001)
2. Bently, D.E., Hatch, C.: Fundamentals of Rotating Machinery Diagnostics. Bently Pressurized Bearing Press (2002)
3. Childs, D.: Turbomachinery Rotordynamics. J. Wiley and Sons Inc. (1993)
4. Den Hartog, J.P.: Mechanical Vibrations. McGraw-Hill (1956)
5. Ehrich, F.: Handbook of Rotordynamics. Krieger Publishing Company (2004)
6. Gasch, R., Nordmann, R., Pfuetzner, H.: Rotordynamik, vol. 2. Auflage, Springer (2006)
7. Genta, G.: Dynamics of Rotating Systems. Springer, Heidelberg (2005)
8. Goodwin, M.J.: Dynamics of Rotor Bearing Systems. Thomson Learning (1989)
9. Gunter, E.J.: Dynamic Stability of Rotor-Bearing Systems. NASA SP-113 (1966)
10. Hori, Y.: Hydrodynamic lubrication. Springer, Heidelberg (2006)
11. Kraemer, E.: Rotordynamics of Rotors and Foundations. Springer, Heidelberg (1993)
12. Lee, C.W.: Vibration Analysis of Rotors. Kluwer Academic (1993)
13. Muszýnska, A.: Rotordynamics. CRC, Taylor and Francis (2005)
14. Neville, F., Rieger, N.F.: Balancing of Rigid and Flexible Rotors. Shock and Vibration Information Center (1986)
15. Rao, J.S.: Rotor Dynamics, 3rd edn. New Age Intl. Publishers (2007)
16. Rieger, N.F.: Rotordynamics 2 - Problems in Turbomachinery. CISM Courses and Lectures No. 297 (1988)
17. Rieger, N.F.: Balancing of Rigid and Flexible Rotors. U.S. DoD (1986)
18. Rieger, N.F., Crofoot, J.F.: Vibrations of Rotating Machinery. Vibration Institute (1977)
19. Schweitzer, G., et al.: Magnetic Bearings. Springer, Heidelberg (2009)
20. Vance, J.: Rotordynamics of Turbomachinery. J. Wiley and Sons Inc. (1988)
21. Vance, J., Zeidan, Murphy, B.: Machinery Vibration and Rotordynamics. J. Wiley (2010)
22. Tondl, A.: Some problems of Rotor Dynamics. Chapman & Hall (1965)
23. Yamamoto, T., Ishida, Y.: Linear and Nonlinear Rotordynamics. J. Wiley and Sons Inc. (2001)
24. Wen, J.C., Gunter, J.: Introduction to Dynamics of Rotor-Bearing Systems. Eigen Technologies ETI (2001)
25. Wowk, V.: Machinery Vibration and Balancing. McGraw-Hill (1995)

# Index